UNIVERSITÀ
DEGLI STUDI
FIRENZE

DOTTORATO DI RICERCA IN
FISICA ED ASTRONOMIA

CICLO **XXXII**

Coordinatore:
Prof. **Raffaello D'Alessandro**

Experiments with strongly interacting Yb atoms in optical lattices

SETTORE SCIENTIFICO DISCIPLINARE: **FIS/03**

Dottorando
Dott. **Lorenzo Franchi**
Lorenzo Franchi

Tutore
Prof. **Leonardo Fallani**
Leonardo Fallani

Coordinatore
Prof. **Raffaello D'Alessandro**
Raffaello D'Alessandro

Anni accademici 2016-2019

Contents

1 | Introduction

During last decades the efforts regarding the research on theoretical and experimental atomic physics have been converted from a self-consistent physics branch based on species characterization to a multi-disciplinary field, based on the possibility to easily control atoms. The transformation of the field was principally caused by the development of pioneering experimental techniques to slow and confine atomic dilute gases [1]. The possibilities offered by atoms are various, they depend on the abundance and the variety of stable (and unstable) species and also on the availability of laser sources and emitters capable to properly excite narrow transitions between two nearly-stable atomic energetic levels.

Trapped atoms offer a rich framework where, by exploiting free-space interactions, quantum degeneracy regimes can be achieved in both bosons [2–4] and fermions [5]. A fundamental tool in order to employ atoms to mimic the Hamiltonians of ideal solid-state systems is the possibility to load atomic samples in spatially-ordered light structures, called optical lattices. Recently, the capabilities offered by atomic systems trapped in optical lattices allowed to simulate, by following the fundamental idea proposed by R. Feynman [6], a plethora of different and multi-disciplinary phenomenon such solid-states systems characterized by non-trivial topological order (induced by an effective intense magnetic field) [7–13], where interactions between atoms are nearly neglected, and systems dominated by interactions, as occur in lattice gauge theories or when the transition from a metallic conducting phase to an insulating phase is considered [14, 15].

Such an amount of different phenomena can be simulated by tailoring the coupling of the lattice Hamiltonian that is realized by the confined atoms, such as the hopping between lattice sites and hopping between lattice sites and the onsite interaction between atoms [16].

Moreover, by exploiting the internal atomic structure it is possible to precisely control the interaction strength between two atoms in (meta-) stable states by realizing experimentally the well-known Feshbach-Fano resonances [17–19]. The possibility to set interactions by exploiting a mixing potential between an open interacting channel and a closed scattering channel allowed the opening of a new field, based on the production of shallow-bound molecules, both homo- and heteronuclear [20]. The production of molecules supported by a Feshbach resonance via photoassociation spectroscopy [21] revealed to be a fundamental tool that permitted to finely characterize interactions between atoms and give rise to experimental quantum chemistry in regimes before unexplored [22].

Possibilities offered by the control of interactions via Feshbach resonances have been strongly characterized in elements of the first group of the periodic table of elements as Lithium (Li), Potassium (K), Rubidium (Rb), ... , in which the external electronic configuration is constituted by one electron and gives rise to magnetic couplings with an external magnetic field [23].

Recently, alkaline-earth (-like) atoms and alkaline earth metals (AEL) gained experimental and theoretical interest principally related to the possibility offered in the metrological field by the excitation of visible and UV clock transitions [24–26]. AEL atoms, in their neutral form and in the ground state, have a null total electronic momentum, resulting in a very low sensitivity to external magnetic fields. While the absence of magnetic coupling does not allow the interactions tuning by exploiting Feshbach resonances as it occurs in alkaline atoms, these atoms are characterized by highly symmetric ground states allowing the simulation of $\mathbb{SU}(\mathsf{N})$ systems [27]. This characteristic, that can be attributed in AEL atoms to the decoupling between electronic and nuclear atomic momenta, can be exploited to perform quantum simulation of a wealth of novel systems and constitutes a fundamental property of isotopes that have a nonzero nuclear spin, as it occurs for all the fermionic species and in particular for $^{173}\mathsf{Yb}$ and $^{87}\mathsf{Sr}$. This feature also ensures the absence of spin-changing collisions in ground state sublevels, implying that nuclear-spin mixtures are observationally stable. This attribute is fundamental for the study of transitions between different nuclear-spin states, for example by exploiting the two-photon Raman coupling [28, 29]. The degeneracy related to the $\mathbb{SU}(\mathsf{N})$ symmetry [30] can be controllably removed by applying a two-photon Raman coupling, allowing for the simulation of systems with broken symmetries.

Besides the possibility to induce couplings within the nuclear-spin degree of freedom, AEL atoms also offer the possibility to access a second, electronic degree of freedom; the possibility to address visible doubly-forbidden transitions between long-lived electronic clock states comprises a fantastic tool that allowed the building of optical lattice clocks improving metrological measurements and offering a richer platform for simulating complex systems [31, 32].

The main difference between the two internal degrees of freedom offered by AEL atoms is that the possibility to address ultranarrow optical clock transitions exists also for AEL bosonic isotopes [33] in which the nuclear-spin degree of freedom is not present because the total atomic momentum is absent.

The possibilities related to the excitation of long-lived metastable triplet levels, that, referring only to the lowest lying atomic levels are $^3\mathsf{P}_{(0,2)}$ (in Russell-Saunders

approximation they result doubly forbidden with respect to the electric dipole operator), are multiple. If bosonic atoms are considered, the metrological applications based on the clock transition at the state of the art have performances comparable to optical lattice clocks realized with fermionic isotopes [34]. Bosonic isotopes, requiring external fields in order to excite transitions from the ground state to long-lived states, have been proposed as good candidates in order to build a reliable and fast system in which controllable qu-bits could be realized [35]. Most of these applications, and in particular the possibility to create quantum computers with neutral atoms, crucially rely on the control of the scattering properties of atoms in different electronic states.
Regarding fermionic isotopes, the clock transitions recently allowed for the demonstration of spin-orbit coupling and quantum simulation via the synthetic dimension approach [36–38].As recently discovered, the clock transitions from the ground to the $^3\mathsf{P}_{(0,2)}$ states give rise to rich interactions between atoms in the ground and in the metastable states. The spin-exchange interaction that has been observed between ground and meta-stable states, supports also a new kind of Feshbach resonance, called Orbital Feshbach Resonance (OrbFR) [39, 40]. As occurs in magnetic Feshbach resonances for alkali atoms, also the OrbFR, that occurs in AEL atoms, supports the existence of extremely shallow homo-nuclear molecules. After considering the (s-wave) scattering parameters of all the AEL atoms that have been characterized experimentally, $^{173}\mathsf{Yb}$ is the only isotope in which the production and manipulation of Orbital Feshbach molecules (produced e.g. with photoassociation) is experimentally viable. Molecules generated by employing this atom, may lead to the investigation of fermionic superfluidity in still-unexplored regimes [41–43].

This thesis work fits in these last arguments, in particular with the characterization of interactions in bosonic $^{174}\mathsf{Yb}$ isotope by probing the clock transition between the singlet $^1\mathsf{S}_0$ ground state and the triplet $^3\mathsf{P}_0$ metastable excited state. Interactions and inelastic losses between ground-state and excited metastable-state atoms have been experimentally determined with high accuracy, resulting consistent with an independent evaluation realized in the same period by another group [44, 45]. The obtained values for the interactions among ground and metastable atoms for the specified nuclide constitute a first step in order to design an experimental system in which a quantum information platform can be realized by means of exploiting the clock transition of bosonic Yb atoms.
This work, by exploiting the internal degrees of freedom of $^{173}\mathsf{Yb}$ atoms, reports on a study of Orbital Feshbach molecules, showing experimentally the possibility to employ the nuclear degree of freedom in $^{173}\mathsf{Yb}$ atoms to manipulate and precisely detect homo-nuclear photoassociated molecules. This first result regarding this new kind of shallow-bound molecules allowed the characterization of interactions

between ground-state and metastable-state $^{173}\mathsf{Yb}$ atoms. This first intensive study of orbital Feshbach molecules is a fundamental step for future studies of the possibilities offered by these homo-nuclear molecules.
Finally, we exploited the ground state $\mathbb{SU}(\mathsf{N})$ symmetry and its controlled breaking via Raman coupling (in $^{173}\mathsf{Yb}$ $\mathsf{N} = 1...6$) to simulate the physical processes that are supposed to be driven by the hybridation of *d*-orbitals of iron atoms in iron based-superconductors, in which orbital-selective Mott insulating phases have been experimentally observed and are suspected to be the fundamental ingredient to achieve high-temperature superconductivity in these compounds.

This thesis has been organized as follows:

- Chapter 2 is dedicated to the theoretical description of the fundamental tools employed in this thesis work. After a textbook introduction about scattering and partial-wave description of collision processes, a fast review is devoted to the description of free-space interactions between neutral atoms. After stressing the principal results regarding ultracold neutral-atom interactions and *s*-wave scattering in free space, we introduce the optical lattices and the Hubbard model when the lattice depth allows the treating of the system by following the second-quantization approach; in this condition we describe the hopping term and the atomic interactions in deep optical lattices, highlighting the differences related to the atomic statistical behaviours;

- Chapter 3 is divided in two main topics, each related to alkaline earth atoms. The first section, that concerns two-electrons atoms (except Helium (He)), and in particular Alkaline-Earth, Alkaline Earth Metals and Alkaline Earth-Like atoms, is devoted to the description of general properties and transitions that can occur in these atoms, focusing on the possibility to address intercombination transitions in bosonic and fermionic isotopes. Also properties related to these transitions are analyzed, in particular describing the effect of external magnetic fields. The second section, that is devoted to the description of the Ytterbium (Yb) atom, in the first part describes the chemical and physical main properties and reactions, highlighting, in the following part, the experimental techniques and laser sources employed to slow and trap Yb gas from chuncks of this pure metal to reach degenerate regimes both for bosonic and fermionic isotopes;

- Chapter 4 is devoted to the description of the main results obtained during this thesis regarding the characterization of interaction and scattering parameters of $^{174}\mathsf{Yb}$ atoms. This chapter introduces the possibility to perform ultranarrow spectroscopy in an optical lattice without changing the atomic external degrees of freedom. This type of spectroscopy is therefore employed to detect interaction parameters of a bosonic atomic sample loaded in a deep 3D cubic optical lattice. The last part of this chapter describes the characterization of inelastic losses between ground and metastable states; these measurements are realized by observing the lifetime of excited atoms in different optical lattice geometries after an interaction-dependent excitation;

- Chapter 5 reports the theoretical and the experimental results regarding the production and manipulation of orbital Feshbach molecules by photoassociation of an atomic sample constituted by fermionic ^{173}Yb atoms confined in a deep 3D cubic optical lattice. The first part of this chapter is devoted to the description of the peculiar characteristic of ^{173}Yb, as the emergence of $\mathbb{SU}(\mathsf{N})$ symmetry in states characterized by absent total electronic momentum (J=0), the rich scattering collisions allowed by the spin-exchange interaction, and the subsequent orbital Feshbach resonance. The second part is instead devoted to the production, by means of photoassociation in a deep optical lattice, of orbital Feshbach molecules and their coherent control. In the last section of the chapter the nuclear-spin degree of freedom is exploited in order to efficiently detect orbital Feshbach molecules in a sample in which the number of un-bound atoms after the photoassociation pulse dominates over the molecules population. Moreover, we demonstrate the long lifetime of isolated molecules and provide first measurements on the lifetime of the molecular states in a many-body setting;

- Chapter 6 is dedicated to the description of the preliminar experimental results regarding the possibility to quantum simulate, by exploiting the internal degree of freedom of fermionic ^{173}Yb atoms, the physics emerging from hybridation of the d orbitals of iron atoms in iron-based superconductor materials. In particular, as a first result, the transition from metallic-phase to Mott-insulating behaviour is characterized by observing the mean number of doubly occupied sites in a $\mathbb{SU}(3)$ sample. The same technique is therefore exploited to determine an enhancement of localization in a system in which the $\mathbb{SU}(\mathsf{N})$ symmetry is controllably broken via the Raman coupling. State-dependent properties of the system are then probed by performing a spin-selective detection of doubly occupied sites;

- Chapter 7 is dedicated to the discussion of final consideration and future perspectives.

Publications

The results described in this thesis are reported in the following references (in chronological order):

- L. F. Livi, G. Cappellini, M. Diem, **L. Franchi**, C. Clivati, M. Frittelli, F. Levi, D. Calonico, J. Catani, M. Inguscio, and L. Fallani - "*Synthetic Dimensions and Spin-Orbit Coupling with an Optical Clock Transition*" - Physical Review Letters, Volume **117**, 220401 - November 2016

- **L. Franchi**, L. F. Livi, G. Cappellini, G. Binella, M. Inguscio, J. Catani, and L. Fallani - "*State-dependent interactions in ultracold ^{174}Yb probed by optical clock spectroscopy*" - New Journal of Physics, Volume **19**, 103037 - October 2017

- G. Cappellini, L. F. Livi, **L. Franchi**, D. Tusi, D. Benedicto Orenes, M. Inguscio, J. Catani, and L. Fallani - "*Coherent Manipulation of Orbital Feshbach Molecules of Two-Electron Atoms*" - Physical Review X, Volume **9**, 011028 - February 2019

- L. F. Livi, D. Tusi, **L. Franchi**, D. Benedicto Orenes et al. - "*Direct observation of orbital-selective localization in interacting SU(N) lattice fermions via controlled symmetry breaking*" (in preparation)

2 Scattering processes and atom-atom interactions

In this chapter we review the fundamental concepts regarding the scattering theory and its application in the framework of ultracold atoms.
The chapter is organized as follows: in section 2.1 we discuss the scattering theory and the case of central potential in the low-energy limit.
Section 2.2 is devoted to the description of optical lattices as a crucial tool to control interactions between atoms.
Section 2.3 is dedicated to the description of the possibilities offered by atomic systems (both bosonic and fermionic) confined in optical lattices.
Concepts and quantities introduced in this chapter will be essential in order to describe the experimental results that will be presented in the following chapters.

2.1 Elementary concepts concerning collisional problems

The initial interest to understand microscopically the process of diffusion, or scattering, between colliding particles probably derives from the first experiments performed in the environment of nuclear physics. There, an incident beam constituted by particles having mass m and a mean momentum $\langle\vec{\mathsf{p}}\rangle$ and propagating along a certain direction, can interact with a stuck target as also shown in figure 2.1.1. In the laboratory frame, in which the mean velocity of the target is zero, it is possible, for those particles, to define the mean flux by the relation $\langle\vec{\mathsf{J}}\rangle = \#\frac{\langle\vec{\mathsf{p}}\rangle}{\mathsf{m}}$ where # represents the number of particles per unit volume in the incident beam. To simplify the notation let us suppose to consider now a one-dimensional motion along the $\hat{x}$ axis of a chosen reference frame. Let us also suppose to consider an ideal mono-energetic beam constituted by all identical particles characterized by

the same mass and the same momentum.
Without losing generality let us suppose to consider only beams in which the mean number of particles per unit volume # is so small that we can completely neglect mutual interactions between incident particles. In that way each particle can be considered as an isolated system and each interaction can be analyzed separately from a microscopic point of view. We also suppose to consider a thin target; this hypothesis ensures that we can neglect multiple scattering processes.
After the interaction has occurred, if we are interested to understand the nature of the collisional process, we can measure the number of particles N that scatter into the infinitesimal solid angle $\mathrm{d}\Omega$ located in the direction $\Omega = (\phi, \vartheta)$. Under the hypothesis introduced above, that are well respected in our experimental conditions (as we will see in the following chapters), N results to be directly proportional to the incident current and then

$$\mathsf{N} = \mathsf{J}\ \#_b\ \sigma\left(\Omega\right)\ \mathrm{d}\Omega, \tag{2.1.1}$$

where $\#_b$ is the number of interacting scattering centers in the target. $\sigma\left(\Omega\right)$ has the dimension of a surface and it is called **differential scattering cross section** and is a characteristic parameter of the collision of the incident particle with the target in the direction determined by Ω.
The total number of particles scattered per unit time is obtained by multiplying J, $\#_b$, and the **total scattering cross section** defined by:

$$\sigma_{\mathsf{tot}} = \int_{\Omega} \sigma\left(\Omega'\right) \mathrm{d}\Omega'. \tag{2.1.2}$$

All the physics in the interaction process between an incident particle and a target particle is contained in the differential scattering cross section that can be connected to the interaction potential $V(\vec{\mathsf{r}})$. In this thesis we will treat neutral atoms so we can avoid the complicancies that are associated to the long-range character of the Coulomb potential. We will consider only elastic collisions, that means that the energy of the incoming particles is conserved after the interaction with the target. To describe properly the physics that underlies the diffusion process and link the potential to the differential scattering section, let us consider an incoming wave packet that at time $t_0 = 0$ is propagating through a surface Σ perpendicular to the incident beam and passing through the target. Let us specify the initial position of the wavepacket center as $\vec{\mathsf{b}}$; particles will have a velocity $\vec{\mathsf{v}}$ so the center of the incident wavepacket before the collision will follow the law

$$\langle\vec{\mathsf{r}}\rangle = \vec{\mathsf{b}} + \vec{\mathsf{v}}(t - t_0). \tag{2.1.3}$$

Following the scattering theory developed in refs. [46–48], in order to describe faithfully the scattering process we introduce the parameters (see figure 2.1.1)

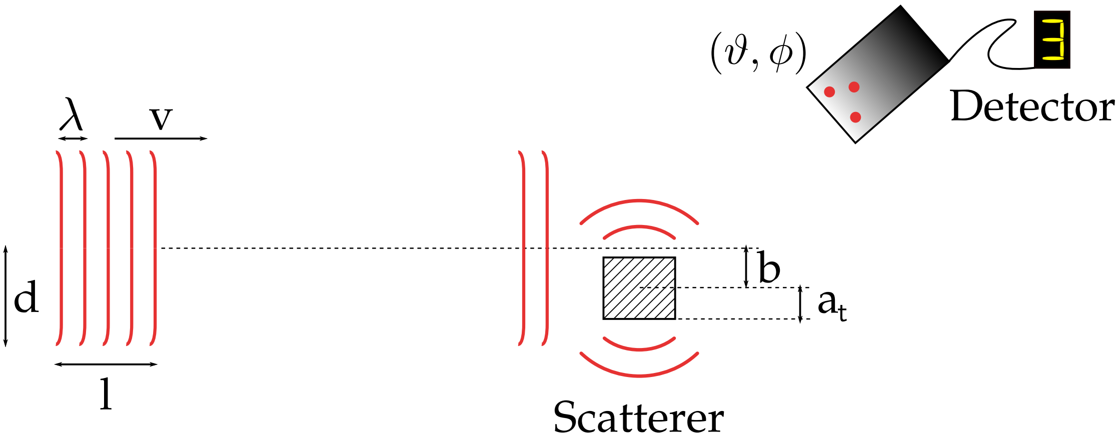

Figure 2.1.1. Schematic drawing of a finite wavepacket colliding with a single scattering center inside the target. In figure all the parameters used to mathematically represent the physical phenomenon are reported.

- d, l that are transverse and longitudinal dimensions of the incident wavepacket;
- a_t that represent the extension of the scattering region;
- $\lambda \equiv \dfrac{h}{m|\vec{v}|}$ that is the mean wavelength of the beam.

If the dimensions l, d of the incident beam are well defined, namely

$$\lambda \ll d \qquad\qquad \lambda \ll l,$$

and the collision process will not depend critically on the shape of the wavepacket,

$$a_t \ll d,\ l,$$

it is possible to assume that each particle can be described by the same $\vec{b}$ and the same t_0.
In order to describe the time evolution of a realistic wavepacket when a collision occurs, it can be useful to introduce the Fourier transform of the spatial incident beam profile $A(\vec{x})$, that describes the spatial evolution of the incident wavepacket in momentum space

$$A(\vec{p}) = \int A(\vec{x}) e^{i\vec{x}\cdot\vec{p}} d\vec{x}. \tag{2.1.4}$$

When $t = t_0$ the wavepacket of the incident beam $\phi_b(\vec{r}, t)$ can be described as a free-particle wavepacket,

$$\phi_b(\vec{r}, 0) = \int A(k' - k)\, e^{i\vec{k}'\cdot(\vec{r}-\vec{b})} d\vec{r}. \tag{2.1.5}$$

After the collision with the target, the scattered wavepacket, $\Psi_b\left(\vec{\mathsf{r}}, t\right)$ can now be obtained by substituting in eq. 2.1.5 the so-called stationary scattering wave $\psi_{\vec{\mathsf{k}}'}(\vec{\mathsf{r}})$, so, neglecting the spread of the incident wave packet during its propagation until the target, can be written :

$$\Psi_{\vec{\mathsf{b}}}\left(\vec{\mathsf{r}}, t\right) \simeq \int A\left(\vec{\mathsf{k}}' - \vec{\mathsf{k}}\right) e^{-i\vec{\mathsf{k}}\cdot\vec{\mathsf{b}}} \psi_{\vec{\mathsf{k}}'}(\vec{\mathsf{r}}) e^{-i\frac{E't}{\hbar}} \mathrm{d}\vec{\mathsf{k}}'. \tag{2.1.6}$$

This equation describes the behaviour of incident particles after the interaction with the target. By substituing the asymptotic behaviour for the stationary scattering wave

$$\psi_{\vec{\mathsf{k}}'}(\vec{\mathsf{r}}) \simeq e^{i\vec{\mathsf{k}}'\cdot\vec{\mathsf{r}}} + f_{\vec{\mathsf{k}}'}(\Omega)\frac{e^{ik'r}}{r} \tag{2.1.7}$$

where $f_{\vec{\mathsf{k}}'}(\Omega)$ is named scattering amplitude function, we obtain the general relation for the scattered wavefunction. The general form acquired by the scattered wavefunction can be expressed in the form:

$$\Psi_{\vec{\mathsf{b}}}\left(\vec{\mathsf{r}}, t\right) = \phi_{\vec{\mathsf{b}}}\left(\vec{\mathsf{r}}, t\right) + \Psi_{\vec{\mathsf{b}}}^{\mathsf{scat}}\left(\vec{\mathsf{r}}, t\right) \tag{2.1.8}$$

where only $\Psi_{\vec{\mathsf{b}}}^{\mathsf{scat}}$ contains the scattering amplitude function and therefore contributes to the probability to observe a scattered particle in a certain direction[1] identified by Ω. By evaluating the probability to detect a scattered particle in the solid angle $(\Omega,\, \Omega + \delta\Omega)$ per time unit and unit flux it is possible to obtain [48, 49]

$$\sigma\left(\Omega\right) = \left|f_{\vec{\mathsf{k}}}\left(\Omega\right)\right|^2 \tag{2.1.9}$$

that directly link the differential cross section introduced in eq. 2.1.2 with the single-particle scattering amplitude function $f_{\vec{\mathsf{k}}}\left(\Omega\right)$. This result can be obtained also taking into account a realistic wavepacket with a finite spatial extension.

In this last part of this section we will clarify if the theory presented above can be used in the case of ultracold atoms. The atomic sample obtained experimentally can be treated as an interacting dilute gas that is confined, as we will see in the following chapters, in a harmonic potential or in a superposition of a harmonic potential and other spatially-dependant potentials. Therefore, this textbook description of the scattering, realized for a finite wavepacket that propagates in free space, in absence of any kind of other potentials except for the interaction term $V(\vec{\mathsf{r}})$, has to be adapted properly to describe our framework. First of all, the presented model can be used to describe atom-atom interactions if we consider, instead of the laboratory frame, the center-of-mass frame in which the target and

---

[1] In any case, experimentally, it is not possible to detect a forward-scattered wave ($\vartheta = 0,\ \forall\phi$) and distinguish those particles from the trasmitted part of the incident beam.

the incident wavepacket have opposite mean momenta. It can be verified [48] that, by performing a frame transformation from the laboratory system to the center-of-mass frame, the total scattering cross section does not change:

$$\sigma_{\mathsf{tot}}^{\mathsf{lab.}} = \sigma_{\mathsf{tot}}^{\mathsf{com}}, \tag{2.1.10}$$

from which we can directly obtain the relation

$$\sigma^{\mathsf{com}}(\Omega^{\mathsf{com}})\ \mathrm{d}\Omega^{\mathsf{com}} = \sigma^{\mathsf{lab}}(\Omega^{\mathsf{lab}})\ \mathrm{d}\Omega^{\mathsf{lab}}, \tag{2.1.11}$$

that allows us to describe the collisions between atoms using the relations shown in this section. The condition of thin target, that has been used to impose the direct proportionality between N and the number of scattering centers $\#_b$, or in other words, that excludes the possibility to have multiple interactions between the incident beam and the target, can be adapted as follows: as we will see in the following sections of this chapter, the scattering between two neutral atoms can be described by a short-range interaction that becomes negligible after a characteristic length scale r_0. The atomic sample that we realize experimentally has a numeric density $\#_{\mathsf{atoms}}$ so low and the mean particle separation $(\#_{\mathsf{atoms}}^{-1/3})$ is so larger than the characteristic length scale, that the probability to find more than two atoms in a sphere of radius r_0 can be neglected $\left(r_0 \gg \#_{\mathsf{atoms}}^{-1/3}\right)$. When a gas verifies this condition we call it dilute.

It can happen that, also if the density is drastically low, the mean velocity of the gas is so high that by chance, the probability to find more than two particles in a sphere of radius r_0 can not be neglected so, to ensure the condition of thin target, we also have to impose that the thermal wavelength, that describes the mean distance between two particles at a certain temperature and that can be directly connected to the particle energy by the relation [50, 51]

$$\Lambda_{\mathsf{th}} = \frac{h}{\sqrt{\pi}} \left(\frac{a}{k_{\mathsf{B}}T}\right)^{\dfrac{1}{s}} \left[\frac{\Gamma\left(\dfrac{n}{2}+1\right)}{\Gamma\left(\dfrac{n}{s}+1\right)}\right]^{\dfrac{1}{n}}, \tag{2.1.12}$$

(where the dispersion relation $E = ap^s$ in n dimensions has been assumed and Γ is the Euler special function) has to be much larger than the characteristic interaction length r_0 $(\Lambda_{\mathsf{th}} \gg r_0)$.

2.1.1 Scattering by a central potential V(r) and low-energy limit

As mentioned above, it is always possible to change the reference frame to describe interaction processes between two particles; in the frame of the center of mass, as expressed by equation 2.1.10, the total scattering cross section $\sigma_{\mathsf{tot}}^{\mathsf{com}}$ is a conserved quantity.
In the center-of-mass frame the Schrödinger equation describing two colliding particles can be separated in two simple equations, one for the center of mass and one for the representative point of the system described by the relative coordinates. The Schrödinger equation for the representative point of the system, considering a potential with spherical symmetry, namely $V(\vec{\mathsf{r}}) \equiv V(r)$, can be written [52] as:

$$\left[\hat{p}_{\mathsf{r}}^2 + \frac{\hat{\vec{\mathsf{L}}}^2}{r^2} - 2m\left(\epsilon - V(r)\right)\right]\Psi = 0 \tag{2.1.13}$$

where $\mathsf{L}_c = \varepsilon_{abc}\mathsf{r}_a\mathsf{p}_b$ and ε_{abc} is the Levi-Civita symbol. Considering the diffusion problem shown in figure 2.1.1 it is possible to note that the wavevector $\vec{\mathsf{k}} \parallel \vec{\mathsf{v}}$ generates a rotational symmetry of the problem; if we choose a reference frame in which $\hat{k}$ is the polar axis, the collision phenomenon has to happen in the plane completely determined by the distance from the collision point r and the polar angle θ. In this case it is possible to expand the wavefunction and the scattering amplitude in a series of Legendre polynomials[2] as follow:

$$\Psi(r,\theta) = \sum_l \frac{\psi_l}{r} P_l(\cos\theta) \qquad\qquad f(\theta) = \sum_l f_l P_l(\cos\theta) \tag{2.1.15}$$

where ψ_l is the regular solution of the radial part of equation 2.1.13 and

$$\hat{\vec{\mathsf{L}}}^2 P_l(\cos\theta) = \hbar^2 l(l+1) P_l(\cos\theta).$$

---

[2] Let us consider a function $F(x)$ and consider also $-1 < x < 1$, then it is possible to expand this function in a series of Legendre polynomials as follows [53]

$$F(x) = \sum_{n=0}^{\infty} a_n P_n(x) \tag{2.1.14}$$

where the coefficients a_n can be evaluated [54] taking into account the orthogonality of the polynomials P_n with respect to the product $\int_{-1}^{1} P_n(x)P_m(x)dx$.

The solution of the radial equation, by considering the asymptotic form, namely $r \to \infty$, can be written as $\psi_l \sim \sin\left(kr - \frac{l\pi}{2} + \delta_l\right)$ while the asympotic scattered wave can be recasted as a sum over the l partial waves of incoming and outgoing waves[3]

$$e^{i\vec{\mathsf{k}}\cdot\vec{\mathsf{r}}} + f(\theta)\frac{e^{ikr}}{r} \sim \sum_i \left[i^{2(l+1)}\frac{2l+1}{2ik}e^{-ikr} + \left(\frac{2l+1}{2ik} + f_l\right)e^{ikr}\right] P_l(\cos\theta) \quad (2.1.16)$$

hence it is possible, by direct comparison, to obtain the explicit expression for the **partial scattering amplitude** f_l:

$$f_l = \frac{2l+1}{k}e^{i\delta_l}\sin\delta_l \equiv \frac{2l+1}{2ik}\left(e^{2i\delta_l} - 1\right) \quad (2.1.17)$$

where δ_l is called **phase shift** and describes the effect of the scattering potential $V(r)$ on the l-th outgoing partial wave.

If we consider now the low-energy limit, that implies $k \to 0$ and that is a condition always valid when we consider collisions between ultracold atoms, we can note that only the $l = 0$ term has a non negligible contribute to the total scattering cross section.

By considering the argument exposed in appendix A, it can be shown that, if we consider a short-range potential, the phase shift can be expressed by the simple relation

$$k\cot\delta \simeq -\frac{1}{a} + \frac{1}{2}k^2 r_{\mathsf{eff}} \quad (2.1.18)$$

where a is the **scattering length** and the r_{eff} is the **effective range**. An interpretation of the role of the scattering length a can be easily obtained if we evaluate, in the low-energy limit, the total cross section σ_{tot} because $\frac{4\pi}{k}\sum_l (2l+1)\sin\delta_l$ reduces to

$$\sigma_{\mathsf{tot}} = 4\pi a^2.$$

The same relation holds for two rigid spheres that can interact only by contact, i.e. $V(r) = \infty \, \forall r \leq r_0$ where r_0 is the sphere radius. Hence, we can interpret the scattering length a as the radius of a disc inside which scattering from a determinate potential can happen.

---

[3] To obtain equation 2.1.16 the sperical-harmonics expansion in plane waves has been used:

$$e^{i\vec{\mathsf{k}}\cdot\vec{\mathsf{r}}} = 4\pi \sum_l \sum_{m=-l}^{l} i^l j_l(kr) Y_l^{m^*}(\hat{k}) Y_l^m(\hat{r})$$

where j_l is the Bessel special function of l-th order. This relation can be simplified if we consider also the addition theorem of spherical harmonics that links these special functions to Legendre polynomials [55].

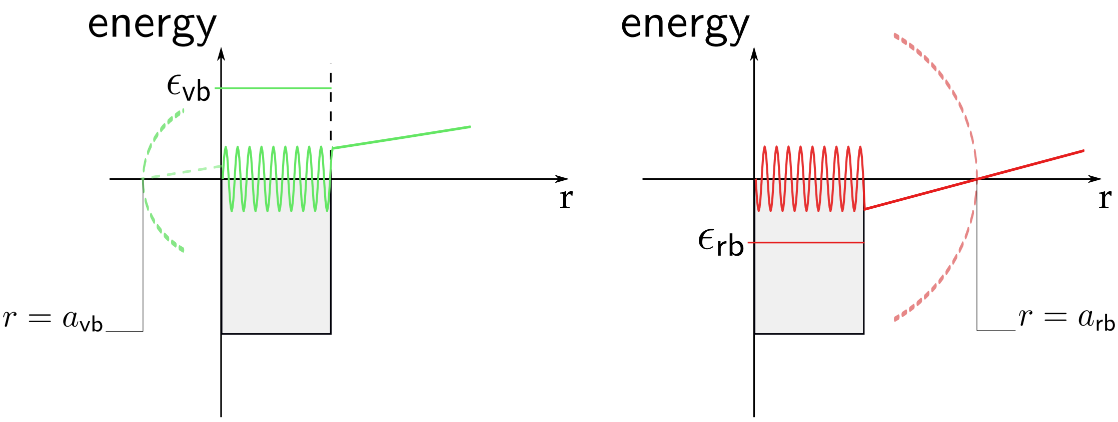

Figure 2.1.2. The sketch shows the scattered wavefunction for a square negative potential $V = V_0 \ \forall r \leq r_{\mathsf{pot}}$. In the case of positive scattering length (red) the related bound state has negative energy ϵ_{rb} and the interaction cross section related to a can be visualized by looking at the red arc with radius $r = a_{\mathsf{rb}}$. In case of negative scattering length (green) the bound state has the positive energy ϵ_{vb}.

The other figurative interpretation of the scattering length a is linked to the asymptotic behaviour of the total wavefunction[4] and its pictorial representation is sketched in figure 2.1.2. By considering only the s-wave scattering ($l = 0$) it can be demonstrated that the wavefunction Ψ, in the asymptotic limit, can be expressed as:

$$\Psi_{\substack{k\to 0\\ r\to\infty}}(r) \sim 1 - \frac{a}{r}.$$

This relation shows that if $a > 0$ it is possible to find a solution that has a node in the real space while if $a < 0$ the node in the solution is in the virtual space (negative distances). In this case, from the mathematical description of Ψ a physical interpretation of the scattering length can be extracted, because the distance of the node, in which $r = a$, can be interpreted as the range over which the interaction potential can modify the total wavefunction. Moreover, the sign of a determines the nature of the least-bound state of the system considered. If the node is in the real space $a > 0$, the bound state is also real ($\epsilon_{\mathsf{bound}} < 0$) while if $a < 0$ the resulting bound state is virtual [49].

The effective range r_{eff} cannot be related to a simple semi-classical or heuristic argument that should link the behaviour of the scattering cross section to the wavefunction of the representative point of the system. A simple argumentation

---

[4] In the limit of low energy the total wavefunction, that in general can be separated into radial and angular terms by employing the Legendre expansion (as shown in equation 2.1.14), is isotropic because it is independent from the polar angle θ. This property derives from the fact that the Legendre polynomial for $l = 0$ is a constant ($P_0(\cos\theta) = \mathsf{const}$) with respect to the polar angle.

on the nature of this term can be obtained if we consider that it is derived by an expansion near $k \simeq 0$ of the phase shift δ, as it has been shown in appendix A. This quantity can be interpreted as a moderate correction to the effective area that characterizes the collision process when the energy cannot be considered completely negligible.

2.1.2 Free-space atom-atom interaction

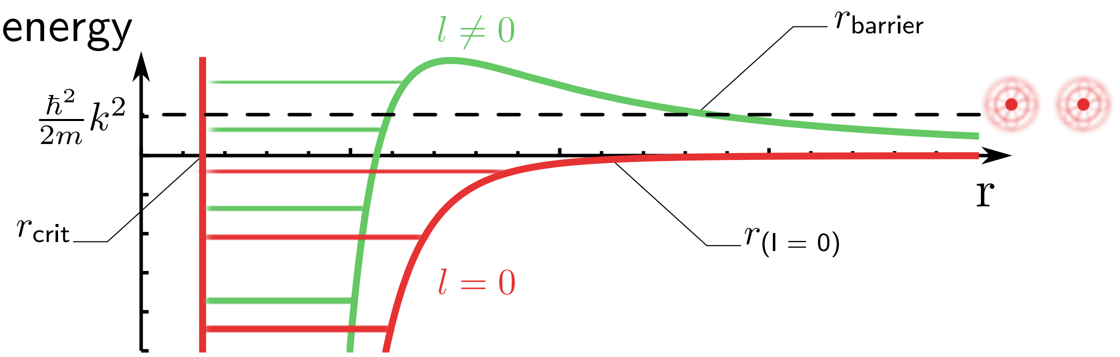

Figure 2.1.3. In this plot the van der Waals radial potentials $V(r)$ are reported for $l = 0$ and $l = 1$; they describe the interaction between two atoms as a function of the relative distance r. When $r < r_{\text{crit.}}$ the potential becomes highly repulsive and its modulus can be approximated as infinitely extended because it represents the atomic incomprimibily at short distances due to interaction between the two electron clouds.

The interaction between two neutral atoms, considering s-wave scattering[5], can be described by imposing $l = 0$ and neglecting all the other contributes due to higher momentum in which $l \neq 0$. This argumentation has been used in section 2.1.1 to simplify the equations and to describe easily the collision dynamic. In this section we will show why this hypothesis is justified when atomic interactions are considered. Moreover we will cite some important results that in the next chapters will allow us to derive experimentally the scattering length, that, as we will highlight in section 5.3.1, is connected to the possibility to produce biatomic homonuclear molecules.

Let us suppose, as the lowest approximation order possible, to consider an atom as composed by only two static charges ($\pm q$) that are in an electrostatic

---

[5] As shown in section 2.1.1, if this hypothesis holds, neglecting the contribution to the scattered wavefunction due to high order expasion with respect to relative momentum k, the whole collision process can be described simply by the scattering length a.

equilibrium. In this condition, the static field measured by an external positive infinitesimal charge can be expressed as [55]

$$\vec{\mathsf{E}}(\vec{\mathsf{r}}) = -\nabla\phi_d(\vec{\mathsf{r}}) = -\frac{q}{4\pi\epsilon_0}\nabla\frac{\vec{\mathsf{d}}\cdot\vec{\mathsf{r}}}{r^3} \tag{2.1.19}$$

where $\vec{\mathsf{d}} = \vec{\mathsf{r}}_{+q} - \vec{\mathsf{r}}_{-q}$.

In order to describe the potential that underlies the phenomenon of the collision between two neutral atoms we can consider an induced dipole-dipole[6] interaction that in first approximation can be described by an isotropic function of the relative distance r.

At short distances ($r \leq r_{\mathsf{crit}}$) atoms cannot permeate each other because the repulsive interaction between electron clouds dominates. Thus we can describe a total effective potential as constituted by an infinite barrier when the relative distance approaches the r_{crit} value and by a induced dipole-dipole interaction when the distance between atoms in bigger than r_{crit}:

$$V(r) = \begin{cases} \infty & r \leq r_{\mathsf{crit}} \\ -\frac{C_6}{r^6} & r > r_{\mathsf{crit}} \end{cases} \tag{2.1.20}$$

where C_6 is called van der Waals coefficient and it is defined by

$$C_6 = 2\hbar^2\frac{\pi^2}{m\lambda_{\mathsf{crit}}^2}\, r_{\mathsf{crit}}^6$$

where $\kappa_{\mathsf{crit}} = 2\pi/\lambda_{\mathsf{crit}}$ is related to the depth of the potential [49].

The potential $V(r)$ introduced in equation 2.1.20 has to be added to the angular momentum contribution reported in equation 2.1.13 that was derived from the partial-wave expansion.

Figure 2.1.3 shows the van der Waals potential introduced by equation 2.1.3. We observe that, if $l \neq 0$, atoms can reach the attractive interaction part of the total potential at $r < r_{\mathsf{barrier}}$ only if they tunnel through the centrifugal barrier. In this sense, if the atomic momentum k is lower than the maximum value assumed by the centrifugal potential, the contribution to the scattering cross section that comes from partial waves characterized by $l \neq 0$ should be negligible[7], as assumed in section 2.1.1.

---

[6] An exception is constituted by the dysprosium atom where an anisotropic pseudopotential due to dipole-dipole interaction can describe properly the long range interaction between two atoms. This is mainly due to the dysprosium atomic electric dipole momentum arising from $\mathsf{J} = 10$ [56, 57].

[7] As we will see in the following sections the possibility to couple an accessible scattering channel to an unaccessible channel will change significantly the interaction dynamic [17].

The total potential for $l = 0$ can be neglected when $r > r_{(\mathrm{l=0})}$ where $r_{(\mathrm{l=0})}$ is usually called van der Waals length and identifies the radius at which the zero point energy $\frac{\hbar^2}{2m}$ exceeds the potential energy. The interatomic distance at which the potential becomes negligible can be related to the potential depth of the attractive interaction by employing the equation [49]

$$r_{(\mathrm{l=0})} = \frac{1}{2}\sqrt[4]{\frac{2m\, C_6}{\hbar^2}}. \tag{2.1.21}$$

The argumentation used to explain the interaction between two neutral particles constituted by positive and negative charges in equilibrium can be treated less heuristically by introducing the multipole expansion [55] to describe, at each order, the potential generated by charges in electrostatic equilibium. By following this procedure it is possible [58] to reach a less intuitive but complete expression that describes the real radial potential $V(r)$:

$$V(r) = \sum_{\jmath,\ell\ =0}^{\infty} \frac{V_{\jmath,\ell}}{r^{\jmath+\ell+1}} \tag{2.1.22}$$

where $V_{\jmath,\ell}$ is related to the $\jmath$-th multipole term for the first atom and to the ℓ-th multipole term for the second atom. Applying the formalism of perturbation theory to the second order and keeping the terms up to induced quadrupole-quadrupole interaction it is possible to approximate the equation 2.1.22 as follows[8]

$$V(r) \approx -\big(\underbrace{C_3/r^3}_{Dipole} + \underbrace{C_6/r^6}_{Dipole-dipole} + \underbrace{C_8/r^8}_{Quadrupole-quadrupole}\big). \tag{2.1.23}$$

This expression has been exploited to evaluate, considering only the lowest lying energy levels, the static and dynamic polarizabilities for the ytterbium atom [59]. To simplify the following discussion, we will consider only the induced dipole-dipole potential because it approximates the most substantial contribution of 2.1.23 in almost all the interaction cases.

The existence[9] of real bound states for the specified potential has been intensively studied [62, 63] also exploiting the quantum defect theory [64–72] and the

---

[8] As specified before, the dipole term expressed in equation 2.1.23 has a non negligible contribution in special cases in which the molecular potential supported by the potential asymptotically connects two states having non null dipole momentum.

[9] In 1981 [60], the virial theorem has been used to argue that potentials of the form $-V_0\left(\frac{r_0}{r}\right)^n$ have no bound states of negative energy, or using the same terminology proposed in the last section, a real bound state for $n > 2$.
A more accurate analysis of the same problem can be found in reference [61]. The authors found out that the virial theorem cannot be used to describe this kind of potentials because basically the quantities $\langle\hat{T}\rangle$ and $\langle\hat{V}\rangle$ are not well defined.

semiclassical approach by means of the WKB approximation [73–75].
By following the semiclassical approach, described in [74, 75] and considering the van der Waals potential limiting our analysis only to the induced dipole-dipole interaction, it can be found that the s-wave scattering length can be expressed as

$$a = \bar{a}\left[1 - \tan\left(\frac{\pi}{n-2}\right)\tan\left(\Phi - \zeta\right)\right]\Bigg|_{n=6} = \bar{a}\left[1 - \tan\left(\Phi - \frac{\pi}{8}\right)\right] \qquad (2.1.24)$$

where

$$\bar{a} = \cos\left(\frac{\pi}{n-2}\right)\left(\frac{\sqrt{2mC_n}}{\hbar\,(n-2)}\right)^{\frac{2}{n-2}}\frac{\Gamma\left(\frac{n-3}{n-2}\right)}{\Gamma\left(\frac{n-1}{n-2}\right)}\Bigg|_{n=6} = \frac{1}{\sqrt{2}}\frac{\Gamma\left(\frac{3}{4}\right)}{\Gamma\left(\frac{5}{4}\right)}r_{(\mathsf{l=0})}$$

is the background or mean scattering length and it is determined only by the asymptotical behaviour of the potential, Φ is the semiclassical phase calculated at zero energy

$$\Phi = \frac{1}{\hbar}\int_{r_{\mathsf{crit}}}^{\infty}\sqrt{-2mV(r)}\mathrm{d}r$$

and $\zeta = \frac{\pi}{2(n-2)}\big|_{n=6} = \frac{\pi}{8}$ is determined by the boundary conditions at the turning point r_{crit}. Equation 2.1.24 expresses the behaviour of the scattering length as a function of the semiclassical phase Φ; this function has a divergence every time the relation

$$\Phi - \frac{\pi}{8} = \frac{1}{2}\pi + \pi\mathsf{n} \qquad\qquad \forall\ \mathsf{n} \in \mathbb{Z}$$

is satisfied. When this condition is valid and the scattering length a diverges a bound state can be supported by the potential. These resonances are usually called shape resonances.
Let us consider the energy of the last bound state supported by the van der Waals potential. If $\mathsf{n_f}$ is the last integer that allows a real bound state[10], we can write $(\mathsf{n_f} - 1/2) < \Phi - \pi/8 < (\mathsf{n_f} + 1/2)$. It can be demonstrated [49] that, by comparing the relation that links the phase shift to the scattering length (2.1.18) and the general relation that allows to obtain the effective range (A.5), in particular by evaluating this relation for $k \to 0$ and $\kappa_{\mathsf{crit}}\ r_{\mathsf{crit}} \ll 1$, it is possible to express the scattering length as a function of κ_{crit} by the relation:

$$-\frac{1}{a} \simeq -\kappa_{\mathsf{crit}} + \frac{1}{2}\left(\kappa_{\mathsf{crit}}\right)^2 r_{\mathsf{eff}}. \qquad (2.1.25)$$

---

[10] The knowledge of the phase shift Φ allows to determine the maximum number of the bound states. By following reference [74], the number of bound states is determined by

$$\mathsf{n_f} = \ulcorner\Phi/\pi - (n-1)/(2n-4)\urcorner\big|_{n=6} + 1$$

where $\ulcorner\urcorner$ indicates the integer part.

The energy of the least-bound state ϵ_{b} can therefore be expressed as:

$$\epsilon_{\mathsf{b}} = -\frac{\hbar^2}{2m}\left(\kappa_{\mathsf{crit}}\right)^2 \underset{\lambda_{\mathsf{crit}}\to\infty}{\simeq} -\frac{\hbar^2}{2ma^2} \tag{2.1.26}$$

that means that the real least-bound state, that corresponds to a negative energy, occurs when the interaction is repulsive. If the least-bound state is virtual thus the scattering length has to be negative and it implies an attractive interaction. Equation 2.1.26 can be considered valid only when the scattering length can be approximated by the potential depth parameter κ_{crit} introduced in equation 2.1.20 and then results bigger than the mean scattering length $\overline{a}$. To generalize this expression including also the conditions in which the scattering length a is comparable to $\overline{a}$, we present now a result obtained by performing quantum defect theory (AQDT) in order to determine the energy of highly-excited molecular states supported by the interacting potential [68]. It is possible to obtain:

$$\epsilon_{\mathsf{b}} = -\frac{\hbar^2}{2m\left(a-\overline{a}\right)^2}\left[1+\mathsf{c1}\frac{\overline{a}}{\left(a-\overline{a}\right)}+\mathsf{c2}\frac{\overline{a}^2}{\left(a-\overline{a}\right)^2}\right] \tag{2.1.27}$$

where[11] $\mathsf{c1} = 3\frac{\Gamma\left(5/4\right)^2}{\Gamma\left(7/4\right)^2} - 2$ and $\mathsf{c2} = \frac{5}{4}\mathsf{c1}^2 - 2$. Also the effective range can be calculated exactly by evaluating the quantum defect theory for a $1/r^6$ potential, and the result, reported in reference [70], is consistent with the expansion of r_{eff} in term of the ratio $(\overline{a}/a)$ [75]:

$$r_{\mathsf{eff}} = \frac{\overline{a}}{3}\frac{\Gamma(1/4)^2}{\Gamma(3/4)^2}\left(1-2\frac{\overline{a}}{a}+2\left(\frac{\overline{a}}{a}\right)^2\right). \tag{2.1.28}$$

This relation ensures the positivity of the effective range as requested by the general theory.

---

[11] Reference [68] exploits the well-known identity $\frac{2\pi}{\Gamma(1/4)^2} \equiv \frac{1}{2\sqrt{2}}\frac{\Gamma(3/4)}{\Gamma(5/4)}$ to express all the physical quantities presented in this work.

2.2 Optical lattices

In the previous sections we have analyzed the dynamics that underlies the interaction between atoms in free space, obtaining the fundamental relations to mathematically describe isotropic atomic collisions. As we will show in the next chapters, the introduced concepts will allow us to obtain explicitly the effective range and the scattering length for two physically promising and nearly unexplored atomic systems. The fundamental tool that, for any system studied in this thesis, allowed us to understand the interaction phenomena is the possibility to load atoms in a spatially-periodic potential of light, named optical lattice.

Atoms loaded in optical lattices represent a unique platform by which it is possible to mimic a large variety of physical system, from one-dimensional interacting systems to three-dimensional electrons in crystals. During the last years, this tool permitted the development of a high number of innovative techniques to simulate physical systems in which the experimental conditions for the observation of interesting quantum effects would have been otherwise unexplorable.

A remarkable example, recently achieved in the laboratory where the results reported in this thesis have been obtained, is the possibility to observe experimentally the behaviour of the electron in crystals permeated by an intense magnetic field (about 10^4 T)[12].

An optical lattice is a spatially-periodic potential generated by a standing wave of far-off resonant light. To describe simply the effect of this kind of radiation let us schematise an atom as an ideal two-level system, in particular we will call the ground state $|g\rangle$ and the excited state $|e\rangle$. In this case the mean force experienced by the ideal two-level atom, when monochromatic light is considered, can be expressed [76] as:

$$\vec{\mathsf{F}} = \frac{1}{2}\hbar\left[\vec{\mathsf{k}}_{\mathsf{L}}\Gamma\frac{\frac{\Omega^2}{2}}{\delta^2+\frac{\Gamma^2}{4}+\frac{\Omega^2}{2}} - \delta\frac{\frac{\nabla\Omega^2}{2}}{\delta^2+\frac{\Gamma^2}{4}+\frac{\Omega^2}{2}}\right] \tag{2.2.1}$$

where $k_{\mathsf{L}} = |\vec{\mathsf{k}}_{\mathsf{L}}| = \frac{2\pi}{\lambda}$ is the wavevector of the monochromatic radiation considered, $\hbar\Omega = q\,\vec{\mathsf{d}}\cdot\vec{\mathsf{E}}$ is the Rabi frequency where $\vec{\mathsf{d}} = \langle\vec{\mathsf{r}}\rangle$ is the dipole operator and $\vec{\mathsf{E}}$ is the electric field associated to the radiation considered, δ is the detuning and Γ is the natural width of the transition $|g\rangle \to |e\rangle$.

This equation is clearly composed by two parts, the first one represents the so called dissipative term and describes the mean effect due to cycles of directional absorptions and isotropic spontaneous emissions while the second part is a conservative term and can be expressed by the following potential:

$$V = \frac{\hbar\delta}{2} \log \left[\frac{\delta^2 + \frac{\Gamma^2}{4} + \frac{\Omega^2}{2}}{\delta^2 + \frac{\Gamma^2}{4}} \right] . \tag{2.2.2}$$

The potential reported in equation 2.2.2 constitutes the so called optical dipole potential and usually it is expressed by considering only the first order of the Taylor expansion[12]

$$V \simeq \hbar \frac{\Omega^2}{4\delta} . \tag{2.2.3}$$

Equation 2.2.3 shows that, if the light is red detuned with respect to the transition $|g\rangle \to |e\rangle$, the potential due to the radiation, neglecting the dissipative term, is attractive and then can be used to trap atoms in the maxima of radiation intensity. In the case of a standing wave, for example obtained by retroreflecting a laser beam, maxima are spatially periodic. The relations shown can be generalized for a real atomic system characterized by many energy levels, as it has been reported in references [76, 77].

Let us consider two counter-propagating plane waves on the $\hat{x}$ direction of a reference frame and take into account ideal plane waves characterized by wavenumber k_L; it is possible to demonstrate that the mean intensity profile can be expressed as

$$I(x) = \frac{\varepsilon_0 c}{2} E_0^2 \left(1 + \cos\left(2k_\mathsf{L} x\right)\right) . \tag{2.2.4}$$

The periodicity of this intensity profile is $\lambda/2$. Light beams used to realize spatially-periodic potentials are not exactly representated as ideal plane waves because the radiation employed in an experimental laboratory can be approximated as Gaussian beams [78] (that are solutions of the Helmholtz equation in paraxial approxiamtion[13]). The real spatial dependance of the electric field E_0, that can be neglected if we are interested in the analysis of lattice physics phenomena, as we will see in the following, has a non-negligible relevance from the experimental point of view because the shape generate an additional light potential. The characteristic trap frequencies generated by the lattice beams can be experimentally measured and represent an important characteristic to determine the physical processes that can occur on confined atoms.

---

[12] The far-off resonant condition implies that $\frac{\frac{\Omega^2}{2}}{\delta^2 + \frac{\Gamma^2}{4}} \ll 1$ that is the requested condition to expand equation 2.2.2 to the first order.

[13] While plane waves are solutions of the equation $\Box \vec{\mathsf{E}}\left(\vec{\mathsf{x}}\right) = 0$ where $\Box$ is the d'Alembert operator.

In general, the potential generated by a retroreflected Gaussian lattice beam can be written as [14]

$$V\left(r,x\right)=V_0 e^{-2\frac{r^2}{\omega(x)}}\cos^2\left(k_\mathsf{L}x\right)\approx V_0\cos^2\left(k_\mathsf{L}x\right)+\frac{1}{2}\omega_r^2 r^2+\frac{1}{2}\omega_x^2 x^2 \tag{2.2.5}$$

where $\frac{\omega_r}{2\pi}=\sqrt{\frac{4E_\mathsf{r}}{mw_0^2}}\sqrt{\mathsf{s}}$, $\frac{\omega_x}{2\pi}=\sqrt{\frac{2E_\mathsf{r}}{mz_0^2}}\sqrt{\mathsf{s}}$ are the trap frequencies along and perpendicular to the propagation direction $\hat{x}$, $(w_0,\ z_0)$ are the beam waist and the Rayleigh parameter $z_0=\frac{\pi w_0^2}{\lambda}$, $E_\mathsf{r}\equiv\frac{\hbar^2 k_\mathsf{L}^2}{2m}$ is the recoil energy of the radiation and $\mathsf{s}\equiv\dfrac{V_0}{E_\mathsf{r}}$ is a dimensionless parameter that indicates the lattice depth with respect to the recoil energy. If we generalize the one-dimensional intensity profile in equation 2.2.4 to the three-dimensional case in which three pairs of (independent) lattice beams are shone along orthogonal directions, a cubic three-dimensional optical lattice forms. If we neglect the trapping potential induced by the real shape of the lattice beams it is possible to describe the motion of an atom in the 3D spatially periodic potential as:

$$\left[-\frac{\hbar}{2m}\nabla^2+E_\mathsf{r}\sum_{i=\{x,y,z\}}\mathsf{s}_i\sin^2\left(k_{(L,i)}\ i\right)-\epsilon\right]\psi\left(\vec{\mathsf{x}}\right)=0. \tag{2.2.6}$$

The resulting Hamiltonian is a separable operator and the wavefunction can be factorised as follows:

$$\psi\left(\vec{\mathsf{x}}\right)=\psi_x\left(x\right)\psi_y\left(y\right)\psi_z\left(z\right).$$

The eigenstates problem reduces to solve three separate Mathieu equations [54, 80]. Solutions of these equations are the Mathieu special functions that are periodic functions characterized by the same periodicity of the lattice and constitute an orthonormal set.

By following a different approach to the solution of the same mathematical problem, it is possible to search a solution of the spatially periodic eigenstate problem by imposing

$$\psi_j\left(j\right)=u_{(n,k_j)}\left(j\right)e^{ik_j j} \qquad \forall j\in\{x,y,z\} \tag{2.2.7}$$

where $u_{(n,k_j)}$ are eigenfunctions characterized by the lattice periodicity and k_j is the quasimomentum in the direction $\hat{j}$. The existence of a set of solutions that can be expressed as reported in equation 2.2.7 is ensured by the Bloch theorem [81]. It is possible to demonstrate that $u_{(n,k_j)}$ is a periodic function in k_j with the

---

[14] Equation 2.2.5 takes into account the electric field only as a function of the radial position x while the axial dependance has been neglected (this contribution should be considered if the dimension of the trapped cloud results comparable to the Rayleigh parameter $z_0=\frac{\pi\omega_0}{\lambda}$)[79].

periodicity of the reciprocal lattice and also the eingenvalues are invariant under traslation of multiples of the reciprocal lattice vectors. As a consequence of this translational symmetry in the momentum space, introducing the band index n it is possible to limit the representation of the eigenvalues to the primitive cell of the reciprocal lattice, that is called first Brillouin zone (FBZ). For the sake of illustration, in figure 2.2.1 we show the first four bands for a simple one-dimensional lattice.

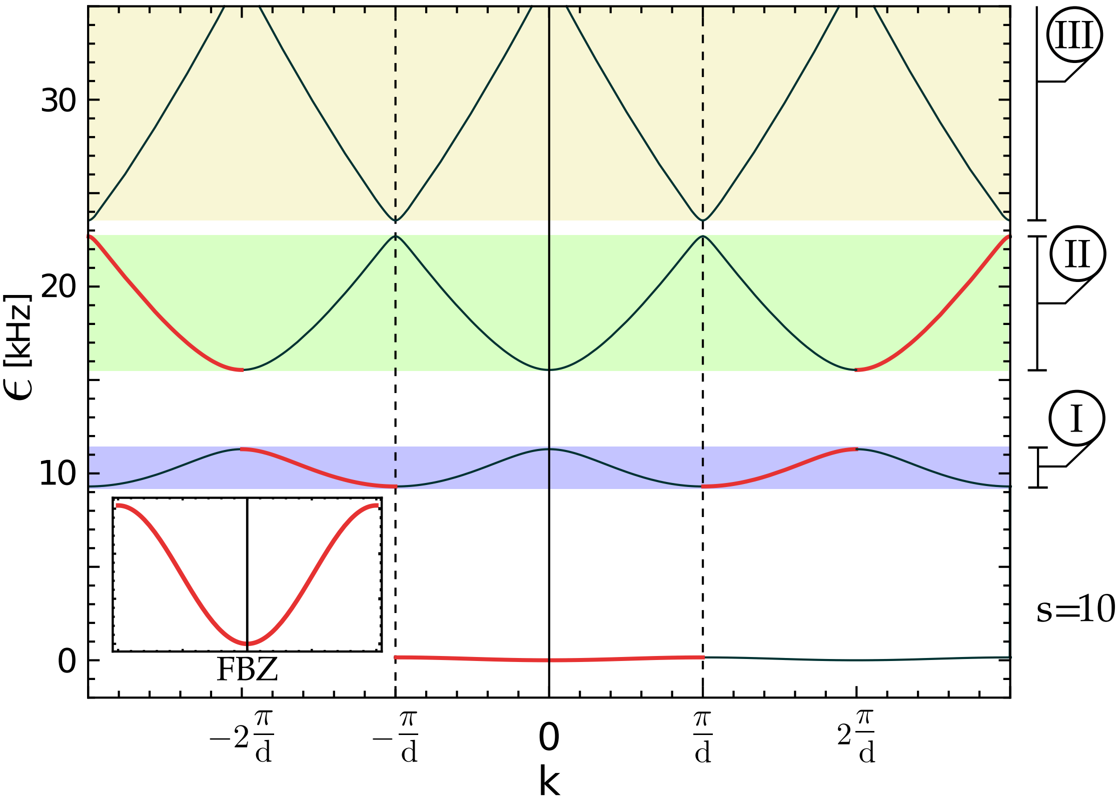

Figure 2.2.1. Lattice band structure evaluated for Yb atoms and s = 10. A solution is plotted in red as a function of the quasimomenta k. Using the invariance under translations in reciprocal space each red-painted branch can be translated in the interval $\{-\pi/d, \pi/d\}$ where $2d$ is the one-dimensional direct primitive cell. In the inset the fundamental band has been reported, to enhanceing its shape as a function of the quasimomenta.

2.2.1 Wannier functions

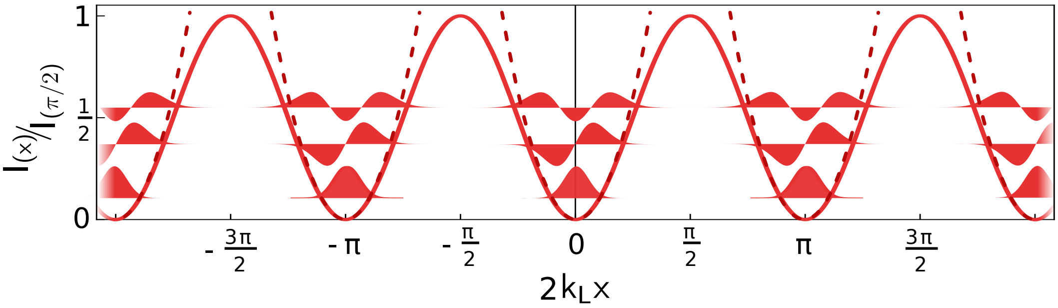

Figure 2.2.2. Sketch of the first order Taylor expansion (dark red) of the lattice potential (red) when the depth $s \gg 1$. The firsts eigenstates and eigenvalues for a pure harmonic potential are also shown.

When $s \gg 1$ the atomic wavefunction, that can be always expressed as a sum of plane waves over the whole lattice, results localized around the lattice sites. That suggest us to introduce an alternative for the solutions of the Schrödinger problem 2.2.6, as combination of the so-called Wannier functions, localized on single lattice sites. If we consider a one-dimensional lattice characterized by a distance d between two nearest-neighbour lattice sites in the direct space, the Wannier functions are defined by [81]

$$w_n(x-la) = N\int_{-k}^{+k} e^{i\left(kla+\theta_{n,k'}\right)}\psi_{n,k'}\left(x\right)\mathrm{d}k' \tag{2.2.8}$$

where N is a normalization constant, $\theta_{n,k'}$ is a phase factor, $\psi_{n,k'}\left(x\right)$ are the Bloch functions and $l \in \mathbb{Z}$. The uncertainty due to the phase factor $\theta_{n,k'}$ can be removed if we choose to work with maximally localized Wannier functions (MLWF). To impose this condition it is sufficient to determine $\theta_{n,k'}\forall n$ that minimize the quantity [82, 83]

$$\Delta x^2 = \langle w_n(x)|\hat{x}^2|w_n(x)\rangle - \langle w_n(x)|\hat{x}|w_n(x)\rangle^2.$$

MLWF are an orthonormal set characterized by the completeness relation

$$\langle w_n\left(x-la\right)|w_{n'}\left(x-l'a\right)\rangle = \delta_{n,n'}\delta_{l,l'}. \tag{2.2.9}$$

From this relation it is possible to note that two particles in the same band ($n = n'$) have orthogonal wavefunctions if they are in two different lattice sites. That means also that, if an atom is perfectly described by a MLWF, the overlap of its wavefunction with the wavefunction of the atom in the nearest neighbour lattice

site can be neglected.
In this condition, it is possible to approximate each lattice site as a harmonic potential, as shown in figure 2.2.2, by approximating the potential 2.2.5 to the first-order Taylor expansion and neglecting also the terms due to the intensity Gaussian shape of the beam employed to realize the lattice[15].

2.2.2 Two interacting particles in a harmonic potential

If we consider the tight-binding condition, the study of atom-atom interactions in a lattice site reduces to the study of the collision process in a harmonic trap. To describe the interaction in a harmonic trap let us assume, as discussed in section 2.1, to consider a dilute and ultra-cold atomic gas. Under these assumptions, by following the idea proposed by Fermi [84], the interaction can be modelled with a pseudo-potential with a contact interaction proportional to the scattering length a as follows:

$$V(r) = \frac{4\pi\hbar^2}{m} a \, \delta_{HY}(r) \tag{2.2.10}$$

where $\delta_{HY} = \delta(r) \frac{\partial}{\partial r}(r\cdot)$ is the regularized delta function introduced by Fermi and exploited by Huang and Yang to analyze the interaction between hard spheres [85, 86].
By following reference [87], if we restrict the problem to a three-dimensional, isotropic ($\omega_x = \omega_y = \omega_z$), harmonic oscillator and we consider that both the kinetic energy term of the two-particles Hamiltonian and the external potential energy are quadratic forms, it is possible to separate the center-of-mass motion from the representative system point described by the relative coordinates.
The center-of-mass Hamiltonian can be expressed as the sum of a kinetic term and a harmonic potential, so the solution is well known and the interaction problem can be attributed only to the representative point of the system Schrödinger equation.
By defining the relative coordinate $\vec{\mathsf{r}} = \frac{1}{\sqrt{2}}(\vec{\mathsf{r}_1} - \vec{\mathsf{r}_2})$, and center-of-mass coordinate consequently[16], we can write:

$$\left[\hat{H}_{\mathsf{ho}} + a\,\pi\sqrt{\frac{2m\omega}{\hbar}}\delta_{HY}(r)\right]\psi(\vec{\mathsf{r}}) = \frac{\epsilon}{\hbar\omega}\,\psi(\vec{\mathsf{r}}) \tag{2.2.11}$$

where $\hat{H}_{\mathsf{ho}}$ is the Hamiltonian of the harmonic oscillator for the representative point of the system.

---

[15] In this case this approximation is completely justified because the shape of the beam has an effect over bigger distances than the dimension of a single lattice site.

[16] The same authors in reference [87] define this choice "unconventional" but they prefer it to balance the masses of center-of-mass and representative point of the system.

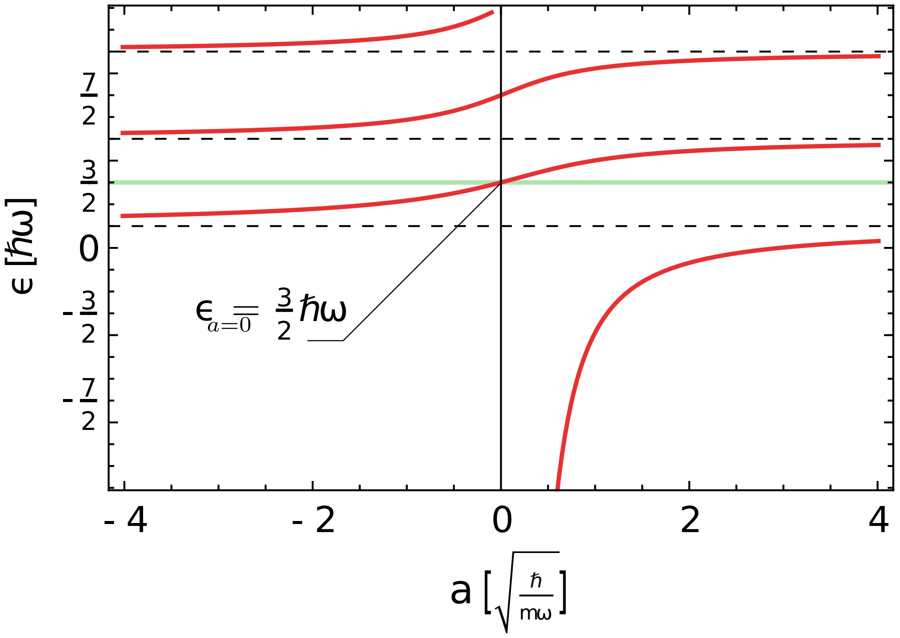

Figure 2.2.3. Energy spectrum of two interacting atoms in a three-dimensional, isotropic harmonic oscillator potential as a function of the scattering length a. The expected behaviour for $a \to \infty$ is reported as dashed black lines. The green line shows the lowest-energy state allowed by the harmonic potential for non-interacting atoms. As it can be observed, due mainly to the induced confinement caused by the trapping potential, both positive and negative scattering lengths support the formation of bound states.

This model can be solved analytically and the energy $E = \epsilon/\hbar\omega$ of two interacting atoms in a harmonic trap can be written as:

$$\sqrt{2}\frac{\Gamma\left(-E/2+3/4\right)}{\Gamma\left(-E/2+1/4\right)} = \frac{1}{a}\sqrt{\frac{m\omega}{\hbar}}. \tag{2.2.12}$$

The energy spectrum can be evaluated by numerically solving equation 2.2.12. In figure 2.2.3 the energy spectrum of two interacting particles in a three-dimensional isotropic harmonic potential is plotted. If the interaction goes to zero, the eigenvalues converge to the non-interacting eigenvalues, namely $\epsilon_n = \left(\frac{3}{2} + 2n\right)\hbar\omega$ where $n \in \mathbb{N}$ is the eigenvalue of the number operator $\hat{n} = \hat{a}^\dagger\hat{a}$.
If the scattering length increases, the energy increases up to the highest possible limit, that is represented by the next oscillator level and atoms start to repel each other as much as possible to reduce the interaction energy cost, providing a node in the relative wavefunction. This mechanism causes the so-called fermionization of identical bosons, that has been observed recently also for distinguishable fermions [88, 89].

We also note that, it is always possible to find a state characterized by a lower energy than the first allowed harmonic state, that is plotted in figure 2.2.3 and has a energy equal to $\epsilon_0 = \frac{3}{2}\hbar\omega$.

2.2.3 Singlet-triplet interactions in a harmonic potential

In reference [87] the interaction between two atoms was parametrized by one parameter, the scattering length a introduced in section 2.1.1. This assumption can be justified for all the collisional processes described, but has to be revisited if we consider particles that obey well-defined statistics. In particular, if we consider the interaction between two particles that obey Bose-Einstein statistics, we have to consider also that the total wavefunction has to be even under exchange $1 \leftrightarrow 2$. In the following sections we will show that this characteristic property allows s-wave scattering between identical particles.
Viceversa, two particles that obey Fermi-Dirac statistics have an antisymmetric total wavefunction under exchange $1 \leftrightarrow 2$ and we will see that this property permits s-wave scattering only between particles characterized by a different collection of quantum numbers.
Usually, when the interaction between fermionic atoms is considered, the degree of freedom that differs between two particles is the projection of the total angular momentum on the quantisation axis m_{F}.
However, two electron atoms have also other stable levels, as we will show in the following sections. In particular, they have spin-triplet states $|e\rangle$ characterized by a lifetime of the order of tens of seconds. The lifetime of some of these excited metastable levels is so long with respect to the atomic dynamics that it is possible to treat these levels as proper stable states of the system. To describe interactions between a ground-state atom $|g\rangle$ and a metastable atom $|e\rangle$ in the presence of a harmonic potential we derived a model following the course reported in reference [87].
In this case, the total wavefunction describing the ground-state and the excited-state atoms has to be antisymmetrized by imposing the oddness over the exchange transformation $1 \leftrightarrow 2$.
The two obtained antisymmetric states

$$|+\rangle = \frac{1}{\sqrt{2}}\left(|ge\rangle + |eg\rangle\right) \equiv |s\rangle, \qquad |-\rangle = \frac{1}{\sqrt{2}}\left(|ge\rangle - |eg\rangle\right) \equiv |t\rangle$$

have, in general, two different scattering lengths named a^+ and a^-.
In this section we[17] will generalize the two-body interaction in a harmonic potential

---

[17] The largest part of this theory has been evaluated by my collegue L. F. Livi.

by introducing two different scattering lengths for the two colliding atoms. The obtained result will collapse on the solution described in the section 2.2.2 [87] if we impose the relation $a^+ \equiv a^-$.
As described in the previous section, in this case it is possible to separate the center-of-mass motion from the representative point of the system that is described by the relative coordinates introduced by the relation $\vec{\mathsf{r}} = \frac{1}{\sqrt{2}}\left(\vec{\mathsf{r}_1} - \vec{\mathsf{r}_2}\right)$.
The Hamiltonian $\hat{H}_{\mathsf{ho}}$ for the system in which the harmonic potential is considered could be expressed as

$$\hat{H}_{\mathsf{ho}} = \sum_n E_n |s,n\rangle\langle s,n| + \sum_n \left(E_n - \Delta\mu B\right)|t,n\rangle\langle t,n| \tag{2.2.13}$$

where $|n\rangle$ are the harmonic oscillator eigenfunctions corresponding to eigenvalues identified by E_n.
In the rotated basis introduced by $|\pm\rangle$ states, where the interaction Hamiltonian is diagonal, the Hamiltonian operator in equation 2.2.13 can be evaluated by performing the transformation $\mathsf{O}\hat{H}_{\mathsf{ho}}\mathsf{O}$ where

$$\mathsf{O} = \frac{1}{\sqrt{2}}\begin{pmatrix} 1 & 1 \\ 1 & -1 \end{pmatrix} \qquad\qquad \mathsf{O} \in \mathbb{SO}_2$$

By following the course of reference [87] we add interactions to the Hamiltonian and expand the unknown solution Ψ of the colliding particles as follows

$$\Psi\left(\vec{\mathsf{r}}\right) = \sum_{n=0}^{\infty}\left(c_n^+ + c_n^-\right)\psi_n\left(\vec{\mathsf{r}}\right) \tag{2.2.14}$$

where $\hat{H}_{\mathsf{ho}}\psi_n = E_n\psi_n$. The resulting system describes a couple of particles that interacts by two scattering lengths $a^{\pm}$:

$$\begin{cases} \sum_{n=0}^{\infty}\left[c_n^+\left(E_n - E + \frac{\Delta\mu B}{2}\right) - c_n^-\frac{\Delta\mu B}{2}\right]\psi_n\left(\vec{\mathsf{r}}\right) + \left[\sqrt{2}\pi a^+\delta_{HY}\right]\sum_{m=0}^{\infty} c_m^+\psi_m\left(\vec{\mathsf{r}}\right) = 0 \\ \\ \sum_{n=0}^{\infty}\left[c_n^-\left(E_n - E + \frac{\Delta\mu B}{2}\right) - c_n^+\frac{\Delta\mu B}{2}\right]\psi_n\left(\vec{\mathsf{r}}\right) + \left[\sqrt{2}\pi a^-\delta_{HY}\right]\sum_{m=0}^{\infty} c_m^-\psi_m\left(\vec{\mathsf{r}}\right) = 0 \end{cases}$$

that can be simplified by projecting the two equations over $\psi_n^*(0)$ and by summing the obtained equations:

$$\left(c_n^+ + c_n^-\right)\left(E_n - E\right) + \psi_n^*(0)\underbrace{\left[\sqrt{2}\pi\frac{\partial}{\partial r}r\sum_m\left(a^+c_m^+ + a^-c_m^-\right)\psi_m\left(\vec{\mathsf{r}}\right)\right]}_{A_S} = 0 \tag{2.2.15}$$

and by subtracting them:

$$\left(c_n^+ - c_n^-\right)\left(E_n - E + \Delta\mu B\right) + \psi_n^*(0) \underbrace{\left[\sqrt{2}\pi \frac{\partial}{\partial r} r \sum_m \left(a^+ c_m^+ - a^- c_m^-\right) \psi_m(\vec{\mathsf{r}})\right]}_{A_D} = 0 \tag{2.2.16}$$

where we have introduced the functions A_S and A_D as shown in relations 2.2.15 and 2.2.16. By reverting these relations we can obtain the system

$$\begin{cases} c_n^+ = \frac{\psi_n^*(0)}{2}\left[\frac{A_S}{E_n - E} + \frac{A_D}{E_n - E + \Delta\mu}\right] \\ \\ c_n^- = \frac{\psi_n^*(0)}{2}\left[\frac{A_S}{E_n - E} - \frac{A_D}{E_n - E + \Delta\mu}\right] \end{cases} \tag{2.2.17}$$

that allows us to indentify the expansion coefficients.
Now, if we are interested to separate the two coefficient A_S, A_D to determine them, by substituing equations 2.2.17 in expansion 2.2.14 it is possible to obtain :

$$\Psi_S = A_S \sum_{n=0}^{\infty} \frac{1}{(E_n - E)} \psi_n^*(0)\, \psi_n(\vec{\mathsf{r}}) \tag{2.2.18}$$

and Ψ_D can consequently derived by evaluating $\sum_{n=0}^{\infty}\left(c_n^+ - c_n^-\right)\psi_n(\vec{\mathsf{r}})$.
Equation 2.2.18 can be expressed in term of Laguerre polynomials [87] and this procedure brings to:

$$\begin{cases} \Psi_S = A_S \frac{\pi^{-3/2}}{2} e^{-r^2/2} \Gamma\left(-E/2 + 3/4\right) U\left(-E/2 + 3/4, 3/2, r^2\right) \\ \\ \Psi_D = A_D \frac{\pi^{-3/2}}{2} e^{-r^2/2} \Gamma\left(-E/2 + 3/4 + \frac{\Delta\mu B}{2}\right) U\left(-E/2 + 3/4 + \frac{\Delta\mu B}{2}, 3/2, r^2\right) \end{cases} \tag{2.2.19}$$

where $U(\dots)$ derives from the integral representation of the confluent hypergeometric function [54, 87].
The last step to find the exact eigenvalues is to obtain A_S, A_D in the limit $r \to 0$. To achieve this result it is possible to substitute the relations 2.2.17 in equations 2.2.15 and 2.2.16 in the limit $r \to 0$. The model obtained has a numerical solution that will be exploited, considering also numerical anharmonic correction to the harmonic potential in order to extend the results of this model to the case of a lattice potential well up to the 4-th order[18], to evaluate the bound-state energy for Yb atoms as will be explained in detail in chapter 5.

---

[18] In the case of 4-th order potential the problem has been analyzed exactly in [90] while a numerical comparison with the usual theory evaluated in reference [87] can be found for example in reference [91] supplementary material.

2.3 Many-body lattice physics

So far we have introduced the problem of collisions in a harmonic trap and we have shown an exact solution only for two isolated interacting atoms. This condition, that can be observed experimentally if we consider very high lattice depth s, has given us an important insight on the role of the external trap in the interaction dynamics because the energy of two particles saturate at the next harmonic oscillator state when the scattering length $a \rightarrow \infty$. Moreover, the presence of a trap allows for the existence of a bound state for each non null scattering length a.
In this section we will go beyond the two body problem and introduce a different formalism that is commonly used to describe many-particles lattice dynamics. As this formalism makes use of single- particle wavefunctions, it cannot properly describe the system when the scattering length diverges, that is the condition analyzed in the previous part.

Figure 2.3.1 shows the possible processes that can occur in a lattice in which the depth s is not so high and the energy scale associated to the motion of the atoms in the lattice cannot be neglected. In particular, on the left side of figure 2.3.1 the atomic occupation number distribution after the lattice loading procedure is reported. Each lattice site can be described by a single MLWF (independently of the number of particles occupying the site) so it is possible to introduce, using these functions, a new description of the lattice dynamics based on the so-called "second quantization approach".
We limit our analysis to a single band and in particular we decide to ignore inter-band processes and consider only the fundamental band[19].
Let us introduce $a_i^\dagger$, a_i as creation and annihilation atom operators corresponding to the i-th lattice site, the field $\hat{\Phi}(x)$ associated to the annihilation of a particle in the x spatial position can be expressed by the relation [92]:

$$\hat{\Phi}(x) = \sum_i w\left(x - id\right) \hat{a}_i \tag{2.3.1}$$

By exploiting the introduced field it is possible to describe the processes graphically represented on the right side of figure 2.3.1. We can define the following quantities

---

[19] As we will see, inter-bands processes can occur, for example by shining on an atom a laser light resonant with the transition $|g\rangle|gb\rangle \rightarrow |e\rangle|eb\rangle$ where $|gb\rangle$ describes the fundamental band and $|eb\rangle$ describes the first excited band shown in figure 2.2.1.

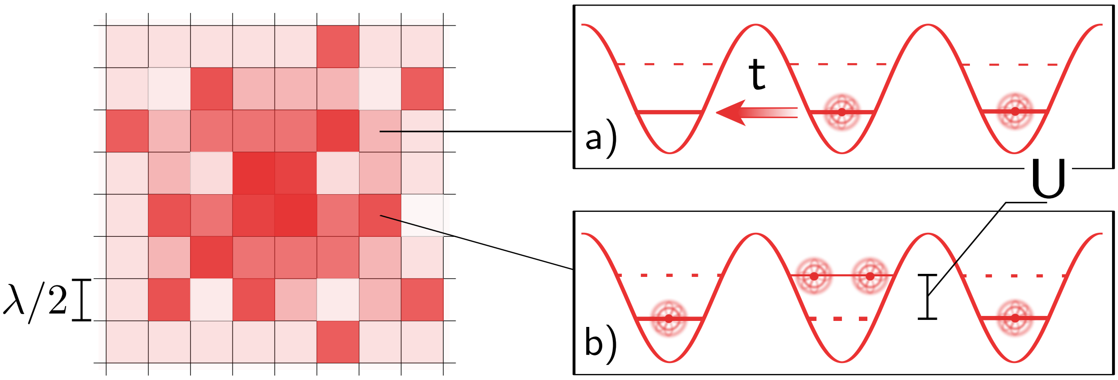

Figure 2.3.1. Sketch of a square lattice system when the atomic cloud has been loaded in the periodic light structure. On the left, a red scale has been used to represent the occupation number in a specified lattice site (more intense red corresponds to higher number of atom per site). On the right are represented the processes that can play a role in the many-body lattice dynamic. In particular a) describes a hopping process in which an atom transfer itself from its site to the nearest neighbour and b) describes the on-site interaction.

related to processes a) and b) of figure 2.3.1: the tunneling energy t and the interaction energy U.

By considering a one-dimensional lattice it is possible to define the tunneling energy by the relation

$$\mathsf{t}_{i,j} = \int w^*(x-x_i)\left(\frac{\hat{p}^2}{2m} + \mathsf{s}E_{\mathsf{r}}\sin^2\left(k_{\mathsf{L}}x\right)\right)w(x-x_j)\mathrm{d}x \tag{2.3.2}$$

that describes the MLWF overlap between the sites (i, j). The tunneling process along one direction, describing the hopping from a lattice site to the nearest neighbour ($j = i \pm 1$), can be represented by the Hamiltonian

$$\hat{H} = -\sum_i \mathsf{t}_{i,i+1}\left(\hat{a}^\dagger_{i+1}\hat{a}_i + \hat{a}^\dagger_i\hat{a}_{i+1}\right) = -\mathsf{t}\sum_i\left(\hat{a}^\dagger_{i+1}\hat{a}_i + \hat{a}^\dagger_i\hat{a}_{i+1}\right), \tag{2.3.3}$$

that has to be evaluated on the many-particle state that describes the atomic occupation number in the lattice. This relation is just the equation 2.2.6 evaluated in the second quantization approach and neglecting the hopping between sites that are not nearest neighbour, because the overlap integral between sites that are further away is exponentially suppressed as the Wannier functions become more localized on the single lattice site. This approximation is valid when the lattice potential V_0 exceeds about $4E_{\mathsf{r}}$.
The expression 2.3.3 of the lattice Hamiltonian in the MLWF basis takes the name of tight binding approximation (tba).

In this approximation, considering a one-dimensional lattice, the dispersion relation of the lowest band becomes a cosinusoidal function of the quasimomenta $\epsilon(k) = -2\mathsf{t}\cos(kd)$ and subsequently the bandwidth $\Delta\epsilon = |\epsilon(0) - \epsilon(\pi/d)| = 4\mathsf{t}$. The obtained relation has been derived for a one-dimensional lattice but, since the Hamiltonian operator 2.2.6 is separable, the total wavefunction can be factorised. In this case the dispersion relation, assuming isotropic lattice depth, can be written as

$$\epsilon_{\mathsf{3D}} = -2\mathsf{t} \sum_{i\in\{x,y,z\}} \cos(k_i d),$$

that implies, as direct consequence, a 3D bandwidth $\Delta\epsilon = 12\mathsf{t}$.

By considering an isotropic three-dimensional lattice it is possible to define the interaction energy U as follows:

$$\mathsf{U} = \frac{4\pi\hbar^2}{m}\, a \prod_{i\in\{x,y,z\}} \int w^4(i)\,\mathrm{d}i, \tag{2.3.4}$$

that describes the on-site overlap of the densities corresponding to two atoms. To introduce the interaction in the many-body Hamiltonian 2.3.3 it is necessary to specify the statistical behaviour of the atoms considered. This is due principally to the Pauli principle [93] that imposes, for identical fermionic particles, an antisymmetric wavefunction under the exchange transformation $1 \leftrightarrow 2$. Consequently, it is not possible to have two fermions characterized by the same quantum numbers and therefore the s-wave scattering cannot occur between two identical atoms. Bosonic atoms, differently, have a symmetric wavefunction under the exchange transformation $1 \leftrightarrow 2$; in this case the interaction between atoms characterized by the same set of quantum numbers is not forbidden and s-wave scattering can occur.

In this thesis we will present experimental results obtained by loading a 3D cubic lattice with atoms of a unique lanthanide, Ytterbium, that we will introduce in detail in chapter 3.4.

This element presents many stable isotopes and in this work we studied mainly ^{174}Yb and ^{173}Yb, that obeys to Bose-Einstein and Fermi-Dirac statistics respectively.

In section 2.3.1 we introduce interactions for bosons and fermions in the many-body Hamiltonian 2.3.3 and we analyze some effects of interactions on the trapped atomic gas.

2.3.1 Hubbard models

In this section atomic interactions, introduced in sections 2.3 and 2.1.2, will be integrated in the lattice Hamiltonian and we will present some important results regarding interactions in a many-body lattice system.
Our starting point is the hopping Hamiltonian, that, by following the second quantization approach and restricting the analysis to the tba, can be expressed as shown in equation 2.3.3.

Interactions between atoms can be modelled in the second quantization approach by inserting an on-site term that can be written in the form [94, 95]

$$\hat{H}_{\mathsf{int}} = \frac{\mathsf{U}}{2} \sum_i \hat{a}_i^\dagger \hat{a}_i^\dagger \hat{a}_i \hat{a}_i. \tag{2.3.5}$$

Bose Hubbard model (BHM)

For bosonic atoms, in which the commutation rules between creation and annihilation operators can be written as

$$\left[\hat{a}_l, \hat{a}_{l'}^\dagger\right] = \delta_{l,l'}, \tag{2.3.6}$$

the interaction term can be written as $\hat{n}_i\left(\hat{n}_i - 1\right)$, where $\hat{n}_i$ is the number operator referred to the i-th lattice site.
The complete Hamiltonian

$$\hat{H}_{\mathsf{BH}} = \hat{H} + \hat{H}_{\mathsf{int}}$$

is the well-known Bose-Hubbard Hamiltonian (BH), and despite its simply form, cannot be resolved exactly except for trivial cases.

In the case in which the on-site collisions can be neglected ($\mathsf{U} \simeq 0$), the eigenvalues of the model have been reported in section 2.1.2 and show an absolute minimum for quasimomentum $k = 0$, while the eigenfunction for the ground state of N atoms is delocalized over the whole lattice and the atomic gas exhibits a superfluid (SF) behaviour. The resulting wavefunction can be written by introducing the total number of lattice sites N_{L}, as [92, 94–96]

$$|\Psi_{\mathsf{SF}}\rangle = \frac{1}{\sqrt{N!}} \left(\frac{1}{\sqrt{N_{\mathsf{L}}}} \sum_i \hat{a}_i^\dagger \right)^N |0\rangle \tag{2.3.7}$$

where $|0\rangle$ is the vacuum state.
In the limit $\mathsf{U/t} \to 0$ the ground state of the BH model is a Gross-Pitaevskii-type

state with a condensate fraction equal to 1. When the number of lattice sites $N_\mathsf{L} \to \infty$ and the number of atoms N increases consequently to keep constant the ratio N/N_L, the ground-state wavefunction becomes indistinguishable from a coherent state [92]:

$$|\Psi_\mathsf{SF}\rangle = e^{\left(\sqrt{N}\hat{a}^\dagger_{k=0}\right)}|0\rangle = \prod_i e^{\left(\sqrt{\frac{N}{N_\mathsf{L}}}\hat{a}^\dagger_{(i,k=0)}\right)}|0\rangle_i. \tag{2.3.8}$$

The resulting coherent state can be factorized into a collection of local coherent states characterized by mean value equal to $\sqrt{N/N_\mathsf{L}}$ and centered on each lattice site as shown in equation 2.3.8.

The other easily evaluable example is the case in which the interaction is predominant over the hopping contribution ($\mathsf{U} \gg \mathsf{t}$). In this case the effect of interactions is to inhibit the tunneling in order not to pay the energy cost of a hopping process in an occupied site, which is proportional to U as sketched in figure 2.3.1 [97]. In this case the system is in a gapped phase called Mott insulator (MI) and the system ground state, if we consider the condition in which the total number of atoms N is exactly equal to the number of lattice sites N_L, can be expressed as the product of Fock states characterized by $\langle \hat{n} \rangle = 1$:

$$|\Psi_\mathsf{MI}\rangle = \prod_i \hat{a}^\dagger_i |0\rangle. \tag{2.3.9}$$

As shown by relation 2.3.9, when the tunneling can be neglected, and the number of atoms is sufficiently low to keep the mean occupation filling under or equal to 1 the number of doubly-occupied sites goes to zero. This characteristic define a ideal MI only when the hopping is forbidden and, consequently, $\mathsf{t} \equiv 0$.
When the tunneling cannot be completely neglected, i.e. a condition that experimentally is always verified, the characteristic of the MI phase is the incompressibility, that means that when the chemical potential μ is changed the density remains unchanged ($\partial_\mu \langle \hat{n} \rangle = 0$).

When t increases, the probability to find a doubly-occupied site becomes non negligible and the BH model describes the competition between the kinetic energy t and the repulsive on-site interaction U: the first lowers the total energy of the system by delocalizing particles over the periodic potential, the latter minimizes the presence of multiple-occupied lattice sites.
A sharp quantum phase transition from an ideal SF, described by 2.3.7, to a MI occurs in the thermodynamic limit in two and three dimensions. When the thermodynamic limit is not fulfilled, the sharp transition between SF and MI becomes a proper crossover and in particular, if we consider the 3D case, the transition

order parameter is the condensed fraction n_{SF}/n. This quantity is equal to 1 in a pure SF while it goes to zero when $\mathsf{U/t} \ll 1$.
By evaluating a mean-field theory [96, 98] it is possible to obtain a critical value at which the transition from MI to SF can occur. For $\langle \hat{n} \rangle = 1$, the critical ratio at which the transition occurs corresponds to

$$(\mathsf{U/t})_{\mathsf{c}} = 5.8\ \zeta \tag{2.3.10}$$

where ζ is the coordination number and it is determined by the lattice geometry (for a cubic lattice $\zeta = 6$).

As briefly introduced in section 2.2, the light beams used to create spatially periodic potentials are not ideal plane waves, rather Gaussian beams that induce an additional harmonic potential that can be quantified by the relation 2.2.5. The presence of an additional harmonic potential that has a long-range curvature with respect to the distance between two nearest neighbour lattice sites, can be modelled by adding a site-dependent potential V_i, proportional to the number of atoms in the site $\hat{n}_i$, in the total Hamiltonian $\hat{H}_{\mathsf{BH}}$. This potential allows for a more faithful description of experimental conditions. Phenomena related to many-body lattice physics usually are not strongly influenced by the presence of a little site potential correction due to the finite curvature of lattice beams. Remarkably, they can even favour the observation of strongly-correlated gapped states like the Mott insulator phase. Indeed, the presence of a smooth confining potential allows the observation of Mott insulating regions regardless of the precise atom number, provided that the density is large enough to reach an integer value in some regions of the trap.

As we will describe in section 4, in this work we will present recent results regarding the experimental estimation of previously unknown scattering lengths in a 3D ^{174}Yb bosonic Mott insulator [44].

Fermi Hubbard model (FHM)

Regarding atoms that obey Fermi-Dirac statistics, as we introduced in section 2.3, the interaction potential cannot be described using relation 2.3.5 because the Pauli principle [93] avoids any s-wave scattering between two particles that are described by the same quantum numbers. Since fermions are characterized by half-odd spin, it is possible to have a s-wave interaction between two atoms if the spin projections (σ, σ') on the quantization axis are different:

$$\hat{H}_{\mathsf{FD}} = \begin{cases} \sum_{\sigma,\sigma',i} \frac{\mathsf{U}_{\sigma,\sigma'}}{2} \hat{a}^{\dagger}_{i,\sigma} \hat{a}_{i,\sigma} \hat{a}^{\dagger}_{i,\sigma'} \hat{a}_{i,\sigma'} & \forall \sigma \neq \sigma' \\ 0 & \text{otherwise} \end{cases} \tag{2.3.11}$$

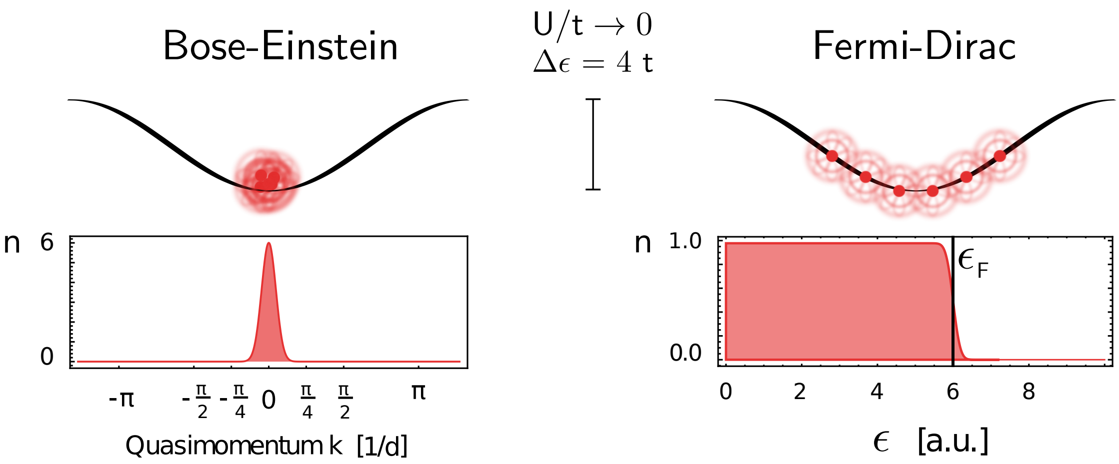

Figure 2.3.2. This sketch compares the occupation of the lowest energy band for bosons and fermions when the interaction energy U can be neglected. The dependence of the occupation number as a function of ϵ for fermions and as a function of the quasimomentum k for bosons is reported. Bosonic atoms constitute a superfluid phase (BEC) ideally described by a Gross-Pitaevskii-type state. The quantity ϵ_{F} is the Fermi energy and represents the highest occupied energy level in a system in which $T = 0$. Fermionic atoms constitute a metal if the band filling is < 1 otherwise it constitute a band insulator.

All the other operators introduced in section 2.3, the tunneling process between two near lattice sites and the potential induced by the real shape of the light beams used to generate lattices are not modified by fermionic statistics because they operate as identity operator[20] in the spin space:

$$\hat{H}_{\mathsf{FD}} = \hat{H} \otimes \mathbb{I}_{\sigma} \qquad\qquad \hat{V}_{(i,\mathsf{FD})}\hat{n}_{(i,\mathsf{FD})} = \hat{V}_i \otimes \mathbb{I}_{\sigma}. \tag{2.3.12}$$

The **Fermi-Hubbard Hamiltonian** (FH) can be obtained by summing all the considered operators:

$$\hat{H}_{\mathsf{FH}} = -\mathsf{t}\sum_{i,\sigma}\left(\hat{a}^{\dagger}_{i+1,\sigma}\hat{a}_{i,\sigma} + h.c.\right) + \sum_{i,\sigma\neq\sigma'}\frac{\mathsf{U}_{\sigma,\sigma'}}{2}\hat{a}^{\dagger}_{i,\sigma}\hat{a}_{i,\sigma}\hat{a}^{\dagger}_{i,\sigma'}\hat{a}_{i,\sigma'} + \sum_{i,\sigma}V_{i,\sigma}\hat{a}^{\dagger}_{i,\sigma}\hat{a}_{i,\sigma}. \tag{2.3.13}$$

The FH Hamiltonian can be solved analitically only by exploiting the Bethe ansatz on the one-dimensional model [99, 100], while for higher dimensions it is not pos-

---

[20] Strictly speaking, as it is shown by relation 3.4.4, the potential generated by a radiation is not completely independent from the nuclear-spin projection considered. The spin-dependent contribution has a non-negligible role only if quasi-resonant light is considered. For that reason, the potential V_i, that is realized by shining far-off resonant light, can be considered diagonal in the spin space as assumed by relation 2.3.12.

sible to solve the model exactly[21]. Despite its simple form, the FH Hamiltonian can describe and simulate the behaviour of interacting electrons in an ideal crystal. The FH model has been intensively studied and allowed the experimental description of the transition from a metallic conducting phase to an insulating phase [105], band magnetism [106], bad metallic phases [107, 108], and there are proposal regarding the possibility to understand the phenomenon that underlies the existence of high-temperature superconductivity in iron-based materials [109] or in cuprates [110].

In general, the interaction energy $\mathsf{U}_{\sigma,\sigma'}$ depends on the internal states of the fermions but, if we consider atomic states for which the interaction energy does not depend on the internal states[22], the interaction and consequently the FH model simplifies to

$$\hat{H}_{\mathsf{sFH}} = -\mathsf{t}\sum_{i,\sigma}\left(\hat{a}^{\dagger}_{i+1,\sigma}\hat{a}_{i,\sigma} + h.c.\right) + \frac{\mathsf{U}}{2}\sum_{i,\sigma\neq\sigma'}\hat{n}_{i,\sigma}\hat{n}_{i,\sigma'} + \sum_{i,\sigma}V_{i,\sigma}\hat{n}_{i,\sigma}. \tag{2.3.14}$$

As we made for the BH model, it can be convenient to evaluate initially the simplest cases possible. In particular, we consider a gas formed by a single spin[23]. In this case the most convenient way to analyze the model is to consider 1D geometry and perform a canonical transformation on creation and annihilation operators:

$$\hat{a}^{\dagger}_{k,\sigma} = \frac{1}{\sqrt{N}}\sum_{j} e^{ikj}\hat{a}^{\dagger}_{j,\sigma}. \tag{2.3.15}$$

The FH model in the quasi-momentum space can therefore be written as:

$$\hat{H}_{\mathsf{U=0}} = \sum_{k}\epsilon_k\ \hat{n}_k \qquad\qquad \text{where}\ \ \epsilon_k = -\mathsf{t}\sum_{j}e^{ikj}. \tag{2.3.16}$$

By summing over the nearest neighbour lattice sites, $j = \pm d$, we obtain:

$$\epsilon_k = -2\mathsf{t}\cos\left(kd\right).$$

Single-spin atoms occupy the lowest energy band accordingly to the Pauli principle as shown in figure 2.3.2. If a mixture of spins in which interactions can be

---

[21] The model, in the presence of a potential that depends on the i-th lattice site, can only be solved by using numerical techniques. Some theoretical methods used to solve this model are Quantum Monte-Carlo (QMC) [101], Density Matrix Renormalization Group (DMRG) [102, 103] and Dynamical Mean-Field Theory (DMFT) [104].

[22] As we will see in detail in section 5.1.1, this property is a characteristic of the hyperfine states of the level characterized by $\mathsf{J} = 0$ of two-electron and two-electron like atoms as Sr, Yb, Hg, Cd, . . .

[23] This condition include also $\mathsf{U} = 0$ as shown by equation 2.3.11.

neglected ($\mathsf{U}/\mathsf{t} \to 0$) is considered instead of a pure polarized gas, the same behaviour is expected for each spin.
If the band filling for each spin is not integer the gas behaves as a **metal** while, if the filling per spin is integer, the gas simulates a crystal in which the conduction is not allowed because the "valence" band is completely filled. This state, called **band insulator**, is an incompressible state in which the mean site occupation is determined but atoms are not localized on the lattice sites. The gas instead results incompressible because the system energy increases by the **energy gap** between the fundamental and the first excited band when an atom is added.

When the interaction energy is much bigger than the hopping term ($\mathsf{U} \gg \mathsf{t}$), and if the filling per lattice site is an integer atoms localize in the lattice sites and a **Mott insulator** generates, similarly to the bosonic case discussed above. When a particle is added, the many-body system, in order to avoid the energy cost U, avoids to create a doubly-occupied site and therefore the sample compressibility vanishes. In this case the hopping term can be neglected and the resulting Hamiltonian can be written as

$$\hat{H}_{\mathsf{atom}} = \frac{\mathsf{U}}{2} \sum_{i,\sigma \neq \sigma'} \hat{n}_{i,\sigma} \hat{n}_{i,\sigma'} + \sum_{i,\sigma} V_{i,\sigma} \hat{n}_{i,\sigma}. \tag{2.3.17}$$

Conditions in which equation 2.3.17 results verified are refereed as **atomic limit**. In this limit the Hamiltonian can be diagonalized analytically. Nevertheless, this operator cannot describe properly a real trapped sample because thermalization processes, that occurs in the lattice, are driven by the tunneling ($\mathsf{t} \neq 0$). For that reason Hamiltonian 2.3.17 can be used as unperturbed Hamiltonian $\hat{H}_0$ of a perturbative approach in which is evaluated the contribution of a finite but non negligible tunneling to the insulating phase.

3 Alkaline-earth like atoms and experimental techniques

This chapter is devoted to the description of two-electron atoms properties and to the experimental procedures adopted to trap and cool down atomic ytterbium to the quantum degeneracy (both bosonic and fermionic isotopes).
The first part (section 3.1) introduces the electronic-structure and the properties of alkaline-earth-like atoms. The following section is devoted to the theoretical description of interactions that allow the excitation of intercombination (section 3.2) and "clock" transitions for both bosonic (section 3.2.2) and fermionic (section 3.2.1) AEL atoms.
In section 3.3, we will illustrate how to coherently couple the nuclear-spin degree of freedom by means of Raman transitions.
In the third part of the chapter the Ytterbium (Yb) atom and its physical and chemical properties are described (section 3.4). Last part is also devoted to the description of the resonant laser sources (section 3.4.1) and the out-of-resonance laser sources (section 3.4.2) employed to trap and cool down Yb atoms in order to reach the degenerate regime.
Finally, section 3.4.3 describes briefly the vacuum setup and the experimental steps necessary to realize and detect ultracold bosonic and fermionic samples in the "Florence Yb" laboratory.
These last subjects are described in detail in references [111–113].

3.1 Basic atomic properties

The denomination alkaline-earth atoms (AE) is a prerogative of the elements that constitute the II group[1] of the periodic table of elements (Be, Mg, Ca, Sr, Ba, Ra), while alkaline-earth like atoms (AEL) is preferred to indicate the elements that are not in the II group of the periodic table but have an external electronic configuration that is constituted by a complete external high-momenta (d,f) shell and a complete external s-shell. This occurs to elements of group $\mathsf{IIB_{CAS}}$ that are characterized by complete d-shells (Zn, Cd, Hg, Cn) or to rare-earth elements in which there are complete f-shells (Yb, No) or, more easily, happens to helium (He) in which there is only one s-shell occupied.

For the specified atoms, AE, AEM, AEL, the structure of the lowest-energy excitations in the spectrum is determined by the presence of the complete external s-shell, in a similar way to what happens in He: due to the fact that the total spin in the most external s-shell can assume only values $\mathsf{S} \in \{0, 1\}$, the quantized energy levels, can be divided into singlet ($\mathsf{S} = 0$) and triplet states ($\mathsf{S} = 1$). Singlet states are characterized by an antisymmetric wavefunction in the spin space under the exchange transformation $1 \leftrightarrow 2$, while triplet states have a symmetric wavefunction in the spin space.

By exposing atoms to a proper electric field, transitions from a singlet state to a triplet state are forbidden[2] because the electric field cannot modify the spin sector ($\mathsf{S} = \mathsf{S'}$) [114]. While this sentence is nearly exact for He, when an AEL atom is considered, the fact that the Russell-Saunders coupling cannot describe exactly the interactions that take place in the atom, makes transitions between singlet and triplet states possible. However, as a strong indication that the Russell-Saunders coupling is still a good approximation to describe AEL atoms, those are very narrow. In any case, by using L-S coupling it is possible to evaluate the coupling strength due to electric-dipole interaction for the low-lying states and in particular between the ground state $^1\mathsf{S}_0$ and the states $^1\mathsf{P}_1$, $^3\mathsf{P}_i$ $\forall i \in \{0, 1, 2\}$. As happened in section 2.3.1, to describe these transitions the atom statistical

---

[1] By following the chemical abstracts service (CAS) standard the right name of the considered group should be $\mathsf{IIA_{CAS}}$. The other II group designed by the CAS standard, named $\mathsf{IIB_{CAS}}$, is represented by transition metals characterized by “complete” external d-shell $\left(l = 2 \text{ with degeneracy } (2s+1)(2l+1) = \left(2 \cdot \frac{1}{2} + 1\right)(2 \cdot 2 + 1) = 10\right)$ and s-shell ($l = 0$ with degeneracy 2). For that reason, the old nomenclature prefers to use, for atoms of the $\mathsf{IIB_{CAS}}$ group, the diction alkaline-earth metal atoms (AEM).

[2] If we consider the electric dipole interaction as coupling operator.

behaviour will play an interesting and unexpected major role.

3.2 Intercombination transitions in AEL

AEL atoms (both fermionic[3] and bosonic isotopes) are characterized by full external electronic configuration, thus the ground state is characterized by momentum $\mathsf{L} = 0$. Moreover, the ground state is a singlet state, that implies $\mathsf{S} = 0$. The whole internal angular momentum that an atom carries in the ground state is only due to the nuclear momentum I.
The Russell-Saunders coupling, used to describe ground and low-lying excited states, does not takes into account the atomic spin-orbit interaction, that can be expressed as

$$\hat{H}_{\mathsf{so}} = \sum_{i=1}^{\#_{\mathsf{el}}} \xi(\vec{\mathsf{r}})\vec{\mathsf{L}}_i \cdot \vec{\mathsf{S}}_i \tag{3.2.1}$$

where i is referred to the i-th atomic electron. Let us consider this Hamiltonian as a perturbative contribution to the unperturbed atomic term, noticing that, if the spin-orbit term is considered, S is not a good quantum number. The first excited state, for each reported AEL, can be written as $e\,s\;e\,p$ where e represents the principal quantum number of the most external s electron[4].
In LS.coupling approximation, if we define the unperturbed states as ${}^1\mathsf{P}_1^0$, ${}^3\mathsf{P}_j^0$ $\forall j \in \{0, 1, 2\}$, it is possible to express $e\,s\;e\,p$ as [115–117]

$$\begin{pmatrix} {}^3\mathsf{P}_0 \\ {}^3\mathsf{P}_1 \\ {}^1\mathsf{P}_1 \\ {}^3\mathsf{P}_2 \end{pmatrix} = \underbrace{\begin{pmatrix} 1 & 0 & 0 & 0 \\ 0 & \alpha & \beta & 0 \\ 0 & -\beta & \alpha & 0 \\ 0 & 0 & 0 & 1 \end{pmatrix}}_{\mathsf{R}} \begin{pmatrix} {}^3\mathsf{P}_0^0 \\ {}^3\mathsf{P}_1^0 \\ {}^1\mathsf{P}_1^0 \\ {}^3\mathsf{P}_2^0 \end{pmatrix} \tag{3.2.2}$$

where the ${}^3\mathsf{P}_{0,2}$ states result unperturbed because J commutes with the perturbation $\hat{H}_{\mathsf{so}}$. The transition ${}^1\mathsf{S}_0^0 \rightarrow {}^1\mathsf{P}_1^0$ occurs in electric-dipole approximation so, if β is non null, also the transition ${}^1\mathsf{S}_0^0 \rightarrow {}^3\mathsf{P}_1$ can happen, because of the stable mixing described in equation 3.2.2. Since experimentally the cited transitions occur, transition frequencies and level lifetimes have been accurately measured

---

[3] The stable fermionic AEL atoms are: ${}^9\mathsf{Be}_{\mathsf{F}=3/2}$, ${}^{25}\mathsf{Mg}_{\mathsf{F}=5/2}$, ${}^{43}\mathsf{Ca}_{\mathsf{F}=7/2}$, ${}^{87}\mathsf{Sr}_{\mathsf{F}=9/2}$, ${}^{135}\mathsf{Ba}_{\mathsf{F}=3/2}$, ${}^{137}\mathsf{Ba}_{\mathsf{F}=3/2}$, ${}^{67}\mathsf{Zn}_{\mathsf{F}=5/2}$, ${}^{111}\mathsf{Cd}_{\mathsf{F}=1/2}$, ${}^{199}\mathsf{Hg}_{\mathsf{F}=1/2}$, ${}^{201}\mathsf{Hg}_{\mathsf{F}=3/2}$, ${}^{171}\mathsf{Yb}_{\mathsf{F}=1/2}$, ${}^{173}\mathsf{Yb}_{\mathsf{F}=5/2}$ but in many cases the natural abundance is so low with respect to the stable bosonic counterparts that is necessary to use enriched samples. The main exception is represented by Be that has a natural abundance about 100%.

[4] In Yb, for example, $e = 6$.

Iso- -tope	Tran- -sition	Final F ($F_{in} = 5/2$)	Frequency (MHz)	δ from ^{174}Yb (MHz)	$\Gamma/2\pi$ (kHz)
^{174}Yb	${}^1S_0 \to {}^1P_1$		$751\ 526\ 533.49 \pm 0.33$ [a]		$28.9 \cdot 10^3$ [b]
^{173}Yb		3/2		-253.418 ± 0.050 [c]	
		5/2		516.26 ± 0.90 [d]	
		7/2		587.986 ± 0.086 [c]	
^{174}Yb	${}^1S_0 \to {}^3P_1$		$539\ 386\ 561 \pm 10$ [e]		182 [f]
^{173}Yb		3/2		3805.66 ± 0.60 [g]	
		5/2		2311.73 ± 0.50 [g]	
		7/2		-2386.49 ± 0.50 [g]	

Table 3.2.1. Transition frequencies ν and linewidths Γ of the dipole permitted transition ${}^1S_0^0 \to {}^1 P_1^0$ and the so called intercombination transition ${}^1S_0^0 \to {}^3 P_1^0$ for most abundant [125] bosonic and fermionic Yb isotopes.
References: [a]:[120], [b]:[121], [c]:[122], [d]:[126], [e] :[123], [f] :[127], [g] :[124]

[118–124]; the method proposed in [117] can be used to directly evaluate α and β. The first condition, that allows the ratio α/β to be calculated, is obtained by the relation

$$\frac{|\alpha|^2}{|\beta|^2} = \frac{\tau_{{}^3P_1}}{\tau_{{}^1P_1}} \left(\frac{\nu_{{}^3P_1}}{\nu_{{}^1P_1}} \right)^3, \tag{3.2.3}$$

while the second condition ($\alpha^2 + \beta^2 = 1$), necessary to determine separately α and β, is obtained by taking into account that $R \in \mathbb{SO}_4$.

Frequencies and linewidths for the mostly abundant [125] bosonic and fermionic Yb isotopes[5] are reported in table 3.2.1. By solving the equation system constituted by equation 3.2.3 and $\alpha^2 + \beta^2 = 1$ we obtain $\alpha = 0.992$ and $\beta = 0.127$.

The statistical nature of atoms involved has not played any role in the physical description of spin-orbit interaction. This means, as it can be observed experimentally, that intercombination transition (in which $\Delta S \neq 0$) between the ground state and the triplet state ${}^3P_1$ can occur for any AEL atom. We have considered the case of Yb explicitly, but the interaction presented is completely general and

---

[5] In Yb, the biggest isotopic frequency difference is represented by the shift between transitions ${}^1S_0 \to {}^3P_1(F = 7/2)$ and ${}^1S_0 \to {}^3P_1(F = 3/2)$ that correspond to [123] $\Delta_{MAX} \simeq 6200$ MHz. By evaluating that $\Delta_{MAX}/\nu \approx 10 \cdot 10^{-6}$ results that α and β are substantial invariant with respect to the isotopic shift.

carries to values of α and β for other AEL[6]. In the following section we will introduce the hyperfine interaction that gives a non trivial contribution only when fermionic atoms are considered.

3.2.1 Doubly forbidden transitions in Fermionic AEL

In any AEL atom, if only the electric dipole interaction is considered, each intercombination transition is prohibited by the Wigner-Eckart theorem [128], that forbids transitions in which the total atomic spin is changed ($\Delta \mathsf{S} \neq 0$). In section 3.2, we briefly analyzed the contribution of the spin-orbit interaction in AEL atoms when the Russell-Saunders approximation is used to describe atomic internal states.

Moreover, as we introduced in section 2.2.3, in AEL atoms other states exist, that are not directly coupled to a state in which a dipole transition from the ground state is allowed. These states are those that in section 3.2 remained unperturbed when the spin-orbit interaction contribution has been evalued. In L-S approximation these states can be expressed by $^3\mathsf{P}_{0,2}$ and the transitions $^1\mathsf{S}_0 \rightarrow {}^3\mathsf{P}_{0,2}$ coupling them to the ground state are called "doubly-forbidden transitions". The first transition rule that is forbidden is the cited spin-singlet to spin-triplet transition while the second transition rule that is not permitted is:

- $J \rightarrow J' = 0$ for $^3\mathsf{P}_0$ state; (at all orders of light-matter interaction)
- $\Delta J \neq \pm 1$ for $^3\mathsf{P}_2$ state. (in electric-dipole coupling approximation)

In this chapter we introduce the fundamental role of hyperfine interaction in fermionic atoms.

The hyperfine interaction $\hat{H}_{\mathsf{hfs}}$ is due principally to the electromagnetic interaction of an incomplete electronic shell with the atomic nucleus. In general, since we are interested in describing the interaction of an AEL atom with an external radiation, we have to consider simultaneously the hyperfine interaction and the coupling with the external electric field. To overcome this circumstance, we will suppose the hyperfine term as the biggest perturbation to the spin-orbit Hamiltonian, knowing that this approach is valid only if the width of the $^3\mathsf{P}_1$ state is much smaller than the fine-structure energy intervals between the components of triplet $^3\mathsf{P}$ level [129]. The Hamiltonian that describes the hyperfine electromagnetic interaction can be

---

[6] As further example, for Sr it is possible to obtain $\alpha = 0.9996$, $\beta = -0.0286$ [117].It can be noted that the coupling between $^3\mathsf{P}_1^0$ and $^1\mathsf{P}_1^0$ is lower in Sr than in Yb, i.e. $\beta_{\mathsf{Sr}} < \beta_{\mathsf{Yb}}$. For that reason, intercombination transitions for Sr, are more prohibited than what happens for Yb; this is due principally to the smaller Z of Sr with respect to Yb, entering the amplitude of the spin-orbit interaction.

written as sum a over multipole nuclear tensors $N^{(q)}_{\lambda}$ of rank q combined with even-parity electronic coupling operators $E^{(q)}_{\lambda}$. The resulting Hamiltonian operator is invariant under parity and rotational transformation, or in other words, is a scalar [116, 129, 130]. A scalar operator ensures that the total angular momentum $\mathsf{F} = \mathsf{I} + \mathsf{J}$ and its projection m_{F} on the quantization axis are conserved.
The interaction Hamiltonian can therefore be expressed as:

$$\hat{H}_{\mathsf{hfs}} = \sum_{q} \left(N^{(q)} E^{(q)} \right). \tag{3.2.4}$$

The first-order corrections to the unperturbed eigenstates, that are marked by superscripts ^{0} (as happened in section 3.2), are obtained by relation

$$|\gamma(\mathsf{IJ}), \mathsf{F}, m_{\mathsf{F}}\rangle = \sum_{\gamma'\mathsf{J}'} |\gamma'(\mathsf{IJ'}), \mathsf{F}, m_{\mathsf{F}}\rangle^0 \frac{\langle\gamma'(\mathsf{IJ'}), \mathsf{F}, m_{\mathsf{F}}|^0 \hat{H}_{\mathsf{hfs}} |\gamma(\mathsf{IJ}), \mathsf{F}, m_{\mathsf{F}}\rangle^0}{E^0_{(\gamma',\mathsf{J}')} - E^0_{(\gamma,\mathsf{J})}} \tag{3.2.5}$$

where γ indicates the collection of good quantum numbers necessary to determine a certain state.
The expectation value of the considered Hamiltonian can be evaluated by using the Wigner-Eckart theorem, to obtain [116]:

$$\begin{aligned} \langle\gamma', \mathsf{F}', m_{\mathsf{F}'}|^0 \hat{H}_{\mathsf{hfs}} |\gamma, \mathsf{F}, m_{\mathsf{F}}\rangle^0 &= \delta_{\mathsf{FF}'} \delta_{m_{\mathsf{F}} m_{\mathsf{F}'}} (-1)^{\mathsf{I}+\mathsf{J}'+\mathsf{F}} \\ &\sum_{q} \langle \mathsf{I}||N^{(q)}||\mathsf{I}\rangle \langle \mathsf{J}'||E^{(q)}||\mathsf{J}\rangle \begin{Bmatrix} \mathsf{I} & \mathsf{I} & q \\ \mathsf{J} & \mathsf{J}' & \mathsf{F} \end{Bmatrix} \end{aligned} \tag{3.2.6}$$

where we introduced the 6-j Wigner symbols [48].
Equation 3.2.6 shows clearly that the hyperfine interaction couples states[7] only if $\mathsf{J}' + \mathsf{J} = q$. Since the lowest correction to the unperturbed atomic potential can be obtained by imposing $q = 1$, it can be noted that the reduced matrix element for $E^{(1)}$ is not diagonal over J and in particular $\mathsf{J}' = \mathsf{J}, \mathsf{J} \pm 1 \ \forall \mathsf{J} > 0,\ \mathsf{J}'$. From this relation, it can be deduced that perturbed states cannot be described properly by states characterized by J because it is not a good quantum number of the perturbed system.
To describe properly the state $^3\mathsf{P}_0$ it is necessary to consider at least the interaction terms corresponding to ($q = 1$), that describes the interaction with the nuclear magnetic dipole (to which the measured quantity $\mu = \langle \mathsf{I}, m_{\mathsf{I}} = \mathsf{I} | N^{(1)} | \mathsf{I}, m_{\mathsf{I}} = \mathsf{I}\rangle$ is associated) and to the second term of multipole expansion ($q = 2$), that describes the interaction of the electromagnetic field generated by electrons with a electric quadrupole (to which the quantity $Q = 2\langle \mathsf{I}, m_{\mathsf{I}} = \mathsf{I} | N^{(2)} | \mathsf{I}, m_{\mathsf{I}} = \mathsf{I}\rangle$ is associated).

---

[7] Remarkably, by using $6 - j$ properties the other equalities that have to be verified are: $\mathsf{I} + \mathsf{I} = q$, $\mathsf{I} + \mathsf{J} = \mathsf{F}$, $\mathsf{I} + \mathsf{J}' = \mathsf{F}$.

Exact calculations regarding higher multipole expansion orders and the explicit evaluation of each reduced matrix element can be found in reference [116].
The perturbed state can therefore be described by the relation [131, 132]:

$$|^3\mathsf{P}_0\rangle = |^3\mathsf{P}_0^0\rangle + (\alpha_0\alpha - \beta_0\beta)\,|^3\mathsf{P}_1^0\rangle + (\alpha_0\beta + \beta_0\alpha)\,|^1\mathsf{P}_1^0\rangle + \gamma_0|^3\mathsf{P}_2^0\rangle \tag{3.2.7}$$

where[8]

$$\begin{aligned}
\alpha_0 &= -\frac{1}{\hbar}\frac{\langle^3\mathsf{P}_1, \mathsf{F}=\mathsf{I}|\hat{H}_\mu|^3\mathsf{P}_0^0, \mathsf{F}=\mathsf{I}\rangle}{\omega_{^3\mathsf{P}_1} - \omega_{^3\mathsf{P}_0^0}},\\
\beta_0 &= -\frac{1}{\hbar}\frac{\langle^1\mathsf{P}_1, \mathsf{F}=\mathsf{I}|\hat{H}_\mu|^3\mathsf{P}_0^0, \mathsf{F}=\mathsf{I}\rangle}{\omega_{^1\mathsf{P}_1} - \omega_{^3\mathsf{P}_0^0}},\\
\gamma_0 &= -\frac{1}{\hbar}\frac{\langle^3\mathsf{P}_2, \mathsf{F}=\mathsf{I}|\hat{H}_Q|^3\mathsf{P}_0^0, \mathsf{F}=\mathsf{I}\rangle}{\omega_{^3\mathsf{P}_2} - \omega_{^3\mathsf{P}_0^0}}.
\end{aligned} \tag{3.2.8}$$

By taking into account the probability to perform a transition from the excited state $|^3\mathsf{P}_0\rangle$ to the ground state $|^1\mathsf{S}_0\rangle$ as a result of the interaction with the dipole operator it is possible to evaluate numerically the decay rate of the doubly forbidden $|^3\mathsf{P}_0\rangle$ state. For $^{173}\mathsf{Yb}$ the decay rate due to dipole interaction corresponds to 38.5 mHz and, consequently the state has a lifetime of 23 s [133, 134].
In 2016 Clivati *et al.* [135] measured the absolute frequency ν of the $|^1\mathsf{S}_0\rangle \to |^3\mathsf{P}_0\rangle$ "clock" transition in $^{173}\mathsf{Yb}$ improving the uncertainty with respect to the previous measured value [136] by exploiting an optical fiber link between a Cesium fountain[9] and the 578 nm clock laser that will be shortly presented in section 3.4.1. The measured frequency is [135]:

$$\nu_{\mathsf{clock}} = (518294576845268 \pm 10)\ \mathsf{Hz}. \tag{3.2.9}$$

3.2.2 Doubly forbidden transitions in Bosonic AEL

Except for the fermionic species reported in section 3.2, all the other stable isotopes are bosons characterized by electronic angular momentum $\mathsf{J} = 0$ and nuclear angular momentum $\mathsf{I} = 0$. The hyperfine interaction introduced in 3.2.4,

---

[8] Each P state, as it happened in equation 3.2.2, can be obtained introducing a matrix $\mathsf{R}_0 \in \mathbb{SO}_4$. In this case we have $\vec{\mathsf{P}} = \mathsf{R}_0\mathsf{R}\vec{\mathsf{P}}^0$. Because R_0 and R have a determinant equal to 1, it can be demonstrated that the state 3.2.7 does not satisfy the relation $\mathsf{R}_0\mathsf{R}_0^T = \mathbb{I}$. The correct form should be $\delta_0|^3\mathsf{P}_0^0\rangle + (\alpha_0\alpha - \beta_0\beta)\,|^3\mathsf{P}_1^0\rangle + (\alpha_0\beta + \beta_0\alpha)\,|^1\mathsf{P}_1^0\rangle + \gamma_0|^3\mathsf{P}_2^0\rangle$ where δ_0 can be determined by the determinant of R_0. Equation 3.2.7 is, howerever, a good approximation because coefficient δ_0 results to be about 1 and all the others about 10^{-4} (in Sr) [117].

[9] It is placed in INRiM institute in Turin (IT), about 642 km distant from LENS institute in Florence (IT), where the clock laser was placed.

that at the $(q = 1)$ order can be written as [137]

$$\hat{H}_{\mathsf{hfs}} = g_{\mathsf{I}} \mu_N \hat{I} \mathsf{E}^{(1)}$$

where

$$E^{(1)} = 2\frac{\mu_0}{4\pi}\mu_{\mathsf{B}} \left[\frac{\vec{\mathsf{L}}}{r^3} - \frac{1}{r^3} \left(\hat{\vec{\mathsf{S}}} - 3\frac{\hat{\vec{\mathsf{S}}} \cdot \vec{\mathsf{r}}}{r^2} \vec{\mathsf{r}} \right) + \frac{2}{3}\frac{\delta\left(r\right)}{r^2} \hat{\vec{\mathsf{S}}} \right],$$

gives always a null contribution because the total angular momentum, that is always a conserved quantity, is equal to $\mathsf{F} = 0$. As a consequence, the mixing mechanism introduced in section 3.2.1 cannot occur and the transition $|^1\mathsf{S}_0\rangle \to |^3\mathsf{P}_0\rangle$ is forbidden.

In the absence of other magnetic or electric fiels, the $|^3\mathsf{P}_0\rangle$ state is connected to the ground state $|^1\mathsf{S}_0\rangle$ only by two-photon transitions that pass through a virtual state $|v\rangle$. The linewidth of this process for Yb has been analyzed in reference [134] and for Sr in Refs. [117, 138], and in any case it results to be about[10] 10^{12} s.

The cited doubly forbidden transition can occur [139–141] if an external field takes the place of the hyperfine interaction in fermionic isotopes. To model properly how this mechanism works let us consider the magnetic dipole interaction Hamiltonian

$$\hat{H}_{\mathsf{z}} = \hat{\vec{\mu}} \cdot \vec{\mathsf{B}} \tag{3.2.10}$$

where $\hat{\vec{\mu}}$ is the magnetic dipole operator and $\vec{\mathsf{B}}$ is the applied external magnetic field. Without losing generality we can consider a magnetic field along the $\hat{z}$ axis of our reference system $\vec{\mathsf{B}} = |B|\hat{z}$ and express the magnetic dipole operator in terms of spin $\hat{\mathsf{S}}$ and angular momentum $\hat{\mathsf{L}}$ operators as follows:

$$\hat{H}_{\mathsf{z}} = \mu_{\mathsf{B}} \left(\hat{\mathsf{L}}_z + g_s \hat{\mathsf{S}}_z \right) |B| \tag{3.2.11}$$

where $\mu_B = \left(\frac{e\hbar}{2m_e}\right)$ is the Bohr magneton and $g_s = (2.00231930436 \pm 152 \cdot 10^{-11})$ [142] is the electron g-factor[11]. By considering the perturbation theory framework, the doubly forbidden $^3\mathsf{P}_0$ state of Hamiltonian $\hat{H}_{\mathsf{tot}} = \hat{H}_{\mathsf{atom}} + \hat{H}_{\mathsf{z}}$, can be expressed as:

$$|^3\mathsf{P}_0\rangle = |^3\mathsf{P}_0^0\rangle + \sum_{i \neq |^3\mathsf{P}_0^0\rangle} \frac{1}{\hbar} \frac{\langle ^3\mathsf{P}_0^0 | \hat{H}_{\mathsf{z}} | i \rangle}{\omega_{|^3\mathsf{P}_0^0\rangle} - \omega_{|i\rangle}} |i\rangle \simeq |^3\mathsf{P}_0^0\rangle + \frac{1}{\hbar} \frac{\langle ^3\mathsf{P}_0^0 | \hat{H}_{\mathsf{z}} | ^3\mathsf{P}_1^0 \rangle}{\omega_{|^3\mathsf{P}_0^0\rangle} - \omega_{|^3\mathsf{P}_1^0\rangle}} |^3\mathsf{P}_1^0\rangle \tag{3.2.12}$$

---

[10] A year corresponds to $3.15 \cdot 10^7$ s.

[11] For the scope of this work it is always possible to approximate it to $g \simeq 2$. This approximation allows to write the Hamiltonian 3.2.11 as $\mu_{\mathsf{B}} \left(J_z + S_z\right)$.

where we neglected all the terms in which the frequency difference between two unperturbed states is big enough to give negligible contributions to the final sum. In order to evaluate numerically the coupling induced by the magnetic interaction, it can be useful to write the atomic states in the basis $|\mathsf{L},\mathsf{S},\mathsf{L}_z,\mathsf{S}_z\rangle \equiv |\mathsf{L}_z,\mathsf{S}_z\rangle$ in which L_z and S_z are diagonal. Since

$$|^3\mathsf{P}_0^0\rangle = \frac{1}{\sqrt{3}}\left(|-1,1\rangle + |0,0\rangle + |1,-1\rangle\right)$$

and

$$|^3\mathsf{P}_1^0\rangle(m_{\mathsf{J}=0}) = \frac{1}{\sqrt{2}}\left(|-1,1\rangle + |1,-1\rangle\right)$$

equation 3.2.12 can be written as:

$$|^3\mathsf{P}_0\rangle = |^3\mathsf{P}_0^0\rangle + \underbrace{\sqrt{\frac{2}{3}}\mu_{\mathsf{B}}|B|}_{\Omega_B}\frac{1}{\Delta}|^3\mathsf{P}_1^0\rangle \tag{3.2.13}$$

where $\Delta/\hbar = \omega_{|^3\mathsf{P}_0^0\rangle} - \omega_{|^3\mathsf{P}_1^0\rangle}$. The electric dipole transition between the perturbed doubly forbidden state and the ground state $|^1\mathsf{S}_0\rangle$ can be described by evaluating the matrix element

$$\langle ^3\mathsf{P}_0|\hat{\vec{\mathsf{d}}}\cdot\vec{E}|^1\mathsf{S}_0\rangle = \frac{\Omega_B}{\Delta}\langle ^3\mathsf{P}_1^0|\hat{\vec{\mathsf{d}}}\cdot\vec{E}|^1\mathsf{S}_0\rangle \tag{3.2.14}$$

where $\hat{\vec{\mathsf{d}}}$ is the electric dipole operator defined in equation 2.1.19 and relation 3.2.13 has been used. The resulting matrix element can be evaluated for $^{174}\mathsf{Yb}$ by taking into account frequencies and linewidths reported in table 3.2.1.

The Rabi frequency of the doubly forbidden transition can be expressed as [143]:

$$\Omega^2 = \left|\frac{\mu_{\mathsf{B}}B}{\Delta}\right|^2 \underbrace{\frac{\lambda^3\Gamma}{2\pi^2\hbar c}}_{\frac{2}{3}\Omega_L^2} I = \alpha_{174}^2|B[G]|^2 I\left[\frac{\mathsf{mW}}{\mathsf{mm}^2}\right] \tag{3.2.15}$$

where $\alpha_{174} = 2\pi\times 0.186$ and I is the intensity of the laser used to excite the transition. Regarding the natural linewidth of this magnetic-induced transition, it can be estimated by the relation [139]

$$\Gamma_{^3\mathsf{P}_0} \simeq \Gamma_{^3\mathsf{P}_1^0}\frac{\Omega_L^2 + (2\Omega_B)^2}{(2\Delta)^2}.$$

This broadening is due mainly to the fraction of unperturbed $^3\mathsf{P}_1^0$ population transfered in the clock state when an external magnetic field is applied, as clearly shown

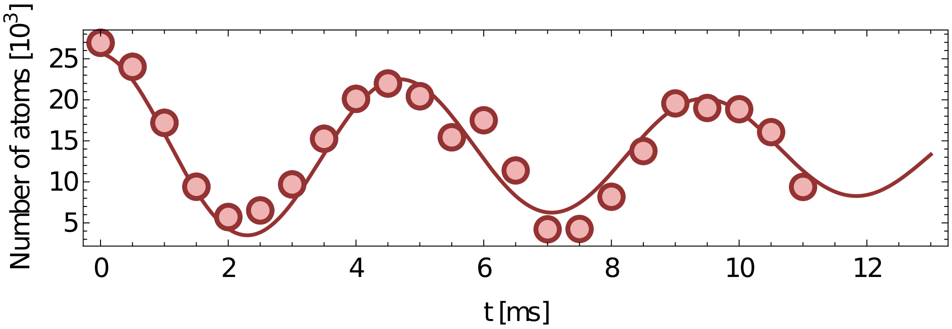

Figure 3.2.1. Coherent Rabi oscillation performed by exciting the clock transition on a singly-occupied Mott insulator constituted by a ^{174}Yb atomic sample in a deep 3D optical lattice. Red points represent the number of ground state atoms remained after the excitation pulse while the red line is a sinusoidal fit that also takes into account an exponential decay to consider decoherence phenomena. The best fit frequency obtained is $\Omega = 2\pi\times(208 \pm 4)$ Hz, that is comparable to the theoretical prediction.

by the previous relation. The energy difference Δ corresponds, in the case of Yb, to 21.1 THz [144], the Rabi frequency obtained by applying a magnetic field of 150 G and an intensity about 10 $\frac{\text{mW}}{\text{mm}^2}$ can reach about $2\pi\times100$ Hz [145] and therefore the theoretical broadening is about or less than some μHz [139]. In figure 3.2.1 a Rabi oscillation performed by expoiting the clock transition $^1\text{S}_0 \rightarrow {}^3\text{P}_0$, when an external magnetic field of 150 G is applied, is reported. In particular, the bosonic sample was loaded in a deep 3D optical lattice to avoid any photon momentum tranfer, as we will see briefly in section 4.1.1 [140]. As it can be observed, it is possible to achieve Rabi frequencies comparable to the ones provided by the model. The most important linewidth-enhancing term results to be the power broadening due to radiation intensity. This contribution is not negligible every time the light intensity exceeds the saturation intensity defined by [143]:

$$I_{\text{sat}} = \frac{\hbar\omega_0^3}{4\pi c^2}\Gamma. \tag{3.2.16}$$

When $I \geq I_{\text{sat}}$, the line broadening is dominated by the power broadening. The observed linewidth thus can be expressed as $\Gamma' = \Gamma\sqrt{1+\frac{I}{I_{\text{sat}}}}$.

3.2.3 Magnetic properties of the transition

When the bosonic species are taken into account, due to a null total momentum for both the $^3\mathsf{P}_0^0$ and $^1\mathsf{S}_0$ states, the effect of an external magnetic field can be evalued by calculating, in the perturbation theory framework, the second[12] order energy shift due to Hamiltonian 3.2.11:

$$\Delta E_{\mathsf{z(II)}} = \frac{|\langle {}^3\mathsf{P}_1|\hat{H}_\mathsf{z}|{}^3\mathsf{P}_0\rangle|^2}{\Delta} = \frac{1}{4\pi^2}\frac{\Omega_B^2}{\Delta} = \beta B^2 \tag{3.2.17}$$

where, for $^{174}\mathsf{Yb}$, $\beta \simeq (-6.12 \pm 0.10)\ 10^{-2}\ \mathsf{Hz/G}^2$ [146].

Having a half-integer total angular momentum F, fermionic species exihibit a magnetic-sensitive substructure that is determined by the total momentum F. If the clock $^3\mathsf{P}_0$ and the ground states are considered, by noticing that the total momentum is $\mathsf{F} = \mathsf{I}$, the Zeeman structure results to be the same for each considered state and in particular, for $^{173}\mathsf{Yb}$ where $\mathsf{F} = 5/2$, the multiplet degeneracy is equal to $2\mathsf{F} + 1 = 6$. Defined a quantization axis of the system, the states can be characterized by the projection of the total momentum F on this axis.
When an external magnetic field is applied, the Zeeman shift [147] removes the energy degeneracy by following the relation

$$\Delta E_\mathsf{z} = \mu_\mathsf{B} g_\mathsf{F} m_\mathsf{F} B \tag{3.2.18}$$

where the external magnetic field has been considered aligned to the quantization axis of the system and g_F is the Landé factor[13] [117, 148]. If unperturbed states are considered, the Landé factor become $g_\mathsf{F} = -\frac{\mu_\mathsf{N}}{\mu_\mathsf{B}} g_\mathsf{I}$ where $\mu_\mathsf{N} = \left(\frac{e\hbar}{2m_p}\right)$ is the nuclear magneton and g_I is the magnetic nuclear factor (for $^{173}\mathsf{Yb}$ $g_\mathsf{I} = -0.6776$ [130]). While the approximation of unperturbed states is completely verified for the ground state, that are not mixed with other states by the hyperfine Hamiltonian, we discussed in detail the role of the latter interaction term on the clock state in

---

[12] The first order correction is related to $\langle\psi|\hat{H}|\psi\rangle$, where ψ is the unperturbed state wavefunction. Being the $^3\mathsf{P}_0^0$ an amagnetic state the matrix element $\langle H\rangle = 0$.

[13] In general it can be defined as

$$g_\mathsf{F} = g_\mathsf{J}\frac{\mathsf{F(F+1)+J(J+1)-I(I+1)}}{\mathsf{2F(F+1)}} + g_\mathsf{I}\frac{\mu_\mathsf{N}}{\mu_\mathsf{B}}\frac{\mathsf{F(F+1)-J(J+1)+I(I+1)}}{\mathsf{2F(F+1)}} \tag{3.2.19}$$

where

$$g_\mathsf{J} = 1 + (g-1)\,\frac{\mathsf{J(J+1)-L(L+1)+S(S+1)}}{\mathsf{2J(J+1)}}. \tag{3.2.20}$$

section 3.2.1. As shown in equation 3.2.7, the mixing of the perturbed $^3\mathsf{P}_0$ state with magnetic-sensitive state ($^3\mathsf{P}_1$) causes a small variation in the effective Landé factor, that produces a differential Zeeman splitting for the two states. For $^{173}\mathsf{Yb}$ it results to be [133]:

$$\Delta E_{(\mathsf{z},{}^1\mathsf{S}_0)}/h \simeq 207.4\ m_\mathsf{F}\ B \qquad \Delta E_{(\mathsf{z},{}^3\mathsf{P}_0)}/h \simeq 320.8\ m_\mathsf{F}\ B \tag{3.2.21}$$

where the field is reported in [G] and the coefficient is expressed in [Hz/G].

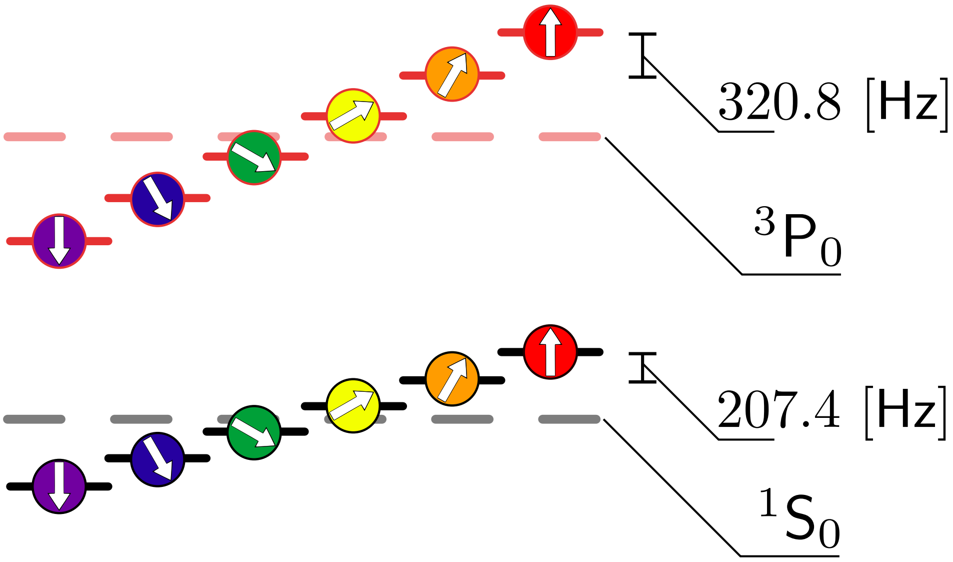

Figure 3.2.2. The Zeeman substructure for $^{173}\mathsf{Yb}$ is reported for the ground and the clock state for an external magnetic field $\mathsf{B} = 1$ G. Sublevels, in the presence of a quantization axis, are parametrized by their projection quantum number m_F. For $^{173}\mathsf{Yb}$ the projections range from $-5/2$ (violet) to $+5/2$ (red).

As it occurs in the bosonic species, the transition frequency is also affected by a second-order Zeeman shift ΔE_z that, as we described in the first part of this section, induces a quadratic dependence of the transition frequency as a function of the external magnetic field applied. As displayed in equation 3.2.17, the second-order shift due to the Zeeman Hamiltonian can be expressed as

$$\Delta E_\mathsf{z}^{(\mathsf{II})} = \beta B^2 \tag{3.2.22}$$

where the parameter $\beta = -(0.064 \pm 0.002)$ Hz/G^2 has been measured experimentally [113].

3.3 Raman transitions between spin states

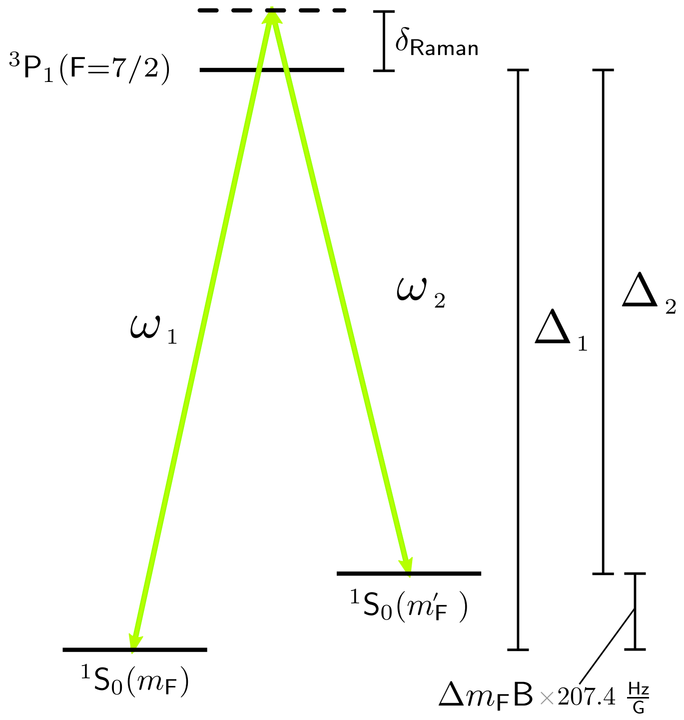

Figure 3.3.1. A simple description of Raman transitions between two states with different nuclear spin projection in ^{173}Yb can be made by oversimplifying the atom as a Λ configuration system. A complete description can be found in [112, 145]

In this section we will focus on the possibility to induce a coherent laser coupling between different nuclear-spin states of AEL atoms. We will introduce the theoretical basis for the description of two-photon Raman transitions, that will be used in the experiments reported in this thesis for the coherent manipulation of the nuclear-spin degree of freedom of ^{173}Yb. For the sake of illustration, we will consider a simplified case in which only two states out of the nuclear-spin manifold are coupled. The complete theory for multi-level system can be found in references [112, 145].

The Λ scheme represented in figure 3.3.1 shows the simplest system in which a Raman transition can occur. Two stable nuclear-spin states of the ground state ($^1\mathsf{S}_0$) identified by the spin projection on the quantization axis $|m_\mathsf{F}\rangle$, $|m'_\mathsf{F}\rangle$ are coupled by two laser fields that induce a two-photon process exploiting the higher-energy state ($^3\mathsf{P}_1$) as intermediate state. The detuning of the laser beams employed to couple the aforementioned states (Δ_1, Δ_2) is big enough to consider the single-photon transition probability $|m_\mathsf{F}\rangle \to |^3\mathsf{P}_1\rangle\ \forall m_\mathsf{F}$ negligible [149].

If the energy differences between $|m_\mathsf{F}\rangle$ and the excited state is $\hbar\Delta_1$ and that for $|m'_\mathsf{F}\rangle$ is $\hbar\Delta_2$, as shown in figure 3.3.1, the total electric field that interacts with the

Λ system can be expressed as

$$\vec{\mathsf{E}}\left(\vec{\mathsf{r}},t\right)=\hat{\varepsilon}_1 E_{01}\cos\left(\vec{\mathsf{k}}_1\cdot\vec{\mathsf{r}}-\left(\Delta_1+\delta_{\mathsf{Raman}}\right)t\right)+\hat{\varepsilon}_2 E_{02}\cos\left(\vec{\mathsf{k}}_2\cdot\vec{\mathsf{r}}-\left(\Delta_2+\delta_{\mathsf{Raman}}\right)t\right) \tag{3.3.1}$$

where $\omega_i=(\Delta_i+\delta_{\mathsf{Raman}})/2\pi$ is the light frequency of the i-th beam employed to perform the transition and $\hat{\varepsilon}_i$ is the i-th beam polarization vector [143].
The Hamiltonian that describes the Λ system can be written, in the rotating frame of the laser field, as:

$$\hat{H}_{\mathsf{Raman}}=\hat{H}_0+\hbar\delta_{\mathsf{Raman}}\left(|m_{\mathsf{F}}\rangle\langle m_{\mathsf{F}}|+|m'_{\mathsf{F}}\rangle\langle m'_{\mathsf{F}}|\right)+\hat{H}_{\mathsf{I}} \tag{3.3.2}$$

where $\delta_{\mathsf{Raman}}=\omega_1-\Delta_1=\omega_2-\Delta_2$ is the detuning with respect to the corresponding single photon transitions and $\hat{H}_0$ contains the kinetic term. The Hamiltonian $\hat{H}_{\mathsf{I}}$, that describes the interaction between the Λ system and the two-colour radiation, can be expressed, in rotating wave-approximation (RWA), as:

$$\hat{H}_{\mathsf{I}}=\frac{\hbar}{2}\left[\Omega_{\mathsf{Raman}}e^{i\vec{\mathsf{q}}\cdot\vec{\mathsf{r}}}|m_{\mathsf{F}}\rangle\langle m'_{\mathsf{F}}|+h.c.\right], \tag{3.3.3}$$

where $\vec{\mathsf{q}}=\vec{\mathsf{k}}_1-\vec{\mathsf{k}}_2$ is the momentum transferred by the radiation to the atoms in the Raman process,

$$\Omega_{\mathsf{Raman}}=\frac{\Omega_1\Omega_2^*}{2\delta_{\mathsf{Raman}}} \tag{3.3.4}$$

is the effective two-photon Rabi frequency. By solving the Schrödinger equation the excited state, that is considered out of resonance, is not involved in the dynamics and the total Hamiltonian can be expressed in the two-dimensional Hilbert subspace generated by $|m_{\mathsf{F}}\rangle$, $|m'_{\mathsf{F}}\rangle$:

$$\hat{H}_{\mathsf{Raman}}=\begin{pmatrix}\hat{H}_0+\mathcal{U}_1 & \frac{\hbar}{2}\Omega_{\mathsf{Raman}}e^{i\vec{\mathsf{q}}\cdot\vec{\mathsf{r}}}\\ \frac{\hbar}{2}\Omega^*_{\mathsf{Raman}}e^{-i\vec{\mathsf{q}}\cdot\vec{\mathsf{r}}} & \hat{H}_0+\mathcal{U}_2\end{pmatrix} \tag{3.3.5}$$

where

$$\mathcal{U}_i=\frac{\hbar|\Omega_i|^2}{4\delta_{\mathsf{Raman}}} \tag{3.3.6}$$

are the light shift on the $|m_{\mathsf{F}}\rangle$, $|m'_{\mathsf{F}}\rangle$ states caused by the radiation.
If the momentum acquired by the system is null ($\vec{\mathsf{q}}=0$), that implies that the two considered beams propagate on the same direction, and we suppose the Rabi frequencies Ω_i real, the Hamiltonian can be further simplified to obtain:

$$\hat{H}_{\mathsf{Raman}}=\frac{\hbar\Omega_{\mathsf{Raman}}}{2}\sigma_x+\left(\hat{H}_0+\mathcal{U}_1\right)\frac{\mathbb{I}_{2\times2}+\sigma_z}{2}+\left(\hat{H}_0+\mathcal{U}_2\right)\frac{\mathbb{I}_{2\times2}-\sigma_z}{2}. \tag{3.3.7}$$

As shown in figure 3.3.1, in the case of interest, that regards ground-state sublevels identified by nuclear-spin projections in $^{173}\mathsf{Yb}$ atoms, when an external magnetic field is applied, a differential energy shift between two sublevels corresponding to $207.4\left[\frac{\mathsf{Hz}}{\mathsf{G}}\right]\times\Delta m_{\mathsf{F}}\mathsf{B}$ (see section 3.2.3) is generated.
The final state $|m'_{\mathsf{F}}\rangle$ that is "connected" to the initial one $|m_{\mathsf{F}}\rangle$ strongly depends on the polarization of the light employed to perform the transition because the angular conservation imposes

$$m_{\mathsf{F}}+j_1+j_2=m'_{\mathsf{F}} \tag{3.3.8}$$

where j_i is the angular momentum transferred by photon to the Λ system. If the transition is performed with the two σ^+/σ^- laser fields, the states that can be coupled are determined by the condition

$$m'_{\mathsf{F}}=m_{\mathsf{F}}\pm 2$$

while, if the transition is performed with two $\sigma_{\pm}/\pi$ laser fields, the final possible states are determined by

$$m'_{\mathsf{F}}=m_{\mathsf{F}}\pm 1.$$

We note that the possibility to induce coherent nuclear-spin filps with an optical field in ensured by the choice of an intermediate excited state in which the hyperfine interaction couples the nuclear spin with the electronic wavefunctions. Specifically, we have chosen to use the $^3\mathsf{P}_1$ as an intermediate state because of the combination of reduced linewidth ($\simeq 180$ kHz) and large hyperfine splitting (several GHz), that allow substantial two-photon Rabi frequencies (on the order of several hundreds of Hz) with very modest heating due to residual single-photon absorption over a timescale of approx. 100 ms. The experimental implementation will be discussed in section 3.4.5

By exciting the $\sigma^+\sigma^-$ Raman transitions, recent experiments in which the Raman beams have been arranged in order to transfer momentum to the atoms ($\vec{\mathsf{q}}\neq 0$) have been performed [12]. In this work, the configuration in which the transferred momentum is null ($\vec{\mathsf{q}}\simeq 0$) has been used. In section 5.4 we employed this technique as a detection tool of $^{173}\mathsf{Yb}$ molecules supported by an Orbital Feshbach Resonance and in chapter 6 this technique has been employed in order to study Fermi-Hubbard models where different spins are coupled.

3.4 Ytterbium and experimental setup

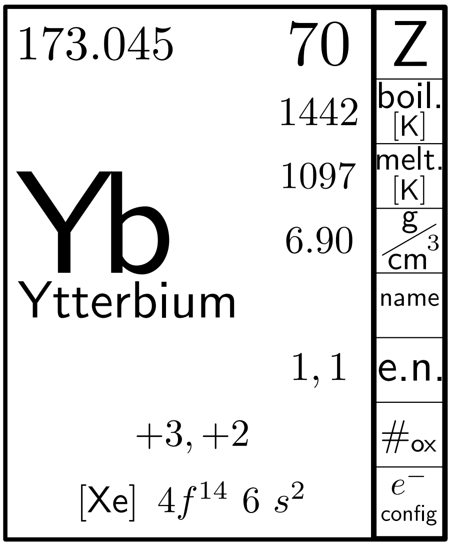

Figure 3.4.1. Chemical and physical properties of Yb are reported. From the left-top to the right-bottom are shown: mean weight in [u] [150], atomic number, boiling and melting temperatures, density, electronegativity, common oxidation numbers, electronic configuration.

Ytterbium (Yb) is the fourteenth lanthanide of the periodic table of elements and has atomic number Z = 70. Lanthanides and actinides have the f-shell[14] as most external shell occupied. Its complete electronic configuration can be written as [Xe] $4f^{14}$ $6s^2$. Since its f-shell is completely occupied[15], its electronic structure is determined by the two electrons in the $6s$-shell. As introduced in section 3.1, for that reason it is possible to consider Ytterbium as an external member of groups $\mathsf{IIA_{CAS}}$ or $\mathsf{IIB_{CAS}}$. By considering that No atom have only unstable isotopes characterized by half-life of the order of tens of minutes, Ytterbium can be considered as the only element of the so-called "f-block" that can be described as a two-electron atom.

As direct consequence of its electronic configuration, it is the rare-earth metal with the lowest magnetic susceptibility. To highlight the uniqueness of this lanthanide it can be noted that, differently from all other elements of its period, in which the preferred oxidation number is +3, the stability of the complete f-shell induces the oxidation number +2, that instead is a peculiar characterstic of $\mathsf{IIA/B_{CAS}}$-group atoms.

If exposed to molecular oxigen, it reacts forming oxides and in particular YbO and Yb_2O_3. It reacts also with atmospherical traces of $\mathsf{VII_{CAS}}$ elements, by forming

---

[14] The f-shell corresponds to angular momentum $l = 3$ and consequently degeneracy $\mathsf{deg} = (2\mathsf{s}+1)(2\mathsf{l}+1) = 14$.

[15] It can be interesting to note that each element of its period has a complete external s-shell but does not present electronic properties of AEL atoms, as a consequence of the partially-filled f-shell.

$\mathsf{YbX_2}$ and $\mathsf{Yb_2X_3}$ where X is a generic element of the cited group. Compounds of Yb(II) are strong reducent and therefore are not stable in acqueous solution where the reaction

$$2\mathsf{YbO} + \mathsf{H_2O} \rightarrow \mathsf{H_2}(g) + \mathsf{Yb_2O_3}$$

can occur[16]. Also if it is not highly reactive in all the other conditions, due to the pureness degree requested by atomic physics experiments[17], it is transported in jars with inert atmosphere.
Except for Hg, this atom is the heaviest stable alkaline-earth-like atom[18].
While at room temperature Hg is a fluid, Yb is a soft, ductile and malleable solid metal.
To obtain chunks of pure Yb, this element is separated by other rare-earth elements by solvent-solvent extraction or ion-exchange techniques. The elemental metal is prepared by the metallothermic reduction of its mostly abundant oxide ($\mathsf{Yb_2O_3}$). When it is purified in chunks it appears bright and silvery[19].
It has a density of 6.90 $\mathsf{g/cm^3}$, a fusion temperature equal to 1097 K and the boiling point is about 1442 K at standard pressure. In this condition, it has the smallest liquid range of all metals [151].
Fundamental physical-chemical characteristics of Yb are summarized in figure 3.4.1. To produce a vapour pressure of about 10^{-2} Torr, that is a necessary condition to produce degenerate gases experimentally, temperatures below the fusion point are used. The vapour pressure can be determined by the empirical relation:

$$\log_{10}\left(P[\mathsf{Pa}]\right) = 14.117 - \frac{8111}{T[\mathsf{K}]} - 1.0849\log_{10}\left(T[\mathsf{K}]\right) \tag{3.4.1}$$

[111], that implies temperatures between 450 and 500 °C. This range of temperatures are achievable by means of a relatively simple oven setup, but unfortunately ytterbium becomes highly reactive when the temperature reaches the specified temperature interval and, in particular, it has been noted that this metal can cause chemical deterioration of silica glass and sapphire [152]. To avoid this kind

---

[16] Similar reactions occur when compounds of halogens are considered. It is possible to revert these reactions to synthetize mono-oxide of Yb as W. K. Klemm and W. Schuth made in 1929 to obtain $\mathsf{YbCl_2}$.

[17] Although this peculiar metal was discovered in 1878 by the Swiss chemist Jean Charles Galissard de Marignac (He named four elements (Yb, Ytterbium - Y, Yttrium - Tb, Terbium - Er, Erbium) referring their name to the village of Ytterby (Sweden) where the minerals in which compounds of the new species was found were extracted.) until 1953 described physical and chemical properties remained unknown, because the low abundance of this element and the difficulties to purify it from all the other rare-earth metals do not permit to obtain a pure sample.

[18] Strictly speaking, Mercury is catalogued as an alkaline metal AEM and thus Ytterbium results the heaviest stable AEL atom.

[19] To inhibit all the unwanted reactions, chunks can be treated with HF. Ytterbium flouride is quite inert and can stop the oxidation with atmospherical moisture.

Nuclide	Mass [u]	F	Statistics	Natural abundance %	μ_I [μ_N]
^{168}Yb	167.933897(5)	0	bosonic	0.13(1)	
^{170}Yb	169.9347618(26)	0	bosonic	3.04(15)	
^{171}Yb	170.9363258(26)	$\frac{1}{2}$	fermionic	14.28(57)	+0.4919
^{172}Yb	171.9363815(26)	0	bosonic	21.83(67)	
^{173}Yb	172.9382108(26)	$\frac{5}{2}$	fermionic	16.13(27)	−0.6776
^{174}Yb	173.9388621(26)	0	bosonic	31.83(92)	
^{176}Yb	175.9425717(28)	0	bosonic	12.76(41)	

Table 3.4.1. Nuclear properties of the seven stable isotopes of Yb. Masses in atomic units ($\mathrm{u} = 1.6605390404(20)\times10^{-27}\mathrm{kg}$) are taken from [153], while natural abundances and magnetic nuclear momentum (including the diamagnetic correction) are taken from [154].

of problem it can be necessary to heat up vacuum viewports exposed to atomic vapours or direct flux[20].

Another interesting property of this metal is the presence of many isotopes with relatively high natural abundancies, as shown in table 3.4.1. This is a considerable difference between this metal and principally all the other AEL elements. The two isotopes with half-integer nuclear spin, ^{171}Yb and ^{173}Yb, are fermionic while all the other isotopes, have zero nuclear spin and are bosonic. Moreover, the possibility to have high abundances for all the isotopes allow studies over Bose-Bose, Bose-Fermi and Fermi-Fermi mixtures [155–159].
Those principal physical properties, as the atomic mass, the spin, the statistical behaviour, the magnetic nuclear momentum and the natural abundancies are reported in table 3.4.1.
Artificially it is possible to synthesize 27 unstable isotopes; as it can be expected, from ^{148}Yb to ^{181}Yb, atoms can change significantly their properties as the half-life time and the type of decay scheme. The description of this atomic catalogue goes beyond the scopes of this thesis, but a particularly interesting synthesized atom is ^{169}Yb, that is the unstable isotope with the longest half-life time (about 32 days) and is used as a portable hard X-ray source when electricity is not available or for medical purposes [163].

In the experiments reported in this thesis we focus on ^{174}Yb and ^{173}Yb, the

---

[20] In our setup the atomic beam that is not captured by the Zeeman slower goes on a viewport that is maintained at 200 °C to overcome chemical bonds between Yb and sapphire.

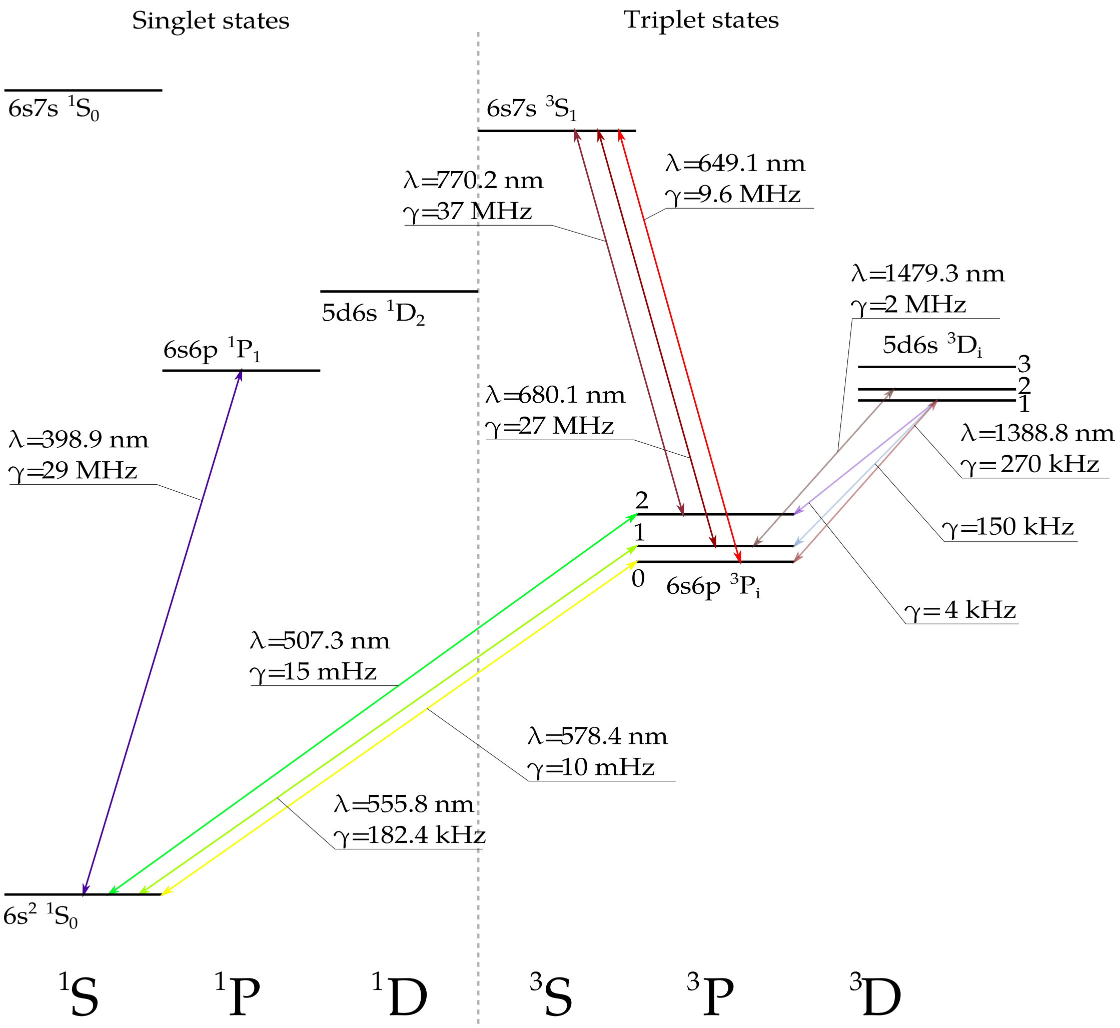

Figure 3.4.2. Grotrian's diagram for Yb atoms. Optical transitions are reported as solid lines connecting involved levels. For each transition the corresponding wavelength and the decay rates defined by $\gamma = \Gamma/2\pi$ are reported. For fermionic isotopes, hyperfine structure has not been displayed. References: linewidths and wavelengths are taken for $|g\rangle \rightarrow {}^1\mathrm{P}_1$ from [120, 121, 126, 160]; $^3\mathrm{P}_1$ [123, 127]; $^3\mathrm{P}_0$ [91, 130]; $|^3\mathrm{P}_0\rangle \rightarrow {}^3\mathrm{D}_i$ [161]; $^3\mathrm{S}_1$ [162].

mostly abundant bosonic and fermionic isotopes respectively. In section 4 we present the experimental characterization of state-dependent interactions in bosonic ^{174}Yb, which realizes a promising platform for the implementation of quantum information schemes based on the control of the electronic degree of freedom with the clock transition $^1\mathrm{S}_0 \rightarrow {}^3\mathrm{P}_0$ in an almost ideal two-level system. In sections 5 and 6 we present experiments performed in fermionic ^{173}Yb, where the additional control of the nuclear spin state ($\mathsf{I} = 5/2$) enriches the range of possibilities that can be explored, allowing the efficient production and control of orbital Feshbach molecules, as well as novel quantum-simulation experiments from the realization of spin-orbit-coupled systems to the study of strongly correlated multi-component Hubbard models.

Regarding its electronic structure and principal transitions, Yb can be described as an AEL atom. In the previous sections we have already discussed the excitation of singly and doubly forbidden intercombination transitions for both bosonic and fermionic species.
In section 3.2.2 instead has been explored the clock intercombination transition by applying an external magnetic field, also in this case all the numerical evaluation has been reported for isotopes employed during experiments.
A more complete Grotrian's diagram [164] for Yb is shown in figure 3.4.2. The transitions reported in this diagram are exploited to produce and manipulate routinely atomic samples of Yb. In the next section the experimental setup and the relevant transitions will be treated.

3.4.1 Resonant laser sources

This section is devoted to the description of the laser sources used to excite the described atomic transitions and the experimental apparatus. Since high-power lasers at transition wavelengths (see figure 3.4.2) were not available when the experiment was built, all the principal transitions are excited by radiation produced by exploiting second-harmonic generation. A complete description and characterization of the sources and of the experimental apparatus can be found in references [111–113]. Regarding the laser devoted to the excitation of the $^3\mathsf{P}_0$ state a complete review can be found in Refs. [113, 165]. In the last part of this section, we introduce a source to detect directly the meta-stable $^3\mathsf{P}_0$ state.

- $^1\mathsf{S}_0 \rightarrow {}^1\mathsf{P}_1$ (Zeeman slower, Imaging)

The laser light necessary to excite the dipole-permitted $^1\mathsf{S}_0 \rightarrow^1 \mathsf{P}_1$ transition, corresponding to 398.9 nm, is generated by starting from a fiber-coupled tapered-amplifier laser-diode system Toptica TA PRO, that emits about 1.2 W at 798 nm. The radiation emitted by the cited source is injected in a home-made bow-tie cavity where, exploiting a non-linear Lithium-Triborate (LBO) crystal, second-harmonic generation (SHG) can occur. The LBO crystal temperature is stabilized at 55 °C to achieve best phase-matching conditions and to stabilize the amount of light generated by the SHG process.
Starting from 1.2 W at 798 nm it is possible to reach a conversion efficiency of about

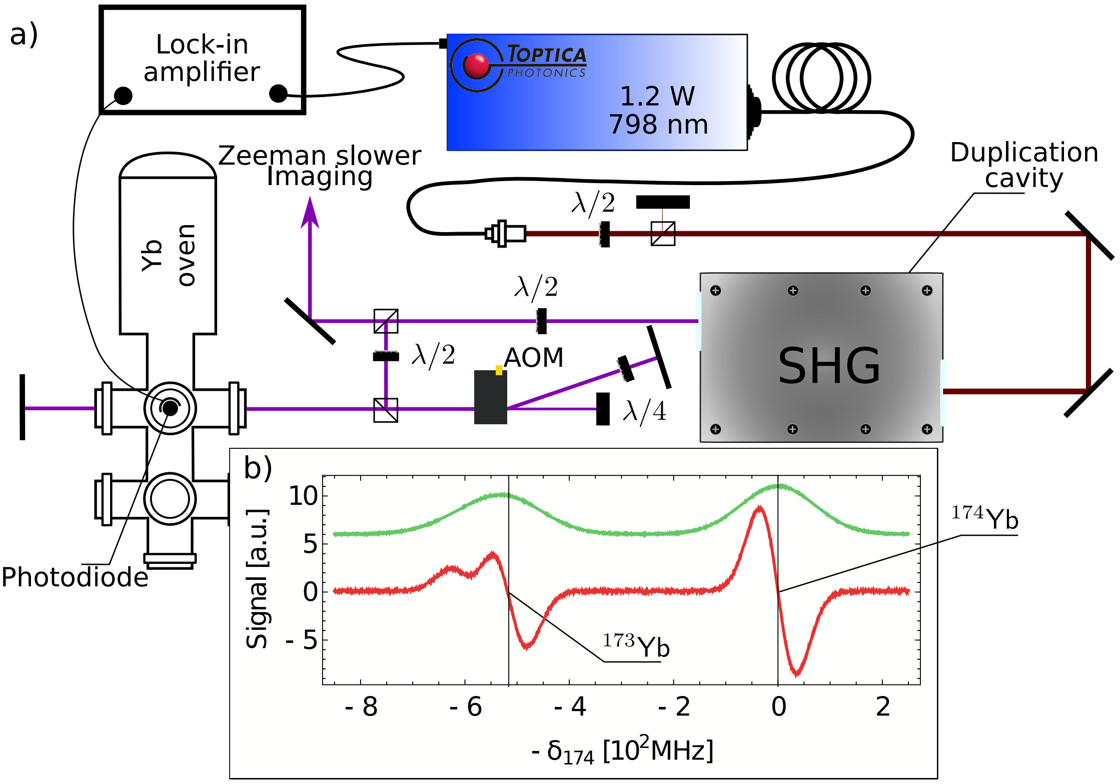

Figure 3.4.3. a): 399 nm radiation generation and atomic spectroscopy on the auxiliary oven are shown. b): A spectrum obtained by applying a linear voltage ramp on the Toptica TA PRO piezo is reported. Atomic resonances for the desired isotopes are shown. In particular, the green trace represents the fluorescence detected by the photodiode and the red trace shows the error signal after the lock-in demodulation. As it can be noted, due to the presence of other transitions the center of the green fluorescence signal does not correspond to the position of the resonance. The selected line $^1S_0\,(F = 5/2) \rightarrow {}^1P_1\,(F = 5/2)$ of ^{173}Yb cannot be distinguished from the ^{172}Yb bosonic transition, while the blueshifted signal with respect to the resonance is due to the $^1S_0\,(F = 5/2) \rightarrow {}^1P_1\,(F = 7/2)$ ^{173}Yb transition. The green trace has been offset vertically for the sake of presentation.

40% by obtaining 480 mW of 399 nm radiation. Acting on a piezo crystal, placed on a cavity mirror mounting, it is possible to slightly change the cavity length in order to optimize the conversion of 399 nm light. To stabilize the frequency of the 399 nm radiation, by applying a variable voltage on the piezo actuator, the Haensch-Couillaud technique [166] is applied.

To stabilize the light frequency emitted by the Toptica TA PRO saturation spectroscopy over an auxiliar Yb oven is performed, as shown in figure 3.4.3a). In particular, pump and probe beams employed to perform saturation spectroscopy

propagate orthogonally to a collimated atomic flux to diminish the Doppler broadening. To perform saturation spectroscopy light is modulated by means of an acousto-optical modulator (AOM) and a lock-in amplifier is employed [167] to generate an error signal starting from the collected flourescence spectrum (see figure 3.4.3b)). By changing finely the piezo position and the temperature of the TA PRO it is possible to select the isotope we decide to work with. As shown in figure 3.4.3b), if ^{174}Yb is considered the line results isolated from the absorption lines of other isotopes. If, instead, ^{173}Yb is considered, line $^1\mathrm{S}_0 \;\rightarrow\; {}^1\mathrm{P}_1$ splits into three lines shifted one from each other by hundreds of MHz (see table 3.2.1). We choose to lock the light on the $^1\mathrm{S}_0(\mathrm{F} = 5/2) \;\rightarrow\; {}^1\mathrm{P}_1(\mathrm{F} = 5/2)$ transition. In this case the transition is not completely isolated and thus cannot be perfectly resolved, as instead happens for the ^{174}Yb. This transition results shifted by tens of MHz with respect (see table 3.2.1) to the $^1\mathrm{S}_0(\mathrm{F} = 5/2) \;\rightarrow\; {}^1\mathrm{P}_1(\mathrm{F} = 7/2)$ resonance and by less than a linewidth with respect to the ^{172}Yb transition (it is the second most abundant bosonic isotope of Ytterbium, as shown in table 3.4.1).
The AOM employed on spectroscopy light introduces a shift of -740 MHz on the radiation that comes out of the SHG-cavity[21]. The radiation locked on atomic transition results red-shifted.

- $^1\mathrm{S}_0 \;\rightarrow\; {}^3\mathrm{P}_1$ (MOT, Optical pumping, Raman, OSG)

The light employed to excite the intercombination atomic transition $^1\mathrm{S}_0 \;\rightarrow\; {}^3\mathrm{P}_1$ is generated by means of second harmonic generation starting from 1112 nm light. The source of this radiation is a fiber laser Menlo System mod. ORANGE ONE that is capable to furnish about 2 W at 1112 nm. This light is injected in a bow-tie home-made cavity[22] in which a 10mm non-linear crystal of periodically-poled Lithium Tantalate (LiTaO_3) performs second-harmonic generation to obtain about 1.1 W of 555.8 nm light, reaching a conversion efficiency of about 55%.
In this case, as it occurs for the 399 nm laser, a piezo actuator mounted on a cavity mirror permits to slightly change the cavity free spectral range in order to optimize the conversion process. As in the previous case, a Haensch-Couillaud technique permits a continuous cavity emission of 555.8 nm radiation.

Due to the reduced linewidth of the selected transition, saturation spectroscopy on the auxiliary oven is performed to lock the ORANGE ONE laser to the atomic line. As in the previous laser system, two counterpropagating laser beams, respectively named pump and probe beams, are used to interrogate, the Yb atomic

---

[21] This frequency shift has been chosen in order to optimize the intensity of the light used for the Zeeman slower beam (detuned by -983 MHz, see also section 3.4.3), as a single high-efficiency single-passage AOM can be used to produce the remaining frequency shift.

[22] The cavity has a measured finesse about $\mathcal{F} \simeq 67$ [111–113].

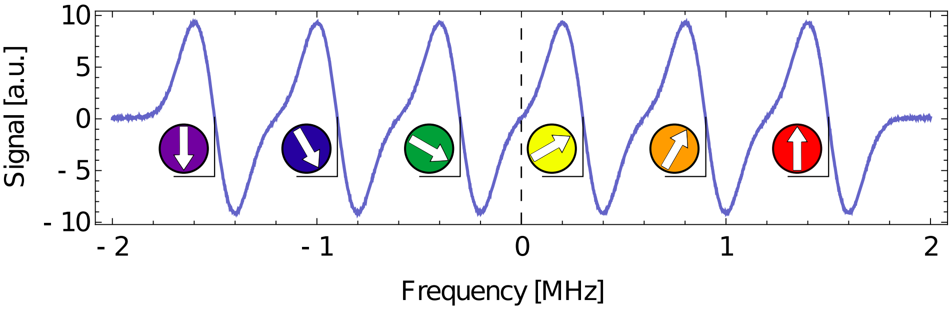

Figure 3.4.4. Error signals obtained from a π-polarized saturation spectroscopy on ^{173}Yb $\left({}^1\mathsf{S}_0(\mathsf{F}=5/2) \rightarrow {}^3\mathsf{P}_1(\mathsf{F}=7/2)\right)$ transition when a magnetic field of about 1 G is applied. Performing only π transitions each hyperfine level in the $|g\rangle$ is excited to its counterpart in the $|{}^3\mathsf{P}_1\rangle$ state.

beam illuminating it trasversally to the atomic motion. The fluorescence light is collected by a photomultiplier and used as input of a lock-in amplifier that permits, by acting on the piezo of the 1112 nm laser source, to lock the emitted laser light to the atomic transition.
In this case selecting an isotope is not as simple as it happens with $^1\mathsf{S}_0 \rightarrow {}^1\mathsf{P}_1$ transition, because the requested shifts (see table 3.2.1) can not be obtained just by varying the position of the pump laser piezo, and a temperature change of the seed laser is required.
To lock the laser light to the ^{174}Yb intercombination transition, the spectroscopy light is modulated by means of a 83 MHz double-passage AOM. The transition chosen is the $^1\mathsf{S}_0(\mathsf{F}=0, m_\mathsf{F}=0) \rightarrow {}^3\mathsf{P}_1(\mathsf{F}=1, m_\mathsf{F}=0)$. To address this magnetic-insensitive transition a magnetic field is applied in order to shift the frequency[23] of all the other projections $m_\mathsf{F}=\pm 1$ and π-polarized radiation is used.

A similar approach is severally complicated to lock fermionic isotopes. To simplify the problem, let us consider $^1\mathsf{S}_0(\mathsf{F}=5/2) \rightarrow {}^3\mathsf{P}_1(\mathsf{F}=7/2)$ transition of ^{173}Yb and, moreover, let us consider a modest magnetic field and π-polarized spectroscopy light. Neglecting other isotopes resonances, for example the contribution due to bosonic ^{170}Yb atom that is nearly coincident with the $\mathsf{F}=5/2 \rightarrow \mathsf{F}=5/2$ transition, the spectroscopy signal obtained in the specified conditions is shown in figure 3.4.4. As the transition linewidth is much smaller than the Zeeman shift, the resonance now splits in six resolved absorption lines and each observed line contributes to the total fluorescence with one sixth of the total intensity.
Since all those lines experience a finite Zeeman shift, in order to have a magnetically, insensitive lock signal (and thus improve the locking stability) a non-trivial

---

[23] The Zeeman shift for magnetic projections of the $^3\mathsf{P}_1(\mathsf{F}=1)$ state corresponds to about $\Delta\nu \simeq 600$ kHz/G$\times m_\mathsf{F}$.

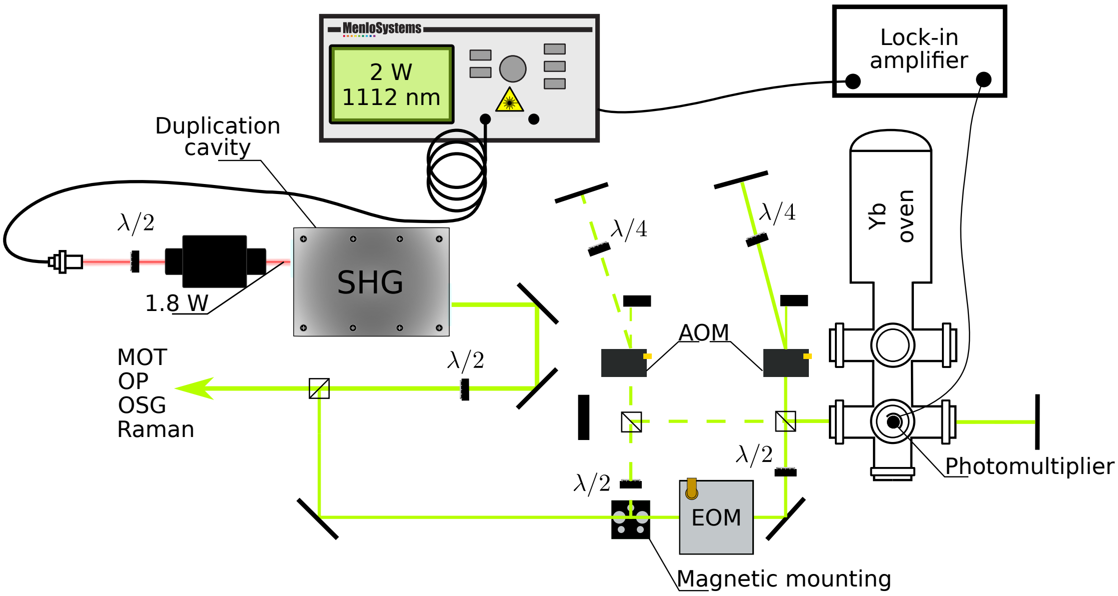

Figure 3.4.5. 555.8 nm radiation generation by means of SHG and saturation spectroscopy on the auxiliary oven are shown. The system has been dramatically simplified for the sake of presentation. Flipping between two spectroscopy-beam paths, by using a removable mirror on a magnetic mount, allows applying the proper frequency shifts either for ^{173}Yb (solid branch) or ^{174}Yb (dashed branch), keeping the same ^{174}Yb spectroscopic signal for stabilization.

locking scheme to the most abundant bosonic isotope of Yb has been implemented. Laser light is then locked to the magnetic-insensitive ^{174}Yb resonance described above employing a spectroscopy radiation shifted by the isotopic shift between ^{173}Yb and ^{174}Yb (2386 MHz - see table 3.2.1). Spectroscopy light passes through an electro-optic modulator that is also used to modulate the radiation (its contribution to the final frequency shift is 1850 MHz) and a double-passage AOM, as shown in figure 3.4.5.

In each case the stabilized laser light is red-detuned by 166 MHz with respect to the transition employed for the magneto-optical trap (MOT). As it can be recognized in figure 3.4.5, a magnetic mirror mounting is employed to switch from bosonic ^{174}Yb to fermionic ^{173}Yb.

In the first part of this work we tried to implement a different locking scheme by employing, instead of spectroscopy of a Yb beam, an external reference [168] constituted by a glass cell containing iodine (I$_2$). The procedure followed to stabilize the frequency emitted by the Menlo ORANGE ONE laser was very similar with respect to the one described above and the presence of an oven was not required.

It is preferable to avoid ovens and localized thermal sources on the system because they can introduce non-negligible thermal gradients. Unfortunately, also the temperature of the iodine cell has to be carefully stabilized at about 100 °C and the signal-to-noise ratio obtained by the spectroscopy of the I_2 molecule was lower (or comparable) with respect to the signal obtained by performing spectroscopy on the Yb beam. Moreover, the shift between the iodine line and the frequency used for the MOT had a slight dependence on external parameters as weak magnetic fields and temperature. Thus this alternative locking scheme has been discarded.

- $^1S_0 \rightarrow {}^3P_0$ ("Clock" transition excitation)

In this section we briefly report the main features of the home-made ECDL laser employed to excite the "clock" transition in ^{173}Yb and ^{174}Yb atoms. These subjects are described in detail in references [113, 165].

The laser at 578 nm used to address the doubly forbidden $^1S_0 \rightarrow {}^3P_0$ transition in bosonic and fermionic Yb atoms is basically constituted by a home-made ECDL laser that emits about 200 mW at 1156 nm. As it occurs for all the other sources previously introduced, also this source is frequency doubled by means of second-harmonic generation in order to obtain $\simeq$ 50 mW at 578 nm.
The peculiarity of the external-cavity diode laser is the presence of an intra-cavity EOM that is used as a "fast" actuator to perform correction on the laser frequency up to a bandwidth of 500 kHz. The "slow" actuator is a piezo crystal mounted on the cavity diffraction grating.
In this way the laser frequency is varied by using two actuators that are not directly related to the diode employed. This frequency-correction scheme allows for a relatively fast diode replacement without losing the possibility to lock the emitter to the chosen reference[24].

The light produced by the ECDL is used to inject a $LiNbO_3$ non-linear crystal placed in a home-made bow-tie cavity in which second-harmonic generation is performed. As in the other sources, the length of the cavity can be slightly varied by changing the voltage applied to a piezo crystal mounted on a cavity mirror. 578 nm radiation is stabilized by means of the Haensch-Couillaud technique. The conversion process has an efficiency[25] of about 30% furnishing 50 mW.

About 60 μW of the generated yellow light is used to stabilize the frequency of

---

[24] During this work, the Innolume quantum-dot chip employed to generate 1156 nm radiation was substituted with a Toptica chip without changing the locking scheme.

[25] Probably limited by the beam shape produced by the ECDL and the subsequent cavity coupling [113].

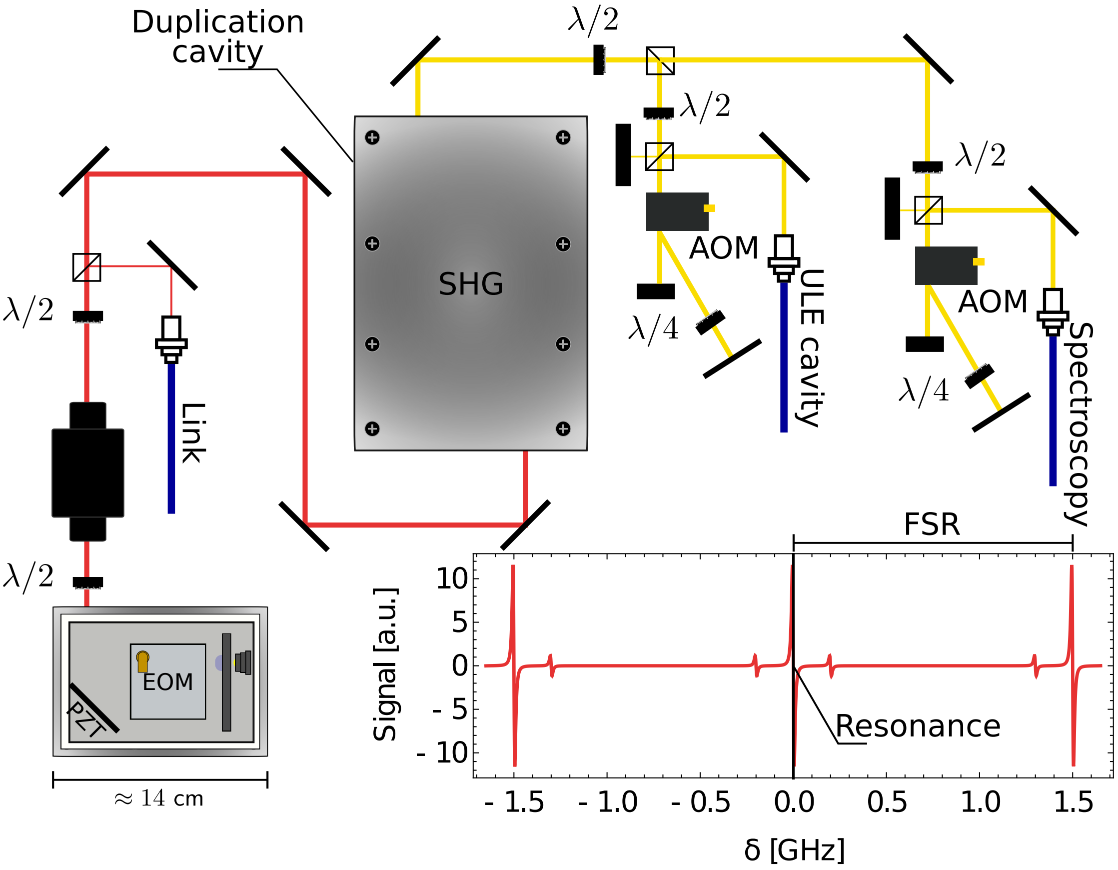

Figure 3.4.6. 578 nm radiation generation by means of SHG and experimental setup used to lock the emitted light are shown. In the lower panel a typical PDH error signal obtained from a high finesse ($\mathcal{F} = 1.7{\times}10^5$) ULE reference cavity is shown. The free spectral range can be evaluated knowing that the cavity is exactly 10 cm long. The lock to the fiber link briefly introduced in section 3.2.1 is performed on the infrared (red) light.

the ECDL laser on a high-finesse ($\mathcal{F} = 1.7{\times}10^5$) ultra-low-expansion (ULE) cavity. The stabilization of the laser frequency is obtained by performing a Pound-Drever-Hall technique [169]. The remaining light is used in the experiment to excite the $^1\mathrm{S}_0 \rightarrow {}^3\mathrm{P}_0$ transition. For that reason the lock is performed on the ULE mode that is nearest to the atomic transition (cavity FSR is 1.5 GHz). The ULE cavity allows us to obtain a final observed linewidth of the laser of the order of tens of Hz on the timescale of ≈ 15 min, while for longer timescales the linewidth is degraded by the ageing of the ULE cavity glass, which determines a shift of the cavity modes of the order of 5 kHz/day [113, 170] and by erratic fluctuations of comparable amplitude, induced presumably by an imperfect temperature stabilization of the cavity.

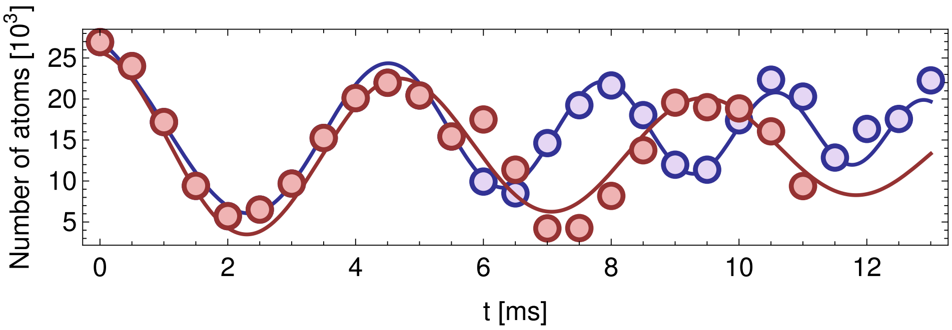

Figure 3.4.7. Coherent Rabi oscillations performed exciting the clock transition in ^{174}Yb atoms trapped in a deep 3D optical lattice in which the presence of lattice doubly-occupied sites is reduced. Each point corresponds to a different clock-laser pulse duration and is obtained by performing spectroscopy (and successive destructive detection) on different atomic sample, produced at a rate of approx. 1 sample/ 40 s. The time sequence of data acquisition follows the pulse duration, from shorter values to longer values. Blue points represent an oscillation in which the resonance has not been spectroscopically checked during the 30 min of measurement time. When the ULE mode starts to drift out of the resonance, the Rabi frequency associated to the clock transition increases according to the relation $\Omega_G^2 = \Omega^2 + \delta^2$ (where Ω is the Rabi frequency on resonance, δ is the shift of the laser with respect to the resonance frequency and Ω_G is the generalized Rabi frequency) and the amplitude decreases, as it can be observed starting from pulses of approx. 6 ms. Red points represent the same Rabi oscillation but adjusting the frequency of the clock transition during the measurement process. Blue and red lines are sinusoidal fits.

This long-term drift cannot be corrected just by changing the emission frequency with the intra-cavity EOM and the cavity piezo crystal, so a double-passage AOM has been used in order to correct the daily shift. In particular, it has been chosen to kept the laser stabilized frequency about -40 MHz with respect to the atomic transition in order to compensate this shift finely by using another AOM on the spectroscopy branch, as shown in figure 3.4.6.
As introduced in section 3.2.1, the long-term drift can be overcome by exploiting a long-term lock on a metrological reference [113, 135].

- ^{3}P$_0$ $\rightarrow$ ^{3}S$_1$ (Imaging of ^{3}P$_0$ atoms)

Due to the extremely long lifetime of the ^{3}P$_0 = |e\rangle$ state, it is possible to treat it as an alternative ground state having a spin-triplet wavefunction. For that reason it can be interesting to study the dipole-permitted transitions from the ^{3}P$_0$ to higher levels. During this thesis two transitions have been considered to directly estimate the population of the metastable $|e\rangle$ state.

Population detection of the $|e\rangle$ state can be performed or by finding a closed dipole-allowed transition that connects the excited state with a higher-lying triplet state (direct imaging) or by transferring the whole atomic population of the excited state in a state that is connected to a third state in which a closed transition can occur (indirect imaging). The latter is the circumstance considered in this thesis.

The first transition that experimentally we tried to address is the transition $|e\rangle \rightarrow {}^3\mathsf{S}_1$ at 649.1 nm. As shown in figure 3.4.2, it is characterized by a short lifetime (see table 3.4.2) and can be exploited to detect atoms in the metastable state [162].
Atoms pumped into the ${}^3\mathsf{S}_1$ state can decay in the ground state $|g\rangle$ passing through the ${}^3\mathsf{P}_1$ state. The atomic population that reaches the ground state can be detected by applying the common absorption imaging procedure based on the closed transition $|g\rangle \rightarrow {}^1\mathsf{P}_1$. The specified transition $|e\rangle \rightarrow {}^3\mathsf{S}_1$ is a common but quite inefficient choice because atoms excited in the ${}^3\mathsf{S}_1$ state can only populate the ${}^3\mathrm{P}$ manifold by following the branching ratios shown in table 3.4.2.
By evaluating the ratio equations it can be demonstrated that, employing only a 649.1 nm laser to excite $|e\rangle$ atoms in the ${}^3\mathsf{S}_1$ state, it is possible to detect only $\sim 43\%$ of the total population [171].
To increase the observed atomic population of $|e\rangle$ atoms another source emitting at 770.2 nm should be employed. This laser would allow one to observe also atoms spontaneously decayed from the ${}^3\mathsf{S}_1$ state to the metastable ${}^3\mathsf{P}_2$ state, reaching $\sim 90\%$ of the initial population in the $|e\rangle$ state.
This repumping scheme results quite complicated, for that reason we preferred to implement a detection scheme based on the ${}^3\mathsf{D}$ states.

- ${}^3\mathsf{P}_0 \rightarrow {}^3\mathsf{D}_1$ (Imaging of ${}^3\mathsf{P}_0$ atoms)

During this work we have implemented an imaging routine based on the dipole-allowed 1388.8 nm transition connecting the $|e\rangle$ state with the $(5d6s)^3\mathsf{D}_1$ state with a 270 kHz natural linewidth [161]. When atoms are excited in the ${}^3\mathsf{D}_1$ state they decay spontaneously to the ${}^3\mathsf{P}$ manifold, but in this case the population that is transferred to the ${}^3\mathsf{P}_2$ state is about the $\sim 1\%$ (see table 3.4.2). It means that the remaining $\sim 99\%$ decay via spontaneous emission to the $|e\rangle$ (branching ratio 64%) or to the ground-linked ${}^3\mathsf{P}_1$ state (branching ratio 35%). Theoretical calculations performed considering the specified branching ratio has been performed in reference [171] and, due to the low population transferred in the ${}^3\mathsf{P}_2$ state, this indirect imaging allowed us to observe, by using a single transition, $\sim 95\%$ of the $|e\rangle$ initial population. In particular it is possible to reach a stationary condition in which $\sim 95\%$ of the $|e\rangle$ population is transferred to the $|g\rangle$ state by shining a relatively

Transition	Wavelength [nm]	γ ^{a,b} [kHz]	Branching Ratio [%]
$^3S_1 \rightarrow {}^3P_0$	649.1	9.6×10^3	13.0
$^3S_1 \rightarrow {}^3P_1$	680.1	27×10^3	36.7
$^3S_1 \rightarrow {}^3P_2$	770.2	37×10^3	50.3
$^3D_1 \rightarrow {}^3P_0$	1388.8	270	63.7
$^3D_1 \rightarrow {}^3P_1$	1539.1	150	35.3
$^3D_1 \rightarrow {}^3P_2$	2092.6	4	1.0

Table 3.4.2. Fundamental properties of the transitions connecting the ^3P manifold with principal states exploited to perform indirect imaging of the $^3P_0$ metastable state.
$\gamma = \Gamma/2\pi$ is the transition probability where $\Gamma = \omega^3/\left(3\pi\epsilon_0\hbar c^3\right)|\langle||\hat{\vec{d}}||\rangle|^2$ [143].
References: ^{a}:[162], ^{b}:[161].

short pulse ($\sim 10\mu s$) on $|e\rangle$ atoms when a laser power of 1 $\frac{mW}{cm^2}$ is considered [171].

In order to address the $|e\rangle \rightarrow {}^3D_1$ transition we employed a distributed feedback (DFB) fiber coupled laser-diode model NLK1E5GAAA produced by NEL Laser Diodes that generates $\sim$ 20 mW at 1388.8 nm.
An AOM is employed to illuminate atoms with a beam characterized by a waist of 150 μm and with a light power of about 10 mW. The saturation intensity, defined by relation 3.2.16, for the considered transition is about 0.13 W/m^2, thus the expected power broadening results $\sim 10^3$ bigger than the natural linewidth Γ (see table 3.4.2). For that reason no locking is performed on the laser frequency, which is left in free running. The center of the resonance frequency is periodically checked by directly observing the efficiency of the repumping process on the atoms[26].

3.4.2 Out-of-resonance laser sources

In order to manipulate properly ytterbium isotopes, laser sources that are not resonant with an atomic transition are also employed. As shown for an ideal two-level system in section 2.2, light causes a force on atoms composed by a dissipative term and a consvervative term (as explicitly shown in equation 2.2.1), that have a stronger or weaker effect depending on the wavelength of light with respect to

---

[26] To measure this efficiency, the difference between the total number of atoms remaining after a π-pulse on the clock transition and the total number of atoms observed shining also the 1388.8 nm laser, is evaluated. Usual experimental efficiencies are about (95 ± 5) %.

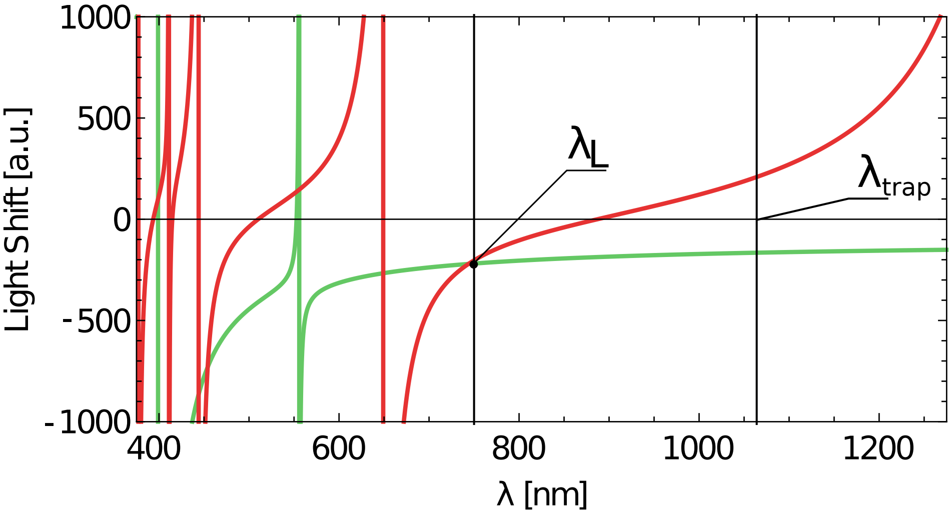

Figure 3.4.8. Light shift as a function of the radiation wavelength λ has been calculated starting from relation 3.4.2. λ_{L} represents the wavelength in which the differential light shift for ground and metastable state is null. λ_{trap} represents the induced light shift when a 1064 nm is employed. The differential light shift can be employed to detect simultaneously ground and excited atoms by performing Optical Stern-Gerlach technique [172, 173].

the atomic resonances. In the far off-resonant case, transitions between internal states do not occur and the dissipative term of the force can be neglected. In this regime, the two-level approximation may also break down and it is important to consider the effect of multiple atomic resonances.

By taking into account red-detuned radiation with respect to all the possible transitions linked to the internal state i, the expression of the dipole potential U^i_{dip} for a multi-level atom can be expressed as [76, 77]:

$$U^i_{\mathsf{dip}}\left(\omega,\vec{\mathsf{r}}\right) = -\frac{3\pi c^2}{2} I\left(\vec{\mathsf{r}}\right) \sum_{n\neq i} \left(\frac{1}{\omega_n^3} \frac{\Gamma_n \beta_n}{\omega_n - \omega} \right) \tag{3.4.2}$$

where $I\left(\vec{\mathsf{r}}\right)$ is the intensity profile of the radiation, $\omega/2\pi$ is its frequency, $\omega_n/2\pi$ are the frequencies of the transitions connecting the n-th state with the i state, Γ_n are the linewidths of these transitions and β_n are their branching ratios.
When two stable levels $|g\rangle$ and $|e\rangle$ with optical energy difference are considered, the potential introduced in equation 3.4.2 changes substantially with the wavelength of the radiation, as shown in figure 3.4.8. In particular, when ultranarrow transitions are considered the frequency shift introduced by the differential light shift induced by the different Grotrian connections for the ground $|g\rangle$ and the

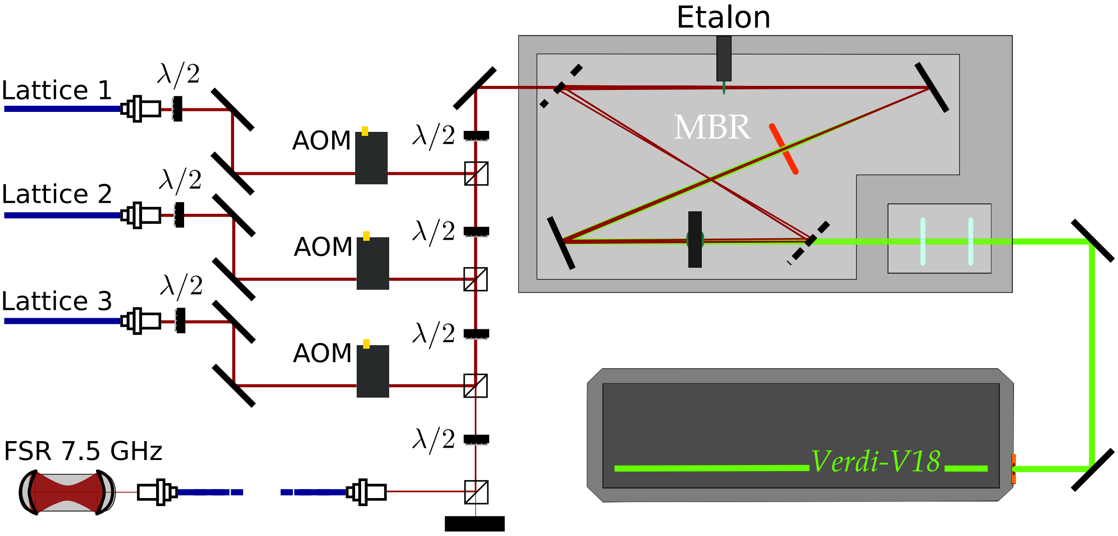

Figure 3.4.9. 759 nm generation by means of Ti:Sa laser emission. A 10 − cm Coherent confocal cavity is used to monitor the single-mode emission of the MBR. An etalon placed inside the cavity of the MBR can be adjusted to ensure single-mode operation of the laser. The light transmitted by the last polarizing beam-splitter cube, here dumped on a beam absorber, can be employed to check the frequency of the emitted radiation.

metastable $|e\rangle$ states can cause an unwanted uncertainty source. To avoid this effect the frequency employed to generate lattices (introduced in section 2.2) has been carefully chosen in order to have the same light shift for the ground and the metastable state. These wavelengths are commonly called magic wavelengths. An accurate calculation in which relativistic many-body effects are taken into account can be found in Ref. [174], where magic wavelengths in the visible range are determined. Many wavelengths, due to the proximity to an atomic resonance, have to be discarded in order to avoid detrimental photon scattering. For that reason, the visible magic wavelength that is commonly employed to realize optical lattices in Yb atoms results to be $\lambda_L = 759.37$ nm [174].

In this section we provide a schematic description of the lasers employed to generate optical lattices at the magic wavelength (759 nm), and to trap and evaporatively cool down to the degeneracy condition the Yb samples (1064 nm). As it happened in the previous section, a complete information about these sources can be found in Refs. [111–113].

- 759 nm

To generate 759 nm radiation a Coherent MBR 110 Ti:Sa laser pumped with a single-mode 532 nm Coherent Verdi V18 is employed. The Ti:Sapphire laser produces about 3.5 W at 759 nm, that are employed to generate a 3D cubic optical lattice in the center of the glass cell in which experiments take place. To achieve this scope the radiation generated by the Coherent MBR 110 is divided into five different branches as shown in figure 3.4.9. On the three branches employed to generate optical lattices the light power is controlled by means of double-frequency[27] AOM. Radiofrequencies employed to drive AOMs are set to avoid interferences between light that arrive on the science cell from different branches. The active control of the beam intensity is achieved by feeding custom PID circuits with the intensity signal detected by the photodiodes on pickup beams (placed close to the atom position), which then feed back onto the AOM RM supply for intensity stabilization. The fourth branch is employed to inject a Coherent Laser Spectrum Analyzer System confocal cavity characterized by a FSR of 0.75 GHz in order to monitor the single-mode emission of the MBR (see figure 3.4.9). The last branch is employed to dump a possible light power surplus.

- 1064 nm

The 45 W radiation emitted by a Coherent Nd:YAG Mephisto MOPA 45 at 1064 nm and a linewidth below 100 kHz is employed to trap atoms in the fundamental $|g\rangle$ state. As shown in figure 3.4.8, for atoms in the $^3\mathsf{P}_0$ state this wavelength is antitrapping and thus cannot be used to confine atoms in the metastable state. The radiation emitted by the MOPA is splitted into three branches whose power is controlled, as it happens for the Ti:Sapphire, by means of three independent double-frequency AOMs.

The first branch is injected in a 9 cm in-vacuum Fabry-Pérot cavity[28] (see figure 3.4.10) characterized by a measured finesse $\mathcal{F} \simeq 1850$ (FSR of 1.67 GHz). The optical cavity in the MOT chamber enhances the collection of atoms from the MOT and pre-cool them before their optical transport in the glass cell. The cavity geometry has been designed to achieve the largest possible beam dimension in order to match the MOT size, compatibly with the trap depth which needs to be higher than the MOT temperature. The cavity beam waist has been chosen to be about 300 μm. With these conditions, using about 1.8 W, it is possible (neglecting the

---

[27] The AOMs are driven by custom double-frequency RF drivers in which the RF is switched between one master value (ensuring proper injection of the diffracted beam into the optical fiber) and one slave value (causing the beam to be dumped onto an absorber), in order to control the beam intensity impinging onto the atoms with no change in the RF power fed to the AOMs (which minimizes unwanted thermal effects).

[28] Similarly to technical solution employed in Ref. [175].

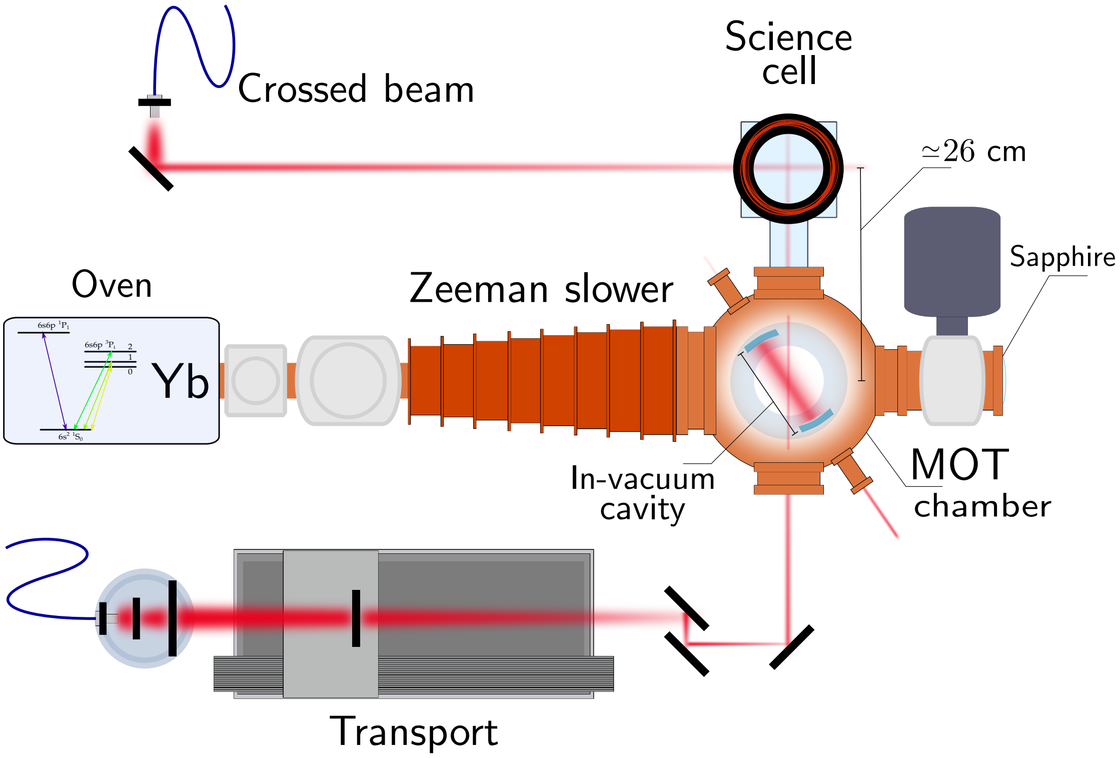

Figure 3.4.10. Sketch of the experimental setup employed to produce a degenerate gas of Yb. The experimental setup has been simplified for the sake of presentation. 1064 nm laser beams has been reported in order to clarify the position of trasport beam, resonator (in-vacuum cavity) and crossed trap. A complete description of the experimental setup can be found in references [111–113] while a graphical representation of the laser beams shone on atoms in the glass cell can be found in reference [145].

cavity losses and mirrors absorption) to obtain a trap depth of $V_0/k_\mathsf{B} \simeq 800\ \mu\mathsf{K}$. The second branch is employed to transport the atomic cloud from the resonator position to the science glass cell (see figure 3.4.10). The transport is realized by means of a magnetically-controlled low-vibration translation stage (Aerotech ABL 1500b) on which a 1 m lens is mounted. This lens is used to realize a movable focus (waist about 30 μm) for the transport beam, which thus operates as an “optical tweezer” to move the atomic cloud over a distance of 26 cm in a time of 2.5 s (see figure 3.4.10). Optimizing the transport parameters we obtained a process efficiency of about 66% with a final sample temperature ($T = 2\mu\mathsf{K}$) only 30% higher than the initial one [111, 176]. The light power requested to transport atoms is about 3.4 W and it corresponds to a trap depth of about $V_0/k_\mathsf{B} \simeq 90\ \mu\mathsf{K}$.
The third branch constitutes the beam that, properly crossed in the glass cell with the transport beam, generates a crossed dipole trap in which the final evaporation

cooling stage is performed (as it is reported in figure 3.4.10). The beam, characterized by a waist of $\simeq 60$ μm, is directly focused onto the atomic position by shining $\simeq 3.5$ W at 1064 nm.
Both the far-off resonance crossed trap (FORT) and the lattices harmonic confinement have been finely characterized to properly manipulate the final potential felt by atoms (see appendix B). The next sections will be devoted to the description of the setup and of the procedures employed to produce a degenerate fermionic or bosonic gas, starting from a thermal atomic beam characterized by propagation velocity of about 300 m/s.

3.4.3 How to obtain a degenerate Yb gas

In this section we describe the main components of the vacuum setup and the experimental procedures employed to trap and manipulate Ytterbium (Yb) atoms. These subjectes are described in detail in references [111–113].

As previously introduced in section 3.1, at room temperature Yb is a solid metal with a negligible vapour pressure. To produce a gaseous sample of this metal an oven has been loaded with about 15 g of 99.9% pure Yb chunks supplied by Sigma-Aldrich. By following the experimental relation 3.4.1 that describes the vapour pressure as a function of the absolute temperature, to obtain a pressure of about 10^{-2} Torr it is necessary to set a temperature of about $450 - 500$ °C. The atomic beam is collimated by means of a square area of 100 micro-tubes characterized by an internal diameter of 0.2 mm and a length of 1 cm before the exit of the oven[29]. The collimated atomic flux is composed by atoms characterized by a mean velocity[30] of about 340 m/s.

Zeeman slower

By exploiting the dipole-permitted transition $^1\mathrm{S}_0 \rightarrow {}^1\mathrm{P}_1$ atoms are decelerated from their initial velocity to a few tens of m/s passing through a 50 cm Zeeman slower (see figure 3.4.10. This tecnique is performed by employing a counterpropagating σ^- radiation red-shifted by 983 MHz with respect to the atomic transition. The magnetic field necessary for the operation of the Zeeman slower is generated by seven sets of coils in order to maintain the atomic sample in resonance with the 399 nm radiation along the Zeeman slower pipe.

---

[29] The front part of the oven is kept at a temperature approx. 50 °C higher than the oven body to reduce the probability of capillary obstruction.

[30] It can be evaluated by means of the virial theorem or by supposing a Boltzmann velocity distribution as proposed in reference [111].

By performing a σ^- Zeeman slower configuration the most intense magnetic field $\mathsf{B}_{\mathsf{ZSmax}}$ is reached at the end of the pipe; for that reason additional compensation coils are used to cancel the residual magnetic field in the MOT chamber.

Magneto-Optical Trap

At the exit of the Zeeman slower, the atomic flux part characterized by a velocity lower than the capture velocity[31] for the intercombination transition ${}^1\mathsf{S}_0 \rightarrow {}^3\mathsf{P}_1$ (see table 3.2.1) are loaded in a 556 nm magneto-optical trap (MOT). For the most abundant fermionic isotope ${}^{173}\mathsf{Yb}$ the transition chosen is the closed transition between hyperfine states $\mathsf{F} = 5/2 \rightarrow \mathsf{F}' = 7/2$. Due to its reduced linewidth, the selected transition allows for a lower Doppler temperature ($k_{\mathsf{B}} T_{\mathsf{D}} = \hbar\Gamma/2$) than what would be achievable on the 399 nm transition, but limits the capture velocity around 10 m/s for our experimental parameters.

To increase the capture velocity range the MOT radiation is splitted on a comb of 18 frequencies separated by 600 kHz and all red-detuned with respect to the ${}^1\mathsf{S}_0 \rightarrow {}^3\mathsf{P}_1$ transition frequency. This multi-frequency stage lasts for 20 s, that is the time necessary to saturate the MOT achieving a stable number of atoms. At the end of this multi-frequency stage we obtain about $\#_{\mathsf{multiF}} = 1.7\times10^8$ atoms trapped in the MOT for ${}^{173}\mathsf{Yb}$ and $\#_{\mathsf{multiB}} = 10\times10^8$ for ${}^{174}\mathsf{Yb}$, achieving a sample with a temperature of $\mathsf{T} \simeq 60\ \mu\mathsf{K}$ [177].

This temperature is significantly higher than the minimum Doppler temperature achievable ($T_{\mathsf{D}} = 4.3\ \mu\mathsf{K}$) since collisional heating mechanisms can occur due to high MOT density [178].

At the end of the 20 s loading the sidebands used to trap atoms in the MOT are switched off in order to pass from a multi-frequency trap capable to capture the highest atomic number possible to a temperature-optimized single-frequency MOT[32]. In the meanwhile a 200 ms exponential ramp is performed to switch on the 1064 nm radiation and trap the atomic cloud inside the in-vacuum cavity briefly introduced in section 3.4.2. In order to optimize the MOT position with respect to the in-vacuum cavity position a magnetic field generated by three additional coils is used. The efficiency of the procedure is about $\approx 80\%$.

---

[31] The capture velocity is, by definition, the maximum velocity class that is possible to trap using a MOT and can be expressed as

$$v_{\mathsf{c}} = \alpha \frac{\Gamma}{2} \frac{I}{I + I_{\mathsf{sat}}} \tag{3.4.3}$$

where α contains all the constants that are not relevant in order to emphasize the behaviour with respect with saturation intensity and the linewidth of the transition considered.

[32] The magnetic gradient is also changed in order to compress the multifrequency MOT into the in-vacuum cavity (every detail can be found in Ref. [111]).

First evaporation in a resonator optical dipole trap

When the cloud is completely trapped in the in-vacuum cavity the single frequency MOT radiation is turned off and a first evaporative cooling is performed by decreasing the light power from 1.8 W to 0.6 W with a 670 ms long exponential ramp. At the end of this stage the obtained sample is consituted by $3{\times}10^7$ fermions or $50{\times}10^7$ bosons with a temperature of about 3 μK. As specified in section 3.4.2, a 1064 nm "transport" beam (see figure 3.4.10) is employed to generate a 70 μK deep optical trap characterized by a waist of 30 μm at the center of the in-vacuum cavity. This beam is turned on by using a 400 ms exponential ramp.

Transport into glass cell and final evaporation

Once the resonator is turned off approximately 30% of the sample remains trapped in the transport beam.
By dynamically changing the position of a 1 m convergent lens, the waist of the beam is moved from the center of the in-vacuum cavity to the center of a glass cell at a distance of 26.4 cm. The reproducibility of the process is guaranteed by the magnetically-driven Aerotech ABL 1500b translation stage. The atomic cloud is moved in 2.5 s, the obtained sample has a temperature increase of only 2 μK and only the 30% of the initial number of atoms get lost during the operation [179].
Finally, when atoms are in the center of the cell, an additional 1064 nm trapping beam (it is reported as "crossed beam" in figure 3.4.10) is adiabatically turned on. The beam, used to generate an optical crossed trap, has a waist of 60 μm. When the crossed trap is loaded, the final evaporative cooling procedure is performed in order to reach the quantum degenerate regime. To obtain this scope the depth of the crossed trap is lowered by means of a double concomitant exponential ramp on the two beam intensities. Each ramp used has the same duration T_{evap} but different decay constant for the transport and the orthogonal beam.
Due to the different scattering cross section imposed by the statistics (see section 2.3.1), for the fermionic sample we use different time constants depending on the number of hyperfine states that are considered in the final sample. Bose-Einstein condensation of ^{174}Yb atoms is obtained decreasing the transport power from 3.5 W to 30 mW and the power of the orthogonal beam from 3 W to 1 W with ramp parameters: $T_{evap} = 2.5$ s and $\tau_{transp} = \tau_{ort} = 2.2$ s.
The resulting gas is characterized by a condensed fraction of about $\simeq 80\%$ and a number of atoms around $\#_B = 2{\times}10^5$.
Fermi degeneracy for a dilute gas in which the six hyperfine components are considered is achieved by performing a ramp from 3.5 W to 30 mW for the transport beam and from 3 W to 1 W for the orthogonal beam. In this case the ramp parameters are: $T_{evap} = 4$ s and $\tau_{transp} = \tau_{ort} = 1$ s.

The atomic sample obtained following this procedure is characterized by a temperature of about $T/T_\mathsf{F} = 0.15$ where T_F is the Fermi temperature, and a number of atoms $\#_F = 4{\times}10^4$.

Imaging

The imaging of the atomic cloud is thus performed with standard absorption imaging. This tecnique is based on the detection of the shadow cast by the atomic sample on a CCD camera when resonant light is shone. The transition employed to perform imaging is the dipole-allowed transition at 399 nm and in particular, when ^{173}Yb is considered, the closed transition $\mathsf{F} = 5/2 \rightarrow \mathsf{F}' = 7/2$. The imaging beam is aligned with the vertical direction. The main imaging setup in the glass cell is performed with a single f = 150 mm achromatic doublet placed at 200 mm from the atomic position. The CCD, that is a Andor iXon^{EM} + DU885KCSO, is placed at 600 mm from the lens providing a magnification of 3x. So far, the main resolution limitation is the numerical aperture that is restricted by the diameter of the doublet (2″). The resolution obtained on the $8{\times}8$ mm^2 CCD, composed by a pixels matrix $1002{\times}1004$, is about 10 μm and does not allow for in-situ imaging.

On the main imaging branch a $\lambda/4$ and a $\lambda/2$ waveplate has been added to maximize the observed number of atoms. The dependance of the number of atoms as a function of the polarization used to perform imaging is theoretically discussed for example in Ref. [143].

To perform in-situ imaging a new optical system with a N.A. that should allow for a resolution better than 1 μm has been studied and tested. In order to implement the setup based on a custom Leica objective on the experimental system it is necessary to stabilize the external physical quantities that can modify the position in the glass cell. Experimentally, the alignments and the position of the atoms, environment temperature variations or spatial temperature gradients caused for example by ovens, high-power laser sources, magnetic field coils not correctly cooled, can cause slight variations on the position of the atomic sample. This kind of phenomena are detrimental and can nullify the effects of high-resolution optics, decreasing the effective point-spread-function resolution and all the efforts proposed to increase the optical imaging system.

For that reason, during this thesis, a flowbox built by Galvani S.R.L. has been mounted on the experimental setup, as sketched in figure 3.4.11. This instrument is devoted to the generation of a constant purified[33] temperature-controlled air flow. The input air, that is pre-filtered, is cooled by means of a couple of copper heat exchangers that employ 1600 dm^3/h of water at $13-18$°C to stabilize, by applying

---

[33] The air expulsed from the plenu passes through an absolute filter (that is illustrated in figure 3.4.11). The air flow has been tested and resulted compatible with ISO 6 standard for clean chambers [180].

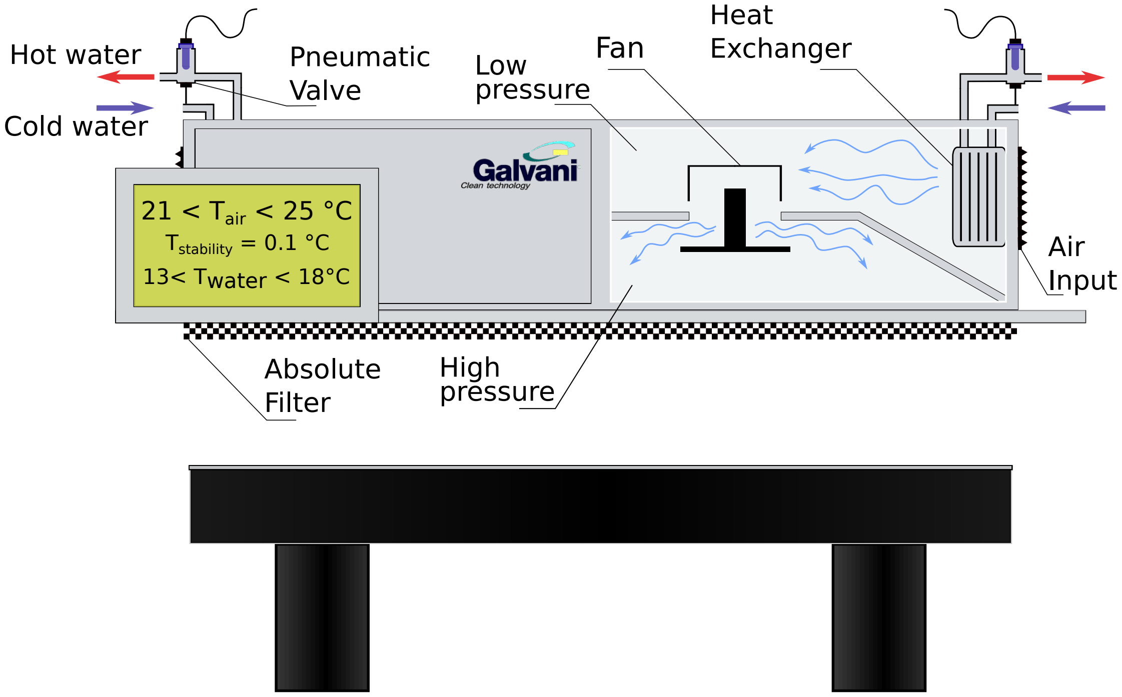

Figure 3.4.11. Schematic representation of the flowbox mounted on the experiment. This apparatus, based on two indipended heat exchanger and fans, can guarantee a purified constant air flow with a temperature uncertainty about 0.1 °C. The noise produced by the operating instrument is lower than 65 dB and the water flux necessary to cool down the input air is about 1600 dm^3/h.

a proportional-integral feedback control system based on pneumatic valves and temperature and pressure controllers, the air temperature in the plenum within 0.1 °C. The air temperature in the plenum can be set from 21.0 to 25.0 °C.
This flowbox allows for a continous air flow on the experimental setup that avoids the formation of dust on optics, reduces the thermal gradients due to the previously mentioned sources and stabilizes the temperature of optics, avoiding principal day-time drifts.

3.4.4 Nuclear spin states selection and manipulation

When the ^{173}Yb fermionic isotope is considered, it is necessary, to describe the cooling procedure employed to reach the quantum degeneracy regime, to specify the spin-mixture under consideration. As mentioned in previous sections, due to Pauli blocking, if two identical atoms are considered, *s*-wave scattering and, conse-

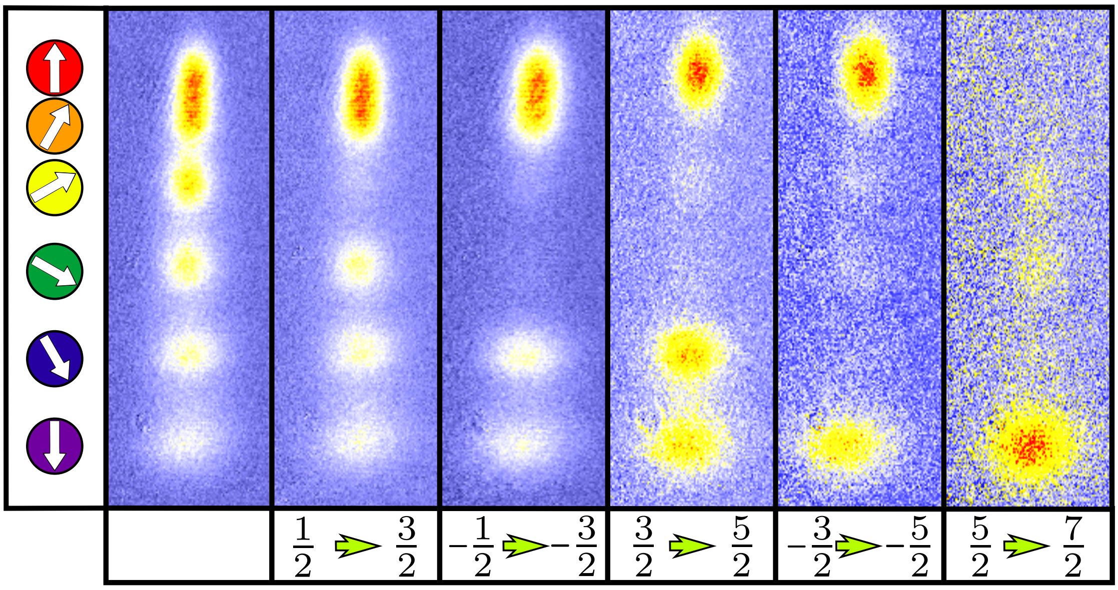

Figure 3.4.12. Optical Stern-Gerlach experiment performed on ^{173}Yb. Nuclear spin ground-state components have been selected by means of optical pumping performed through σ^+ and σ^--polarized beams resonant on specific Zeeman components of the $^1\mathsf{S}_0 \rightarrow {}^3\mathsf{P}_1$ transition. In the lower part the transitions from the ground to the $^3\mathsf{P}_1$ hyperfine components are reported. The last transition $|g\rangle(m_\mathsf{F} = \frac{5}{2}) \rightarrow |^3\mathsf{P}_1\rangle(m_\mathsf{F} = \frac{7}{2})$ is a closed transition that is employed to blast a nuclear spin component.

quently, the re-thermalization processes necessary to the evaporative cooling, can not occur. Spin mixtures are obtained by optical pumping exploiting the intercombination transition $^1\mathsf{S}_0\,(\mathsf{F} = 5/2) \rightarrow {}^3\mathsf{P}_1\,(\mathsf{F} = 7/2)$ that has been described in section 3.2, and that is excited by employing a 556 nm radiation that is stabilized experimentally by the scheme described in section 3.4.1. Due to the reduced linewidth of the cited transition, it is possible to address the nuclear spin states individually by just applying a moderate external magnetic field that removes the levels energy degeneracy.

In figure 3.4.12 we report the nuclear-spin composition, detected after Optical Stern-Gerlach (OSG) separation (see below), for different samples of ^{173}Yb. As it can be observed it is possible to obtain a nearly perfect Zeeman states selection by properly adjusting the light frequency and the polarization used to excite the mentioned transitions. In order to transfer the population of $|g\rangle m_\mathsf{F}$ state to the $|g\rangle m_{\mathsf{F}'} = m_\mathsf{F} \pm 1$ state the transition from the initial state to the $|^3\mathsf{P}_1\rangle m_{\mathsf{F}'} = m_\mathsf{F} \pm 1$ level is excited by shining resonant light characterized by $\sigma^\pm$ polarization, respectively. A 23 G magnetic field is applied to properly address the cited transition. The considered excited state is a magnetic-sensitive state and thus the Zeeman shift induced by an external magnetic field, as described in equation 3.2.18, causes

a splitting between adjacent hyperfine states $\Delta E_{\mathsf{z}} = 2\pi\times 13.7$ MHz, that is sufficient to separate each transition and avoid unwanted nuclear spin states in the final atomic sample.
The preparation of a sample constituted by a certain nuclear spin mixture is performed before the final evaporative cooling stage; in this way, atoms have the possibility to thermalize properly by distributing the momentum transferred by the photon to the atomic sample.

In this work we realized principally two fermionic mixtures of ^{173}Yb: the mixtures composed by $\pm\frac{5}{2}$ and $\pm\frac{5}{2} \cap \frac{1}{2}$, as we will introduce in the next chapters.
In order to select $\pm\frac{5}{2}$ spins we start from a sample composed by all the possible spins as shown in figure 3.4.12. The first two concomitant pulses are performed by using 75 μW of $\sigma^{\pm}$ radiation at 556 nm and are devoted[34] to transfer completely the population of $\pm\frac{1}{2}$ in the $m_{\mathsf{F}} = \pm\frac{3}{2}$ spin states. The second couple of pulses is performed by shining 50 μW of $\sigma^{\pm}$ radiation and transfers the population from the $m_{\mathsf{F}} = \pm 3/2$ to the $m_{\mathsf{F}} = \pm 5/2$ spin states.
From the obtained mixture, if we are interested in a spin-polarized sample it is possible to excite the closed transition $|g\rangle\,(m_{\mathsf{F}} = \pm 5/2) \;\rightarrow\; |^3\mathsf{P}_1\rangle\,(m_{\mathsf{F}} = \pm 7/2)$ in order to selectively remove one spin from the dipole trap. This optical blast is performed at the end of evaporating ramp because the polarized sample cannot interact by s-wave scattering and thus cannot be cooled further by evaporation. Although this pulse has a duration of only 30 μs, it inevitably causes a heating of the sample that can reach a temperature up to $T/T_{\mathsf{F}} \simeq 0.2$.

The other spins-mixture used in this work is obtained by performing an “anomalous” but efficient pumping procedure in order to obtain a balanced mixture. The pumping scheme starts as usual, from an unpolarized atomic sample. As a first step a σ^{+} pulse resonant with the transition $|g\rangle\,(m_{\mathsf{F}} = -1/2) \;\rightarrow\; ^3\mathsf{P}_1\,(m_{\mathsf{F}} = 1/2)$ is performed in order to unbalance considerably the $+1/2$ and $-1/2$ spin populations.
After this stage, two concomitant $\sigma^{\pm}$ pulses are performed to transfer the atomic population to the $|g\rangle$ nuclear spin $m_{\mathsf{F}} = \pm 3/2$ states. At this stage a σ^{-} pulse resonant with the transition $|g\rangle\,(m_{\mathsf{F}} = 3/2) \;\rightarrow\; ^3\mathsf{P}_1\,(m_{\mathsf{F}} = 1/2)$ and a π pulse resonant with the transition $(m_{\mathsf{F}} = 3/2) \rightarrow (m_{\mathsf{F}} = 3/2)$ are performed. Finally, by exploiting the transitions $|g\rangle\,(m_{\mathsf{F}} = \pm 3/2) \rightarrow |^3\mathsf{P}_1\rangle\,(m_{\mathsf{F}} = \pm 5/2)$, the selected mixture is obtained. A negligible $|g\rangle\,(m_{\mathsf{F}} = -1/2)$ population remains as residual unwanted state. The sample obtained following this procedure is constituted by about 2.5×10^4 atoms in each spin state and has a typical temperature $\approx T/T_{\mathsf{F}} \simeq 0.17$.

---

[34] The pulse necessary to transfer completely the population has a duration of 1.5 ms.

In order to detect the hyperfine composition of the atomic sample, due to the magnetic-insensitive nature of the ground state, explored in detail in section 3.2.3, we cannot perform a standard Stern-Gerlach magnetic detection[35]. As we introduced in section 3.4.2, the conservative potential introduced in relation 2.2.2 can be generalized to the case of multi-level atoms with equation 3.4.2. This relation can be further generalized for radiation that is nearly-resonant with the specific transitions by the equation:

$$U^{i}_{\mathsf{dip}}\left(\omega,\vec{\mathsf{r}}\right)=-\frac{3\pi c^2}{2}I\left(\vec{\mathsf{r}}\right)\sum_{n\neq i}|\mathcal{C}_n(q)|^2\frac{1}{\omega_n^3}\left(\frac{\Gamma_n\beta_n}{\omega_n-\omega}+\frac{\Gamma_n\beta_n}{\omega_n+\omega}\right) \tag{3.4.4}$$

where $\mathcal{C}_n(q)$ is the Clebsch-Gordan coefficient that connects the initial state $|i\rangle = |\mathsf{J},\mathsf{F},m_\mathsf{F}\rangle$ to the final state $|n\rangle = |\mathsf{J}',\mathsf{F}',m_{\mathsf{F}'}\rangle$ and (q) is the polarization of the photon expressed in the spherical basis [143].
The dependence of the Clebsch-Gordan coefficients on m_F and on the light polarization (q) is related to different line strenghts between transitions from different magnetic sublevels of the initial-state manifold excited by a certain polarization. This implies different light shifts for different m_F states, which are also strongly dependent on the polarization of the incident radiation [143, 173].
The possibility to apply a nuclear spin state-dependent potential represents a powerful tool that substitute the effect of the magnetic field in the Stern-Gerlach experiment [172, 173].
In particular, a 472.6 MHz red-detuned radiation is experimentally employed to spatially separate different spin populations. The beam used to cause a spin-selective spatial displacement of the atomic cloud is a 60 μm waist slightly misaligned with respect to the sample position [156]. To obtain the images shown in figure 3.4.12, a 13 mW pulse is turned on for the first 1.5 ms after the release of the atomic cloud from the trap, then the image is taken after 7.0 ms of time-of-flight free evolution.

3.4.5 Raman setup

In section 3.3 we have introduced Raman two-photon transitions as an experimental technique for the coherent manipulation of the nuclear-spin degree of freedom in ^{173}Yb. These transitions are induced by using the ^{3}P$_1$ state as the intermediate level in a Λ scheme. In order to implement this scheme is necessary to employ non-resonant 556 nm radiation that minimizes the probability of single-particle transitions $|m_\mathsf{F}\rangle \rightarrow |^3\mathsf{P}_1\rangle$ as requested by the simplified theory presented

---

[35] This technique, originally used in 1922 by Stern and Gerlach [172] to observe the spin of Silver (Ag) atoms, would require unpratical magnetic field gradients in our case [172].

in section 3.3. The best detuning interval for $^{173}\mathsf{Yb}$, taking into account single-particle transitions from the ground state to the $|^3\mathsf{P}_1\rangle$ level, has been evaluated numerically in reference [112] by maximizing the ratio between the Raman Rabi frequency Ω_{Raman} and the light scattering rate and results $\sim 1.6 \div 2.2$ GHz blue-shifted with respect to the resonance frequency.
A system of four double-passage AOMs has been developed to obtain 556 nm laser-light blue-shifted by 1756 MHz and a complete description of this experimental setup can be found in reference [112]. As it can be easily imagined, a chain of four double-passage AOMs is a quite complex configuration and, unfortunately, the efficiency, measured as the ratio between the light power before the first AOM and the output of the fiber that brings the light to the atoms, corresponds to only $\sim 3\%$.
For that reason, in order to achieve a Raman Rabi frequency $\Omega_{\mathsf{Raman}}/2\pi \simeq 100$ Hz, during this work the setup sketched in figure 3.4.5 has been improved with a programmable waveplate that has the role, when the MOT phase in the experimental cycle is concluded, of diverting the resonant light employed to load the MOT to the Raman branch.
This technical improvement allows us to probe the Raman transition with about 30 mW of 1756 MHz blue-shifted light with respect to the $|g\rangle \rightarrow |^3\mathsf{P}_1, (m_{\mathsf{F}} = 7/2)\rangle$ transition.

4 | Clock spectroscopy on ultracold ^{174}Yb

This chapter is dedicated to the description of the experimental results related to the measurement of the scattering properties of ^{174}Yb bosonic atoms in a 3D optical lattice system [44]. Similar measurements have been performed independently by Yb BEC group at LKB [45].

The chapter is divided into three parts: section 4.1 describes the experimental techniques employed to excite the so-called "clock" transition, $^1\mathsf{S}_0 \rightarrow {}^3\mathsf{P}_0$, in a ultracold bosonic ^{174}Yb sample loaded in a 3D lattice system.

In section 4.2 we show the possibility to use the optical clock transition to resolve the atom occupancy of the sites in a bosonic Mott insulator and we use this information to determine scattering lengths for collisions regarding atoms in the e state.

Finally, in section 4.3 the state-dependent loss rates coefficients for the collisions involving atoms in the ground state (g) and in the metastable state (e) are derived[1].

The knowledge of scattering parameters (as scattering lengths and loss rates) is crucial for the realization of quantum information platforms relying on the possibility to excite ground state AEL atoms to the $^3\mathsf{P}_0$ metastable state [31, 182, 183].

---

[1] A similar experimental study based on the magnetic-sensitive $^1\mathsf{S}_0 \rightarrow {}^3\mathsf{P}_2$ "clock" transition in ^{174}Yb has been recently performed [181].

4.1 Realising clock spectroscopy

In this section we describe the experimental procedures employed to excite the bosonic doubly-forbidden transition described in section 3.2.2.

To experimentally address the clock transition in ^{174}Yb sample we start from the realization of a Bose-Einstein condensate by means of evaporative cooling in a crossed FOR Trap characterized by final trap frequencies
$\omega_{x,y,z} = 2\pi\times(92.8, 72.6, 86.3)$ Hz (see appendix B for details).
The obtained degenerate sample is constituted by about 2×10^5 atoms with a condensed fraction of 80%, as introduced in section 3.4.3. The number of atoms in this sample can be easily decreased exploiting three-body losses collisions by extending the time in which atoms are trapped into the crossed trap.
Finally, the bosonic gas is adiabatically loaded into a 3D cubic optical lattice (see section 2.2) realized by shining three orthogonal retro-reflected beams at the magic wavelength for the clock transition (see section 3.4.2). The depth of each lattice can be set by varying the light intensity up to s = 40 E_r, where E_r is the recoil energy evaluated for the ^{174}Yb isotope (see table 3.4.1). The light intensity of each lattice beam is exponentially ramped up in 150 ms in order to adiabatically load the atomic sample into the 3D optical lattice. After this process the FOR Trap is adabatically turned off by means of a 250 ms long linear ramp (see figure 4.1.1 (inset)); during this process half of the atoms get lost by means of inelastic collisions in multiply-occupied lattice sites.
The final sample is constituted by 1.2×10^5 atoms, a number that can easily lowered by extending the waiting time in the lattice after the FOR Trap has been turned off, as shown in figure 4.1.1, or by changing the trap frequencies.
In order to excite the magnetically-induced clock transition introduced in section 3.2.2 it is necessary to modify the setup presented in section 3.4.1 in order to compensate the isotopic shift between ^{173}Yb and ^{174}Yb, that has been evaluated in Ref. [135] and corresponds to

$$\delta\nu = \nu_{^{173}\mathsf{Yb}} - \nu_{^{174}\mathsf{Yb}} = (551536050 \pm 10)\ \mathsf{Hz}.$$

Since the spacing between ULE modes is 1.5 GHz $\gg \delta\nu$, to compensate for the isotopic shift it is sufficient to substitute the double-passage AOM that sets the clock laser frequency on the ULE branch (see figure 3.4.6). Clock spectroscopy is then performed by shining a 578 nm light pulse on the sample, that causes an excitation

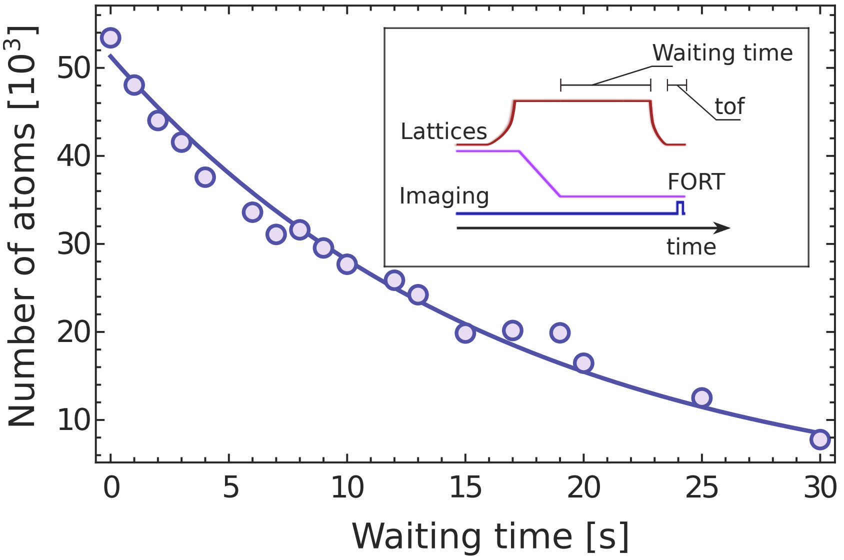

Figure 4.1.1. The number of atoms in the final sample can be precisely selected by increasing the time in the 3D optical lattice (in this case $s = 30$). The line represents an exponential fit characterized by decay rate $\tau = (16.7 \pm 0.6)$ s. In the inset the experimental procedure used to load the optical lattice is graphically reported.

of part of the population from the ground $|g\rangle$ state to the metastable $|e\rangle = {}^3\mathsf{P}_0$ state. As introduced in section 3.2.2, the presence of an external field[2] is necessary to permit a non-negligible coupling in the ^{3}P manifold, and the spectroscopic linewidth can be set by varying the light intensity or the magnetic-field intensity. All the measurements presented in this and in the following sections are performed without taking advantage of the optical-fiber link reference provided by the INRiM institute. This means that, as explicitly shown in figure 3.4.7, transitions can be probed only as long as the drift of the ULE cavity does not become larger than other involved effects. For example, for a light intensity corresponding to a power broadening of 1 kHz, the resonance can be easily addressed for about half a day. On the other side, if the power broadening is comparable or lower with respect to the linewidth of the laser (≈ 50 Hz), the transition can be probed only for half an hour.

---

[2] In section 3.2.2 the case of an external magnetic field has been described. Otherwise, it has been proposed to excite doubly-forbidden transition in bosonic AEL species also by exploiting multiphoton schemes [184, 185].

4.1.1 The Lamb-Dicke regime

As mentioned in chapters 3.2.1 and 3.2.2, the most important peculiarity of the doubly-forbidden transition is represented by the extremely narrow natural linewidth[3].

The momentum exchanged in the interaction between the radiation field and the atoms represents a non negligible limit in the identification of the transition frequency and linewidth. As a matter of fact, by requiring the momentum conservation it is possible to obtain, for an atom in free space:

$$\omega_{\mathsf{abs}} = \omega + \vec{\mathsf{k}} \cdot \frac{\vec{\mathsf{p}}}{m} + \frac{\hbar k^2}{2m} \tag{4.1.1}$$

where ω is the absolute transition frequency, $\vec{\mathsf{k}}$ is the photon momentum, $\vec{\mathsf{p}}$ is the atomic momentum, and m is the atomic mass. The presence of the two additive terms, linked to Doppler broadening and recoil shift, respectively, constitutes a problem that is of particular relevance in the optical spectroscopy framework, differently from microwave spectroscopy, where motional effects can be easily disregarded because of the negligible photon wavenumber [186]. For this reason, to overcome unwanted broadening, clock transition spectroscopy is performed in deep optical lattices, in which the external degree of freedom connected to the motional state of the atom can be frozen, allowing for Doppler-free, recoil-free spectroscopy. This is the so-called Lamb-Dicke regime [187], in which the absorption (emission) of a photon can not change the motional state of the trapped atom. To formalize this condition, we can consider a two-level $|g\rangle - |e\rangle$ atom in a 1D harmonic potential[4] with harmonic frequency ω_{ho} interacting with a monochromatic radiation of frequency ω and wavevector k. The total Hamiltonian of the system, in a frame co-rotating with the laser field, in second quantization approach and by considering only electric-dipole interaction, can be expressed as [188]:

$$\hat{H} = \underbrace{-\hbar\Delta|e\rangle\langle e| + \hbar\omega_{\mathsf{ho}}\left(\hat{a}^\dagger\hat{a} + \frac{1}{2}\right)}_{\hat{H}_0} + \underbrace{\frac{\hbar\Omega}{2}\left[e^{i\eta\left(\hat{a}^\dagger+\hat{a}\right)}|e\rangle\langle g| + h.c.\right]}_{\hat{H}_{\mathsf{int}}} \tag{4.1.2}$$

where Δ is the detuning from the resonance condition, Ω is the Rabi frequency for the unconfined atom at rest, $\hat{a}^\dagger$ is the creation operator and η is known as

---

[3] In the case of bosonic AEL species, due to the lack of hyperfine interaction, if multiphoton processes are neglected and external fields are not applied the transition can not occur.

[4] A lattice site can be described as a harmonic potential, as explained in section 2.2.1.

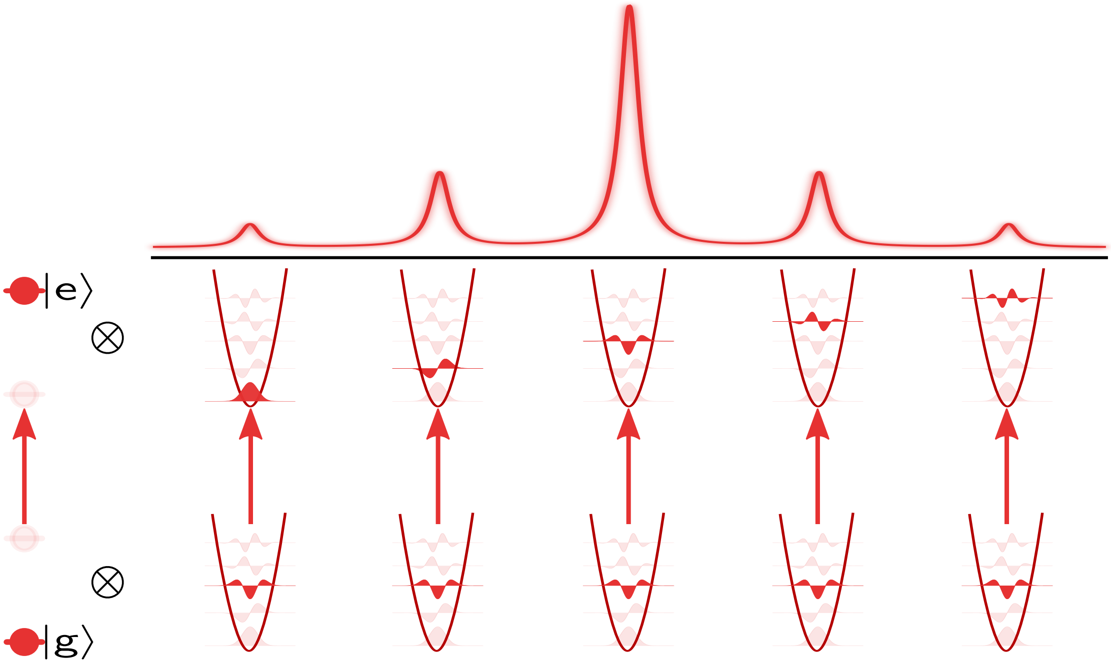

Figure 4.1.2. Lamb-Dicke regime spectrum: the most intense line reprents the Carrier, transitions in which higher harmonic levels are excited by radiation constitute the blue sidebands, other transitions constitutes the red sidebands. Peak intensities of I blue- and red- sidebands scale as η^2 while for II blue- and red- sidebands the scaling factor is $2\eta^4$.

Lamb-Dicke parameter and is defined as:

$$\eta = k\sqrt{\frac{\hbar}{2m\omega_{\mathsf{ho}}}} = \sqrt{\frac{\omega_{\mathsf{rec}}}{\omega_{\mathsf{ho}}}}. \tag{4.1.3}$$

In order to separate the atomic internal and external degrees of freedom, it is possible to write a general state of $\hat{H}_0$ as direct product of the internal and external states $|i\rangle = \sum_n |n\rangle \otimes |i\rangle$ where $|n\rangle$ is the autostate of the harmonic-oscillator number operator $\hat{n} = \hat{a}^\dagger\hat{a}$.

As shown in Ref. [189], if the atom is confined in such a way that the spatial extent of the atomic wavefunction is much smaller[5] than $1/k$, the argument of the exponential is $\ll 1$ and can be expanded to the lowest order in η.
The transition probability, evaluated by considering the interaction Hamiltonian

---

[5] Equivalently, it occurs when the recoil energy $E_{\mathsf{r}} = \frac{\hbar^2 k^2}{2m}$ associated to the photon absorption is much smaller than the harmonic oscillator energy quantum $\hbar\omega_{\mathsf{ho}}$.

$\mathsf{H_{int}}$, can therefore be written as

$$P_{n\to n'} \propto |\langle n'|1+\eta\left(\hat{a}^\dagger+\hat{a}\right)|n\rangle|^2 = \left|\delta_{n,n'}+\eta\left(\sqrt{n+1}\delta_{n',n+1}+\sqrt{n'+1}\delta_{n'+1,n}\right)\right|^2. \tag{4.1.4}$$

From this relation it results evident that, if the expansion is justified, the most intense line in the emission or absorption spectra is the transition that occurs without varying the atomic external degree of freedom. Typically this resonance is referred as carrier transition [189] and it is characterized by a total suppression of recoil and Doppler broadening, since the interacting photon cannot influence the spatial part of the atomic wavefunction.

The other allowed transitions, that are referred to as first red sideband and first blue sideband, correspond to transitions from the n-th harmonic oscillator level to the $(n-1)$-th and to the $(n+1)$-th, respectively. The probability associated to these transitions is lowered by a factor η^2 with respect to the carrier transition, as shown in figure 4.1.2. These transitions result energy-shifted by $\pm\omega_{\mathsf{ho}}$ and so can be individually resolved only if the broadening of the transition is smaller than the harmonic-oscillator spacing between two consecutive levels. Remarkably, since the discrete energy spectrum of the harmonic oscillator has an absolute minimum, that is reached for $n=0$, the so-called red sideband transitions can occur only if the initial state n allows lower energy levels $(n>1)$.

4.1.2 Measurement of second-order Zeeman shift by narrow spectroscopy

To obtain the clock transition spectra, we address the ultranarrow induced transition $|g\rangle \to |e\rangle$ (described in section 3.2.2) by shining clock-laser pulses from 500 ms to 1 s long. The Rabi frequency and the width of the resonance can be modified by changing the light intensity by means of power broadening, or the external magnetic field applied to the sample, allowing for an accurate control of the transition parameters. Spectra have been obtained by reporting the number of $|g\rangle$ atoms remained after the excitation as a function of the clock laser frequency. When the clock radiation frequency is resonant with respect to the atomic transition, a dip in the observed number of $|g\rangle$ atoms can be observed.

As shown in references [38, 145, 171], many beam paths have been implemented in order to excite the trapped atoms from different directions by exploiting the clock transition. Regarding our actual scopes, each branch is characterized by a well-defined waist and in particular, the smallest waist[6] is achieved when the clock

---

[6] And consequently the branch that allows for the biggest Rabi frequencies achievable.

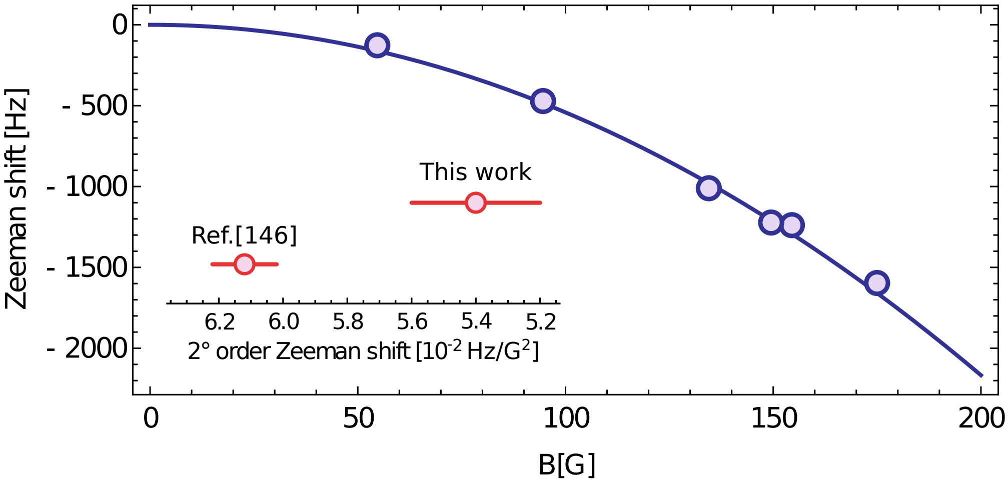

Figure 4.1.3. Characterization of the second-order Zeeman shift. The resonance position has been reported as a function of the applied magnetic field. The experimental data, obtained as mean value of multiple acquisitions, have been fitted by using a quadratic function. In the inset a comparison between our estimation of β and the value reported in reference [146] has been reported. As explained in the main text, the discrepancy between the two measurements could be due to an underestimation of the uncertainty error on the magnetic field value. Blue points represent the resonance frequency of single measurements as a function of the magnetic field.

radiation is collinear to one of the lattices used to confine atoms.

This choice permits us to reach the Lamb-Dicke regime, previously described, by just varying the intensity of the lattice collinear to the clock radiation, while no particular constraints exist for the other lattices. As we will describe in the following section, although the Lamb-Dicke regime is required to perform very narrow spectroscopy without taking into account the photon recoil, it does not represent the only condition that we have to take into account if we are interested in measuring experimentally lattice parameters as the interaction energy U introduced in equation 2.3.4. In a first experiment we investigated the clock transition frequency as a function of the external applied magnetic field. We excited the transition with a 500 ms pulse characterized by an intensity of 10 $\frac{\mathrm{mW}}{\mathrm{mm}^2}$. We acquired many spectra in order to determine the transition frequency for applied magnetic fields ranging from 50 to 175 G. Each spectrum has been fitted with a gaussian curve in order to determine the mean resonance value. The error on the resonance position has been obtained as a standard deviation. The resonance frequencies as a function of the external magnetic field, that are shown in figure 4.1.3, have been fitted with a parabolic function in order to evaluate the second-order Zeeman shift described in section 3.2.3.

From the $\beta \equiv \frac{\Delta E_{z(\mathrm{II})}}{B^2}$ parameter introduced in equation 3.2.17, it is possible to obtain the second order Zeeman shift

$$\beta = -\,(5.4 \pm 0.2)\,10^{-2}\,\frac{\mathsf{Hz}}{\mathsf{G}^2}$$

that is not consistent with the value reported in reference [146] shown, for comparison, in the inset of figure 4.1.3.

The magnetic field has been calibrated by performing a spectroscopy over a mixture of fermionic ^{173}Yb composed by ±5/2 states and evaluating the Zeeman separation of their transition frequencies, assuming a linear Zeeman effect only[7]. The scattering of the data around the fit line could be ascribed to fluctuations of the ULE reference cavity stabilization, as discussed in section 3.4.1.A possible reason for the discrepancy between the two independent measurements, can be an unidentified effect in the calibration on the magnetic field leading to an underestimation of the calibration uncertainty. Another uncertainty source is connected to the observed width, corresponding in each measurement to about 500 Hz, that does not follow the predicted linear scaling law between the Rabi frequency and the magnetic field reported in equation 3.2.15. This suggests the existence of a substructure hidden by the power broadening. The following sections are devoted to the description and to the indentification of this substructure.

---

[7] For the fermionic isotopes, the second-order Zeeman effect provides only a shift of the transition center, not a change in the separation between spin components [190].

4.2 Interaction-peaks resolved spectroscopy

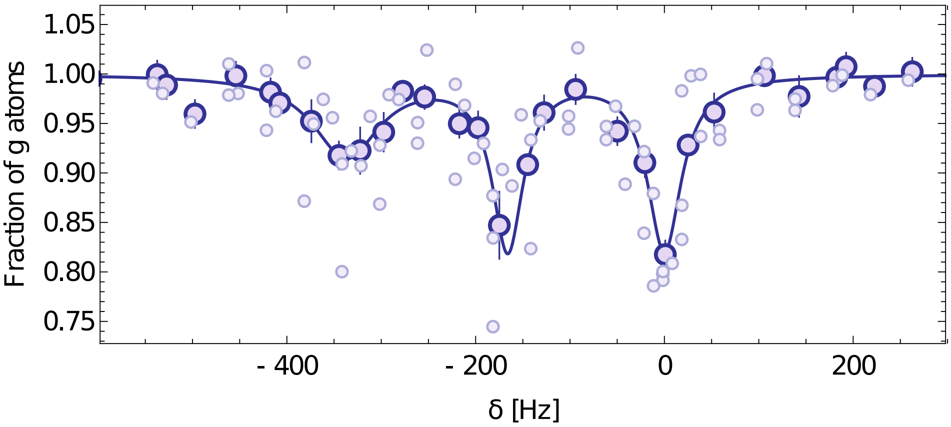

Figure 4.2.1. Typical 500 ms time pulse, 1.5 $\frac{\mathsf{mW}}{\mathsf{mm}^2}$ spectroscopy scanning the frequencies near the atomic peak. The external applied magnetic field corresponds to 55 G. Light blue points represent raw normalized data obtained by rescaling all the frequencies with respect to the fitted frequency position, for each acquisition, of the high frequency resonance. Due to frequencies rescaling it is not possible to obtain statistics over the same frequencies, for that reason, to obtain dark blue points raw points has been binned using as bin interval 25 Hz. Dark blue points represent the mean value of each binned interval dataset, standard deviation instead has been used as error.

To investigate the presence of a substructure in the resonance peak we tried to perform spectroscopy lowering the light intensity on atoms in order to decrease drastically the power broadening. Atoms are loaded in a 3D cubic optical lattice at the magic wavelength corresponding to 759 nm; the lattice depth is increased to reach the Lamb-Dicke regime along the clock radiation direction and bring atoms in a bosonic Mott-insulating phase. As explained in section 2.3.1, to reach a Mott insulating phase it is necessary to overcome the ratio $(\mathsf{U}/\mathsf{t})_\mathsf{c} = 5.8\ \zeta$ where $\zeta = 6$ is the coordination number for a cubic lattice geometry. This condition is realized, by considering isotropic lattice depth ($\mathsf{s}_1 = \mathsf{s}_2 = \mathsf{s}_3 = \mathsf{s}$), when $\mathsf{s} \geq 12$.
Reducing the coupling to the $|e\rangle$ state by lowering the intensity of the clock laser (set to 1 mW/mm^2) and the external magnetic field (set to 55 G), we observe the appearance of a series of resonances that were hidden by the power broadening. An averaged spectrum acquired for a sample of $\approx 5{\times}10^4$ bosons in the specified

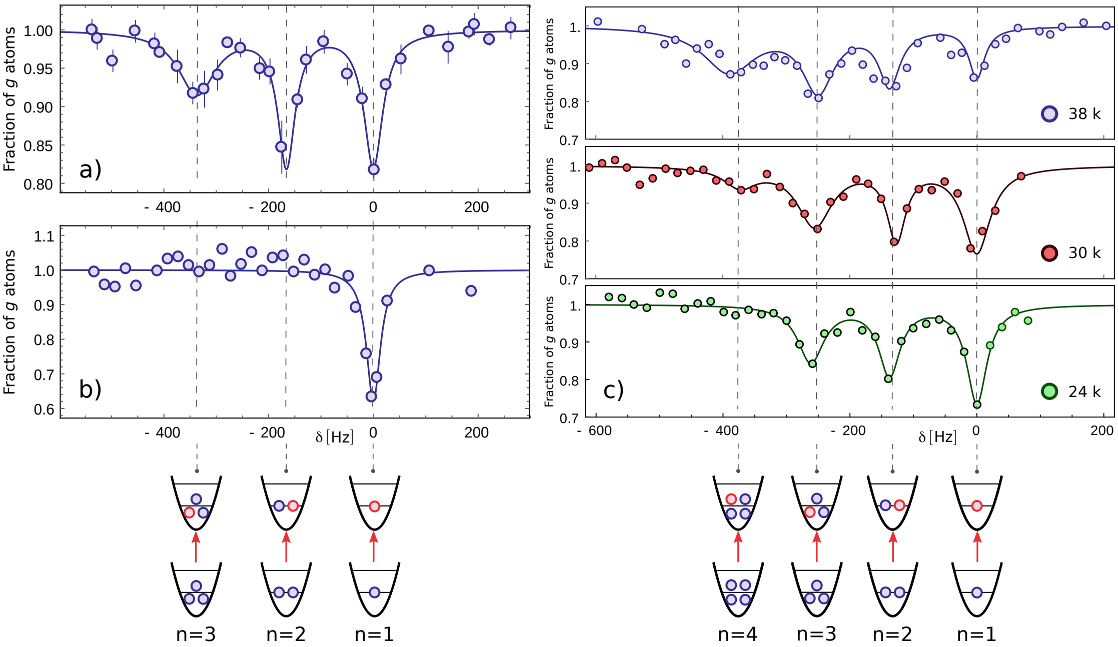

Figure 4.2.2. Clock spectroscopy on ^{174}Yb in a 3D optical lattice. All the shown spectra report the fraction of $|g\rangle$ atoms remaining after a 500 ms long pulse performed shining $1\ \frac{\text{mW}}{\text{mm}^2}$ of clock radiation. All the frequencies are expressed as shifts with respect to the highest-energy resonance. Panel a) shows the typical spectrum, also shown in figure 4.2.1. Panel b) represents a clock spectrum performed on the atomic sample on which a photoassociation (PA) pulse has been applied to remove multiply-occupied lattice sites. Direct comparison between a) and b) allows to detect clearly the single-particle peak. As specified by legends of each plot, in panel c) spectra obtained by gradually lowering the number of atoms inside the lattice are shown. By decreasing the number of loaded bosons a corresponding area reduction of the resonances attributed to multiply-occupied lattice sites can be noted. This feature is in agreement with the hypothesis about the nature of the redshifted peaks ($\delta < 0$).

conditions is shown in figure 4.2.1. Due to the unpredictable residual frequency drift of the ULE cavity presented in section 3.4.1, the laser frequency changes during the measurement and during the day; for that reason, since a full spectrum needs about 20 min, it is necessary to take into account the drift by acquiring and averaging over many realizations.

In order to average over many acquisitions each spectrum is fitted with a multi-gaussian function and all the frequencies are shifted to make the highest-frequency peak coincident in the different spectra[8]. Offsetting the frequencies to the fitted

---

[8] That is taken as a reference because we are interested in relative shifts and not in absolute frequencies.

position of the observed peak at highest energy, the resulting points are spread all over the abscissa axis. Since it is not possible to acquire statistics for all the resulting sparse frequencies, it is necessary to bin the obtained points; we choose a bin interval of 25 Hz, that is consistent with the observed short-term linewidth of the clock laser. Mean values and standard deviations of points in an abscissa interval $\{-12.5+\nu, 12.5+\nu\}$ [Hz] are used as dataset for each averaged spectrum as shown by the dark blue points of figure 4.2.1.

The final experimental dataset is fitted with a sum of gaussian functions, and the frequency shift with respect to the highest energy peak are determined. By following this procedure the substructure shown in figure 4.2.1 arises clearly.

The spectrum is characterized by several resonances that we ascribe to processes where a single $|g\rangle$ atom in a lattice site occupied by n particles is excited to the $|e\rangle$ state. To describe this process by employing a compact notation we introduce $|\,(\mathsf{n})\,g\rangle$ as the lattice site occupied by n $|g\rangle$ bosons.

The excitation of one atom in this lattice site can be written by the notation $|\,(\mathsf{n})\,g\rangle \rightarrow |\,(\mathsf{n\text{-}1})\,g, e\rangle$.

We attribute the splitting of the resonances to the effect of state-dependent atom-atom interactions, that shift the different resonances according to the value of n, as it will be discussed in the next section.

We identify the highest-energy resonance in the spectra as the excitation of the $|g\rangle \rightarrow |e\rangle$ in singly-occupied sites. This attribution is justified by the results of two independent experiments in which we probe a sample in which the number of multiply-occupied lattice sites is drastically reduced by means of a photoassociation (PA) pulse (see figure 4.2.2 a), b)) and by performing spectra as a function of the total number of atoms loaded in the lattice[9] (see figure 4.2.2 c)), respectively.

In the first experiment, shown in figure 4.2.2 b), after the loading of the degenerate sample in the 3D optical lattice, we shine a photoassociation (PA) 556 nm pulse resonant with the two-atoms transition $|(2)g\rangle \rightarrow |^3\mathsf{P}_1 \cdot g\rangle$ where $^3\mathsf{P}_1 \cdot g$ has been introduced to describe a shallow molecule composed by a ground atom and an excited atom in the same lattice site. The molecular state generated by this transition is in a high vibrational state (the binding energy is $\simeq 10$ [MHz]$\times h$) and the finite lifetime of the $^3\mathsf{P}_1$ isolated state causes a fast decay to ground state molecules in high vibrational states or to an unbound state in which $|(2)g\rangle$ atoms can newly absorb resonant radiation in order to form again a molecule. After many absorption-decay cycle the absorbed energy is sufficient to overcome the lat-

---

[9] As mentioned in the previous sections (see section 4.1), it is possible to reduce the number of atoms by changing the final evaporation powers of the crossed trap or, in order to preserve the same experimental conditions for all the spectra, it is possible to wait in the lattice (see figure 4.1.1).

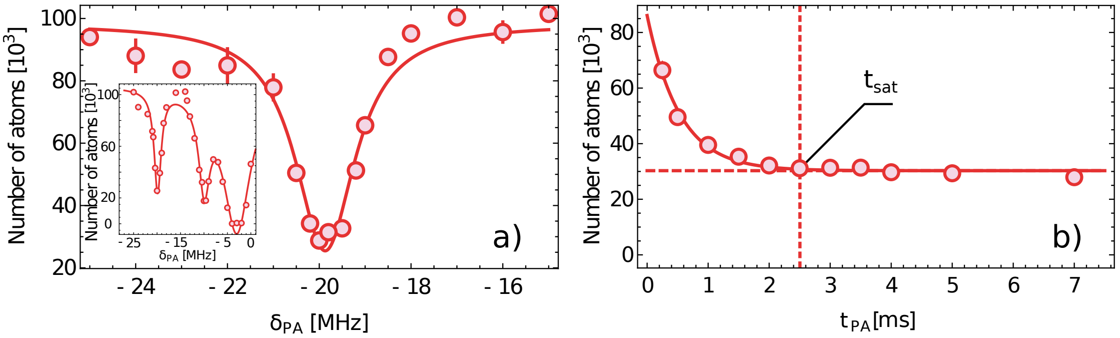

Figure 4.2.3. 556 nm photoassociation transition characterization. In the inset of panel a) a PA spectrum performed by employing 5 ms long pulses and an intensity of about 3 $\frac{\text{mW}}{\text{mm}^2}$ is reported. Three resonances can be detected and the observed resonances positions with respect to the $^1S_0 \rightarrow ^3P_1$ frequency are consistent with references [192, 193]. The main graph in panel a) shows a spectrum near the chosen PA line in order to excite multiply-occupied lattice sites. Panel b) shows the remaining population as a function of the PA pulse duration. For pulses longer than $t_{sat} = 2.5$ ms the number of remaining atoms saturates on 30×10^3 bosons, suggesting that no multiply-occupied lattice sites are left. After 7 ms photon scattering causes a heating of the sample, reflected by a slowest decay of atomic population.

tice confinement potential [191]. This transition has been characterized accurately in bosonic Yb atoms in Refs. [192, 193]. This transition can occur only if a lattice site has at least two ground atoms, hence the photoassociation transition can be employed as a selective tool to reduce only multiply-occupied lattice sites[10]. The resulting atomic sample is characterized mainly by singly occupied sites, that we probe by performing clock spectroscopy.
In order to employ the PA to remove multiply-occupied lattice sites we started by characterizing this process. We loaded about 100×10^3 atoms in a $s = 30$ 3D optical lattice and by means of a 5 ms long pulse of 556 nm radiation (intensity set to 3 $\frac{\text{mW}}{\text{mm}^2}$) we performed spectroscopy. Resonances have been identified by observing the number of remaining $|g\rangle$ atoms when the excitation pulse was shone on the sample. The spectrum reported in the inset of the panel 4.2.3a) shows three resonance peaks; these represent the transitions from the doubly-occupied lattice site $|(2)g\rangle$ to the three least-bound vibrational state of the $|^3P_1 \cdot g\rangle$ molecule. We decided to employ the transition centered at -20 MHz with respect to the $^1S_0 \rightarrow {}^3P_1$ frequency because the resonance can be easily addressed (as shown in figure 4.2.3 a), avoiding an excessive photon scattering, as instead it occurs for the resonances

---

[10] Remarkably, this simplified picture can be used if we neglect the effects of the tunneling. If the lowest lattice depth in order to have a Mott insulating phase ($s = 12$) is considered tunneling processes are characterized by a timescale $t^{-1} \simeq 40$ ms, while PA pulses employed are about $1/20$ t^{-1}.

centered at -6 and -10 MHz.
In figure 4.2.3 b) the population decay obtained by increasing the PA pulse time is reported.
Due to the effectiveness of the described PA pulse, in figure 4.2.2 b) only the highest frequency transition occurs as a consequence of the diminished number of doubly-occupied lattice sites, which allows for the identification of the single-particle $|g\rangle \rightarrow |e\rangle$ transition.

In a second experiment (see figure 4.2.2 c)) we perform spectroscopy on samples containing different atom numbers. As the atom number is reduced, the relative weight of the lower-energy transitions decreases, which indicates that these processes can be attributed to $|(\mathsf{n})g\rangle \rightarrow |(\mathsf{n\text{-}1})g, e\rangle$ transitions with $\mathsf{n} > 1$. On the other hand, the weight of the highest-energy resonance increases as the atom number is reduced, which shows an increased relative number of singly-occupied lattice sites, further confirming the validity of our hypothesis.

4.2.1 Measurement of e-g scattering length

As already introduced in the previous section, the splitting of the resonances in the low-intensity spectrum of figure 4.2.1, is attributed to state-dependent atom-atom interactions. The identification of the resonances (as corresponding to lattice sites with different occupation) represents the starting point for the determination of the s-wave scattering length a_{eg} that describes the interaction between $|g\rangle$ and $|e\rangle$ states atoms in ^{174}Yb. To our knowledge, this value was not reported before. If the single-band Hubbard model introduced in section 2.3.1 describes properly the processes that occur in the lattice[11], relation 2.3.4 can be used to determine the unknown scattering length a_{eg}. The frequency shift experimentally measured by means of narrow spectroscopy is the energy difference between the ground-ground and the ground-excited states interaction energies $\mathsf{U}_{eg} - \mathsf{U}_{gg} \equiv \Delta_{eg}$. Equation 2.3.4 is generalized in order to take into account the interaction energy U_{ij} regarding $\{i, j\}$ particles by equation:

$$\mathsf{U}_{ij} = \frac{4\pi\hbar^2}{m} a_{ij} \int w\,(\vec{\mathsf{r}})^4 \,\mathrm{d}\vec{\mathsf{r}} \tag{4.2.1}$$

---

[11] As shown in section 2.2.2, if the interaction energy is of the order of the lattice band gap, U saturates to the band gap and the relation 2.3.4 can not describe properly the connection between the interaction energy and the scattering length a. This condition is always verified because the band gap of an isotropic lattice for $\mathsf{s} = 15$ (the shallowest lattice used in these measurements) corresponds to 12.5 kHz while the observed frequency shift is of the order of hundreds of Hz.

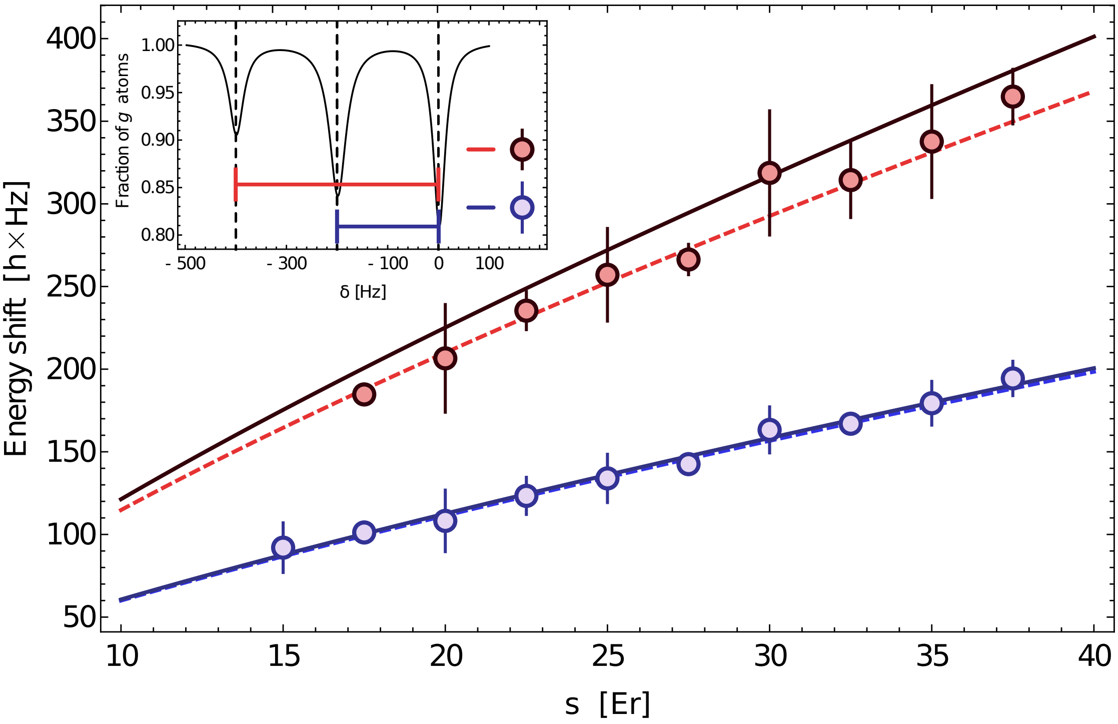

Figure 4.2.4. Measured frequency shifts for two (**blue points**) or three (**red points**) interacting ^{174}Yb bosons one of whom is the excite metastable state $|e\rangle$, with respect to the single particle transition $|g\rangle \rightarrow |e\rangle$ as a function of the lattice depth s. **Inset** reports a spectrum simulation for s = 30, **blue** and **dark red points** of the main plot represent the frequency shifts between the peaks center as shown in **inset**. **Solid lines** represent the fitted function 4.2.2 by considering the best fitted a_{eg}. The specified fit function takes into occount only two-body on-site interactions. **Dashed lines** represent a fit that takes into account two-body and three-body interactions. As shown the agreement between theoretical and experimental dataset is very good.

where m is the atomic mass. By reverting the definition for Δ_{eg} it is possible to obtain:

$$a_{eg} = a_{gg} + \frac{m}{4\pi\hbar^2} \frac{\Delta_{eg}}{\int w\left(\vec{\mathsf{r}}\right)^4 \mathrm{d}\vec{\mathsf{r}}} \tag{4.2.2}$$

where a_{gg} is the s-wave scattering length for ground-ground interaction and is known to be equal to

$$a_{gg} = (104.9 \pm 1.5)\, \mathsf{a}_0 \tag{4.2.3}$$

where a_0 is the Bohr radius [194]. The frequency shift between the $|g\rangle \rightarrow |e\rangle$ transition and the resonances shown in figure 4.2.1 has been experimentally observed as a function of the lattice depth s, as shown in figure 4.2.4. The energy shifts $\Delta_{eg}(\mathsf{s})$ for the transition $|(2)g\rangle \rightarrow |g, e\rangle$ (**blue points**), measured for different values of s,

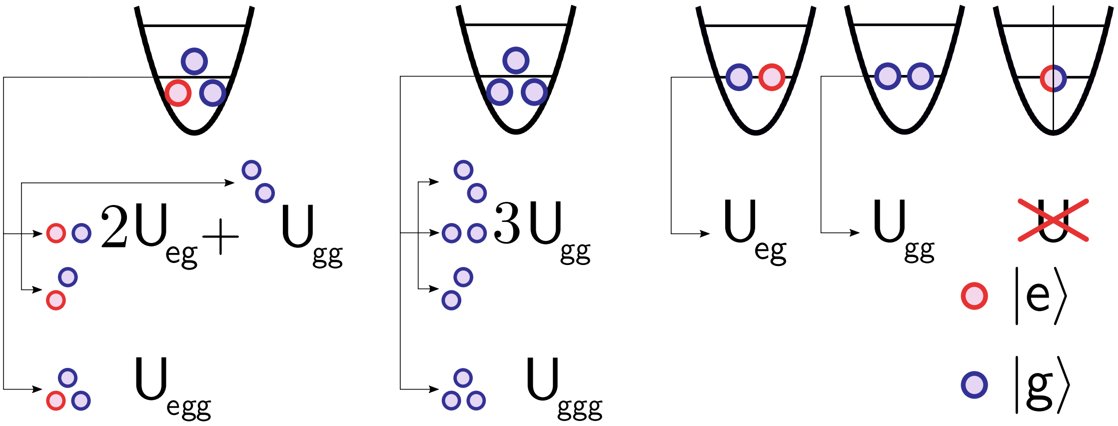

Figure 4.2.5. Sketch of the interaction contributions when a lattice site is occupied by n bosons. Blue circles represent atoms in the fundamental state while red cicles represent atoms in the metastable excited state $|e\rangle$. When $n = 1$ the on-site interaction can not cause an interaction shift to the transition $|g\rangle \rightarrow |e\rangle$. When two particles are considered ($n = 2$) only one interaction energy plays a role. For triply-occupied lattice sites it is necessary to consider two- and (effective) three-body interactions, as explained in the main text; these contributions are shown in the first and second rows, respectively.

have been fitted with equation 4.2.2, using the known dependency of the Wannier functions $w(\vec{r})$ on s, leaving $a_{eg} - a_{gg}$ as the only free parameter. The resulting fit is reported in figure 4.2.4 as blue solid line. The agreement with the observed behaviour is quite good and from the best-fitting value $a_{eg} = a_{gg} - 10.19 \times a_0$, it results immediately:

$$a_{eg} = (94.7 \pm 1.6)\, a_0. \tag{4.2.4}$$

In figure 4.2.4 experimental shifts between the single-particle excitation and the transition $|(3)g\rangle \rightarrow |(2)g, e\rangle$ are also reported (red points). As it can be observed, if the obtained value a_{eg} and only two-body interactions are considered (red solid line), the agreement between experimental data and theoretical behaviour is not good. Contributions to the total interaction energy for a triply-occupied lattice site are shown in figure 4.2.5. By considering only two-body interactions the expected energy shift due to the presence of a metastable state in a triply-occupied lattice site $|(2)g, e\rangle$ can be expressed as

$$\Delta_{egg} = U_{gg} + 2U_{eg} - 3U_{gg} = 2(U_{eg} - U_{gg}) = 2\Delta_{eg}, \tag{4.2.5}$$

or equivalently $\Delta_{egg}/\Delta_{eg} = 2$, where the two-body interactions have been graphically schematized in figure 4.2.5. This result, as shown by red solid line in figure 4.2.4, deviates from the observed shift. We ascribe this deviation to an additional correction arising from three-body effective interactions (see figure 4.2.5).

As demonstrated in reference [195] in a second-quantization approach, by taking into account the many-body Hamiltonian for spin polarized neutral bosons in a deep optical lattice beyond the single-band approximation, it is possible to obtain an effective interaction Hamiltonian

$$\hat{H}_{\mathsf{eff}} = \underbrace{\mathsf{U}_2 \frac{\hat{a}^{\dagger 2}\hat{a}^2}{2}}_{\hat{H}_2} + \underbrace{\mathsf{U}_3 \frac{\hat{a}^{\dagger 3}\hat{a}^3}{6}}_{\hat{H}_3} \tag{4.2.6}$$

that gives rise to a second-order energy correction, due to $\hat{H}_3$, equal to

$$E^{\mathsf{II}}\left(n\right) = \delta\mathsf{U}_2 \frac{n\left(n-1\right)}{2} + \delta\mathsf{U}_3 \frac{n\left(n-1\right)\left(n-2\right)}{6} \tag{4.2.7}$$

where n is the number of atoms in a lattice site and $\delta\mathsf{U}_2$, $\delta\mathsf{U}_3$ are first-order energy corrections arising from virtual transitions to higher lattice bands. At the lowest order possible, it can be demonstrated that $\delta\mathsf{U}_2 = 0$ and the effective elastic three-body interaction can be expressed as

$$\delta\mathsf{U}_3\left(a,\mathsf{s}\right) = -\frac{\beta\mathsf{U}_2\left(a,\mathsf{s}\right)^2}{\hbar\omega(\mathsf{s})} \tag{4.2.8}$$

where $\beta = 4\sqrt{3} - 6\left[1 - \log\left(\frac{4}{\sqrt{3}+2}\right)\right] \simeq 1.34$ is a constant, U_2 is the two-body interaction energy and $\omega(\mathsf{s})$ is the harmonic frequency characterizing the confinement within one lattice site. Relation 4.2.8 allows us to evaluate the second-order correction to the interaction energy for the $|\,(3)\,g\rangle$ state:

$$\begin{aligned} E^{\mathsf{tot}}_{|(3)g\rangle}\left(3\right) = & \left[\frac{n(n-1)}{2} - \frac{4\beta\pi\hbar}{m\omega}a_{gg}\frac{n(n-1)(n-2)}{6}\int w\left(\vec{\mathsf{r}}\right)^4 \mathrm{d}\vec{\mathsf{r}}\right] \\ & \left.\left(\frac{4\pi\hbar^2}{m}a_{gg}\int w\left(\vec{\mathsf{r}}\right)^4 \mathrm{d}\vec{\mathsf{r}}\right)\right|_{n=3}. \end{aligned} \tag{4.2.9}$$

We note that this energy correction could also be interpreted as arising from an effective modification of the single particle Wannier function (dependent of the number of particles in the lattice site), that was also at the basis of the physics discussed in section 2.2.2 for two particles out of the perturbative regime.

For the $|(2)g,e\rangle$ state, since particles are not identical, the theoretical approach developed in reference [195] could not be directly employed. In order to describe heuristically the three-body interaction energy for this state, let us suppose the validity of equation 4.2.9 in which the scattering length a_{gg} is substituted by the geometric average[12] scattering length $\overline{a}_{egg} = \left(a_{gg}a_{eg}a_{eg}\right)^{1/3} \simeq 98\times\mathsf{a}_0$.

---

[12] As it has been graphically represented in figure 4.2.5, in a lattice site occupied by $(2)g$, e atoms, the two-body possible interactions are: $g-e$, $g-e$, $g-g$.

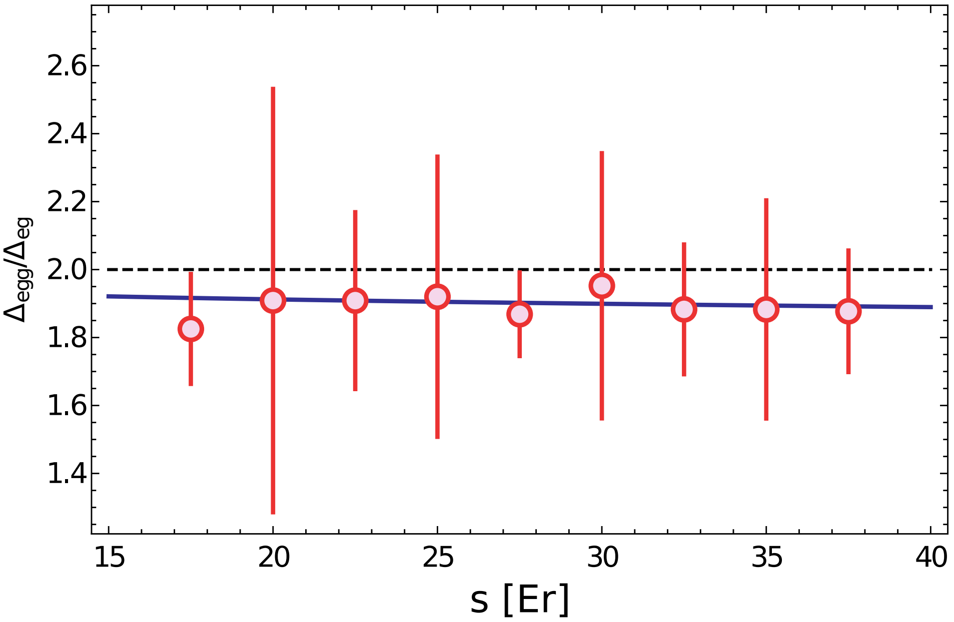

Figure 4.2.6. Red points show the ratio between the frequency shift for triply-occupied and doubly-occupied lattice sites as a function of s. The dashed black line represents the theoretical ratio obtained by taking into account only two-body interactions. While the experimental mean value is (1.9 ± 0.2), by neglecting three-body interactions the theoretical value is constantly equal to 2. If three-body interactions are considered (blue solid line), by means of equation 4.2.8, the agreement between experimental data and theoretical model results very good.

With this hypothesis, the measured $|(3)g\rangle \rightarrow |(2)g,e\rangle$ transitions as a function of s reported in figure 4.2.4 can be employed to estimate a_{eg}. Also in this case, by using equation 4.2.8 (and its extension to the $|(2)g,e\rangle$ state) to express the total energy shift between the $|(3)g\rangle$ and the $|(2)g,e\rangle$ state, a combined fit has been performed by considering all the experimental dataset shown as red and blue points in figure 4.2.4, leaving the differential scattering length $a_{eg} - a_{gg}$ as the only free parameter. The result of the fit, that is in a very good agreement with the measured shifts (and is shown as dashed lines in figure 4.2.4) permits us to obtain a determination of the scattering length $a_{eg} = a_{gg} - 10.08 \times \mathrm{a}_0$:

$$a_{eg} = (94.8 \pm 1.6)\,\mathrm{a}_0 \tag{4.2.10}$$

that is consistent with the value obtained previously (see relation 4.2.4).

Regarding the ratio Δ_{egg}/Δ_{ge}, by neglecting effective three-body interactions theoretically it should be equal to 2, as shown by relation 4.2.5. As it can be observed in figure 4.2.6, the mean experimental value of the considered ratio is

$$\frac{\Delta_{egg}}{\Delta_{eg}} = (1.9 \pm 0.2)\,.$$

Although this value is consistent with 2 within the error bars, we clearly observe that the points in figure 4.2.6 lie all below the theoretical prediction (dashed black line). If instead three-body interaction are considered, by means of including the term described by equation 4.2.8, the ratio between three-body and two-body shifts gains a weak dependence on the lattice depth s as shown in relation

$$\frac{\Delta_{egg}}{\Delta_{eg}} = 2 + \frac{\delta \mathsf{U}_3\left(a_{gg}, s\right) - \delta \mathsf{U}_3\left(\overline{a}_{egg}, s\right)}{\mathsf{U}_{gg} - \mathsf{U}_{eg}}. \tag{4.2.11}$$

The weak dependence can be observed in the blue solid line of figure 4.2.6. In this case a better agreement between theoretical expected value and measured values can be noted.

By evaluating similar excitation spectra, Bouganne et al. [45] obtained independently, in the same time period, a scattering length equal to

$$a_{eg} = (86 \pm 11)\,\mathsf{a}_0,$$

that is consistent with the value obtained in this work, as it can be observed in figure 4.2.7 (numerical values are reported in table 4.2.1). The weighted arithmetical mean between the values obtained in reference [45] and in this work, shown in figure 4.2.7, is

$$\overline{a}_{eg} = (94.6 \pm 1.6)\,\mathsf{a}_0. \tag{4.2.12}$$

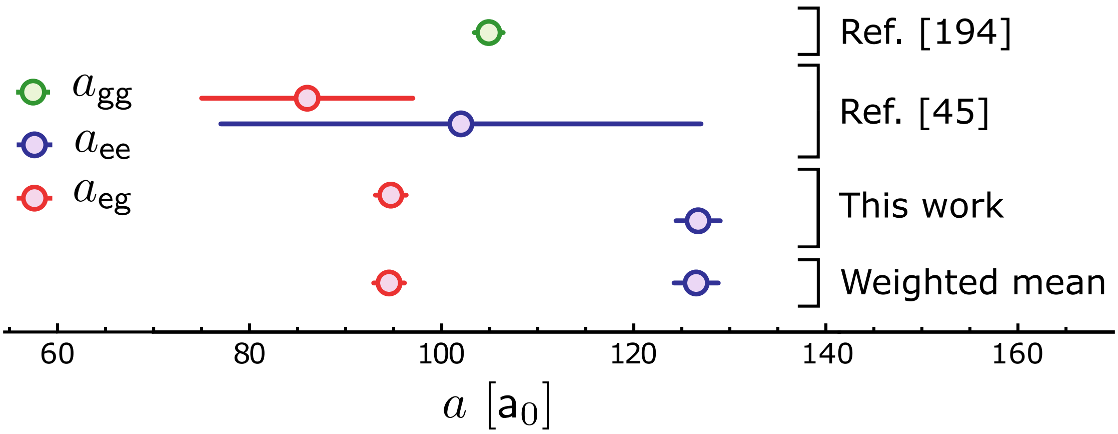

Figure 4.2.7. Direct comparison between the values of a_{eg} (red points) and a_{ee} (blue points) obtained in this work and in reference [45]. All the scattering lengths have been derived by assuming the ground-ground scattering length a_{gg} reported in reference [194] (green point).

4.2.2 Measurement of e-e scattering length

Performing spectroscopy by employing 1.5 s long pulses, a blue-shifted peak $\Delta\nu \simeq 160$ Hz (for $s = 30$) with respect to the single-particle excitation arises, as shown in figure 4.2.8 (blue points).
We ascribed this resonance to the two-photon process $|(2)g\rangle \rightarrow |(2)e\rangle$ which simultaneously transfers two ground particles confined in the same lattice site to a state with two excited particles state, via an intermediate state $|g, e\rangle$ (where we used the notation introduced in the previous sections).
In order to confirm the nature of this transition we performed a "two-colour" spectroscopy by exciting atoms with a clock laser beam characterized by two frequencies $f_\pm = f \pm \delta f$, shifted by $\delta f = \pm 800$ Hz with respect to the carrier frequency f. Spectra are obtained by scanning the carrier f frequency and the number of remained $|g\rangle$ state atoms are reported in figure 4.2.8.
In order to detect the very weak blue-shifted transition identified in figure 4.2.8, the "two-colour" spectroscopy is performed by shining about 30 $\frac{\mathrm{mW}}{\mathrm{mm}^2}$. For that reason the single-photon resonances corresponding to clock frequencies $-\delta f$ and $+\delta f$ are power-broadened and their interaction substructure cannot be resolved, as shown by the red points in figure 4.2.8. This spectrum also shows a weak transition that is not shifted with respect to the "single-colour" spectrum. That suggests that the peak corresponds to a simultaneous absorption of two photons, one characterized by frequency f_+ and the other by frequency f_-, in such a way that the

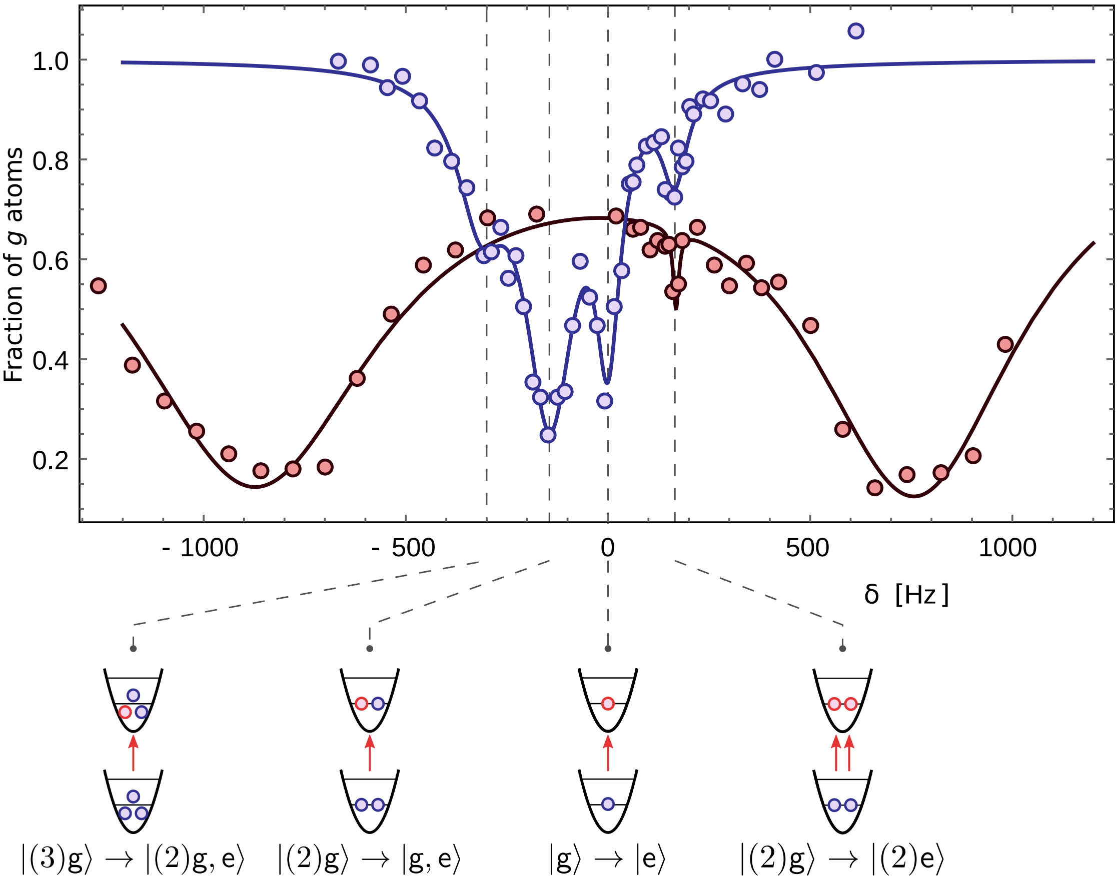

Figure 4.2.8. Single-frequency (blue points) and two-frequency (red points) clock spectroscopy of an atomic ^{174}Yb sample confined in a 3D optical lattice with $\mathsf{s} = 30$. In the “single-colour” spectrum, we ascribe the weak resonance blue shifted with respect to the single particle frequency transition $|g\rangle \rightarrow |e\rangle$ to the two-photon process corresponding to the transition $|(2)g\rangle \rightarrow |(2)e\rangle$. This identification is confirmed by the presence of a resonance having the same frequency in the “two-colour” spectrum taken at frequencies $f_{\pm} = f \pm \delta f$ (see explanation in the main text).

total energy transferred to the system is $h\times(f_+ + f_-) = 2h\times f$, i.e. in the same position as in the “single-colour” spectrum. The two-photon nature $|(2)g\rangle \rightarrow |(2)e\rangle$ of this resonance is then experimentally confirmed and it is possible to determine the interaction energy shift $\Delta_{ee} \equiv \mathsf{U}_{ee} - \mathsf{U}_{gg}$.

By imposing energy conservation for the two-photon transition, it is possible to obtain

$$\nu_0 = \nu_{|g\rangle\rightarrow|e\rangle} + \frac{\mathsf{U}_{ee} - \mathsf{U}_{gg}}{2h}$$

where ν_0 is the resonance frequency i.e. $\nu_{|g\rangle\rightarrow|e\rangle} + \Delta\nu$; that relation implies that the experimental shift $\Delta\nu$ corresponds only to half of the interaction energy between

Scattering channel	Measured value [a_0]	Reference
a_{gg}	104.9 ± 1.5	[194]
a_{eg}	94.8 ± 1.6	This work
	86 ± 11	[45]
$\overline{a}_{eg}$	94.6 ± 1.6	This work & [45]
a_{ee}	126.7 ± 2.3	This work
	102 ± 25	[45]
$\overline{a}_{ee}$	126.5 ± 2.3	This work & [45]

Table 4.2.1. Summary of the measured s-wave scattering lengths of ^{174}Yb for different interaction channels involving the ground and the metastable states.

states $|(2)e\rangle$ and $|(2)g\rangle$. Adopting an argumentation similar to that carried on in section 4.2.1, it is possible to connect this interaction shift to the scattering length a_{ee} via the relation

$$\Delta_{ee} = \frac{4\pi\hbar^2}{m}\left(a_{ee} - a_{gg}\right)\int w^4\left(\vec{\mathsf{r}}\right)\mathrm{d}\vec{\mathsf{r}}. \tag{4.2.13}$$

Averaging over several spectra (both single- and two-colour) acquired at mean lattice depth $\mathsf{s} = (29.3 \pm 0.3)$ it is possible to determine the scattering length for the $|(2)e\rangle$ state by employing equation 4.2.13:

$$a_{ee} = (126.7 \pm 2.3)\,\mathsf{a}_0 \tag{4.2.14}$$

that has been obtained by using the knowledge of the a_{gg} scattering length (see equation 4.2.3).

This scattering length has been evaluated independently by Bouganne et al. [45], obtaining

$$a_{ee} = (102 \pm 25)\,\mathsf{a}_0,$$

and also in this case the obtained value is consistent with the value obtained in this work, as it can be observed in figure 4.2.7.

The weighted arithmetical average between these values has also been reported in figure 4.2.7 (numerical values are reported instead in table 4.2.1) and corresponds to

$$\overline{a}_{ee} = (126.5 \pm 2.3)\,\mathsf{a}_0. \tag{4.2.15}$$

4.3 Interaction-dependent state addressing and inelastic losses

This section is devoted to the description of the experimental procedure employed to excite selectively one of the resonances presented in section 4.2.1 in order to determine the losses due to inelastic collisions between particles in a lattice site. In particular,in section 4.3.1 we firstly present the possibility to address selectively each interaction state introduced in section 4.2.1 by performing Rabi coherent oscillations.
In the second part of this section 4.3.2 we characterize the number of remaining $|g\rangle$ atoms after a selective excitation pulse in the optical lattice providing, at our knowledge for the first time, the loss rate coefficients β for $^{174}\mathsf{Yb}$ in the $|e\rangle$ state.

4.3.1 Coherent addressing of the transition

As shown in the previous section, by performing narrow spectroscopy at low magnetic field ($\simeq 55$ G) it is possible to selectively address resonances corresponding to transitions $|(\mathsf{n})g\rangle \rightarrow |(\mathsf{n}-1)g, e\rangle \; \forall \mathsf{n} = \{1, 2, 3\}$.
$^{174}\mathsf{Yb}$ atoms are trapped in a 3D optical lattice realized at the magic wavelength by exponentially increasing the lattice depth up to $\mathsf{s} = 30$. An intensity of $1.0 \; \frac{\mathsf{mW}}{\mathsf{mm}^2}$ of clock radiation is shone on the sample for variable pulse times and the population of $|g\rangle$ atoms is reported as a function of the excitation time. For this laser intensity and long illumination times (0.5 s), we observed a frequency shift of about 200 Hz between resonances corresponding to different atom number, as shown in figure 4.2.1.
A Rabi oscillation on the resonance $|g\rangle \rightarrow |e\rangle$, exhibiting coherence times exceeding 100 ms, is shown in figure 4.3.1 a). The fitted frequency of this oscillation is $\Omega_{\mathsf{a})} = 2\pi \times 26.9$ Hz. In figure 4.3.1 b) and c) we report Rabi oscillations performed on the n-particle resonances $|(\mathsf{n})g\rangle \rightarrow |(\mathsf{n}-1)g, e\rangle$ in the same experimental configuration employed to achieve the single-particle excitation, in order to compare directly the oscillation frequencies obtained by the sinusoidal fit.
The resulting oscillation frequencies are $\Omega_{\mathsf{b})} = 2\pi \times 36.8$ Hz and $\Omega_{\mathsf{c})} = 2\pi \times 45.5$ Hz. The subscripts $\{\mathsf{a}), \mathsf{b}), \mathsf{c})\}$ have been used to indicate the excitation processes connected to the panels scheme of figure 4.3.1.

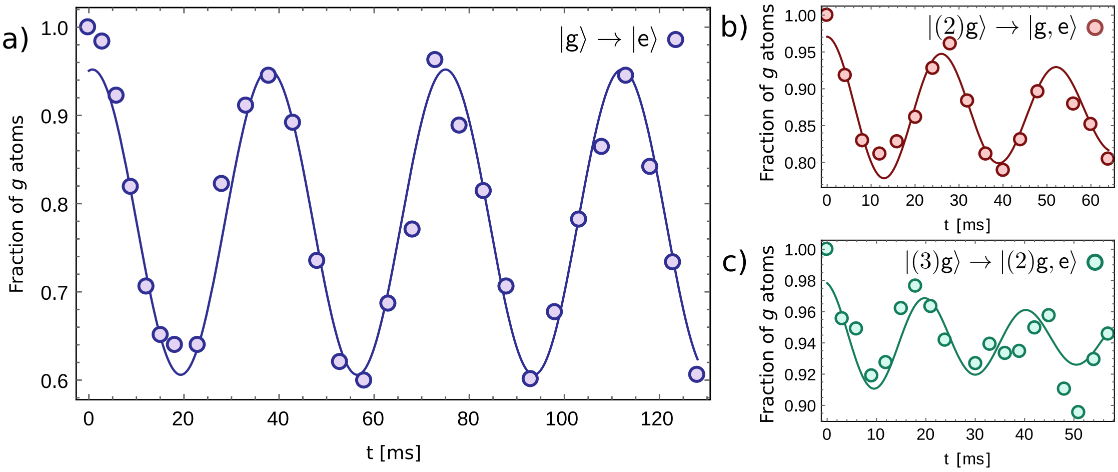

Figure 4.3.1. Rabi oscillations corresponding to selective excitation performed in 3D optical lattice characterized by depth $\mathsf{s} = 30$. Clock radiation pulses are performed by employing 1.0 $\frac{\mathsf{mW}}{\mathsf{mm}^2}$ and a magnetic field of 55 G. Panel a) shows an excitation of the single-particle transition, panels (b,c) instead report Rabi oscillations on two and three particle resonances, respectively.

The ratios between the single-particle excitation and the n-particle excitation frequencies are $\Omega_{\mathsf{b})}/\Omega_{\mathsf{a})} = 0.97\sqrt{2}$, for $\mathsf{n} = 2$ and $\Omega_{\mathsf{c})}/\Omega_{\mathsf{a})} = 0.98\sqrt{3}$ for $\mathsf{n} = 3$. Therefore, we verify the relation

$$\Omega_{|(\mathsf{n})g\rangle \to |(\mathsf{n\text{-}1})g,e\rangle} = \sqrt{\mathsf{n}}\ \Omega_{\mathsf{a})}$$

obtained in reference [196]. This evidence further confirms our hypothesis on the nature of the resonances observed in figure 4.2.1.

4.3.2 Measurement of state-dependent loss rates

In this section we will describe measurements aimed to the characterization of inelastic collisions of ^{174}Yb atoms in the metastable (e) state. To measure the state-dependent loss rates relative to the $e - g$ and $e - e$ interaction channels it is useful to detect atoms in the metastable $^3\mathsf{P}_0$ state (e).

As initially introduced in section 3.4.1, during this work we implemented a laser source that allowed for the direct detection of the population of the $|e\rangle$ state by means of rempumping transitions from the metastable clock to the $^3\mathsf{D}_1$ states. The repumping scheme has been described in section 3.4.1; for the scopes of this section the only interesting characteristic is the detection efficiency, that allows for

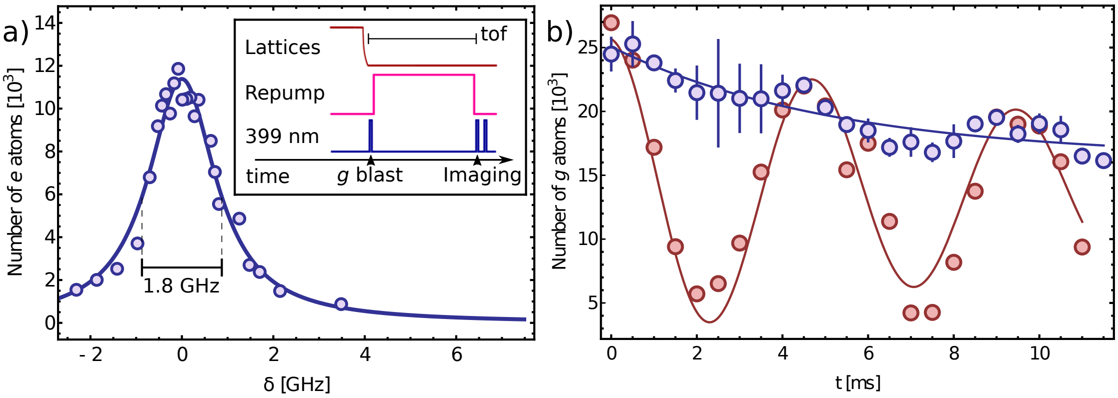

Figure 4.3.2. a) 1388.8 nm spectroscopy: the number of repumped bosons is reported as a function of frequency (expressed as shift δ with respect to the mean value). By performing a Lorentzian fit the experimental linewidth obtained is about 1.8 GHz. In the inset the experimental procedure to blast $|g\rangle$ atoms in order to only observe $|e\rangle$ repumped atoms is shown. b) Rabi oscillation (red points) obtained by exciting the atoms on the clock transition with an intensity of 50 mW/mm^2 and an external magnetic field of 175 G. The blue points represent the sum of ground and rempumped metastable atoms after the excitation pulse. The repumped detection efficiency is about 95% so the decay observable in both the red and blue points can be attributed to inelastic collisions occurring in the sample.

the detection $\sim$ 95% of the total number of excited atoms.
In order to observe just $|e\rangle$ atoms, after ramping down the light intensity of the lattice beams in 150 μs, a $|g\rangle$ blast procedure, performed by employing a 100 μs long pulse resonant with the 399 nm transition $\mathsf{g} \rightarrow |^1\mathsf{P}_1\rangle$ $(\mathsf{F} = 7/2, m_\mathsf{F} = 7/2)$, is used to induce a strong selective heating of the atoms originally in the ground state, in such a way to make them "invisible" to the imaging beam.
During the subsequent time of flight (TOF $=$ 10 ms) the 1388.8 nm radiation is continously shone on the sample, trasferring about 95% of the excited population in the $|g\rangle$ state. After the TOF the usual $|g\rangle$-atoms imaging is performed on the sample in order to detect the atoms originally in the $|e\rangle$ state.
The sequence of experimental pulses used to detect exclusively the $|e\rangle$ atoms are shown in the inset of figure 4.3.2 a).
The power broadening of the $|e\rangle \rightarrow$ ^{3}D$_1$ transition, caused by the $\sim$ 10 mW 1388.8 nm radiation focused onto a waist of about 150 μm is approximately 1.8 GHz, as it can be observed in figure 4.3.2 a). The power broadening, that results about 10^4 times bigger than the natural linewidth (see table 3.4.2), is sufficient to overcome the daily drift of the laser, that is used in free running configuration, allowing many days between frequency resonance checks.

In order to evidence the effects of inelastic collisions involving $|e\rangle$ atoms, as a

first exemplifying case we consider the Rabi oscillations induced by a clock excitation of intensity ~ 50 mW/mm^2 in the presence of a 175 G magnetic field. In these conditions, the frequency shift between resonances corresponding to different atom number, observed in figure 4.2.1, is completely dominated by the power broadening caused by the clock laser. For that reason, in order to simplify the dynamics and avoid other excitation processes, preliminarly to the clock excitation, we performed a 5 ms photoassociation pulse to decrease drastically the number of multiply-occupied sites in the sample. The clock excitation is thus performed after the PA pulse and the resulting Rabi oscillation is shown by the red points of figure 4.3.2b); the best fitted frequency is (208 ± 4) Hz.
As it is shown in figure 4.3.2 b), the first π pulse, corresponding to ~ 2.4 ms, cannot excite properly the total sample, showing the presence of a small amount of non-resonant occupied lattice sites remained after the PA pulse.
This insight is confirmed by the second π pulse, corresponding to $\sim$ 7ms, which results in the same number of detected $|g\rangle$ atoms as the first π pulse. This behaviour cannot be associated to a loss of coherence of the laser or of the atomic dynamics, since it should imply a smaller depletion at the second π pulse, instead it is coherent with a loss of number of atoms in the lattice sites that are affected by the clock pulse.
This hypothesis is also confirmed by the blue points of figure 4.3.2 b) showing the total number of atoms, given by the sum of $|g\rangle$ and repumped $|e\rangle$ atoms. In this case, due to the high and stable detection efficiency of the repumping process, the depletion in the total number of atoms is clearly shown.
We attribute this depletion to the presence of doubly-occupied sites where the interaction between $|g\rangle$ and $|e\rangle$ or between two excited $|e\rangle$ atoms can represent a fast decay interaction channel. The last part of this section will be devoted to the characterization of the possible inelastic interaction channels, that to our knowledge were unknown for ^{174}Yb (while they are well known for interaction between ground and metastable states ^{3}P$_{0,2}$ in fermionic isotopes[13] such as ^{171}Yb, ^{173}Yb [40, 197, 198]).

- Detection of e-g inelastic collision losses

In a following experiment aimed at a better characterization of inelastic losses, we selectively excite the transition $|(2)g\rangle \rightarrow |g,e\rangle$ by employing 10 ms long π pulse in order to obtain the largest possible number of excited doubly occupied sites. To maximize the number of doubly-occupied sites and minimize at the same time the amount of sites with larger occupancy, lattice ramps and waiting time in the FOR Trap before the lattice loading are adjusted.

---

[13] The next chapter will be dedicated to the description of interaction in ^{173}Yb.

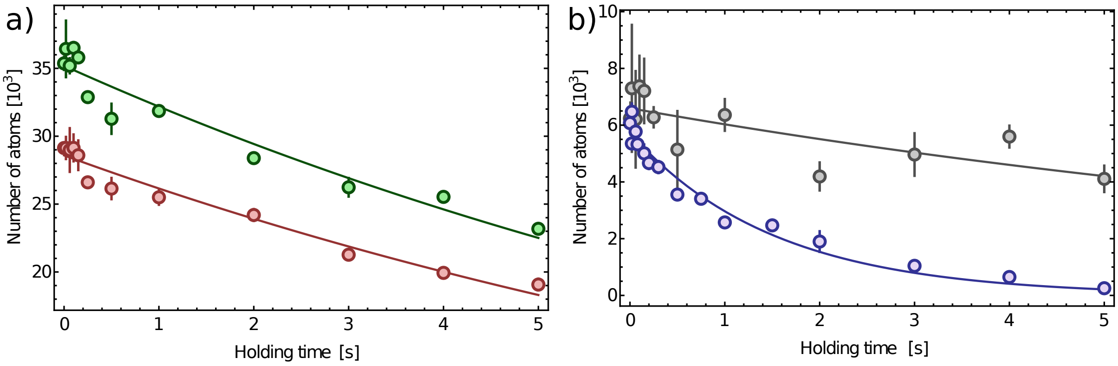

Figure 4.3.3. Inelastic $e - g$ collisions have been investigated by exciting atoms in the $|(2)g\rangle$ state in the $|g, e\rangle$ state by selectively addressing the $|(2)g\rangle \rightarrow |g, e\rangle$ transition in a cubic 3D optical lattice characterized by lattice depth $\mathsf{s} = 27.5$. Panel a) shows the number of g atoms remaining after the clock pulse (red points) and the number of g atoms in the absence of the clock excitation (green points). The slow decay that can be observed is attributed to the finite single-particle lifetime in the lattice. Green and red lines are exponential guides to the eye. Panel b) shows the number of atoms detected in the excited state (blue points) as a function of the holding time in the optical lattice after the excitation of the transition. This number is compared with the difference between the number of g atoms without and with the clock excitation (gray points), that displays an approximately time-independent behaviour. The solid blue line represents an exponential fit of the experimental data characterized by $\tau = (1.52 \pm 0.14)$ s.

To characterize $e - g$ inelastic losses, atoms are trapped in a 3D optical lattice (characterized by depth $\mathsf{s} = (27.5 \pm 1.0)$) at the magic wavelength for the clock transition $|g\rangle \rightarrow |e\rangle$. Then a clock laser π-pulse excitation is performed and, after waiting a variable holding time in the lattice, the atomic population of $|g\rangle$ and $|e\rangle$ are measured.

The collected data measured as a function of the holding time are reported in the panels of figure 4.3.3 as red points for g state atoms and blue points for repumped e state atoms. Green points, instead, represent the initial number of g atoms in a sample on which the excitation pulse is not applied. Red and Green solid lines are exponential fits characterized by τ of the order of ten seconds but are intended only as guides to the eye.

Panel 4.3.3 b) shows clearly that atoms in the e state decay on a timescale of the order of 1.5 s while g atoms, as shown by the red points in panel a), decay in decades of seconds. To properly understand if the observed long decay of g atoms is connected to excited state atoms, we consider the difference between the initial atomic sample and the ground state population when the excitation pulse has been performed, plotted as gray points in panel b). As can be noted, when the holding time is very short, the number of e state atoms is equal to the difference

between the total population and the number of $|g\rangle$ atoms after the excitation. When the holding time is about 1 s, excited atoms are no longer in the trap and the difference between $|g\rangle$ atoms with and without the excitation is approximately constant. This behaviour implies that the losses in the e state population are not caused by inelastic collisions with g atoms otherwise the slow behaviour shown by the gray points should be observed also in the blue points.
The slow decrease of the g atoms has been ascribed to the finite single-particle lifetime of the atoms in the lattice.
Regarding e atoms, the decay rate γ, that is the inverse of the τ reported in the caption of figure 4.3.3, can be estimated as

$$\gamma = (0.66 \pm 0.06)\ \mathrm{Hz}.$$

This timescale is comparable with a tunneling rate of the order of 3 Hz at the lattice depth of the experiment, suggesting that the e atoms, initially in lattice sites with g atoms, could be lost after tunneling processes to neighbour sites via $e - e$ inelastic collisions.

The observed inelastic loss dynamics can be used to provide an upper limit to the $e - g$ inelastic loss rate coefficient.
The rate equation for the $e - g$ inelastic losses can be written as:

$$\frac{\dot{n}_g}{n_g} = -\beta_{eg} n_e = -\gamma_{eg}$$

where β_{eg} is the density-dependent loss rate coefficient.
As the decay time of g atoms is not affected by the excitation to the e state, we can assume $\gamma_{eg} \ll \gamma$ and, evaluating the in-site mean density from the Wannier functions in the 3D lattice, we obtain:

$$\beta_{eg} \ll 10^{-14}\ \frac{\mathrm{cm}^3}{\mathrm{s}}. \tag{4.3.1}$$

- Detection of e-e inelastic collision losses

The data in figure 4.3.3 b), suggest the existence of atom losses involving only the e state, with a faster decay in the first $\simeq 100$ ms, probably due to the e-e interaction in the excited lattice bands (where tunneling times are shorter). However, since the timescale of the observed losses is attributed principally to the tunneling time before the interaction events, it is not possible to extract a reasonable e-e loss rate coefficient from this data.
In order to characterize the e-e inelastic losses we implemented a different strategy, that overcomes the technical difficulties to obtain a reasonable signal-to-noise ratio

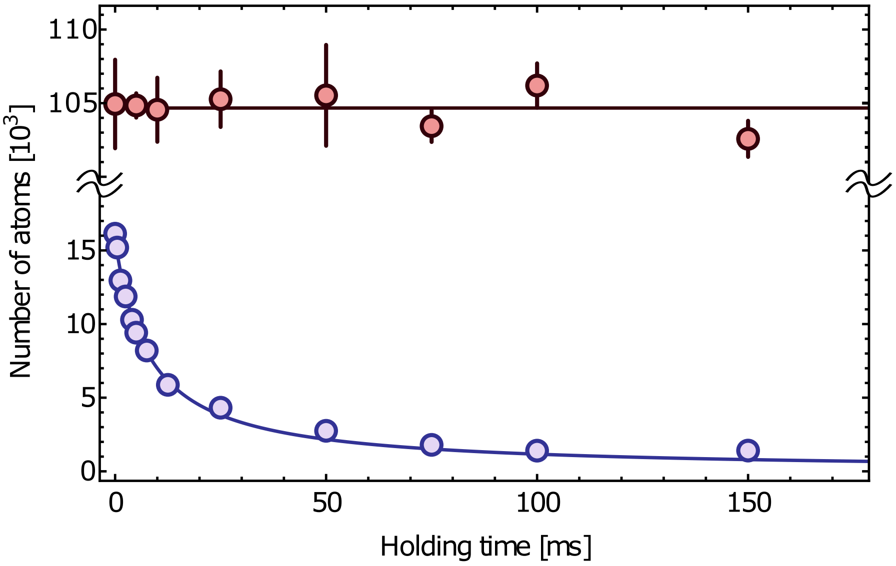

Figure 4.3.4. Blue points represent the number of excited atoms as a function of the holding time in the lattice after a 10 ms long clock excitation pulse in a 1D lattice. Red points represent instead the number of ground state atoms after the excitation pulse in the same lattice geometry. As it is shown by red solid line, that is constantly equal to the mean value of the ground state atoms (104.8 ± 1.8), the number of g atoms can be considered independent to the holding time on this timescale. Blue solid line is the result of a fit to the e data with the two body inelastic mechanics described by equation 4.3.3.

connected to the selective excitation of the e-e transition shown in figure 4.2.8. We decided to change the lattice geometry where atoms are trapped, by reducing it from a 3D cubic optical lattice to a 1D vertical optical lattice at a depth $\mathsf{s} = 27.5$. The confining potential is constituted by an array of two-dimensional pancakes characterized by a radial trapping frequency about $\omega = 2\pi \times 34.5$ Hz. In order to detect the e-e inelastic loss rate part of the population is excited to the metastable state by performing a 10 ms long clock pulse directed along the pancakes plane. After the excitation the 1D vertical lattice is maintained for a variable holding time and, finally, the population of ground and metastable states are measured by releasing the confining potential and performing absorption imaging.

As shown in figure 4.3.4, the excited population (blue points) exhibits fast losses on the timescale of ms, while the population in the ground state (red points) does not depend on the holding time in the specified timescale and can be approximated with a constant function (red solid line). The only process that we will take into account will be an $e - e$ loss rate, that can be described by a two-body inelastic scattering model. Other interaction losses can be neglected on this timescale, as it can be deducted by the previous experiment on e-g losses. As shown in references

[40, 199], $e-e$ two-body losses usually represent the principal loss term and are attributed to principal-number-changing collisions.
In terms of population in the excited state, the dynamics of the two-body inelastic losses can be described by the equation

$$\dot{n}_e = -\beta_{ee} n_e^2 \tag{4.3.2}$$

where n_e is the density of e state atoms. The straightforward solution is given by

$$n_e\left(t\right) = \frac{1}{\frac{1}{n_{e0}} - \beta_{ee} t} \tag{4.3.3}$$

where n_{e0} is the initial e atom density and β_{ee} is the the two body loss rate coefficient.
In order to determine the β_{ee} coefficient we derived a simplified model to obtain the density in the pancakes from the number of g atoms in the optical dipole trap. From a bimodal fit of time-of-flight images of the sample it is possible to directly extract the fraction of condensed atoms, that corresponds to $f = 65\%$ of the total number of atoms for the experiment of figure 4.3.4. The thermal distribution instead is characterized by a temperature of about $T_{\mathsf{3D}} = 60$ nK. This bosonic sample can be described by the equation

$$n_{\mathsf{3D}} = \frac{mf}{4\pi\hbar^2 a_{gg}} \left(\mu_{\mathsf{3D}} - \frac{1}{2} m \sum_{i\in\{x,y,z\}} \omega_i^2 i^2 \right) + \frac{\left(1-f\right) N_{g0}}{\sqrt[3]{\pi^2} r_x r_y r_z} e^{-\sum_{i\in\{x,y,z\}} \frac{i^2}{r_i^2}} \tag{4.3.4}$$

Where $r_i = \sqrt{2k_{\mathsf{B}} T_{\mathsf{3D}}/m\omega_i}$ are the thermal distribution radii, $\omega_i/2\pi$ are the trap frequencies, μ_{3D} is the chemical potential [200] and the initial number of atoms is $N_{g0} \simeq 180\times10^3$. We then consider the density profile in the pancakes assuming no population redistribution during the loading of the lattice.
In order to describe the distribution in the pancakes we cut the 3D distribution along the $\hat{z}$ axis in slices having thickness equal to the lattice periodicity. As we made for atoms confined in the trap, the bimodal fit of the experimental data loaded in the 1D vertical lattice allows us to estimate the condensed fraction ($f_{\mathsf{1D}} = 20\%$) and the temperature of the thermal part ($T_{\mathsf{1D}} \simeq 45$ nK). For each pancake the radial distribution as a sum of a two-dimensional Thomas-Fermi and thermal distributions are thus evaluated.
Finally, the 3D density function in each pancake is obtained by multipling the in-plane 2D density by the square of the fundamental state eigenfunction of a 1D harmonic oscillator aligned to the $\hat{z}$ direction and characterized by the harmonic oscillator length $a_{\mathsf{ho}}^{\hat{z}}$.

We then assume a linear relation between the atom number and the density[14], so the excited state density $n_e\left(t\right)$ after the clock excitation can be determined as

$$n_e(t) = N_e(t)\frac{n_{g0}}{N_{g0}},$$

where $N_e(t)$ is the measured number of atoms in the excited state. From the fit shown as blue solid line in figure 4.3.4 it is possible to determine the parameter β_{ee} as

$$\beta_{ee} = (1.3 \pm 0.7) \times 10^{-11}\ \frac{\mathsf{cm}^3}{\mathsf{s}}. \tag{4.3.5}$$

During the realization of this work we noticed the results reported in reference [45], where, by broadening the transition $|(2)g\rangle \rightarrow |(2)e\rangle$ in a 3D optical lattice, the loss decay value

$$\beta_{ee} = (2.6 \pm 0.3) \times 10^{-11}\ \frac{\mathsf{cm}^3}{\mathsf{s}}.$$

This value is consistent with the value obtained independently in our work within two error bars. The largest uncertainty of our determination comes from the theoretical assumptions used to extract this value from the e population decay shown in figure 4.3.4.

The weighted average of the two independent measurements is

$$\overline{\beta}_{ee} = (2.4 \pm 0.3) \times 10^{-11}\ \frac{\mathsf{cm}^3}{\mathsf{s}}. \tag{4.3.6}$$

---

[14] This assumption follows from the consideration that the observed decay mostly happens on a timescale that is faster than the inverse trap frequency, which means that the size of the sample is expected not to change significantly during the loss dynamics.

5 ^{173}Yb orbital Feshbach molecules production and manipulation

This chapter is dedicated to the description of the possibility to produce and manipulate shallow homo-nuclear Feshbach molecules constituted by AEL atoms in different electronic states ($^1\mathsf{S}_0 = |g\rangle$, $^3\mathsf{P}_0 = |e\rangle$). Moreover, we provide a first measurement of the molecules lifetime in a many-body environment [159].
The chapter is organized as follows: in section 5.1.1 we review the emergence of $\mathbb{SU}(\mathsf{N})$ symmetry for states characterized by null total electronic angular momentum ($\mathsf{J} = 0$) in fermionic AEL atoms.
Interorbital interactions between g and e states are described in section 5.1.2.
Section 5.2 is devoted to the description of Orbital Feshbach Resonance in fermionic ^{173}Yb.
Finally, section 5.3 describes the experimental production, by means of direct photoassociation in a 3D optical lattice setting, of homo-nuclear Feshbach molecules starting from an ultracold sample of ^{173}Yb.
In section 5.4 we demonstrate that the internal molecular state can be controlled by exploiting Raman transitions that swap between different nuclear-spin states of the g state atom forming the molecule. This manipulation scheme has been used as detection tool for orbital molecules (section 5.5.1).
In section 5.5 we report the first lifetime measurement of shallow-bound orbital molecules in a many-body environment.

5.1 Interactions characterization and symmetries in Yb atoms

In chapter 4 we characterized completely the interactions between ground-state atoms ($^1\mathsf{S}_0$) and metastable excited-state atoms ($^3\mathsf{P}_0$) using a general method based on the experimental excitation of the ultranarrow clock transition. The spectroscopy technique employed in our work has been recently used to determine the Hubbard energies in a bosonic sample exploiting the clock transition between ground and the magnetic metastable[1] state $^3\mathsf{P}_2$ in reference [201]. Moreover, the losses of atoms in $^3\mathsf{P}_2$ have been extensively studied, characterizing completely the losses and the interactions offered by ^{174}Yb bosonic atoms [181].
The obtained knowledge of interaction energy and losses allowed also the formulation of more complex systems, based on bosonic Yb, as a possible tool to achieve new accuracy and precision limits, as shown in reference [202].
Regarding interactions in fermionic isotopes of Ytterbium, so far we have already discussed some effects that are linked to the statistical behaviour of the atoms, (section 2.3.1), but we ignored one of the most fundamental properties of AEL atoms as Yb and Sr, that is the possibility to have interactions that does not cause depolarization by means of spin-changing collisions.
In this section, in order to properly present one of the most interesting results obtained in this work, we will introduce the symmetries that characterize the Fermi-Hubbard Hamiltonian regarding the case of Yb atoms[2].

5.1.1 Emergence of $\mathbb{SU}(\mathsf{N})$ symmetry in $\mathsf{J} = 0$ states of two-electron atoms

For a non-interacting atomic system composed by half-integer fermions, the Hamiltonian that describes the system admits a $\mathbb{SU}(2)$ symmetry, because it is in-

---

[1] Despite its importance in the Grotrian diagram of low-lying transitions of Yb (shown in figure 3.4.2), in this thesis the $^3\mathsf{P}_2$ metastable state has been neglected in order to emphasize the possibilities offered by the nearly amagnetic metastable state $^3\mathsf{P}_0$.

[2] From now on all the experiments will be performed by using fermionic ^{173}Yb atoms.

variant under three-dimensional rotations (whose generator is represented by the operator $\hat{U}_R(\hat{\vec{\mathsf{n}}},\theta) = e^{-i\hat{\vec{\mathsf{F}}}\cdot\vec{\mathsf{n}}\theta}$), as potentials that break the Hamiltonian symmetry by means of defining a preferred direction are absent.
That implies that, if no other interactions are considered, this symmetry induces a degeneracy of order $2\mathsf{F}+1$, because the Hamiltonian, $\hat{\vec{\mathsf{F}}}^2$, $\hat{\mathsf{F}}_z$ can be diagonalized simultaneously. States with different values of m_F, the projection of the angular momentum on the quantization axis, have the same energy and F, m_F are good quantum numbers.
Let us consider now an interaction potential, for example by taking into account the interparticle potential described by equation 2.2.10. When the wavefunctions of the external electrons of an atom start to overlap the electronic cloud of the other atom, F and m_F are not good quantum numbers, because the energy connected to the overlapping electron wavefunctions overcome the single-atom hyperfine interaction energies. The colliding-pair Hamiltonian shows $\mathbb{SU}(2)$ symmetry. In this case, in the s-wave scattering regime, where the orbital angular momentum of the colliding pair is equal to zero ($\vec{\mathsf{L}}_\mathsf{P}=0$), the angular momentum of the pair $\vec{\mathsf{F}}_\mathsf{P}$ takes the role of the total momentum operator for an isolated non-interacting atom. In this case the symmetry can be described by the $(2\mathsf{F}_\mathsf{P}+1)$ dimensional representation of $\mathbb{SU}(2)$.
Due to the symmetry with respect to pair rotation, the F_P operator and its projection on the quantization axis are conserved in the collision process.
On other hand, if atoms are described in the absence of interaction (namely when $r\to+\infty$) by the good quantum numbers $|\mathsf{f}_1, m_{\mathsf{f}_1}\rangle$, $|\mathsf{f}_2, m_{\mathsf{f}_2}\rangle$, by considering Hamiltonian symmetry in s-wave scattering regime, immediately results $\vec{\mathsf{F}}_P = \vec{\mathsf{f}}_1+\vec{\mathsf{f}}_2$, $m_{\mathsf{f}_1}+m_{\mathsf{f}_2}=M_{\mathsf{F}_\mathsf{P}}$.
In order to formalize the interaction dynamics, the pseudo-potential introduced in equation 2.2.10 for a pair of spin-F fermions can be generalized by the modified pseudo-potential [203]:

$$\hat{V}(\vec{\mathsf{r}}) = \frac{4\pi\hbar^2}{m}\sum_{\mathsf{F}_\mathsf{P}=0}^{2\mathsf{F}_\mathsf{P}-1} a_{\mathsf{F}_\mathsf{P}}\mathsf{P}_{\mathsf{F}_\mathsf{P}}\delta_{HY}(\vec{\mathsf{r}}) \tag{5.1.1}$$

where F_P is the modulus of the total spin of the pair and $\mathsf{P}_{\mathsf{F}_\mathsf{P}}$ is the projection operator onto the states with total spin F_P. The sum is evaluated only on even results of $\vec{\mathsf{f}}_1+\vec{\mathsf{f}}_2$ in order to fulfill the condition on the symmetry of the total wavefunction [204].
As matter of fact, the s-wave scattering spatial wavefunction is always even under $1\leftrightarrow 2$ exchange transformation and it is necessary to impose the spin-wavefunction anti-symmetrization. Under this transformation the single-particle[3] spin-f wave-

---

[3] We assumed $\mathsf{f}_1=\mathsf{f}_2=\mathsf{f}$ in order to simplify the equations.

functions change by a factor $(-1)^{2\mathsf{f}}$ while the pair spin wavefunction changes by a factor $(-1)^{2\mathsf{f}+\mathsf{F_P}}$.
Thus, to impose the total wavefunction antisymmetrization, the condition
$1 = (-1)^{\mathsf{F_P}}$ has to be verified.

From equation 5.1.1 it seems clear that, to describe completely the interaction between two interacting fermionic particles characterized by spin-f, it is necessary to know of $(2\mathsf{f}+1)/2$ scattering lengths, corresponding to each possible interaction channel.
After the collision each particle can be described again in terms of $|\mathsf{f}, m_\mathsf{f}\rangle$, since the short-range potential is no longer effective and those eigenvalues represent again good quantum numbers for the system. Hence, it is possible to describe the collision process by evaluating the quantity

$$\begin{gathered}\langle \mathsf{f}, m_3| \otimes \langle \mathsf{f}, m_4|\hat{V}(\vec{\mathsf{r}})\,|\mathsf{f}, m_1\rangle \otimes |\mathsf{f}, m_2\rangle = \\ \frac{4\pi\hbar^2}{m}\delta_{HY}(\vec{\mathsf{r}}) \sum_{\mathsf{F_P}} \sum_{m_{\mathsf{F_P}}} a_{\mathsf{F_P}} \langle \mathsf{f}, m_3; \mathsf{f}, m_4|\mathsf{F_P}, m_{\mathsf{F_P}}\rangle\langle \mathsf{F_P}, m_{\mathsf{F_P}}|\mathsf{f}, m_1; \mathsf{f}, m_2\rangle\end{gathered} \tag{5.1.2}$$

where $\langle\cdots;\cdots|\cdots\rangle$ are Clebsch-Gordan coefficients and where we inserted the explicit form of the projection operator P as expansion on $|\mathsf{F_P}, m_{\mathsf{F_P}}\rangle$ pair states.
From equation 5.1.2, if all the scattering lengths have the same value, as it occurs for ground-state components in AEL atoms (as further discussed below), it is possible to simplify this equation by exploiting the completeness relation for $\mathsf{F_P}$ and $m_{\mathsf{F_P}}$. The term $\langle m_3; m_4|m_1; m_2\rangle$ where f has been omitted because it is present in all the terms considered, can be evaluated by invoking the orthogonality relation [48], that allows us to obtain immediately

$$\langle m_3; m_4|m_1; m_2\rangle = \delta_{m_1,m_3}\delta_{m_2,m_4}. \tag{5.1.3}$$

Equation 5.1.3 shows clearly that, if the scattering lengths are the same for each possible $|\mathsf{F_P}, m_{\mathsf{F_P}}\rangle$, s-wave scattering interactions can not cause spin-changing collisions.
In order to derive more formally the symmetries that characterize the Hamiltonian of an interacting fermionic gas of spin-f, let us write, in the second quantization approach, the interaction part of the complete Hamiltonian, associated to the modified pseudo-potential introduced in equation 5.1.1, and let us call $a_{\mathsf{F_P}} = a$ for each possible $\mathsf{F_P}$. In this formalism it is possible to write

$$\begin{aligned}\hat{\mathsf{H}}_\mathsf{U} &= \frac{4\pi\hbar^2 a}{m}\frac{1}{2}\sum_{mm'}\int \hat{\psi}^\dagger_m(\vec{\mathsf{r}})\,\hat{\psi}^\dagger_{m'}(\vec{\mathsf{r}})\,\hat{\psi}_{m'}(\vec{\mathsf{r}})\,\hat{\psi}_m(\vec{\mathsf{r}})\,\mathrm{d}\vec{\mathsf{r}} \\ &= \frac{4\pi\hbar^2 a}{m}\frac{1}{2}\sum_{m\neq m'}\int \hat{n}_m(\vec{\mathsf{r}})\,\hat{n}_{m'}(\vec{\mathsf{r}})\,\mathrm{d}\vec{\mathsf{r}}\end{aligned} \tag{5.1.4}$$

where $\hat{\psi}_m(\vec{\mathsf{r}})$ is the second-quantization field operator that annihilates an atom of spin m and the number field operator for the m spin state is $\hat{n}_m = \hat{\psi}^\dagger_m \hat{\psi}_m$. To obtain the final relation in terms of the number operators the anticommutation relation for fermionic operators has been used. Equation 5.1.4 shows clearly that the interaction between two particles in the same spin state can not occur when s-wave scattering is considered. This result is just a modelization of the Pauli principle for two indistinguishable fermions, as already discussed in section 2.3.1. Equation 5.1.4 finally justifies the presence of the interaction Hamiltonian 2.3.14 heuristically introduced for fermionic interacting particles.
Other Hamiltonian terms (i.e. the kinetic term) operate as identity operators in the spin space ($\mathbb{I}_{\mathsf{f}\times\mathsf{f}}$) thus, to understand the symmetries of the total Hamiltonian describing an interacting system of spin-f fermions, it is necessary to evaluate spin operators that commute with the interaction term described in equation 5.1.4.
The cited interaction Hamiltonian commutes with any spin-permutation operator acting on $(2\mathsf{f}+1)$-dimensional spinors [205]:

$$\begin{aligned} &\left[\hat{\mathsf{H}}_{\mathsf{U}}, \hat{S}^p_q\right] = 0 \qquad\qquad \forall p, q = -\mathsf{f}, \dots, \mathsf{f} \\ &\text{where} \qquad\quad \hat{S}^p_q = \int \hat{\psi}^\dagger_q(\vec{\mathsf{r}})\, \hat{\psi}_p(\vec{\mathsf{r}})\, \mathrm{d}\vec{\mathsf{r}}. \end{aligned} \tag{5.1.5}$$

This property of the interaction Hamiltonian 5.1.4 can be transposed to the total Hamiltonian. In particular, if $q = p$ the found relation implies that the total atomic population corresponding to the m spin $N_m = \hat{S}^m_m = \int \hat{n}_m(\vec{\mathsf{r}})\, \mathrm{d}\vec{\mathsf{r}}$ is conserved, that emphasizes again the lack of spin-changing collisions. Moreover, the absence of spin-changing collisions is remarked by the fact that, if $\hat{S}^m_m = 0$ for the m-th spin projection state, that means that no m-th component is present in the atomic sample even in the ensuing dynamics, and the system behaves as having a lower effective spin.
The spin-permutation operators defined in equation 5.1.5 are generators of the $\mathbb{SU}(\mathsf{N})$ group and, since this group is a Lie group [48], its irreducible representations can be obtained by exploiting the Lie algebra of its generators [206]:

$$\left[\hat{S}^d_q, \hat{S}^p_n\right] = \delta_{dn} \hat{S}^p_q - \delta_{pq} \hat{S}^d_n. \tag{5.1.6}$$

The Hamiltonian commutes with all the generators of $\mathbb{SU}(\mathsf{N})$ and it is therefore $\mathbb{SU}(\mathsf{N})$ symmetric [27].

An unpolarized gas of ^{173}Yb, where all the possible spin components are present can be treated as a gas with $\mathbb{SU}(6)$ symmetry. The lack of spin-changing collisions for a sample with lower spin components is shown in figure 3.4.12, where different spin states are experimentally detected by exploiting a state-dependent optical dipole force (as explained in section 3.4.4). As described in the previous part of this section, the symmetry that characterizes an atomic sample in which, for example, only two spin components are maintained, corresponds to $\mathbb{SU}\,(2)$.

The absence of hyperfine interaction caused by the lack of electronic angular momentum J in the ground state $^1\mathsf{S}_0$ allows the perfect decoupling of the nuclear-spin degree of freedom with respect to the electronic degrees of freedom, and induces the $\mathbb{SU}(\mathsf{N})$ Hamiltonian symmetry. As shown in section 3.2.1, AEL fermions, and among those ^{173}Yb atoms, are characterized by the presence of a metastable state $^3\mathsf{P}_0$, that has the same internal structure of the ground state. Therefore, atoms in that state are expected to show nearly the same symmetries detected for interacting atoms in the ground state. However, in section 3.2.1 we have shown how the hyperfine interaction causes a very weak coupling of the cited metastable state with the $^1\mathsf{P}_1$ state; we have also discussed that the possibility to address the doubly forbidden transition from the ground to the metastable state is only a consequence of a non well defined F quantum number for the P states of AEL atoms.
For that reason, strictly speaking, the symmetry associated to the metastable state cannot be exactly $\mathbb{SU}\,(\mathsf{N})$. These observations can be ignored, and therefore the Hamiltonian symmetries can be recovered, if the energy shift associated to the effect of these contributions, as the presence of an external magnetic field in the case of the hyperfine mixing of P states, is lower than the energy scale associated to the hyperfine interaction that define the m_F state in in the excited metastable states.
In reference [205] the contribution of the hyperfine mixing between P states has been taken into account and, due to this phenomenon, the spin independence of the scattering lengths in the metastable state is expected to be slightly reduced with respect to the ground state (in which deviation from $\mathbb{SU}\,(\mathsf{N})$ model are of the order of $\delta a_{\mathsf{F}_\mathsf{P}}/a_{\mathsf{F}_\mathsf{P}} \sim 10^{-9}$) and variations of the order of $\delta a_{\mathsf{F}_\mathsf{P}}/a_{\mathsf{F}_\mathsf{P}} \sim 10^{-3}$ are expected.

Since in the ground-state of AEL atoms the hyperfine interaction is completely absent, $\mathsf{F} = \mathsf{I}$ and $m_\mathsf{F} = m_\mathsf{I}$ are good quantum numbers also if an external magnetic field is applied.

The possibility to have an interacting gas characterized by $\mathbb{SU}\,(\mathsf{N})$ symmetry[4] with $N \in \{2, \ldots, 6\}$ makes two-electron atomic systems a unique resource for

---

[4] Evidently, if a polarized gas is considered, the particles can not collide and the gas becomes effectively non-interacting. In this case the symmetry that characterizes the sample is simply the $\mathbb{SU}\,(2)$ symmetry that allows the identification of $\hat{\vec{\mathsf{F}}}$ and m_F as good quantum numbers.

quantum simulation of many fields of physics. Inspired by the case of quantum chromodynamics, where quarks interact by exchanging $\mathbb{SU}(3)$ gauge bosons [207], the application of $\mathbb{SU}(\mathsf{N})$-symmetric atomic gases to the quantum simulation of gauge theories has been discussed in several studies, as demonstrated by references [109, 208, 209]. Moreover, quantum mixtures of different $\mathbb{SU}(\mathsf{N})$ fermionic atomic systems have been realized experimentally, showing the possibility to implement frameworks for quantum simulation characterized by higher symmetries with respect to the simple $\mathbb{SU}(\mathsf{N})$ case, as shown in Ref. [156].

5.1.2 Inter-orbital interactions

So far we described the collisions that characterize interacting $|g\rangle$ and $|e\rangle$ atoms (in which the electronic angular momentum $\mathsf{J} = 0$).
By considering only the s-wave scattering collisions, that properly describe the interaction between atoms when the degenerate regime is reached, we introduced the scattering lengths a_{gg} and a_{ee} in order to characterize the collisions of fermionic atoms in the same electronic orbital but in different nuclear spin states.
In this section we generalize the described phenomenon to the inter-orbital collisions between atoms in the $|g\rangle$ state and in the excited metastable $|e\rangle$ state, exploring all the possibilities furnished by those states in the framework of two-electron fermions.
We finally introduce the scattering lengths corresponding to the orbital states $\Psi_\pm$ that validate the antisymmetrization of the total wavefunction under the exchange transformation $1 \leftrightarrow 2$.

In order to introduce the inter-orbital collision let us consider two interacting AEL atoms, one in the ground state $^1\mathsf{S}_0 = |g\rangle$ and the other in the excited state $^3\mathsf{P}_0 = |e\rangle$. These atoms are trapped in the same lattice site, sharing the same spatial wavefunction $\Phi(\vec{\mathsf{r}})$. The possible states that take into account the antisymmetrization of the total wavefunction can be expressed as:

$$\begin{aligned}
|\Psi_+\rangle &= \underbrace{\frac{1}{\sqrt{2}}\left(|ge\rangle + |eg\rangle\right)}_{\text{Symmetric } 1\leftrightarrow 2} \otimes |\mathsf{s}\rangle \otimes \underbrace{\Phi(\vec{\mathsf{r}_1})\,\Phi(\vec{\mathsf{r}_2})}_{\text{Spatial}} \\
|\Psi_-\rangle &= \underbrace{\frac{1}{\sqrt{2}}\left(|ge\rangle - |eg\rangle\right)}_{\text{Antisymmetric } 1\leftrightarrow 2} \otimes |\mathsf{t}\rangle \otimes \underbrace{\Phi(\vec{\mathsf{r}_1})\,\Phi(\vec{\mathsf{r}_2})}_{\text{Spatial}}
\end{aligned} \tag{5.1.7}$$

where in general

$$|\mathsf{t}\rangle = \begin{cases} |\uparrow;\uparrow\rangle \\ (|\uparrow;\downarrow\rangle + |\downarrow;\uparrow\rangle)\frac{1}{\sqrt{2}} \\ |\downarrow;\downarrow\rangle \end{cases} \qquad |\mathsf{s}\rangle = (|\uparrow;\downarrow\rangle - |\downarrow;\uparrow\rangle)\frac{1}{\sqrt{2}}. \tag{5.1.8}$$

We are interested in describing processes that can occur in a "real lattice site" in which $|e\rangle$ states are obtained by promoting a $|g\rangle$ atom to the excited state as a consequence of the interaction with the clock radiation. For that reason, and also to simplify the description of the physical phenomena that undelies the inter-orbital collisions, we can discard the states corresponding to maximum and minimum total momentum projection on the quantization axis because the $|(2)\,g\rangle|\uparrow;\uparrow\rangle$ and $|(2)\,g\rangle|\downarrow;\downarrow\rangle$ states cannot be experimentally achieved as direct consequence of the Pauli principle.
The four states and the corresponding scattering lengths that completely describe the collisions in a system of $|e\rangle$, $|g\rangle$ atoms can be summarized as:

$$|(2)\,g\rangle \to a_{gg} \qquad |\Psi_+\rangle \to a^+_{eg} \qquad |\Psi_-\rangle \to a^-_{eg} \qquad |(2)\,e\rangle \to a_{ee}. \tag{5.1.9}$$

To describe the inter-orbital collisions let us further generalize the pseudo-potential introduced by equation 5.1.1 by taking into account the presence of two other interaction channels:

$$\hat{V}(\vec{\mathsf{r}}) = \frac{4\pi\hbar^2}{m}\delta_{HY}(\vec{\mathsf{r}}) \sum_{i\in\{\mathsf{c.c.}\}} a_i \underbrace{|i\rangle\langle i|}_{\mathsf{P}_i} \tag{5.1.10}$$

where c.c. are the mentioned possible collision channels expressed in equation 5.1.9 and P_i is the projector on the i-th channel.
Collision channels related to states $|(2)g\rangle$ and $|(2)e\rangle$ represent the interaction between atoms in the same electronic state and different nuclear spin states, and have been accurately described, identifying also symmetries corresponding to homo-orbital interaction, in section 5.1.1 of this work.
The remaning two terms, in which "bare" states $|ge\rangle$, $|eg\rangle$ are mixed by the antisymmetrization of the total wavefunction, constitute a two-dimensional Hilbert subspace on which each operator can be mapped in terms of Pauli matrices and the identity:

$$\mathsf{M} = \alpha\, \mathbb{I}_{2\times 2} + \vec{\beta}\cdot\vec{\sigma} \tag{5.1.11}$$

where M is a generic operator and $\vec{\sigma}$ is the usual vector of Pauli matrices.
The projectors $\mathsf{P}_\pm$ can be expressed in the two-dimensional space spanned by the

$|eg\rangle, |ge\rangle$ states by just evaluating $|\Psi_+\rangle\langle\Psi_+|$, $|\Psi_-\rangle\langle\Psi_-|$:

$$\begin{aligned} \mathsf{P}_+ &\equiv |\Psi_+\rangle\langle\Psi_+| = \frac{1}{2}\Big(\mathbb{I}_{2\times 2} + \sigma_x\Big)|\mathsf{s}\rangle\langle\mathsf{s}| \\ \mathsf{P}_- &\equiv |\Psi_-\rangle\langle\Psi_-| = \frac{1}{2}\Big(\mathbb{I}_{2\times 2} - \sigma_x\Big)|\mathsf{t}\rangle\langle\mathsf{t}|. \end{aligned} \tag{5.1.12}$$

By substituting these expressions in equation 5.1.10 the resulting pseudopotential reads:

$$\begin{aligned} \hat{V}(\vec{\mathsf{r}}) &= \frac{4\pi\hbar^2}{m}\delta_{HY}(\vec{\mathsf{r}})\left(a_+\mathsf{P}_+ + a_-\mathsf{P}_-\right) = \\ = \frac{4\pi\hbar^2}{m}\delta_{HY}(\vec{\mathsf{r}})&\left[\left(\frac{a_{eg}^+ + a_{eg}^-}{2}\right)\mathbb{I}_{2\times 2}\left(|\mathsf{s}\rangle\langle\mathsf{s}| + |\mathsf{t}\rangle\langle\mathsf{t}|\right) + \left(\frac{a_{eg}^+ - a_{eg}^-}{2}\right)\sigma_x\left(|\mathsf{s}\rangle\langle\mathsf{s}| - |\mathsf{t}\rangle\langle\mathsf{t}|\right)\right] \end{aligned} \tag{5.1.13}$$

also states $|\mathsf{s}\rangle$, $|\mathsf{t}\rangle$ generate a two-dimensional Hilbert subspace, thus it is possible to express each operator again as expansion on the Pauli matrices and the identity; we indicate operators that operate on this spin subspace with subscript S.
By introducing $\mathbb{I}_\mathsf{S}$ and $\sigma_{z\mathsf{S}}$, equation 5.1.13 can be written as:

$$\hat{V}(\vec{\mathsf{r}}) = \frac{4\pi\hbar^2}{m}\delta_{HY}(\vec{\mathsf{r}})\left[\underbrace{\left(\frac{a_{eg}^+ + a_{eg}^-}{2}\right)\mathbb{I}_{2\times 2}\mathbb{I}_\mathsf{S}}_{\mathbf{V}} + \underbrace{\left(\frac{a_{eg}^+ - a_{eg}^-}{2}\right)\sigma_x\sigma_{z\mathsf{S}}}_{\mathbf{V}_\mathsf{ex}}\right] \tag{5.1.14}$$

where we introduced $\mathbf{V}$, $\mathbf{V}_\mathsf{ex}$ terms. By introducing the basis

$$|\Psi_\pm\rangle = \frac{1}{\sqrt{2}}\Big(|g\uparrow, e\downarrow\rangle \pm |g\downarrow, e\uparrow\rangle\Big)\Phi(\vec{\mathsf{r}_1})\,\Phi(\vec{\mathsf{r}_2}) \tag{5.1.15}$$

it can be easily demonstrated that the $\mathbf{V}$ term, expressed in this rotated basis, keeps unchanged the spin of the particles, while $\mathbf{V}_\mathsf{ex}$ exchanges the two spins [145, 205]. In particular, the latter term depends on the difference of scattering lengths between the orbital-symmetric channel a_{eg}^+ and the orbital-antisymmetric channel a_{eg}^- as shown in equation 5.1.14. If $a_{eg}^+ = a_{eg}^-$ this term does not contribute to the pseudo-potential 5.1.14 and only the direct term $\mathbf{V}$ contributes. Remarkably, the presented model can be applied for each collision process in which two internal degrees of freedom participate to the scattering dynamics.

Defined the scattering lengths that characterize the main interaction channels when ground and excited levels are considered, we report the most accurate available measurements of these quantities in table 5.1.1 and in figure 5.1.1. As it can be observed, the agreement between the different determination of about $a_{eg}^\pm$ is

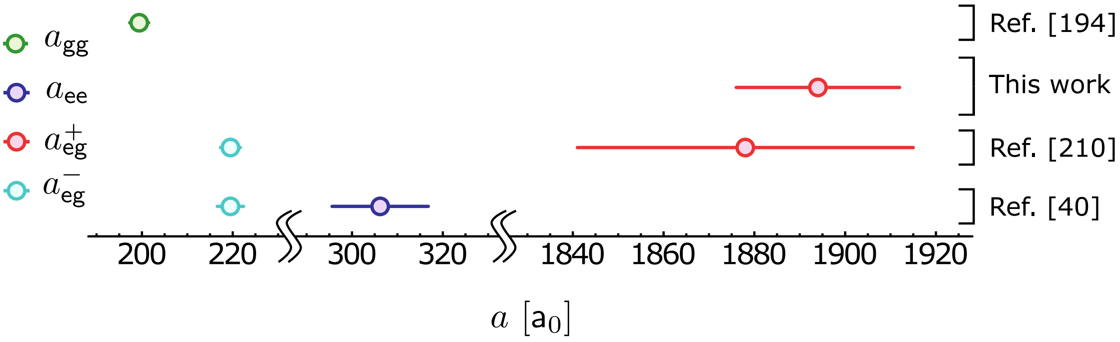

Figure 5.1.1. Pictorial comparison between available known values of a_{eg}^{+} (red points), a_{eg}^{-} (cyan points) in ^{173}Yb. The measured scattering lengths describing the interactions between atoms in the same orbitals a_{gg} (green point), a_{ee} (blue point) are also shown.

Scattering channel	Measured value [a$_0$]	Reference
a_{gg}	199.4 ± 2.1	[194]
a_{eg}^{+}	1894 ± 18 1878 ± 37	This work [210]
a_{eg}^{-}	219.5 ± 2.9 219.7 ± 2.2	[40] [210]
a_{ee}	306.2 ± 10.6	[40]

Table 5.1.1. Summary of the measured s-wave scattering lengths of ^{173}Yb for different interaction channels involving the ground $|g\rangle$ and the metastable $|e\rangle$ states.

very good.

The exchange pseudopotential can contribute considerably only if the two scattering lengths a_{eg}^{+} and a_{eg}^{-} are substantially different. Two-electron atoms offer a variety of possibilities, since some are characterized by similar scattering lengths, as it happens in fermionic ^{87}Sr where $a_{eg}^{+} = (169 \pm 8)\,\mathrm{a}_0$, $a_{eg}^{-} = (68 \pm 22)\,\mathrm{a}_0$ (in which the exchange phenomenon has been observed by probing the clock transition in a optical clock experiment [211]) or in ^{171}Yb where $a_{eg}^{+} = (225 \pm 13)\,\mathrm{a}_0$, $a_{eg}^{-} = (335 \pm 6)\,\mathrm{a}_0$ [212], while others are characterized by a very different scattering lengths as it occurs in ^{173}Yb where $\delta a \equiv a_{eg}^{+} - a_{eg}^{-} = (1894 - 219.5)\,\mathrm{a}_0$ [39, 40, 159].

As a matter of fact, the presence of a non negligible coupling term between different collision channels allows us to control the interaction strength by operating on external parameters as the magnetic field via the Feshbach resonance between open and closed interaction channels.
In the next chapter we will introduce the mechanism that underlies the possibility to change interactions in a ^{173}Yb atomic sample by means of the so-called Orbital Feshbach Resonance (OrbFR).

5.2 Feshbach resonances

In this section we introduce the most used tool[5] that allows the fine control of interactions in an atomic sample: the Feshbach resonances [17–19]

So far we have described the physical phenomenon that underlies interactions in atomic systems and until section 5.1.2 the possibility to have two colliding channels associated to the same atomic interacting pair has not been considered in order to simplify the description of the interaction processes.

Despite that, in the aforementioned section it has been stressed out that, in the case of AEL atoms and in particular of ^{173}Yb, two possible interaction channels for the colliding pair e-g exist. In the s-wave scattering regime they can be characterized by the scattering lenghts $a^+ \equiv a_{eg}^+$ and $a^- \equiv a_{eg}^-$ (experimental values are reported in table 5.1.1).

These scattering lenghts are very different, $\delta a = a_{eg}^+ - a_{eg}^- \sim 1500$, and, as shown in section 5.1.2, this causes a peculiar non-negligible exchange interaction that occurs only when mixtures $|g\rangle$, $|e\rangle$ are considered. The difference between $a^\pm$ arises from the asymptotic energy associated to the two specified scattering channels as shown in figure 5.2.1.

In section 2.1.2 we connected the scattering length of a scattering channel to the least bound state of the scattering potential by equation 2.1.26. The last relation ensures that the least bound state corresponding to such a high scattering length as a^+ (it is in the case of ^{173}Yb) is related to the existence of an extremely shallow bound state (see section 2.1.2 or reference [76] for an alternative description). The least bound state has an energy of the order of 10 kHz below the continuum energy for the aforementioned values. The existence of this extremely shallow bound state motivated the theoretical research [213] on the possibility to tune interactions in $|g\rangle$, $|e\rangle$ mixtures via a new kind of Feshbach resonance, defined Orbital Feshbach Resonance to emphasize the role of the two-different electronic orbitals (and their symmetries) involved in the scattering process.

---

[5] The initial theoretical proposal by Feshbach [17] was focused on the properties of scattering resonances in nuclear physics experiments. The "interplay" between interactions in atomic physics and nuclear physics has been largely demonstrated in chapter 2.1.2.

5.2.1 Two coupled-channels model

In order to describe the general mechanism that underlies the Feshbach resonance let us introduce a generic two-level system $|\mathsf{o}\rangle$, $|\mathsf{c}\rangle$ in which o, c are two-body states corresponding to two different scattering lengths a_{o}, a_{c}, associated to the open and the closed collision channels, respectively[6]. Also in this case, $|\mathsf{o}\rangle$, $|\mathsf{c}\rangle$ define a two-dimensional Hilbert subspace in which each operator can be expressed as a linear combination of the identity and the Pauli matrices, as shown in equation 5.1.11. In this basis a generic Hamiltonian operator that takes into account also a coupling term between $|\mathsf{o}\rangle$ and $|\mathsf{c}\rangle$ can be described by the relation:

$$H_{2\times 2} = \begin{pmatrix} H_{\mathsf{o}} & \mathsf{W} \\ \mathsf{W} & H_{\mathsf{c}} \end{pmatrix} = H_{\mathsf{o}} \left(\frac{\mathbb{I}_{2\times 2} + \sigma_z}{2} \right) + \mathsf{W}\sigma_x + H_{\mathsf{c}} \left(\frac{\mathbb{I}_{2\times 2} - \sigma_z}{2} \right) \qquad (5.2.1)$$

where $H_{\mathsf{o,c}}$ describe the single-channel Hamiltonian of the corresponding state and W is the coupling between the two interaction channels.

In order to simplify the following equations let us consider the so-called single-resonance approximation, for which all the eigenstates of H_{c} are not involved in the dynamics except for the bound state $|\mathsf{res}\rangle$ that is characterized by nearly null energy. Colliding particles are characterized by energy $E \simeq 0$ thus all the other eigenstates characterized by non null energies (both scattering states and bound states) are far from resonance and, compared to $|\mathsf{res}\rangle$, their contribution can be considered negligible. The closed-channel Hamiltonian can be schematized as:

$$H_{\mathsf{c}} = E_{\mathsf{res}} |\mathsf{res}\rangle\langle\mathsf{res}|$$

Let us suppose that the state $\{|\mathsf{o}\rangle, |\mathsf{c}\rangle\}$ is an eigenstate of Hamiltonian 5.2.1 corresponding to eigenvalue E, this hypothesis leads to the system of coupled equations:

$$\begin{cases} H_{\mathsf{o}}|\mathsf{o}\rangle + \mathsf{W}|\mathsf{c}\rangle = E|\mathsf{o}\rangle \\ H_{\mathsf{c}}|\mathsf{c}\rangle + \mathsf{W}|\mathsf{o}\rangle = E|\mathsf{c}\rangle \end{cases} \qquad (5.2.2)$$

By recalling Rouchè-Capelli[7] theorem (and its lemmas) it is possible to express the solution of the system as a sum of a homogeneous solution [8] and the solution

---

[6] The open channel referes to the state of the colliding pair enter the scattering, while the closed channel refers to a different collisional channel to which the open channel can be coupled (as explained in the following).

[7] Sometimes it is also called Kronecker or Frobenius theorem.

[8] Following reference [76] we introduce $|\phi\rangle$ as the solution of the uncoupled open channel Hamiltonian $\hat{H}_{\mathsf{o}}$.

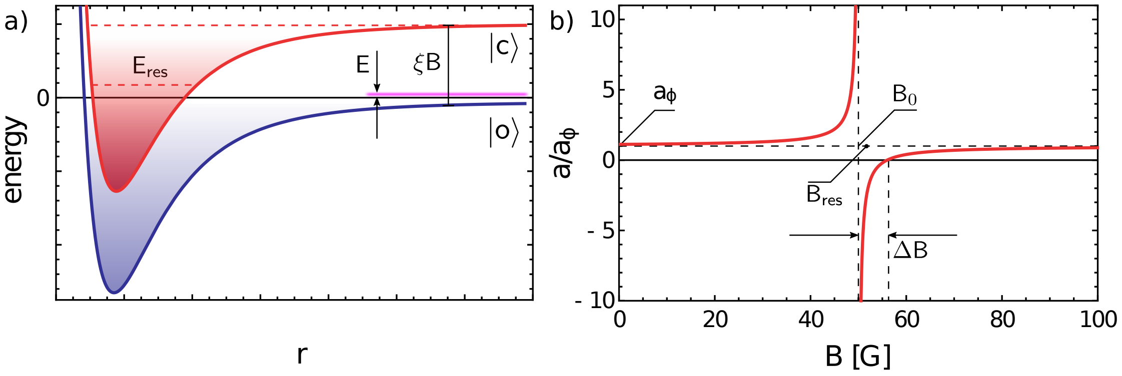

Figure 5.2.1. Panel a) shows the uncoupled open-channel $|\mathsf{o}\rangle$ (blue solid line) and closed-channel $|\mathsf{c}\rangle$ (red solid line) molecular potentials. At energy E (purple solid line) only the open channel is accessible. Painted areas (red and blue for closed and open channel, respectively) represent the conditions in which real bound states are supported. In panel b, the red solid line reports the normalized scattering length with respect to the background scattering length a_ϕ as a function of the external magnetic field B. See the main text to interpret the positions of B_0, $\mathsf{B}_{\mathsf{res}}$, $\Delta\mathsf{B}$.

of the full equation with the coupling term considered as a source term [76]:

$$\begin{cases} |\mathsf{o}\rangle = |\phi\rangle + \mathsf{G_o}(E)\,\mathsf{W}|\mathsf{c}\rangle \\ \\ |\mathsf{c}\rangle = \dfrac{\langle\mathsf{res}|\mathsf{W}|\mathsf{o}\rangle}{E - E_{\mathsf{res}}}|\mathsf{res}\rangle \end{cases} \tag{5.2.3}$$

where $\mathsf{G_o}(E) = (E - E_{\mathsf{res}} + i\epsilon)^{-1}$ is a Green function of H_o. From these equations results evident that states $|\mathsf{o}\rangle$, $|\mathsf{c}\rangle$ include the coupling potential W while, by definition, states $|\mathsf{res}\rangle$ and $|\phi\rangle$ are solutions of the uncoupled system. For that reason the latter are called **bare states** while the firsts are named **dressed states**.

By properly manipulating equations 5.2.3 it is possible to express the eigenstate $|\mathsf{o}\rangle$ as a function of only bare states:

$$|\mathsf{o}\rangle = \left(1 + \mathsf{G_o}(E)\underbrace{\frac{\mathsf{W}|\mathsf{res}\rangle\langle\mathsf{res}|\mathsf{W}}{E - E_{\mathsf{res}} - \langle\mathsf{res}|\mathsf{W}\mathsf{G_o}(E)\,\mathsf{W}|\mathsf{res}\rangle}}_{\mathsf{V_{eff}}}\right)|\phi\rangle \tag{5.2.4}$$

where $\mathsf{V_{eff}}$ is an effective potential that operates on the $|\phi\rangle$ space and takes into account the effect of virtual transitions to the closed-channel subspace [214].
The denominator of $\mathsf{V_{eff}}$ explicitly shows the effect of the coupling term W on the resonance energy. In the case $E \to 0$ the resonance energy is shifted by the

second-order correction caused by the coupling W evaluated between "bare" $|\mathsf{res}\rangle$, $|\phi\rangle$ states.

Assuming that the spin configurations of the two channels have different magnetic moments, the energies of the states in these channels vary differently when an external magnetic field is applied.

$$E_{\mathsf{res}} = \xi\left(B - B_{\mathsf{res}}\right)$$

where B_{res} is the magnetic field for which E_{res} is degenerate with the energy $E \simeq 0$ of the ultracold collision state.

The position of the resonance is given not by the "zero" of E_{res}, but by the relation

$$E_{\mathsf{res}} + \langle \mathsf{res}|\mathsf{W}\mathsf{G}_{\mathsf{o}}(E)\mathsf{W}|\mathsf{res}\rangle = \xi\left(B - B_0\right)$$

where we introduced B_0 that takes into account the coupling W and the differential magnetic moments of channels.

If the coupling is not present ($\mathsf{W} = 0$) the dressed $|\mathsf{o}\rangle$ state collapses on the bare $|\phi\rangle$ state; the scattering length associated to this condition is usually called background scattering length.

If instead equation 5.2.4 is taken into account, it is necessary to consider the explicit form of the Green function in order to evaluate the scattering length [48]. By evaluating it for $r \to \infty$ it is possible to obtain [215]:

$$a = a_\phi\left(1 - \frac{\Delta B}{B - B_0}\right) \tag{5.2.5}$$

where

$$\Delta B = \frac{2m}{\hbar^2}2\pi^2\frac{|\langle\phi|\mathsf{W}|\mathsf{res}\rangle|^2}{\xi a_\phi}.$$

Equation 5.2.5 explicitly shows the divergence of the scattering length when the applied magnetic field B corresponds to B_0. Remarkably, due to the presence of the coupling potential, the scattering length divergence does not occur when the magnetic shift compensates the bare energy of the $|\mathsf{res}\rangle$ bound state ($E_{\mathsf{res}} = \xi\mathsf{B}_{\mathsf{res}}$), because of the correction in equation 5.2.4 induced by the coupling W, as explicitly shown in figure 5.2.1 b).

The distance from the resonance to the magnetic field value for which the scattering length vanishes defines ΔB reported in figure 5.2.1.

5.2.2 Orbital Feshbach Resonance in ^{173}Yb

In order to adapt the two-channel model described in section 5.2.1 to the case of AEL atoms, and in particular to the ^{173}Yb atom that has been employed to generate, observe and manipulate very shallow orbital molecules supported by a OrbFR [159], let us consider two atoms characterized by different spins (↑ and ↓) and orbital degree of freedom ($|g\rangle$ and $|e\rangle$). At large inter-atomic distance ($r \to \infty$), atoms do not interact and the eigenstates of the two-particles system are given by:

$$\begin{aligned} |\mathsf{o}\rangle &= \frac{1}{\sqrt{2}}\Big(|g,\uparrow\rangle|e,\downarrow\rangle - |e,\downarrow\rangle|g,\uparrow\rangle\Big) \equiv |g\uparrow, e\downarrow\rangle \\ |\mathsf{c}\rangle &= \frac{1}{\sqrt{2}}\Big(|e,\uparrow\rangle|g,\downarrow\rangle - |g,\downarrow\rangle|e,\uparrow\rangle\Big) \equiv |e\uparrow, g\downarrow\rangle \end{aligned} \tag{5.2.6}$$

where $|\mathsf{o}\rangle$ is the open channel and $|\mathsf{c}\rangle$ is the closed channel of the system.
In the asymptotic condition the energy shift between $|\mathsf{c}\rangle$ and $|\mathsf{o}\rangle$ channels can be expressed as

$$\delta_\mu \mathsf{B} = h\delta_g|\Delta m|\mathsf{B}$$

where Δm is the difference in the nuclear spin projection on the quantization axis of the system, B is the external magnetic field applied and δ_g is the differential Landé factor between $|g\rangle$ and $|e\rangle$ states introduced in section 3.2.3. For ^{173}Yb it corresponds to $\delta_g = (113 \pm 1)$ Hz/G.
Considerably, in the case of null external magnetic field the asymptotic states become degenerate, a condition that does not occur in usual Feshbach resonances with alkali atoms.
When the relative distance diminishes, interaction energy takes a role and the total Hamiltonian becomes not diagonal on the $|\mathsf{o}\rangle$, $|\mathsf{c}\rangle$ basis.
As shown in section 5.1.2, in this condition two different interaction potentials exist and the scattering lengths related to scattering in these potentials, called a^+_{eg} and a^-_{eg}, are not directly connected to states with defined spin orientation.
By taking into account states in which the spin orientation are defined
($|g\uparrow, e\downarrow\rangle$ and $|g\downarrow, e\uparrow\rangle$) and recalling the basis change rule in quantum mechanics for operators and states:

$$|\Phi\rangle = \mathsf{U}\ |\phi\rangle \qquad\qquad \hat{\mathsf{O}} = \mathsf{U}\ \hat{\mathsf{o}}\ \mathsf{U}^{\mathsf{t}} \tag{5.2.7}$$

where $\mathsf{U} \in \mathbb{SO}(\mathsf{N})$, it is possible to express these states in terms of eigenstates of the interaction pseudo-potential operator $|\Psi_\pm\rangle$ (defined by equation 5.1.10).

In particular, by recalling equation 5.1.15 it is possible to deduce the rotation matrix U that allows changing from one basis to the other:

$$\mathsf{U} = \frac{1}{\sqrt{2}} \begin{pmatrix} 1 & 1 \\ -1 & 1 \end{pmatrix} = \frac{1}{\sqrt{2}} \left(\mathbb{I}_{2\times 2} + i\sigma_y \right).$$

The complete Hamiltonian, expressed in terms of open and closed channels, reads:

$$H_{\mathsf{OrbFR}} = \begin{pmatrix} H_{\mathsf{o}} + \mathsf{V}(a_d) & \mathsf{V}_{\mathsf{ex}}(a_{ex}) \\ \mathsf{V}_{\mathsf{ex}}(a_{ex}) & H_{\mathsf{c}}(\mathsf{B}) + \mathsf{V}(a_d) \end{pmatrix}, \tag{5.2.8}$$

where the closed-channel Hamiltonian can be expressed in this basis as $H_{\mathsf{c}} = (E_{\mathsf{c}} + \delta_\mu \mathsf{B}) \left|\mathsf{c}\right\rangle\left\langle\mathsf{c}\right|$, $\mathsf{V}(\mathsf{a}) = \frac{4\pi\hbar^2}{m}\mathsf{a}\delta_{HY}(\vec{\mathsf{r}})$ and we introduced the direct and exchange scattering lengths defined by relations:

$$a_d = \frac{a_+ + a_-}{2} \qquad\qquad a_{ex} = \frac{a_+ - a_-}{2}.$$

As it can be observed by direct comparison, the Hamiltonians reported in equation 5.2.1 and equation 5.2.8 have the same form and thus the model described in the previous section can be easily adapted to describe the OrbFR.
In this case the coupling term, that was not made explicit in section 5.2.1, is represented by the exchange interaction, that, operating on the spin space, has no classical counterpart and thus can be treated as a pure quantum effect.
The resulting scattering length for the open channel can be expressed as [213]

$$a_{\mathsf{o}} = \frac{\left(a_d^2 - a_{ex}^2\right)\sqrt{m\delta_\mu \mathsf{B}} - \hbar a_d}{a_d\sqrt{m\delta_\mu \mathsf{B}} - \hbar}. \tag{5.2.9}$$

Equation 5.2.9 explicitly shows the dependence of the scattering length on the applied magnetic field. In order to recover the general form obtained in section 5.2.1 (see equation 5.2.5), it is possible to manipulate this relation properly to obtain

$$a_{\mathsf{o}} = a_d \left(1 - \frac{\mathsf{B}\left(a_{ex}/a_d\right)^2}{\mathsf{B} - \hbar/a_d\sqrt{m\delta_\mu/\mathsf{B}}} \right) = a_d \left(1 - \frac{\Delta \mathsf{B}_{\mathsf{Orb}}}{\mathsf{B} - \mathsf{B}_{\mathsf{Orb}}} \right). \tag{5.2.10}$$

From 5.2.10 results clear the “unconventional nature” of this kind of Feshbach resonance because the magnetic field interval

$$\Delta \mathsf{B}_{\mathsf{Orb}} = \mathsf{B} \left(\frac{a_+ - a_-}{a_+ + a_-} \right)^2 \tag{5.2.11}$$

expresses a direct dependance on the applied external magnetic field.

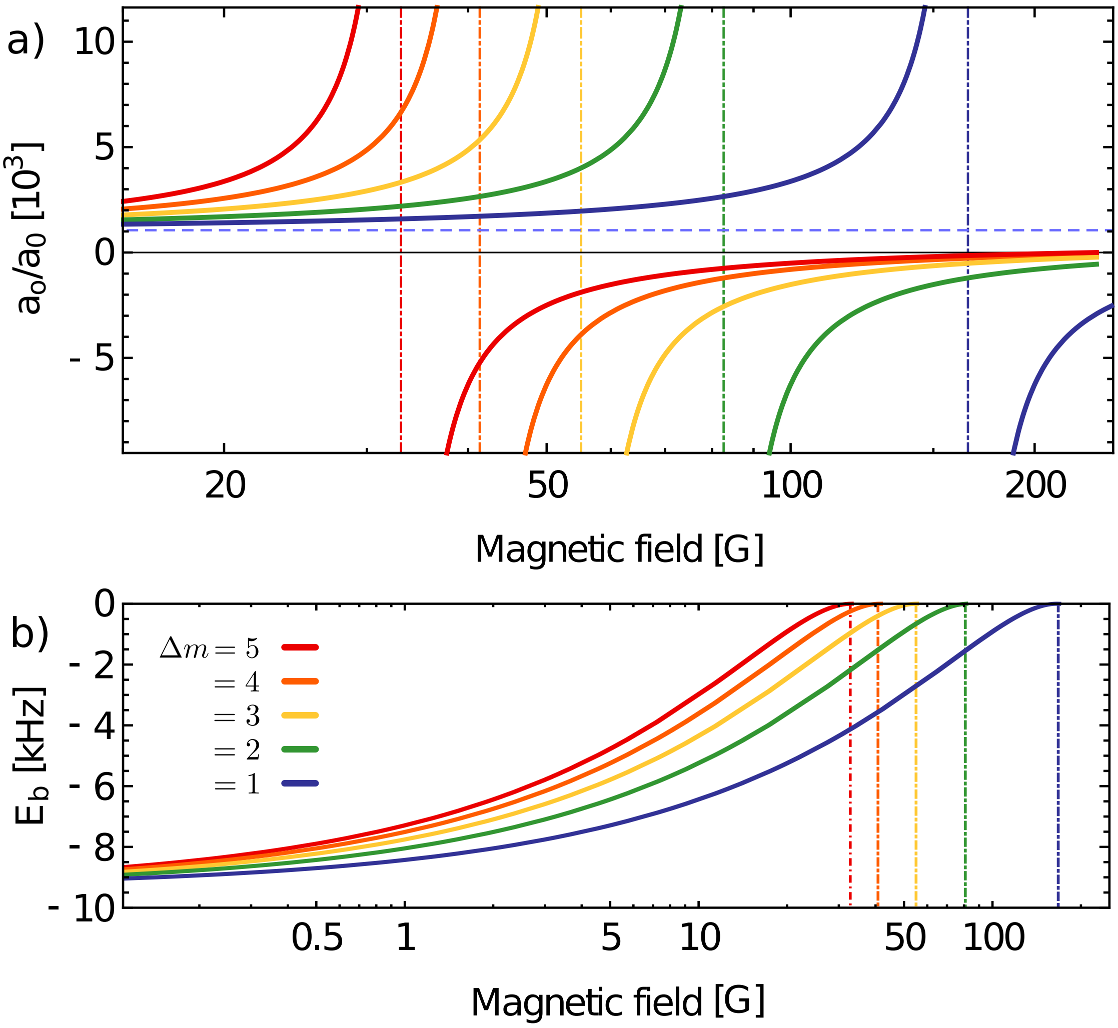

Figure 5.2.2. Panel a) shows the magnetic-field dependence of the s-wave scattering length in the open channel described in equation 5.2.10 for different ^{173}Yb atomic mixtures. The **dashed purple line** represents the background scattering length a_d. Panel b) represents the energy of the least bound state described in equation 2.1.26 evaluated for a_o as a function of the external magnetic field. Finite-range contributions are not taken into account for the sake of the presentation.

The resonance position is identified by the condition

$$\mathsf{B} = \mathsf{B}_{\mathsf{Orb}} \equiv \frac{\hbar^2}{m\delta_\mu a_d^2}. \tag{5.2.12}$$

The described mechanism can been observed in ^{173}Yb for a different couples m_1, m_2 of nuclear spin states ($m_1 \neq m_2$) [210, 216]. Although the scattering lengths a_d,

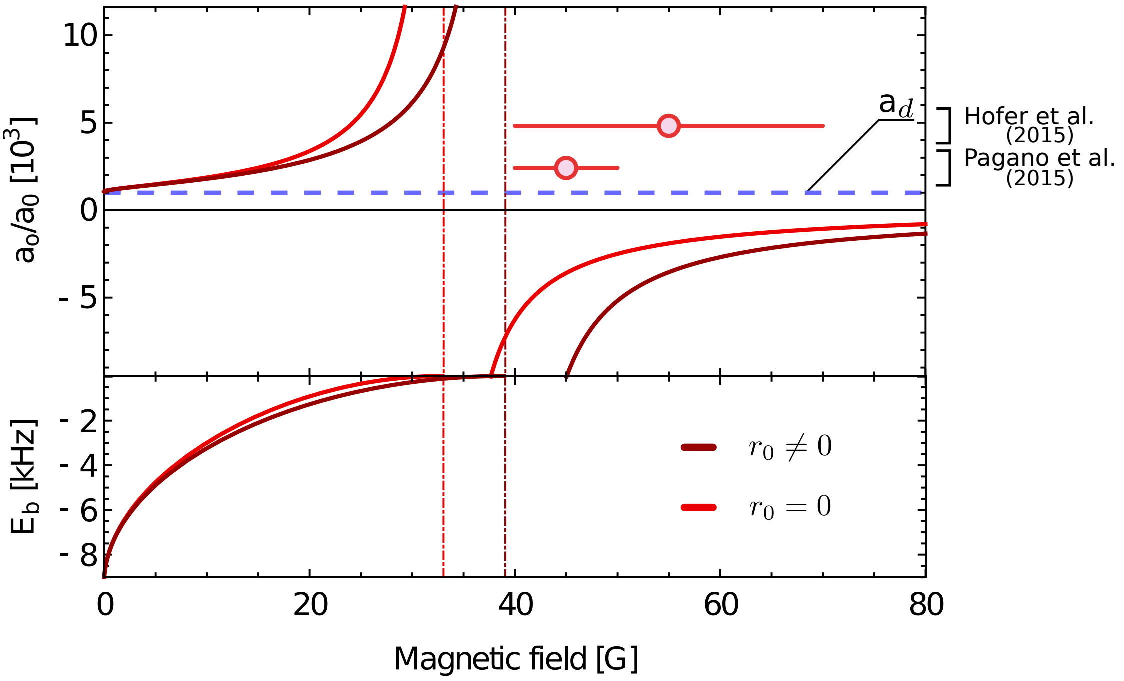

Figure 5.2.3. Magnetic-field dependence of the s-wave scattering length (upper panel) in the open channel, as described in equation 5.2.13, and bound-state energy (lower panel). Solid red lines show the dependence on the magnetic field without considering finite-range effects, while solid dark red lines represent the case in which finite-range contributions are taken into account ($r_0 = 84.8\mathsf{a}_0$). Experimental points shows resonance positions reported in literature [210, 216].

a_{ex} are the same for each possible nuclear-spins couple m_1, m_2, the resonance position changes as a result of the $\mathsf{B}_{\mathsf{Orb}}$ dependence on the magnetic moment difference $\delta_\mu = h\delta_g|\Delta m|$ where $\Delta m = |m_1 - m_2|$. The dependence of the scattering length as a function of the magnetic field, for different values of Δm, is shown in figure 5.2.2.

In references [210, 216] the position of the OrbFR in ^{173}Yb was experimentally determined for $\delta m = 5$ (that can be obtained only by generating a $\mathbb{SU}(2)$ sample constituted by $|m_{\mathsf{F}} = \pm\frac{5}{2}\rangle$ atoms). The obtained values

$$\mathsf{B}_{\mathsf{res}} = (45 \pm 5)\ \mathsf{G}\ (\text{ref.}[216])$$

and

$$\mathsf{B}_{\mathsf{res}} = (55 \pm 15)\ \mathsf{G}\ (\text{ref.}[210]),$$

are consistent[9] with each other, but are bigger than the predicted theoretical value, as shown in figure 5.2.3. The discrepancy between the theoretical prediction and the experimental results is related to the lack of corrections connected to the finite-range of the interaction potential.
Reference [213] evaluated the contribution of the finite-range potential, obtaining the relation

$$a_{\mathsf{o}} = a_d \left(1 - \frac{\mathsf{B}\ a_{ex}^2/\left(a_d^2 - a_d r_0\right)}{\mathsf{B} - \hbar/\left(a_d - r_0\right)\sqrt{m\delta_\mu/\mathsf{B}}} \right) = a_d \left(1 - \frac{\Delta \mathsf{B}_{\mathsf{r}_0}}{\mathsf{B} - \mathsf{B}_{\mathsf{r}_0}} \right). \qquad (5.2.13)$$

The position at which the scattering length diverges, obtained in equation 5.2.12 neglecting finite-range corrections, is modified by simply substituing a_d with $(a_d - r_0)$ (as it can be obtained[10] from equation 5.2.13) where $r_0 \simeq 84.8\ \mathsf{a}_0$ is the van der Waals length introduced by equation 2.1.21.
As shown in figure 5.2.3, the inclusion of finite-range corrections improves the agreement between the theoretical prediction and the experimental results. As also shown in figure 5.2.3, when the external magnetic field is almost absent (about 4.34 G if r_0 and $\Delta m = 5$ are considered) the open-channel scattering length a_{o} shows a peculiar change of concavity that, as far as we know, has never been experimentally observed and characterized. This feature is connected to the fact that $|+\rangle$ and $|\text{-}\rangle$ channels have different energies only when an external magnetic field B is applied.

---

[9] In [210] the fit used to estimate $\mathsf{B}_{\mathsf{Orb}}$ is employed also to determine $\Delta\mathsf{B} = (417 \pm 40)$ G. They also estimate this quantity by performing spectroscopy in a 3D lattice obtaining $\Delta\mathsf{B} = (327^{+86}_{-62})$ G that is a consistent with the first value reported.

[10] The C_6 value for the $|g\rangle - |g\rangle$ potential can be found in reference [217] and corresponds to (1932 ± 35) a.u. while for $|g\rangle - |e\rangle$ corresponds to $C_6 = 2561$ a.u., as it can be found in references [59, 210].

5.3 Production of orbital Feshbach molecules of fermionic ^{173}Yb

In section 5.1 we described symmetries and deeply characterized interactions in AEL atoms, and in particular in fermionic ^{173}Yb, also introducing the $\mathbb{SU}(\mathsf{N})$ transformation invariance and inter-orbital collisions.
In section 5.2 we introduced Feshbach resonances by exploiting a generic model in which two coupled scattering channels are defined.
Finally, we described the orbital Feshbach resonance in ^{173}Yb as a useful tool to control the interaction strength, in s-wave scattering, of interacting spin mixtures in different orbital states.
In the last part of section 5.2.2 we recalled concepts introduced in chapter 2, connecting the least-bound state energy supported by the interaction potential to change of the scattering length furnished by OrbFR.
In this section we describe a series of experiments in which we have demonstrated the possibility to excite a clock photoassociation transition coupling the $|(2)g\rangle|\uparrow,\downarrow\rangle$ state to the highly excited $|g;e\rangle|\uparrow,\downarrow\rangle$ molecular state.
In particular, by exploiting the model described in section 2.2.3 for the case of ^{173}Yb in which a_d, a_{ex} have the same order of magnitude, we characterize the experimentally observed photoassociation transition in a 3D cubic optical lattice operating at the magic wavelength.

The study of molecular systems gained significant momentum in the past decades principally because molecules extend the possibilities furnished by atomic systems, e.g. introducing new parameters range in which theoretical models can be tested by means of quantum simulation [218–221] and enabling the development of quantum chemistry [222] and few-body physics [223].
From a many-body perspective, interactions between molecules offer a richer physics than that of neutral atoms. For that reason great effort has been devoted to the realization of ultracold gases of polar (heteronuclear) molecules, eventually reaching the Fermi-degenerate regime [224].
As remarked in section 5.1 for the case of bosonic homo-nuclear ^{174}Yb atoms, the possibility to generate and control molecules with ultranarrow clock transitions may constitute an unexplored platform on which perform precision measurements could be performed [202].

So far, many theoretical proposals have been developed for polar heteronuclear and non-polar homonuclear molecules [218, 220, 225–228]. Major experimental efforts have been focused on the production of polar molecules starting from a cold mixture of two alkali-atoms [229, 230], where the presence of Feshbach resonances permits to finely adjust the interaction between atoms and associate them in weakly bound dimers with tunable binding energy [231].
This work, by following and enhancing the investigation started in reference [210], extends the study of shallow homonuclear molecules generated by ^{173}Yb atoms in which the molecule binding energy can be varied by exploiting the orbital Feshbach resonance (OrbFR) described in section 5.2.2.
The production of OrbFR molecules and the manipulation of their internal degree of freedom represents a first step in the path to the complete control of this new kind of molecules in order to obtain a reliable tool e.g. for the study of fermionic superfluidity and the BEC-BCS crossover in still-unexplored regimes [232, 233].
In the specific case of ^{173}Yb, the binding energy of photoassociated molecules is of only a few kilohertz.
This very small value allows the possibility of accessing the resonance regime even if the magnetic-field tuning is strongly suppressed by the purely nuclear character of the atomic spin (see section 3.2.3).
It is indeed because of the last property discussed above that the OrbFR exhibits the character of a narrow Feshbach resonance [42], while keeping a very broad tunability in terms of magnetic field accessibility.
This unusual feature could lead to the first experimental investigation of the BEC-BCS crossover close to a narrow Feshbach resonance, allowing us to overcome the strict magnetic-field stability requirements for ordinary Feshbach resonances in alkali gases [42].
The OrbFR is also characterized by an unusually small energy separation between the coupled scattering channels [234], lying in the same kilohertz range as the Fermi energy.
This property results in intriguing many-body physics. It was suggested that the resulting many-body superfluid state has to be described in terms of two coupled order parameters [213], opening the door to study the physics of two-gap superconductors, with the prediction of new collective excitations and the emergence of the long-sought massive Leggett mode [41, 43].

The next section will be devoted to the description of the experimental procedure employed to produce orbital "clock" molecules in a 3D optical lattice by means of clock photoassociation.

5.3.1 Molecules photoassociation in 3D optical lattice

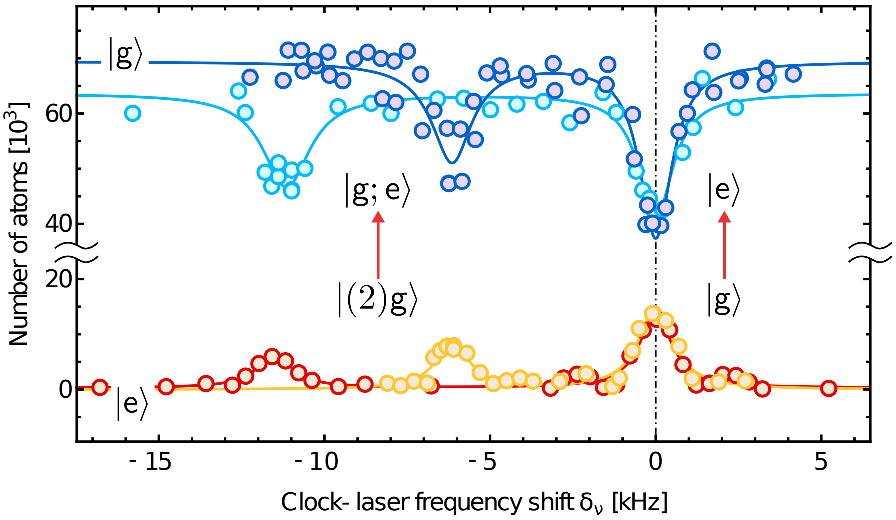

Figure 5.3.1. Clock spectra obtained by shining a π-polarized radiation on a $\Delta m = 5$ sample at 150 G and variable lattice depth $\mathsf{s}_{\mathsf{fin}}$. Yellow and blue points represent two acquisitions of the system loaded at $\mathsf{s}_{\mathsf{fin}} = 15$, obtained performing the imaging procedure on $|e\rangle$ and $|g\rangle$ atoms respectively. Red and light blue points represent a sample loaded at $\mathsf{s}_{\mathsf{fin}} = 30$. Solid lines are Lorentzian fits performed in order to determine the center of each observed resonance. It is possible to note that areas corresponding transitions observed in $|g\rangle$ atoms are bigger than areas corresponding to the same physical process observed in $|e\rangle$ atoms, showing the presence of a yet-undetermined inelastic loss channel.

In order to acquire clock spectra and reveal the presence of the molecular photoassociation peak supported by the orbital Feshbach resonance introduced in section 5.2.2, the experiment is performed by generating a $\mathbb{SU}(2)$ Fermi degenerate gas constituted by approximately 70×10^3 fermionic ^{173}Yb atoms, characterized by a temperature of $T = 0.25 \times T_{\mathsf{F}}$ and $\Delta m = 5$.
As described in section 3.4.3, the sample is obtained by performing evaporative cooling in a crossed trap (purple in the time sequence in the inset of figure 5.3.3) characterized by final trap frequencies $\omega_{\{x,y,z\}} = 2\pi \times \{93, 73, 86\}$ Hz. As specified in section 3.4.4, the requested spin mixture $m_{\mathsf{F}} = +5/2, -5/2$ is obtained by performing optical pumpings before the final evaporative cooling stage. As shown by the red solid line in the inset of figure 5.3.3, after the evaporative cooling stage, the 3D lattice intensity is increased with an exponential ramp in order to reach a confining potential characterized by $\mathsf{s}_{\mathsf{l}} = 15$. At this point, the FOR Trap is adiabatically turned off by performing a 1 s long linear ramp and lattices are sub-

sequently increased in 1 ms to the final depth $\mathsf{s_{fin}}$.
To perform Lamb-Dicke spectroscopy (described in section 4.1.1) the final lattice depth $\mathsf{s_{fin}}$ varies from 15 to 30 depending on the specific experiment.
This lattice loading procedure has been experimentally optimized to obtain the highest possible number of doubly occupied sites.
In order to produce orbital molecules we excite the $|g\rangle \rightarrow |e\rangle$ clock transition at a specific magnetic field B and final lattice depth $\mathsf{s_{fin}}$ by probing the atomic mixture in the Lamb-Dicke regime with pulses of 578 nm, π-polarized light produced by the source described in section 3.4.1.
While two-particle states of fermions with repulsive $g - e$ interactions have been investigated in references [210, 216] for ^{173}Yb, in reference [235] for ^{87}Sr and in reference [212] for ^{171}Yb, at our knowledge only a study regarding the photoassociation resonance position in an 3D optical lattice has been executed [210].
In this work we intend to extend the study of the molecular branch located at lower energies with respect to the single-particle $|g, \downarrow\rangle \rightarrow |e, \downarrow\rangle$ transition, and provide information on the lifetime of those states.
Figure 5.3.1 reports two clock spectra, corresponding to $\mathsf{s} = 30$ and $\mathsf{s} = 15$, obtained by measuring the number of atoms in the ground state (blue, light blue points) and in the excited state (red, yellow points) after the clock-laser pulse.
As described in section 4.3.2, in order to measure the number of excited-state atoms $|e\rangle$, as shown in the inset of figure 5.3.3, a 100 μs, 399 nm resonant pulse is performed after the atoms are released from the lattice to transfer momentum and heat only the $|g\rangle$ atoms. After this $|g\rangle$ blast pulse, the 1389 nm laser is turned on to pump the $|e\rangle$ atoms into the $|g\rangle$ state (after a population transfer to the ^{3}D$_1$ state) and usual imaging is performed. The repumping scheme is described in sections 3.4.1 and 4.3.2, and allow to measure about 90% of the excited population.
The excited detection efficiency is measured by evaluating the difference between the number of $|g\rangle$ atoms remained and the number of $|e\rangle$ atoms detected after a clock-laser π-pulse of a spin-polarized ^{173}Yb sample.

Each spectrum reported in figure 5.3.1 is characterized by two resonance peaks. We ascribed to the process $|g, \downarrow\rangle \rightarrow |e, \downarrow\rangle$ the transition reported at clock-laser frequency $\delta_\nu = 0$ where a single $|g, \downarrow\rangle$ atom in a lattice site is promoted to the excited state $|e, \downarrow\rangle$ as a result of the interaction with the clock-laser. This attribution is justified by the result of a spectroscopy performed on a spin polarized $|g, \downarrow\rangle$ ^{173}Yb sample. The other peak can be observed only if clock spectroscopy is performed on a sample constituted by a spin mixture ($m_\mathsf{F} = +5/2, -5/2$). The position of this resonance, that is red shifted with respect to the single-particle excitation, has been attributed to the process $|g\downarrow, g\uparrow\rangle \rightarrow |g\uparrow; e\downarrow\rangle$ where a doubly-occupied lattice site is excited to a molecular states by means of a photoassociation process.

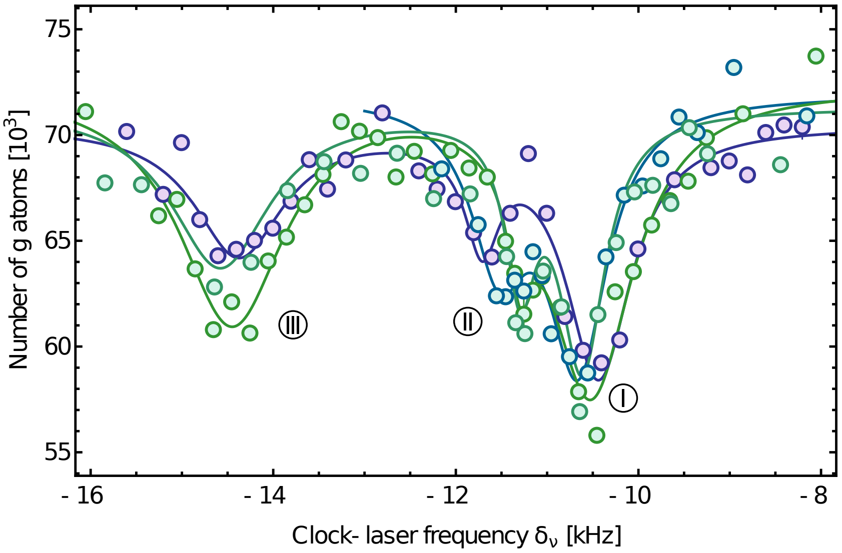

Figure 5.3.2. Clock spectroscopy on ^{173}Yb samples confined in a deep 3D optical lattice ($s_{\text{fin}} = 30$) and a magnetic field of 150 G. The spectra report the number of $|g\rangle$ atoms remained after an excitation pulse of 100 ms with 50 μW of clock light focused on a waist of about 300 μm. As clearly shown, narrow spectroscopy unveils three peaks that in previous spectroscopies were hidden by the power broadening.

This attribution is justified by the good agreement of the photoassociation resonance position as a function of the magnetic field B and the lattice depth s with respect to the theoretical model (described in section 2.2.3) as we will discuss in the following part.

As it can be noted in figure 5.3.1, the decrease of the $|g\rangle$ atoms is larger than the number of observed excited atoms, especially for the photoassociation resonances. This effect can be attributed to the presence of a yet-undetermined loss channel that, due to the power broadening, is excited when the clock-laser is resonant with respect to the photoassociation transition.

Figure 5.3.2 shows a narrow-line spectroscopy performed by shining clock laser light on a sample constituted by 70×10^3 fermionic atoms of ^{173}Yb. As it can be clearly observed, by reducing the power broadening caused by the clock intensity, three transitions are unveiled. We ascribed the peak marked as III in figure 5.3.2 as the first red-sideband transition, because the measured shift with respect to the single-particle transition $|g\rangle \rightarrow |e\rangle$ is consistent to the expected first red sideband for $s_{\text{fin}} = 30$ (see section 4.1.1).

Peaks I and II have been ascribed to the molecule photoassociation resonance (I) and to a fast inelastic process (II), respectively. We identified the latter as the resonance that induces a decay in the repumped $|e\rangle$ population. In the next section, in which we evaluate the possibility to coherently address the photoassociation

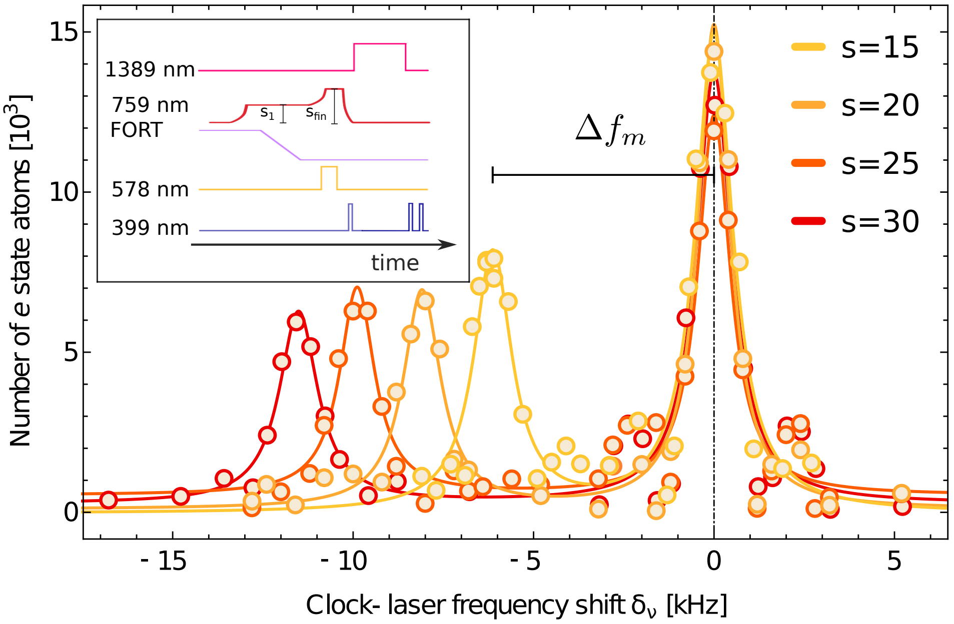

Figure 5.3.3. Clock spectroscopy (at 578 nm) of a $\Delta m = 5$ ^{173}Yb sample in a 3D optical lattice operating at the magic wavelength $\lambda_L = 759.4$ nm for different values of lattice depth and 150 G. In order to show the shift with respect to the $|g\downarrow\rangle \rightarrow |e\downarrow\rangle$ transition all the acquired spectra have been shifted to set the single-particle resonance as the origin of the axis. In the inset a sketch of the experimental procedure employed to perform an acquisition is reported.

transition, we further motivate the nature of the II transition.

In section 5.2.2 and we introduced the dependence of the least bound state energy on the applied external magnetic field B.
In sections 2.2.2 and 2.2.3, we evaluated the effect of an external harmonic potential on a system characterized by two scattering channels in order to quantify the contribution caused by the confinement induced by a deep lattice (that can be approximated at the first order with a harmonic potential) to the energy of the least bound state supported by the orbital Feshbach resonance.

Figure 5.3.3 reports a series of typical clock spectra performed on a $\mathbb{SU}(2)$ sample characterized by $\Delta m = 5$ at B = 150 G for different depths of the 3D lattice, obtained by measuring the number of atoms in the excited state $|e\rangle$ after the clock-laser pulse. In all the spectra collected, the frequency shift is measured with respect to the single-particle transition $|g\downarrow\rangle \rightarrow |e\downarrow\rangle$ for individual atoms. As described in section 3.2.3, the transition chosen as the origin of the frequency axis depends only on the applied magnetic field, and not on the lattice depth, and

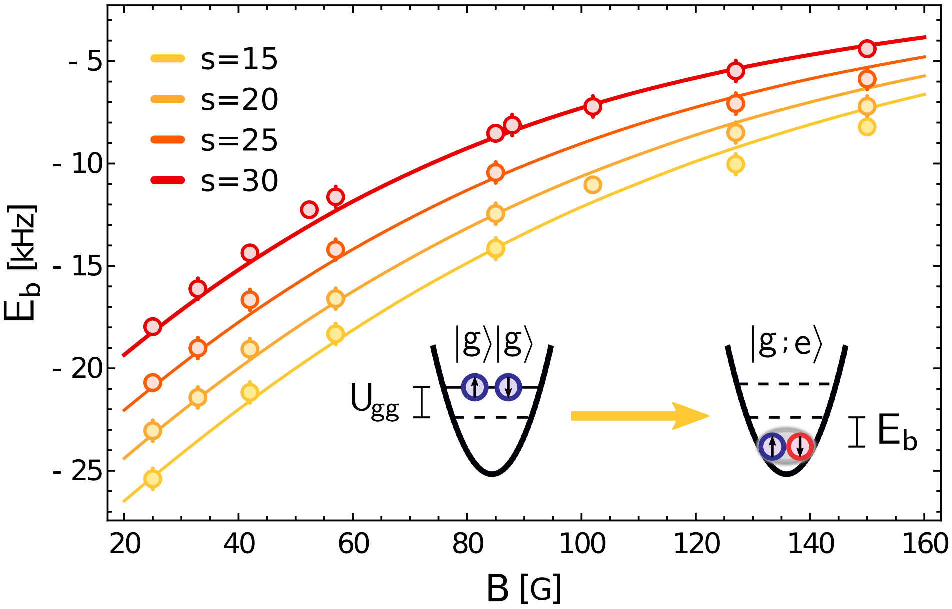

Figure 5.3.4. Values of the molecular binding energy as a function of the magnetic field for different lattice depths. In order to maintain the Lamb-Dicke regime $\mathsf{s_{fin}}$ varies from 15 to 30 for each magnetic field explored. Solid lines represent a global fit that takes into account the Busch model for two scattering channels described in section 2.2.3, anharmonic corrections due to the finite depth of the lattice, and the dependence on the magnetic field due to the orbital Feshbach resonance. The best fitted value $a_+ = (1894 \pm 18)\,\mathsf{a}_0$ is consistent with a previously reported value [210], as shown in figure 5.2.3.

corresponds to the total energy of a pair of non interacting $|g,\uparrow\rangle|e,\downarrow\rangle$ atoms, that is the threshold energy of the orbital Feshbach resonance.

By measuring the (negative) frequency shift Δf_m between the photoassociation transition and the single-particle excitation, the molecular binding energy can be determined as

$$\mathsf{E_b} = h\Delta f_m - \mathsf{U}_{gg} \tag{5.3.1}$$

where U_{gg}, corresponding to the initial (repulsive) energy of a pair of g atoms in the same lattice site, has been introduced in section 2.3 and examined in detail for ^{173}Yb in section 5.1.1. A graphical representation of the photoassociation process has been sketched in the inset of figure 5.3.4. Following this approach, we measured the binding energy of a $|\mathsf{o}\rangle \equiv |g,\uparrow;e,\downarrow\rangle$ molecule as a function of the magnetic field B for several lattice depths ranging from $\mathsf{s_{fin}} = 15$ to $\mathsf{s_{fin}} = 30$.

The results of these measurements are reported in figure 5.3.4. As it can be noted, the bound-state transition can be detected when the modulus of the external magnetic field exceeds the free-space orbital Feshabach resonance (located at around

40 G, as shown in figure 5.2.3 [210, 216]) due to the lattice confinement potential.

The model developed in section 2.2.3 has been employed to perform a global fit of all the datasets, leaving the scattering length a_{eg}^{+} related to the spin-singlet colliding channel as the only free-parameter. To perform the fit anharmonic corrections have been taken into account diagonalizing the full Hamiltonian of the problem considering the coupling between the relative and the center-of-mass motion up to the fourth lattice band. The estimated scattering length corresponds to

$$a_{eg}^{+} = (1894 \pm 18)\ \mathsf{a}_0.$$

The knowledge of a_{eg}^{+} allows us to evaluate the effective range r_{eff}^{+} by employing equation 2.1.28. The estimated effective range value $r_{\mathsf{eff}}^{+} \sim 218\ \mathsf{a}_0$ results consistent with respect to a previously reported value [210].

5.3.2 Coherent control of photoassociation transition

In a subsequent experiment we demonstrated the capability to drive a coherent molecule photoassociation process as previously obtained e.g. in reference [236] for molecules supported by a Feshbach resonance in ^{40}K, in reference [237] by employing bosonic ^{88}Sr and in reference [238] by exploiting the photoassociation transition of $|g;^{3}\mathsf{P}_2\rangle$ molecules in ^{171}Yb.
In this experiment the laser frequency is kept constant on the photoassociation transition[11] and the atomic sample confined in the 3D optical lattice is probed by increasing the pulse time duration of the excitation laser.

Figure 5.3.5 reports a typical oscillation at an external magnetic field $\mathsf{B} = 150$ G and a 3D lattice depth $\mathsf{s_{fin}} = 30$ between pairs of interacting $|g\uparrow\rangle|g\downarrow\rangle$ atoms and orbital bound states $|g;e\rangle$ in doubly occupied lattice sites, obtained by detecting the number of $|e\rangle$-state atoms with the same technique described in section 4.3.2 and employed in the previous section. Reported points are the experimental data and the solid line is the result of a fit to the data with a damped sinusoidal function.
Several cycles of photo-association and dissociation can be observed with a decay time constant of $\tau_{|e\rangle} = (7.5 \pm 1.6)$ ms. The ratio between the frequency $\Omega/2\pi$ of this oscillation and its single-particle counterpart $\Omega_0/2\pi$, driven with

---

[11] As specified in section 3.4.1, in order to overcome the long-term drift of the cavity at which the laser frequency is stabilized it is necessary to check the photoassociation frequency about once in a hour.

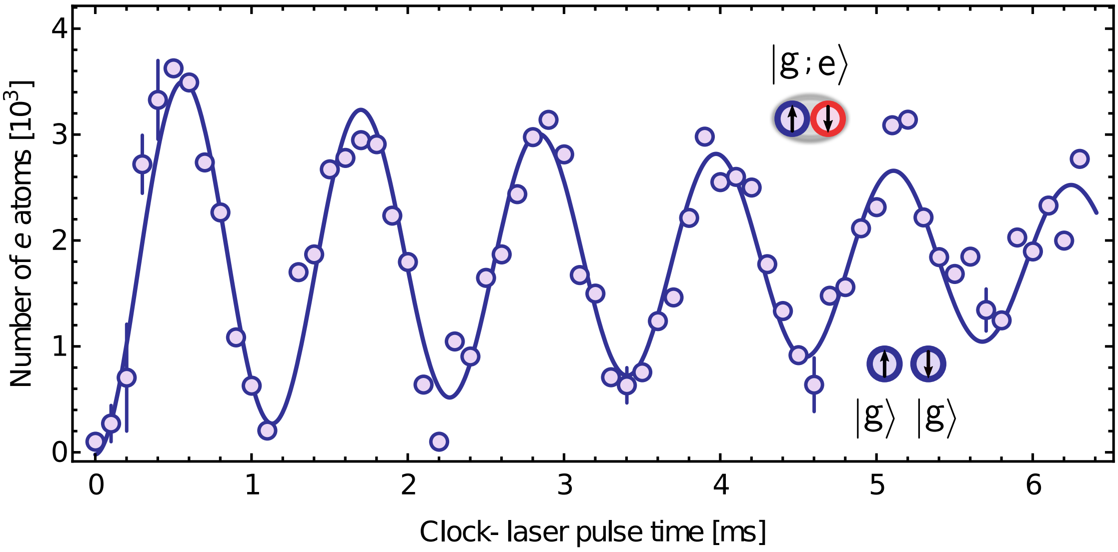

Figure 5.3.5. Rabi oscillation on a $|g\rangle - |e\rangle$ photoassociation transition performed at a magnetic field of $\mathsf{B} = 150$ G and final lattice depth $\mathsf{s_{fin}} = 30$. The sample is probed by shining 1.0 mW of clock light on a beam waist $w_0 \simeq 300$ μm.

the same clock-laser intensity, is a direct measurement of the Franck-Condon factor between the single-particle wavefunctions Ψ_{gg} and the molecule wavefunction Ψ_{ge}^{mol}, defined as $\mathcal{FC} = \int \Psi_{gg}(\vec{\mathsf{r}}_1, \vec{\mathsf{r}}_2)\, \Psi_{ge}^{\mathsf{mol}*}(\vec{\mathsf{r}}_1, \vec{\mathsf{r}}_2)\, \mathrm{d}\vec{\mathsf{r}}_1 \mathrm{d}\vec{\mathsf{r}}_2$, which results to be $\mathcal{FC} = \Omega/\Omega_0 = (0.81 \pm 0.06)$ at this magnetic field value ($\mathsf{B} = 150$ G) [238].

As mentioned in section 5.3.1, and shown in figure 5.3.2, the photoassociation peak hides a near resonance that we ascribed to a fast inelastic process that can not be properly characterized by only means of spectroscopy. All the measurements reported in this section have been realized by shining at least 1 mW of clock radiation on atoms (on a beam characterized by a waist of about 300 μm). Thus, in each case reported below, due to the power broadening, transitions I and II shown in figure 5.3.2 are excited simultaneously, causing the loss dynamics observed on $|g\rangle$ state atoms and reported in figure 5.3.6a).

As it can be easily noted in figure 5.3.6, the number of missing $|g\rangle$ state atoms after the first π-pulse does not correspond to the number of detected $|e\rangle$ state atoms. We have ascribed this discrepancy to the presence of an inelastic scattering channel that dominates the collision dynamics when the sample is released from the lattice. We decided not to further investigate this feature, because the experimental study of this process would have required a selective excitation of the transitions (indicated as I and II) shown in figure 5.3.2.

This measurement would have needed the frequency stabilization of the clock laser by employing the 642 km long fiber-link described in references [113, 135] that, at

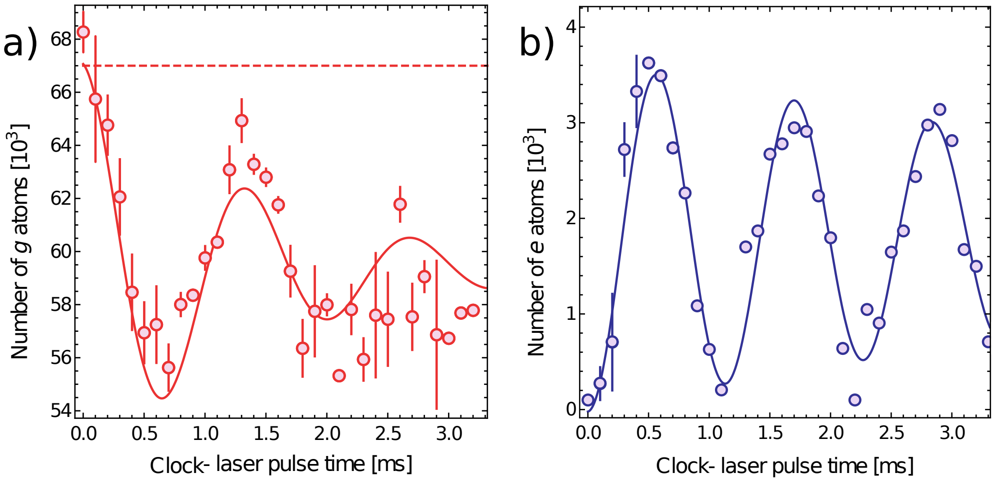

Figure 5.3.6. Rabi oscillation on a $|g\rangle$-$|e\rangle$ photoassociation resonance performed by applying an external magnetic field $\mathsf{B} = 150$ G and a 3D lattice depth $\mathsf{s_{fin}} = 30$. Panel a) shows the number of atoms left in the $|g\rangle$ state, while panel b) shows the number of atoms in the $|e\rangle$ state for the same excitation parameters. Solid curves in panels a),b) are damped sinusoidal functions characterized by very different decay times but same frequency $\nu = (0.77 \pm 0.03)$ kHz. In particular, the decay time and consequent loss of coherence observed in $|g\rangle$ state atoms is characterized by a timescale of $\tau_{|g\rangle} = (1.4 \pm 0.4)$ ms, while the decoherence observed in $|e\rangle$ state atoms has a decay time of about 8 ms.

the time of this work, was not available for technical upgrades.
The presence of an inelastic scattering channel can cause a strong decrease in the number of molecules that can be obtained in this kind of systems. Future experiments, devoted to the study of the many-body properties of a molecular (possibly degenerate) gas, must take into account the presence of inelastic channels that limit the efficiency of the photoassociation process.

Nevertheless, the possibility to coherently excite pairs of interacting ground-state atoms in an isolated lattice site [12] to a bound state $|g;e\rangle$ is a remarkable feature that, in our experiment, is fundamental to maximize the number of orbital Feshbach molecules in the sample.
As highlighted in the aforementioned sections, the possibility to associate shallow bound molecules is interesting for the implementation of new experimental protocols involving the coherent manipulation of two-particle states, but the incomplete characterization of the photoassociation transition does not allow to maximize the molecules production process .

---

[12] The tunneling time t for $\mathsf{s_{fin}} = 30$ corresponds to about 1 s that is much longer than the timescale of the experimental procedure

So far we have focused on the orbital degree of freedom that characterizes the fermionic ^{173}Yb atoms and we have experimentally explored the possibilities offered by the orbital Feshbach resonance described in section 5.2.2.

The next section will be devoted to the description of spin-manipulation experiments in which the nuclear-spin projection of the atoms constituting the molecule is modified via Raman two-photon transitions.

5.4 Spin manipulation of orbital molecules in 3D optical lattice

In order to detect the shallow molecules generated by photoassociation processes, many techniques have been developed in last decades [239], exploiting for example the different mass of the bound molecule with respect to the single atom [230] or the possibility to generate deeply-bound ground-state molecules [240–242], that can be directly observed by selectively heating up isolated atoms.
Shallow bound molecules can also be produced by performing a adiabatic magnetic sweep through the Feshbach resonance [240, 243–245]. A well-known procedure employed to generate and observe Feshbach molecules sample produced in such a way is the so-called "purification". A possible purification strategy exploits the difference in magnetic moments of molecules and atoms. In particular, the two components of the gas can be spatially separated with the Stern-Gerlach technique that employ magnetic gradients [243, 245, 246]. An alternative fast and efficient technique, in order to obtain a sample constituted by Feshbach molecules, uses light resonant with an atomic closed transition to perform a "blast" that does not acts on molecules [247–249].
In our case these techniques are not suitable because the photoassociated molecules binding energy ($\simeq 10$ kHz) is lower than the imaging transition ($^1\mathsf{S}_0 \rightarrow {}^1\mathsf{P}_1$) natural linewidth ($\simeq 30$ MHz - see table 3.2.1).
The molecular binding energy results also lower than the intercombination transition ($^1\mathsf{S}_0 \rightarrow {}^3\mathsf{P}_1$) natural linewidth ($\simeq 180$ kHz - see table 3.2.1). For that reason we developed a molecules detection method that exploits bound-to-bound transitions via a two-photon Raman processes [250]. We show also that this process can be driven coherently, allowing us to cycle between molecular states with different ground-state components.

In section 3.3 we introduced the possibility to perform transitions between different stable nuclear-spin states via a two-photon process. In this section we show the possibility to use that technique for the coherent manipulation of the shallow-bound molecules supported by the orbital Feshbach resonance (described in section 5.2.2).
As discussed in section 5.3.1, we prepare a ^{173}Yb degenerate gas constituted by a $\mathbb{SU}(2)$ mixture characterized by $\Delta m = 5$ (necessarily composed by $|m_\mathsf{F} = \pm 5/2\rangle$

atoms).
The degenerate gas is loaded in a 3D optical lattice operating at the magic wavelength for the clock transition $|g\rangle \rightarrow |e\rangle$. As described in section 5.3.1, the loading into the lattice is performed by increasing the beams intensity in two steps, in order to experimentally increase the number of doubly-occupied sites.
By exploiting the coherent coupling demonstrated in section 5.3.2 between interacting pairs of fermions $|g\rangle|g\rangle$ and shallow molecules $|g;e\rangle$, a π-pulse excitation can be performed on confined atoms in order to generate the highest number available of shallow-bound molecules.
As shown in figure 5.3.2, the presence of an undetermined resonance at lower frequencies with respect to the photoassociation transition, limits the effectiveness of the generation process, reducing also the amount of photoassociated molecules that is possible to obtain in our experimental system. In order to optimize the number of photoassociated molecules further studies on the presence of inelastic scattering channels are required.
After the π pulse, the sample is constituted by a 3D array of $|g, m_\mathsf{F} = +5/2; e, m_\mathsf{F} = -5/2\rangle$ molecules and individual atoms in $|m_\mathsf{F} = \pm 5/2\rangle$ states.
We performed Raman spectroscopy with a pair of copropagating ($\vec{\mathsf{q}} \simeq 0$) Raman beams with frequencies ν and $\nu + \Delta\nu$ detuned by 1756 MHz with respect to the intercombination transition. As specified in section 3.3, the shift with respect to the atomic transition is chosen in order to maximize the ratio between the obtainable Rabi frequency and the heating due to light scattering.
The polarization of the two copropagating laser beams at 556 nm employed to perform Raman transitions is orthogonal to the quantization axis of the system, resulting in a balanced sum of $\sigma^\pm$ polarizations. This choice, as specified in section 3.3, implies the possibility to perform only transitions $|m_\mathsf{F} = \pm 5/2\rangle \rightarrow |m_\mathsf{F} = \pm 1/2\rangle$.
A typical spectrum on a $\mathbb{SU}(2)$, $\Delta m = 5$ sample, in the absence of photoassociation and for an external magnetic field of 50 G and a 3D lattice depth $\mathsf{s_{fin}} = 30$, is shown in figure 5.4.1 as a function of the frequency difference $\Delta\nu$ between Raman beams. In order to perform a zero-background measurement, states $|m_\mathsf{F} = \pm 5/2\rangle$ are selectively blasted with pulses resonant with the magnetically-sensitive $|^1\mathsf{S}_0(m_\mathsf{F} = 5/2)\rangle \rightarrow |^3\mathsf{P}_1(m_\mathsf{F} = 7/2)\rangle$ transition during the time of flight. As a result, only atoms having flipped their spin to other nuclear-spin states as a consequence of the Raman process are detected.
As we will see in the next section, this detection is affected by a small background of a few hundreds of atoms that can be attributed to an imperfection of the optical pumping preparation procedure.

As it can be noted in figure 5.4.1, the $\mathbb{SU}(2)$ sample on which Raman spectroscopy is performed shows three well dishinguishable peaks that are located in

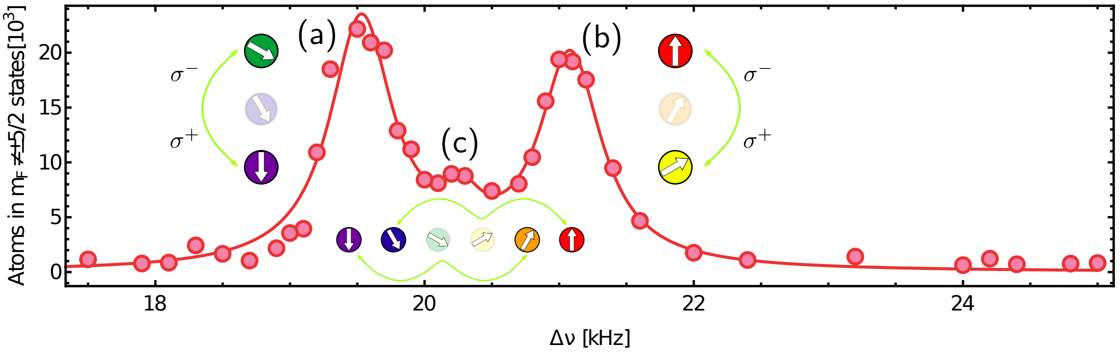

Figure 5.4.1. Raman spectroscopy of a $\Delta m = 5$ ($m_\mathsf{F} = \pm 5/2$) sample for an external applied magnetic field $\mathsf{B} = 150$ G and final lattice depth $\mathsf{s_{fin}} = 30$. As it can be observed, the peak corresponding to the $|{+5/2}\rangle \rightarrow |{+1/2}\rangle$ transition (b) has nearly the same height of the peak connected to the $|-5/2\rangle \rightarrow |-1/2\rangle$ transition (a). The small difference in the height of the two resonance peaks can be ascribed to an imperfect population balance between ±5/2 atoms in the initial sample. The central, weaker peak (c) is related to the two "four photon" transitions, shown in the lower part of the picture, in which ±5/2 atoms are transferred to ∓3/2 states [112, 145].

the two-photon detuning interval $\Delta\nu$ between 18 and 22 kHz. We ascribed the peak at the lowest two-photon detuning (a) to the $|-5/2\rangle \rightarrow |-1/2\rangle$ transition. For this attribution we have employed the OSG technique described in section 3.4.4, which allows the direct detection of the nuclear-spin population changes induced by the Raman excitation. Similarly, the peak at the highest two-photon detuning $\Delta\nu$ (b) has been ascribed to the $|+5/2\rangle \rightarrow |+1/2\rangle$ transition. The distance between the two specified peaks is attributed to the presence of a state-dependent light shift caused by the incident radiation; this contribution is included in the $\mathcal{U}_{m_\mathsf{F}}$ term of equation 3.3.5 of the simplified model introduced in section 3.3.
The third resonance observed (c), that is constituted by two indistinguishable peaks, represents the so-called "four photon" transition that connects states, if $\sigma^\pm$ radiation is considered, whose nuclear-spin projections differ by $\Delta m_\mathsf{F} = m_{\mathsf{F}'} - m_\mathsf{F} = 4$. The possible four-photon transitions starting from a ±5/2 mixture are sketched in the lower part of figure 5.4.1.

The Raman spectroscopy has been acquired also on a $\mathbb{SU}(2)$, $\Delta m = 5$ sample on which a clock photoassociation π pulse has been previously shone in order to generate, in the 3D optical lattice, the highest number of orbital molecules achievable; the resulting spectrum is reported in figure 5.4.2 for a magnetic field $\mathsf{B} = 88$ G.

The spectrum shows four peaks. As it happens in figure 5.4.1, near the Raman resonance condition, that is determined, excluding the differential light shift

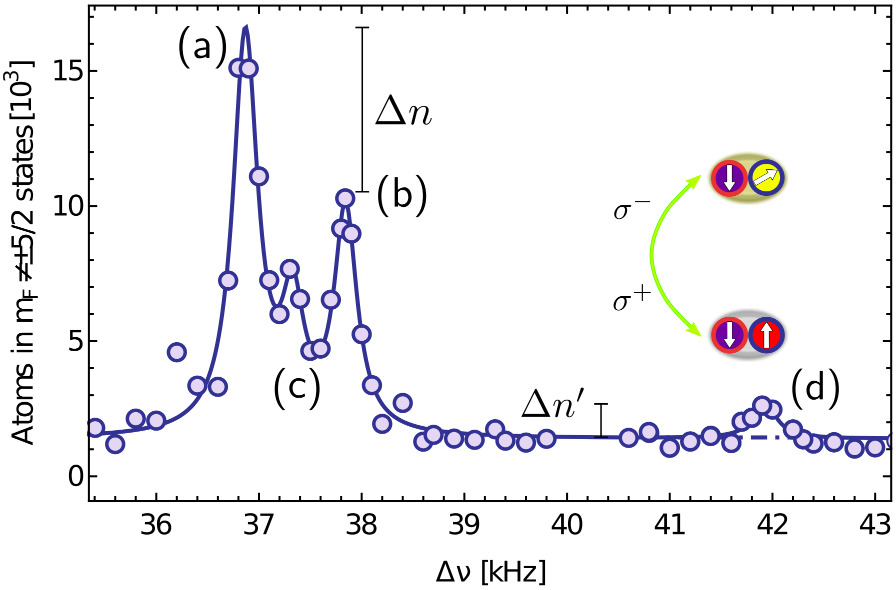

Figure 5.4.2. Raman spectroscopy of a sample containing individual atoms with $m_\mathsf{F} = \pm5/2$ and orbital molecules at $\mathsf{B} = 88$ G and lattice depth $\mathsf{s}_\mathsf{fin} = 15$. The peaks in the interval $36 \div 39$ kHz correspond to spin flips of individual atoms while the small peak near 42 kHz corresponds to a bound-to-bound transition between orbital molecules constituted by atoms in different spin states. Nuclear spins and orbital degree of freedom have been represented by following the colour scheme introduced in figure 3.2.2.

$\mathcal{U}_{m_\mathsf{F}}$, by the condition $\Delta\nu = \Delta m \mathsf{B}\,[\mathsf{G}] \times 207.4\ \left[\frac{\mathsf{Hz}}{\mathsf{G}}\right]$ (as previously sketched in figure 3.3.1), the individual peaks (a), (b), (c) corresponding to the aforementioned single-particle Raman transitions are present. In particular, in this case, the peak height corresponding to the $|5/2\rangle \rightarrow |1/2\rangle$ transition (b), also starting from the same balanced mixture of $|\pm5/2\rangle$ atoms, is significantly lower than the peak height corresponding to the $|-5/2\rangle \rightarrow |-1/2\rangle$ transition (a). This difference is due to the 578 nm π pulse that, by exciting atoms from doubly-occupied lattice sites into molecules, decreases the number of $|g, m_\mathsf{F} = 5/2\rangle$ atoms in the system.
In addition, we identified the peak located at a two-photon detuning of about 42 kHz (d) as a bound-to-bound transition between Feshbach molecules that differ for the total molecular spin projection, as explained below. Figure 5.4.2 shows that the number of $|g, m_\mathsf{F} = 5/2\rangle$ atoms excited by the photoassociation π pulse (and consequently of doubly-occupied sites in the lattice) is $\Delta n \approx 7{\times}10^3$, while only $\Delta n' \simeq 4{\times}10^3$ can be detected by Raman spectroscopy in the molecular peak (d). As also discussed in section 5.3.1, we ascribed the difference between Δn and $\Delta n'$ to the excitation of the transition marked as II that is reported in figure 5.3.2.

Let us now discuss the origin of the molecular peak (d) with more detail. The

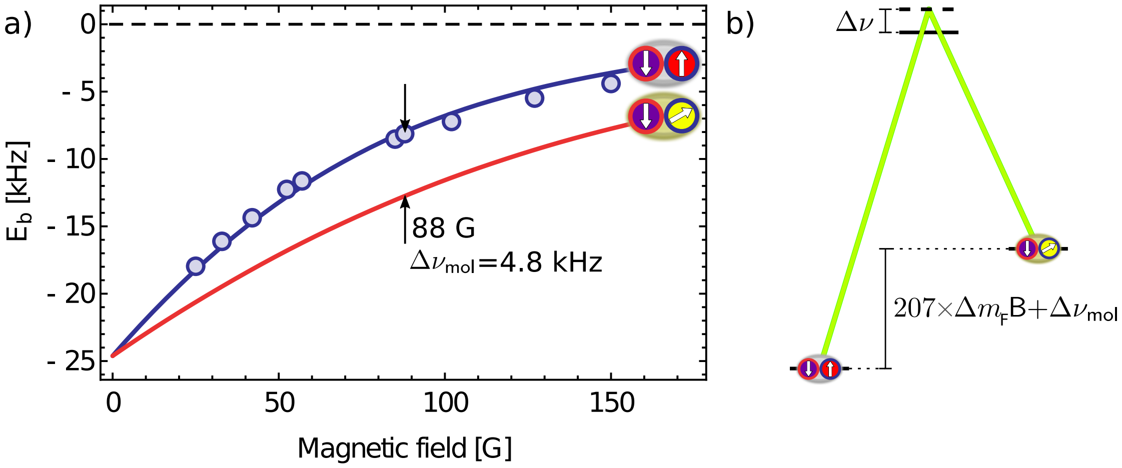

Figure 5.4.3. The points in panel a) show the experimental binding energies measured with photoassociation clock spectroscopy for $s_{\mathrm{fin}} = 15$ and $\Delta m = 5$, as already shown in figure 5.4.2. The blue solid line in panel a) is the fitted model used to determine the molecule binding-energy dependence as a function of the magnetic field. The red solid line represents the binding energy of molecules with $\Delta m = 3$, as derived from the scaling law discussed in the main text. As it is shown, at 88 G the frequency shift between the two binding energies corresponds to $\Delta\nu_{\mathrm{mol}} = 4.8$ kHz. Panel b) shows the Raman transition, sketched as Λ process, between two bound states. The resonance occurs when $\Delta\nu = [207.4\times\Delta m_F \mathrm{B} + \Delta\nu_{\mathrm{mol}}]\big|_{\mathrm{B}=88\ \mathrm{G}} \simeq 41.3$ kHz, that is consistent with the two-photon shift $\Delta\nu$ measured experimentally and reported in figure 5.4.2.

Raman transition, acting as a spin-flip operator on the ground-state costituent of the photoassociated orbital molecule, can occur only when the two-photon frequency shift $\Delta\nu$ corresponds to the Zeeman shift (described in section 3.2.3) plus the difference between the binding energy of a $|g, 5/2; e, -5/2\rangle$ molecule and that of a $|g, 1/2; e, -5/2\rangle$ molecule.

In general, the binding energies of Feshbach molecules obtained from different spin mixtures is not simply evaluable, because each mixture is characterized by different interactions. However, as explored in section 5.1.1, if orbital molecules of AEL atoms are considered, due to the symmetries of the $\mathrm{J} = 0$ states, the interaction properties of mixtures characterized by different Δm follow a magnetic-field scaling law depending only on the product $\Delta m\times \mathrm{B}$ as experimentally demonstrated in [210, 216].

For that reason, the model developed to describe bound state energies as a function of the magnetic field and the lattice confinement for a $\Delta m = 5$ molecule (presented in section 5.3.1 and theoretically introduced in section 2.2.3), can be easily adapted to describe the binding energy of an orbital molecule characterized

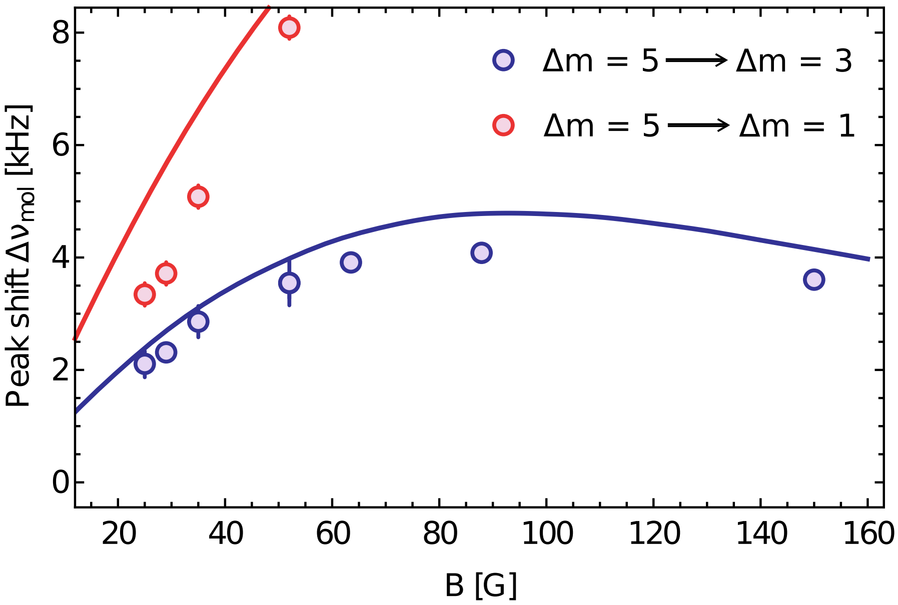

Figure 5.4.4. Shift of the bound-to-bound transition peak measured as a function of the external magnetic field B at fixed lattice confinement $s_{\mathrm{fin}} = 15$. The **blue point** are the measured peak shifts with respect to the single-particle $|+5/2\rangle \rightarrow |+1/2\rangle$ while the **blue solid line** represents the binding energy difference between the $\Delta m = 5$ and the $\Delta m = 3$ molecular states calculated from our model. By performing Raman spectroscopy at low magnetic field a narrow peak at higher frequencies can also be detected. We ascribed this resonance to the four-photon transition from a molecular state characterized by $\Delta m = 5$ to a molecular state in which $\Delta m = 1$. **Red points** are the measured peak shift for the latter process with respect to the single particle $|+5/2\rangle \rightarrow |+1/2\rangle$ transition, while the **red solid line** is the calculated binding energy difference between $\Delta m = 5$ and $\Delta m = 1$ molecules. While the agreement between blue measured value and theory is very good, red points are affected by a systematic error due to the uncertainty of the single-particle resonance position (as shown in 5.4.1).

by $\Delta m' = 3$. The binding energies for mixtures characterized by $\Delta m = 5$ and $\Delta m' = 3$ are sketched in figure 5.4.3.
In order to corroborate our hypothesis on the nature of the peak (d) observed near 42 kHz in figure 5.4.3, we realized two independent experiments:

- in the first one, we repeated the Raman spectroscopy characterizing the shift $\Delta\nu_{\mathrm{mol}}$ as a function of the magnetic field at a fixed lattice confinement;
- in the second, we photodissociate molecules before and after the Raman excitation pulse in order to experimentally evaluate the binding energy of each molecule produced.

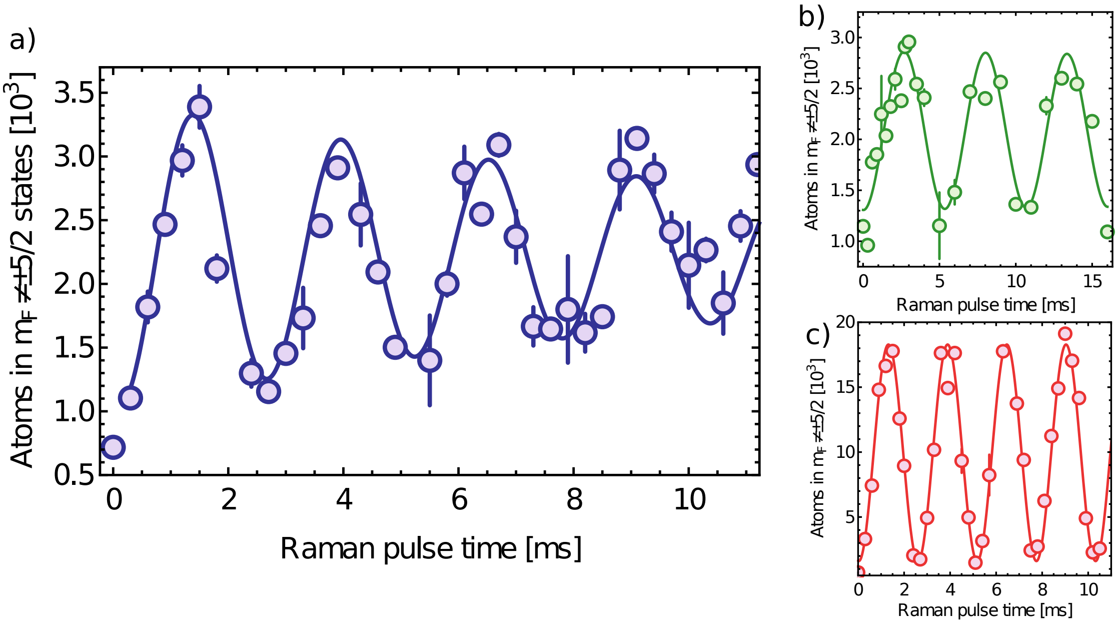

Figure 5.4.5. a): Rabi oscillations on the bound-to-bound Raman transition peak performed at B = 150 G and a final lattice confinement $s_{\mathrm{fin}} = 30$. The Raman light coherently flips the ground-state nuclear-spin component of the molecules between $m_F = 5/2$ and $m_F = 1/2$, showing a frequency of (390 ± 3) Hz and a decay time constant of about $\tau_{a)} = (13 \pm 3)$ ms. b): Rabi oscillation measured for the same bound-to-bound Raman excitation after a decrease of the magnetic field from B = 150 G (used for photoassociation) to B = 50 G, the Rabi oscillation is performed observing a considerably lower frequency with respect to the oscillation shown in panel a) because of the reduced atom-molecule Franck-Condon factor. c) Rabi oscillation on the single particle Raman transition $|g, +5/2\rangle \rightarrow |g, +1/2\rangle$ performed at B = 150 G and final lattice confinement $s_{\mathrm{fin}} = 30$. As it can be noted, the Rabi oscillation frequency (390 ± 1.9) Hz is consistent with the oscillation frequency obtained for the Rabi bound-to-bound oscillation shown in panel a).

In the first experiment we measured the shift of the bound-to-bound Raman transition peak as a function of the magnetic field at a fixed final lattice depth $s_{\mathrm{fin}} = 15$. The results of these measurements are reported by the blue points in figure 5.4.4. Experimental data are compared to the theoretical prediction of the binding energy difference between molecules with $\Delta m = 5$ and $\Delta m = 3$ calculated from the model described in section 2.2.3. As it can be noted, there is a good agreement between the data and the theory (blue points and line in figure 5.4.4), with some slight deviation at higher magnetic-field values.

Similarly to what we observed for the photoassociation process with the clock

laser, also the bound-to-bound Raman transition can be driven coherently, as shown in figure 5.4.5a), where we report a Rabi oscillation performed at a field of B = 150 G and a 3D lattice depth $s_{\mathrm{fin}} = 30$, with Rabi frequency (390 ± 3) Hz and a decay time constant of $\tau_{\mathrm{a)}} = (13 \pm 3)$ ms. Also in this case it should be noted that the oscillation frequency is compatible with that of its single-particle counterpart ($|+5/2\rangle \rightarrow |+1/2\rangle$), shown in figure 5.4.5 c), demonstrating a Franck-Condon factor which approaches unity.
In panel b) of the same figure we also show a measurement at lower magnetic field B = 50 G, evidencing a lower Rabi frequency, corresponding to a smaller Franck-Condon factor (caused by the tighter molecule binding). The possibility to coherently address the bound-to-bound transition shown in figure 5.4.2 has been exploited to perform a "triple-pulse" experiment (the second measurement aforementioned), in which we combine clock-laser photoassociation/dissociation and Raman manipulation with the scope to verify the nature of the observed bound-to-bound peak and the capability to manipulate the orbital and the nuclear-spin degrees of freedom.

In this second experiment, we generate a $\mathbb{SU}(2)$ sample characterized by $\Delta m = 5$ and constituted by about $70{\times}10^3$ atoms. As specified in section 5.3.1, this gas is loaded in a deep 3D optical lattice in such a way to maximize the number of doubly-occupied sites.
A clock-laser π pulse resonant with the photoassociation transition is performed, producing a sample in which the doubly occupied lattice sites are excited to generate about $6{\times}10^3$ $|g, +5/2; e, -5/2\rangle$ orbital molecules.
We then perform a Raman π pulse at the bound-to-bound transition frequency in order to convert photoassociated molecules into $|g, +1/2; e, -5/2\rangle$ molecules. Finally, a second clock laser π pulse is shone onto the atoms. The frequency of the second 578 nm laser pulse is scanned in order to perform photodissociation spectroscopy.
The results of this experiment for B = 150 G and final lattice depth $s_{\mathrm{fin}} = 30$ are reported in figure 5.4.6. In this case the observable is the number of $|e\rangle$ atoms remaining after the photodissociation-laser pulse. Depending on the frequency of the clock laser during the second π-pulse, different outcomes are possible. Let us first discuss the red points in figure 5.4.6 (the red solid line being a fit with Lorentzian functions to guide the eye) If the second clock-laser π pulse is not resonant with any possible transition (a) the number of $|e\rangle$ atoms corresponds simply to the number of photoassociated molecules (it corresponds to about $6{\times}10^3$ atoms, as it can be observed in the red points of figure 5.4.6).
If the second clock pulse is resonant with the single-particle transition (b) $|g, -5/2\rangle \rightarrow |e, -5/2\rangle$ we detect an increase of $|e\rangle$-state atoms as a consequence of

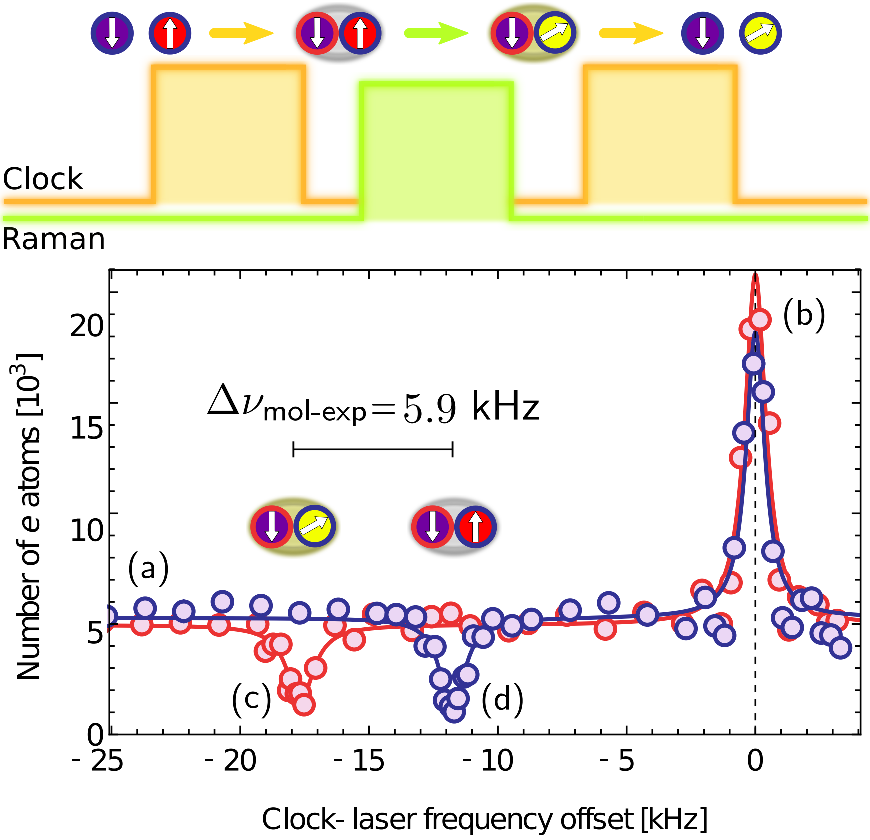

Figure 5.4.6. Clock-laser spectroscopy of a sample with individual atoms and orbital molecules produced with a preliminary photoassociation clock-laser π pulse. The excitation of individual atoms (b) is detected as an increase in the number of $|e\rangle$ state atoms with respect to the background (a) and serves as a zero-frequency reference. The dissociation of orbital molecules is instead detected as a decrease of $|e\rangle$ state atoms ((c), (d)). Blue points correspond to an experiment in which the sample is probed by clock radiation immediately after the photoassociation π-pulse, while red points correspond to an experiment in which photoassociated molecules are illuminated with Raman radiation in order to excite the $\sigma^+\sigma^-$ transition between the $(|g;+5/2\rangle \rightarrow |g;+1/2\rangle)$ nuclear-spin states of the molecular ground-state constituent and thus probed again by clock radiation. The frequency difference between the two dissociation peaks is in fair agreement with the expected $\Delta\nu_{\text{mol}} \simeq 6.2$ kHz calculated evaluating our model for $\text{s}_{\text{fin}} = 30$ and applied magnetic field of $\text{B} = 150$ G.

additional individual $|e\rangle$ atoms summing to the preexisting $|e\rangle$ atoms forming the orbital molecules generated by the first clock-laser π-pulse. The frequency of this transition has been set as zero-frequency reference as shown in figure 5.4.6.
Finally, when the second clock-laser pulse frequency is resonant with respect to the atoms to bound-state-transition, the generated orbital molecules, are photodisso-

ciated to interacting pairs of $|g\rangle$-state atoms. This process causes a depletion of the excited atoms, that can be noted by observing the red points in figure 5.4.6 (c). At the center of the resonance, the depletion is noticeably high, with less than 10^3 excited atoms remained, corresponding to $< 20\%$ of the initial number of photoassociated molecules.

The blue points and blue solid line show the results of a similar experiment, in which the only difference is the absence of Raman excitation between the first photoassociation pulse and the second photodissociation pulse. In this case, the orbital molecules dissociated by the second pulse, shown as the depletion marked as (d) in figure 5.4.6, are in the same $\Delta m = 5$ state in which they were photoassociated. The energy shift $\Delta\nu_{\text{mol-exp}}$ between the depletion peaks (c) and (d) observed with and without the intermediate Raman nuclear-spin-flip transition, corresponds to about 5.9 kHz. This value, considering the long-term drift of the clock-laser and the time necessary to perform this kind of measurement, is consistent with the theoretical binding energy difference between $\Delta m = 5$ and $\Delta m = 3$ that corresponds, for $\mathsf{B} = 150$ G and $\mathsf{s}_{\text{fin}} = 30$, to about $\Delta\nu_{\text{mol}} = 6.2$ kHz. This evidence is a further confirmation of the bound-to-bound nature of the peak observed in the Raman spectra (shown in figure 5.4.2).

5.5 Lifetime of the molecular sample

In this section we introduce the possibility to perform Raman-induced bound-to-bound transitions as a detection tool to identify the presence of orbital molecules in different lattice configurations.
In the last sections we introduced the possibility to coherently address the orbital degree of freedom of fermionic ytterbium in order to produce, by means of exciting the photoassociation transition, a new kind of homonuclear Feshbach molecules. The rich internal structure of AEL $\mathsf{J} = 0$ states has been exploited in order to manipulate the nuclear spin of the ground-state fraction of the photoassociated molecule and we have verified the effectiveness of this technique and the possibility to coherently drive this transition.
The measurements described until now in this chapter have been realized by confining atoms in a deep 3D optical lattice. In this condition, that corresponds to the Lamb-Dicke regime, the external degrees of freedom of the trapped atoms are frozen and the collision dynamics can be described in a second quantization approach by introducing the on-site interaction term parametrized by U (see section 2.3) in a Hubbard-like model.
In section 5.5.1 we will explore the possibility to generate orbital molecules in a deep 3D optical lattice (as described in section 5.3.1) and, by dynamically changing the lattice confinement geometry, we will verify, exploiting the bound-to-bound transition described in section 5.4, the possibility to observe molecules in an interacting many-body gas in which both orbital molecules and ground-state atoms are present.
This first evidence introduces the subsequent measurement described in section 5.5.2, in which the lifetime of the photoassociated bound states has been characterized in two different lattice geometries.

5.5.1 Bound-to-bound transition as detection tool

In this section we describe the possibility to employ the Raman-induced bound-to-bound transition described and identified in section 5.4 as an accurate method that ensures the detection of orbital molecules in a confined sample in which the number of photoassociated molecules is only about 10% of the total number of particles. This detection method will be used to verify the presence of orbital molecules in vertical pancakes-like traps, where the dominating scattering channel is represented by atom-molecule interactions.

The necessity to develop a non-trivial detection scheme to identify orbital molecules is motivated by the fact that the "simple" detection of $|e\rangle$-state atoms cannot be used, because it could be possible for the orbital molecules to dissociate into pairs of independent $|e\rangle$, $|g\rangle$ atoms as a result of an interaction process. The possibility to dissociate molecules via on-site interactions has been neglected up to now because atom-molecule or molecule-molecule collisions in very deep lattices can occur only if an atom performs a tunneling process. In the Lamb-Dicke regime, the tunneling time t is longer than the time used to probe the atoms, so they cannot perform tunneling processes and therefore collisions cannot occur.
In this section we describe the possibility to dynamically change the lattice geometry switching from a 3D lattice, in which interactions are regulated by the tunneling time between two nearest-neighbour lattice sites, to a vertical pancakes configuration, in which collisions between atoms and molecules can occur.

We start from a 70×10^3 degenerate ($T = 0.23\times T_{\mathsf{F}}$) $\mathbb{SU}(2)$ atomic sample constituted by a $\Delta m = 5$ mixture ($|g, m_{\mathsf{F}} = \pm5/2\rangle$). The atomic sample is loaded in a 3D optical lattice with final depth $\mathsf{s}_{\mathsf{fin}}$ following the procedure described in section 5.3.1, then the 1064 nm FOR Trap in which the system reached the degenerate regime by means of evaporative cooling is adiabatically turned off by performing a 1 s intensity linear ramp. Finally, the atoms are illuminated by the 578 nm laser, resonant with the photoassociation transition, in order to produce the highest possible number of orbital molecules.
By comparing the number of $|e\rangle$ atoms detected in the deep 3D lattice and the maximum number of molecules observable by performing bound-to-bound Raman transitions described in section 5.4, it results that, due to the Frank-Condon factor that approaches unity, the bound-to-bound transition nearly detects the whole amount of photoassociated molecules.
In order to dynamically change the lattice confinement geometry, we lower the intensity of the horizontal lattices with a 4 ms long linear ramp, permitting atoms and molecules motion in the horizontal plane. The vertical lattice, instead, is kept at $\mathsf{s}_{\mathsf{fin}}$ in order to confine the atoms in a vertical pancakes structure in which in-plane interactions are allowed.

To perform bound-to-bound transitions, that are an unambiguous signature of orbital molecules in the sample, after a variable holding time we increase the horizontal lattices intensity with another 4 ms long linear ramp in order to reach

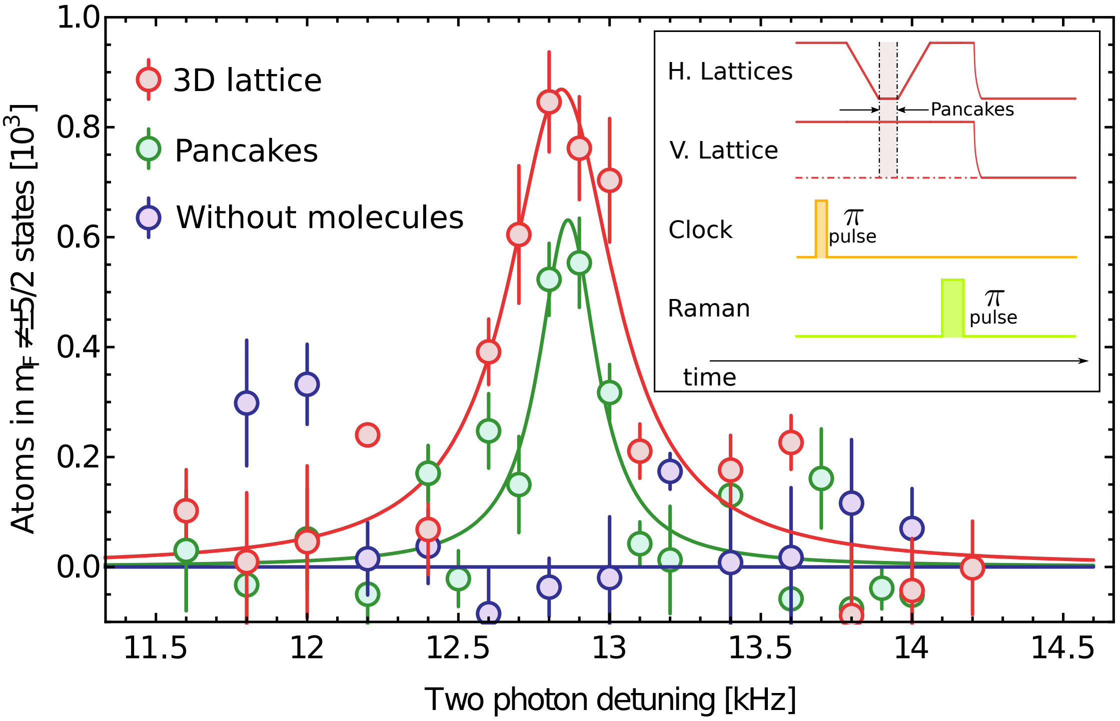

Figure 5.5.1. Raman spectroscopy detecting the Raman $\sigma^+\sigma^-$ bound-to-bound transition identified in section 5.4 for three cases: the red points are measurements in a 3D lattice characterized by depth $s_{fin} = 15$ and magnetic field equal to 30 G. The blue points represent Raman spectroscopy on a sample in which the photoassociation pulse was not performed. As it can be noted, in this case the bound-to-bound transition can not be excited. The green points show the Raman bound-to-bound transition when, after the photoassociation clock-pulse, the lattice geometry is changed from a 3D lattice to pancakes (see text for details). The height of the peak is decreased as an effect of collisions between molecules and atoms in pancakes. The experimental procedure for this last configuration is sketched in the inset.

again a homogeneous 3D lattice configuration. After refreezing the external degrees of freedom in the 3D optical lattice, a Raman bound-to-bound spectroscopy is performed, in order to detect the number of remaining orbital molecules after interactions in the 1D lattice. The measurement results are shown in figure 5.5.1, while the experimental scheme is shown as inset of the same figure.
As it can be observed in figure 5.5.1, the bound-to-bound Raman peak identified and characterized in section 5.4, that has been observed in a 3D lattice characterized by final depth $s_{fin} = 15$ and external magnetic field equal to 30 G (red points) can be observed also if the photoassociated orbital molecules are probed by Raman spectroscopy after 1.0 ms in a pure 1D vertical lattice (green points).

This observation guarantees that orbital molecules are not completely dissociated when collisions with atoms and other molecules occur. We note that the magnetic field used for this measurement, $\mathsf{B} = 30$ G, lying below the 3D OrbFR position where the atom-atom scattering length is positive ensures the presence of a bound state even when the horizontal confinement is released. Moreover, the number of molecules detected in the 1D vertical lattice, that is directly connected to the height of the observed Raman peak (green points), does not differ considerably with respect to the 3D case (red points), suggesting a measurable lifetime of molecules in the 1D lattice geometry.
This argument will be discussed in the following section.

5.5.2 Molecules lifetime

In this section we discuss the measurements performed to determine the lifetime of photoassociated orbital molecules in two different lattice configurations: 3D lattice and 1D vertical array of pancakes. The possibility to detect the number of molecules by means of bound-to-bound transitions in these lattice configurations has been explored in section 5.5.1.

In a first experiment, we study the lifetime of isolated molecules confined in a 3D optical lattice. This is done by photoassociating molecules with a clock-laser π pulse in a 3D optical lattice of depth $\mathsf{s}_{\mathsf{fin}}$ and at a magnetic field B, as specified in section 5.3.1. The sample is then held in the 3D lattice for a variable time in order to detect the number of molecules. Red points in figure 5.5.2 correspond to the result of this measurement as a function of the hold time in a $\mathsf{s}_{\mathsf{fin}} = 15$ 3D lattice performed at an external magnetic field $\mathsf{B} = 25$ G. We fit the data with an exponential function obtaining a lifetime of isolated molecules of $\tau_{\mathsf{3D}} = (0.35 \pm 0.07)$ s, a remarkably long value despite one of the atoms forming the molecule being in a highly excited state. The main limiting factor to the lifetime could be identified as inelastic losses due to collisions after a tunneling process to an occupied neighbouring site (the tunneling time t is of the order of 0.1 s).

In a second experiment, we use the possibility to selectively address orbital molecules to perform a first study of lifetime in a many-body environment. After the clock photoassociation of molecules in the 3D lattice, as specified in section 5.5.1 and sketched in figure 5.5.1, the horizontal lattice beams are turned off with a 1 ms-long linear ramp to obtain a vertical collection of pancankes, characterized by an optical lattice depth of $\mathsf{s}_{\mathsf{fin}} = 15$ along the vertical direction. The sample is held in this pancakes configuration for a variable time, then the horizontal lattices are turned on again by increasing the beam intensity with a specular 1 ms-long

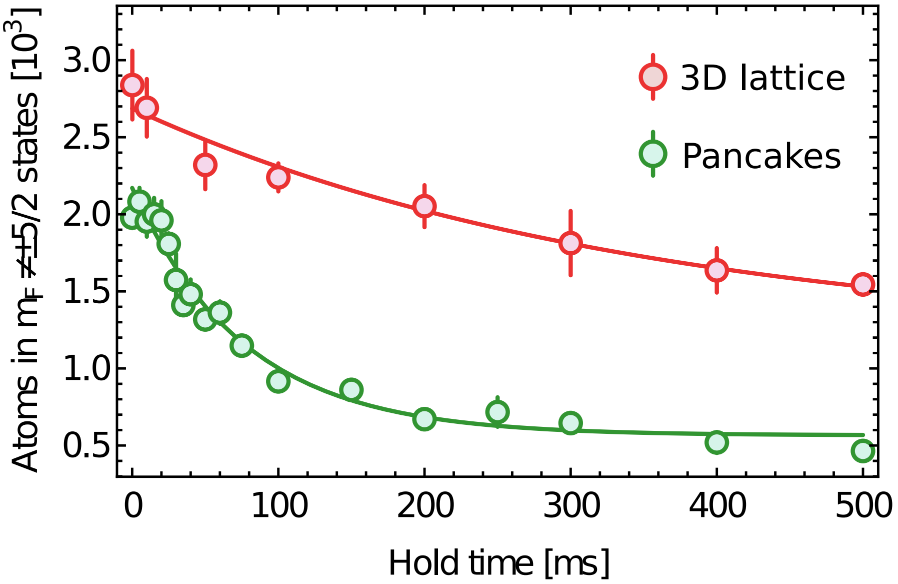

Figure 5.5.2. Lifetime measurement of orbital molecules in different optical lattice configurations. The colour code is the same used to identify the measurements shown in figure 5.5.1. Red points provide a measurement of the lifetime of isolated orbital molecules in a $\mathsf{s}_{\mathsf{fin}} = 15$ 3D lattice. The red solid line is an exponential fit to the data resulting in a decay constant of $\tau_{\mathsf{3D}} = (0.35 \pm 0.07)$ s. Green points provide a measurement of the lifetime of interacting molecules in a vertical array of pancakes. In this scenario, orbital molecules can interact with other molecules and with atoms constituting the sample, leading to a shorter lifetime with respect to the 3D lattice case. The green solid line is an exponential fit to the data resulting in a decay constant $\tau_{\mathsf{1D}} = (77 \pm 8)$ ms.

linear ramp. The sample, confined again in a 3D homogeneous lattice, is finally probed by a Raman π pulse in order to detect the number of remaining molecules. The results of this experiment, performed at an external magnetic field of 25 G, are reported by the green points of figure 5.5.2, where the lifetime of isolated orbital molecules in the 3D lattice is also shown for comparison (red points).

In order to describe the molecule number decay observed in figure 5.5.2, it is necessary to consider all the possible loss channels that a molecule can experience. In a pancake an orbital molecule can interact with another molecule, with a ground-state atom, or with an excited atom produced after the previous dissociation of a molecule.
The rate equations can be described as:

$$\dot{n}_{\mathsf{m}} = -\beta_{\mathsf{ma}} n_{\mathsf{m}} n_{\mathsf{a}} - \beta_{\mathsf{mm}} n_{\mathsf{m}}^2 - \beta_{\mathsf{me}} n_{\mathsf{m}} n_{\mathsf{e}} \tag{5.5.1}$$

where n_{m}, n_{a} and n_{e} are the density of molecules, individual atoms and dissociated

excited atoms, respectively, and β_{ma}, β_{mm} and β_{me} are the loss rate coefficients of the molecule-atom, molecule-molecule and molecule-excited atom loss processes, respectively. In our experimental conditions, the typical number of molecules, that correspond barely to a few thousands, is much smaller than the typical number of ground-state atoms (this value corresponds to about 50×10^3), so it is reasonable to assume that the dominant loss mechanism is represented by molecule-atom interactions. The number of free excited atoms, after the photoassociation pulse is negligible and increases when molecules start to dissociate as a result of interactions in pancakes. In any case, the number of free excited-state atoms is limited by the initial number of molecules.
In this case, the second and the third terms on right hand side in equation 5.5.1 can be neglected, and the rate equation can be approximated by the relation

$$\dot{n}_{\mathsf{m}} = -\beta_{\mathsf{ma}} n_{\mathsf{m}} n_{\mathsf{a}} \tag{5.5.2}$$

which is resolved by a single exponential curve

$$n_{\mathsf{m}}(t) = e^{-\beta_{\mathsf{ma}} n_{\mathsf{a}} t} = e^{-\gamma_{\mathsf{ma}} t}.$$

We fit the green data of figure 5.5.2 with an exponential fit (green solid line) obtaining a lifetime of

$$\tau_{\mathsf{1D}} = \frac{1}{\gamma_{\mathsf{ma}}} = (77 \pm 8)\ \mathsf{ms} \tag{5.5.3}$$

In order to quantify the loss rate coefficient related to this process, we use a simplified model to calculate the average atomic density n_{a} in each pancake starting from our initial sample with N atoms and temperature $T = 0.23\times T_{\mathsf{F}}$, similarly to the model used to calculate the density of bosonic ^{174}Yb presented in section 4.3.2 of this work [44].
We then average over all the pancakes to obtain a mean density value of $n_{\mathsf{a}} \simeq (6.3 \pm 3.1)\,10^{12}\ \mathsf{cm}^{-3}$, to which we attribute a conservative error due to several assumptions in the theoretical model. From this value we can determine the loss rate coefficient $\beta_{\mathsf{ma}} = (2.1 \pm 1.2)\,10^{-12}\ \mathsf{cm}^{-3}$.

This measurement has been repeated for several applied magnetic field values in order to measure the molecule lifetime in the sample across the free-space orbital Feshbach resonance (located at B $\simeq$ 50 G [210, 216]). The results of these measurements are reported in figure 5.5.3. Each point is the average of two independent experiments performed in different days and the error bar is the average of the fit errors of the individual experiments.

Remarkably, there is not a clearly visible trend and the measured lifetimes are compatible within the error bars, independently of the magnetic field being set below or near the free-space resonance. This is generally not true for molecules supported by Feshbach resonances of fermionic alkali atoms, which show faster

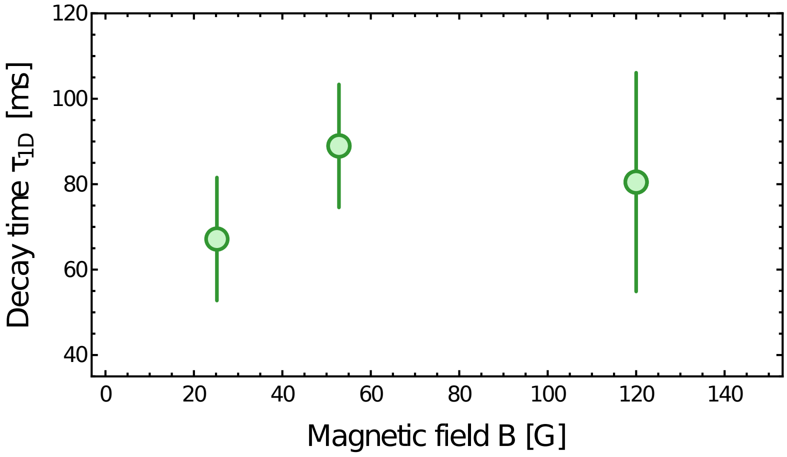

Figure 5.5.3. Measured lifetime of orbital molecules in pancakes for different values of applied magnetic field across the orbital Feshbach resonance. Lifetime values are compatible, within the experimental errors, and no evident trend can be observed.

losses on the BEC side of the resonance and a longer lifetime near resonance arising from the Pauli exclusion principle which suppresses collisions between the fermionic constituents of the weakly bound dimers [251–253]. This fact is a further suggestion that our lifetime measurements are dominated by molecule-atom losses, which are not protected by the Pauli exclusion principle due to the presence of atoms in a “third” state (the $|g, m_\mathsf{F} = -5/2\rangle$ atoms in the singly occupied sites of the initial 3D lattice), different from both the states of atoms forming the $|g, m_\mathsf{F} = +5/2; e, m_\mathsf{F} = -5/2\rangle$ orbital molecule.

A more detailed investigation of inelastic interactions, especially collisions concerning the molecule-molecule interaction, that have been neglected in this work, would require a higher photoassociation efficiency, or the possibility to create a pure sample of orbital molecules. This request results in a difficult task in ^{173}Yb samples due to the small binding energy of the molecules supported by the orbital Feshbach resonance, that does not allow to simply blast away single atoms exploiting “permitted” or “ordinary intercombination” transitions in dipole approximation.

6 | Controllable $\mathbb{SU}(\mathsf{N})$ symmetry breaking via Raman transitions in ^{173}Yb

This chapter is devoted to the description of the experimental measurements realized employing fermionic ^{173}Yb in an 3D optical lattice. In particular, we report the first evidence of state-dependent localization in an atomic lattice system in which the $\mathbb{SU}(\mathsf{N})$ symmetry, that characterize ^{173}Yb levels with null angular electronic momentum (see section 5.1.1), is controllably broken via two-photon Raman coupling.

The chapter is organized as follows: in section 6.1 we review the Fermi Hubbard model (introduced in chapter 2) taking into account the Raman coupling as a tool to break the $\mathbb{SU}(\mathsf{N})$ symmetry of the ground state in fermionic ^{173}Yb.

This system is therefore introduced as a “good candidate” to simulate, following the proposal reported in reference [109], the minimal Hamiltonian that capture the basic processes happening in iron-based-superconductor materials.

Section 6.2 describes the experimental techniques developed to observe the number of doubly-occupied sites in the lattice system. This observable has been used to perform a characterization of the metal-insulator transition in presence and in absence of Raman coupling.

The measurements performed captured the basic mechanism of selective localization, allowing us to obtain a first set of evidences that could open the way to the observation of exotic, and still unexplored phases of matter.

6.1 Raman interaction and multicomponent Fermi-Hubbard models

In section 5.1.1 we have extensively discussed the $\mathbb{SU}(\mathsf{N})$ interaction symmetry that emerges when one considers the scattering between AEL atoms in states characterized by electronic angular momentum J=0. This peculiar feature of AEL atoms allows the realization of experimental systems in which the full many body Hamiltonian satisfies a global $\mathbb{SU}(\mathsf{N})$ symmetry. An emblematic case is the N-flavour Fermi-Hubbard Hamiltonian already discussed in section 2.3:

$$\hat{H} = -\mathsf{t}\sum_{i,\sigma}\left(\hat{a}^{\dagger}_{i+1,\sigma}\hat{a}_{i,\sigma} + h.c.\right) + \frac{\mathsf{U}}{2}\sum_{i,\sigma\neq\sigma'}\hat{n}_{i,\sigma}\hat{n}_{i,\sigma'} \tag{6.1.1}$$

In this section we will show the possibility to induce a controlled, explicit breaking of the $\mathbb{SU}(\mathsf{N})$ symmetry of the many-body Hamiltonian 6.1.1 by including a Raman coupling between internal states, as that used in the previous chapter to probe the properties of $^{173}\mathsf{Yb}$ orbital molecules.
The resulting Hamiltonian, that we will introduce in the subsequent section of this work, has been intensively studied from both the theoretical and experimental [11, 12] points of view because, if the Raman transition described in section 3.3 transfers momentum to the atomic sample ($\vec{\mathsf{q}} \neq 0$), the resulting spin-orbit coupling [145] allows engineering systems (e.g. the Hall ribbon systems realized in Ref. [12]) characterized by a topological properties. An accurate description of SOC can be found in the theses of a former collegue of mine [112] and one of my current collegues [145].
More recently, the $\mathbb{SU}(\mathsf{N})$ Fermi-Hubbard Hamiltonian in the presence of Raman coupling has been studied in order to simulate some of the physical phenomena that are believed to take place in recently discovered types of multiorbital correlated materials, such as the iron-based superconductors [254]. In these materials, the evidence of orbital-selective correlations, that imply a different conduction behaviour for electrons that populate different iron atoms orbitals, has been recently observed [255–257]. Moreover, first evidences of orbital selective Mott transitions have been recently detected [258, 259], pointing to an exotic state of matter in which, depending on the iron orbitals occupied by the electrons, some electrons can be localized by interactions while others are in a metallic delocalized phase.
The experimental investigation and the theoretical simulation of real solid-state systems is complicated by the fact that, as it usually happens in this physics

branch, real materials are quite complicated systems in which many unresolved phenomena take place.

A minimal Hamiltonian that is supposed to capture basic processes happening in iron-based superconductor materials, can be expressed as the sum of two terms:

$$\hat{H}_{\mathsf{Fe}} = \hat{H}_{\mathsf{int}} + \hat{H}_{\mathsf{t}} \tag{6.1.2}$$

where $\hat{H}_{\mathsf{t}}$ is a tight-binding tunneling Hamiltonian that takes into account both intra-orbital and inter-orbital hopping from the i-th lattice site to its j-th neighbour site, and therefore can be written as [257]

$$\hat{H}_{\mathsf{t}} = -\sum_{i\neq j,m,m',\sigma} \mathsf{t}_{i,j}^{m,m'} a_{i,m,\sigma}^{\dagger} a_{j,m',\sigma} + \sum_{i,m,\sigma} (\varepsilon_m - \mu)\, n_{i,m,\sigma} \tag{6.1.3}$$

where $a_{i,m,\sigma}^{\dagger}$ is the creation operator of an electron of spin σ in the lattice site i and in the orbital m and $\mathsf{t}_{i,j}^{m,m'}$ is a "multi-orbital" generalization of equation 2.3.2. In order to describe crystals in which the iron atoms have the major role, Hamiltonian 6.1.3 takes into account the five d orbitals that constitute the most external electronic structure of iron atoms. ε_m is an orbital-dependent energy and μ is the chemical potential. The interaction Hamiltonian in these crystals, that is the Kanamori interaction Hamiltonian reported in reference [256] or in the supplementary materials of reference [257], in second-quantization approach reads:

$$\hat{H}_{\mathsf{int}} = \mathsf{U}\sum_{i,m} \hat{n}_{im\uparrow}\hat{n}_{im\downarrow} + \mathsf{U}' \sum_{i,m>m',\sigma,\sigma'} \hat{n}_{im\sigma}\hat{n}_{im'\sigma'} + (\mathsf{U}' - \mathsf{J}) \sum_{i,m>m',\sigma} \hat{n}_{im\sigma}\hat{n}_{im'\sigma} \tag{6.1.4}$$

where U is the intra-orbital repulsion between two electrons, $\mathsf{U}' = \mathsf{U} - 2\mathsf{J}$ is the inter-orbital interaction and J represents the Hund's coupling.

By following the concept of quantum simulation in the next section the possibility to employ $^{173}\mathsf{Yb}$ atoms as a suitable platform to understand some of the physics that underlies the behaviour of in Iron-based materials will be introduced.

6.1.1 Broken $\mathbb{SU}(\mathsf{N})$ as multi-orbital Iron based system

As shown by equation 6.1.2, the total Hamiltonian considered to describe Iron-based superconductors, takes into account the possibility to have multi-orbital hopping and interaction terms. In order to simulate relevant aspects of this multi-orbital-based system employing $^{173}\mathsf{Yb}$ confined atoms, a theoretical proposal has been recently developed by Del Re and Capone [109]; this proposal introduced the possibility to employ the Raman coupling between nuclear-spin ground states to

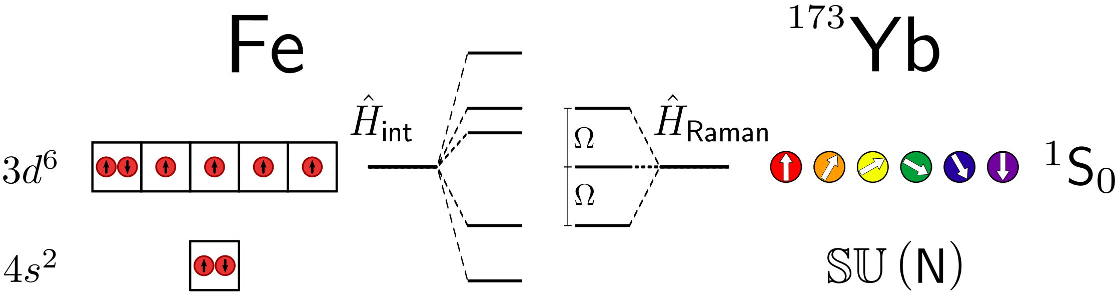

Figure 6.1.1. This sketch shows the similarity between hybridation of d orbitals in Iron atoms, that is related to the possibility to obtain high-temperature iron-based superconductors and Raman-induced nuclear-spin mixing in ^{173}Yb ground-state atoms, where, for the effect of the Raman coupling described by equation 6.1.5, the $\mathbb{SU}$(N) simmetry (introduced in section 5.1.1) is explicitly broken.

emulate the Hund's coupling between different Iron orbitals. This experimental technique, briefly described in section 3.3, provides a Hamiltonian term that, as will we show in this section, does not conserve the Hamiltonian symmetries introduced in section 5.1.1.

In this section, the Raman Hamiltonian term that allows an explicit breaking of the spin-invariance under $\mathbb{SU}$(N) transformation will be introduced in the tight-binding approximation, describing also the main results obtained by Del Re and Capone [109].

In the tight-binding approximation, in which Wannier functions constitute the proper basis to be considered in order to describe atomic wavefunction in the 3D lattice (see section 2.2.1), the Raman interaction, limiting this analysis to the simplified Λ-configuration scheme proposed in section 3.3, can be written as

$$\hat{H}_{\mathsf{Raman}} = \sum_{i,\sigma,\sigma'} \frac{\Omega_{\sigma\sigma'}}{2} \left(a^\dagger_{i,\sigma} a_{i,\sigma'} \right) = \sum_{i,\sigma,\sigma'} a^\dagger_{i,\sigma} \tau_{\sigma\sigma'} a_{i,\sigma'} \tag{6.1.5}$$

where $a_{i,\sigma}$ is the annihilation operator that destroys a particle of spin σ in the lattice site i and $\Omega_{\sigma\sigma'}$ is the Rabi frequency associated to the two-photon Raman process from σ to σ' determined by equation 3.3.6. Let us consider the case in which the momentum transferred by the Raman coupling to the atom is null ($\vec{\mathsf{q}} \simeq 0$). In this case $\Omega_{\sigma\sigma'} = \Omega_{\sigma'\sigma}$ that implies that the coupling is real. In this condition it can be demonstrated that, if we reduce the spin Hilbert space to the subspace spanned by σ and σ', the Raman coupling is a pure mixing matrix, as shown by equation 3.3.7. This term does not commute with respect to the spin permutation operator S^q_p introduced by equation 5.1.5 because in this case we have

$$\left[\hat{S}^q_r, \hat{a}^\dagger_p \hat{a}_s \right] = \delta_{rp} \hat{S}^q_s - \delta_{qs} \hat{S}^p_r \tag{6.1.6}$$

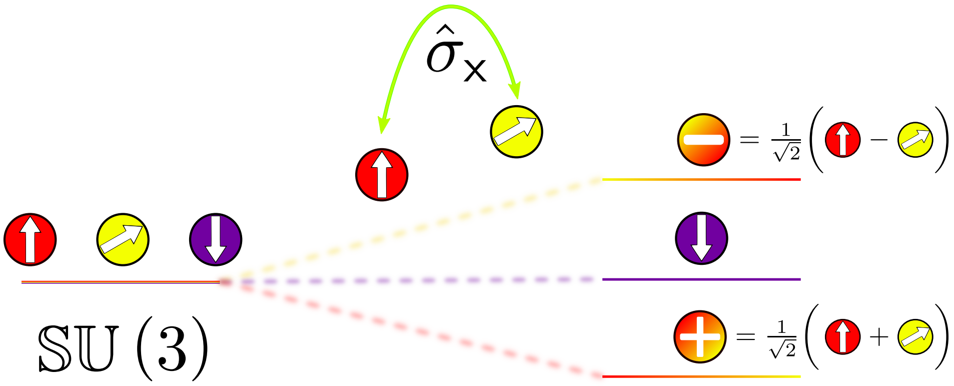

Figure 6.1.2. Sketch of controllable $\mathbb{SU}\,(3)$ symmetry breaking via two-photon Raman transitions, as realized experimentally in this work. The Raman transitions shown in figure, acting as $\hat{\sigma}_x$ in the Hilbert subspace mapped by states $|+5/2\rangle$, $|+1/2\rangle$, generates dressed states $|\pm\rangle$ that are obtained as rotation of bare states. The $|-5/2\rangle$ spin state does not enter the Raman transition, as shown by its unchanged energy.

that is exactly the commutation rule reported in 5.1.6 for the generators of the $\mathbb{SU}\,(\mathsf{N})$ Lie group. This relation implies that the Raman Hamiltonian removes the symmetry of the many-body Hamiltonian and, therefore, removes the spin degeneracy related to the $\mathbb{SU}\,(\mathsf{N})$ invariance. The possibility to generate atomic stable levels characterized by controllable mixing and different energies results to be a fundamental tool in order to simulate the hybridized orbitals of the Iron atoms in chemical compounds that realize iron-based superconductivity; the similarity between the two systems is sketched in figure 6.1.1.

By following reference [109], we will consider a $\mathbb{SU}\,(3)$ sample constituted by $\pm\frac{5}{2}\cap+\frac{1}{2}$ nuclear-spin states, that experimentally can be realized by employing the pumping scheme reported in section 3.4.4. If we neglect the effect of the external magnetic field (that is used to address the Raman transitions selectively and can be considered as an effective state-dependent chemical potential, as discussed in section 5.1), these "bare" states are degenerate as a result of the global $\mathbb{SU}(\mathsf{N})$. A two-photon Raman coupling between the $+5/2$ and the $+1/2$ nuclear-spin states is then introduced in the system. When the Raman coupling is applied the eigenstates of the systems become the "dressed" states

$$|\pm\rangle = \frac{1}{\sqrt{2}}\Big(|1/2\rangle \pm |5/2\rangle\Big) \qquad \cap \qquad |-5/2\rangle, \tag{6.1.7}$$

and their "dressing" energies are graphically represented in figure 6.1.2. As suggested in reference [109] and shown in figure 6.1.1, the possibility to break the global Hamiltonian symmetry by the Raman coupling term (see equation 6.1.5), is a good framework to better understand the fundamental phenomenon of orbital selectivity (here, spin selectivity) that is supposed to play a key role in iron-based superconductivity. In particular, the possibility to observe phases characterized by different conduction properties, as orbital-dependent Mott-insulating phases, should be accessible by evaluating the conduction properties of the different spin components of the presented lattice system, as numerically shown by reference [109].

6.2 Mott-insulating phase and doubly-occupied lattice sites detection

In reference [109] the authors highlight that the Raman coupling between spin states described in section 6.1.1 can cause, even in interaction regimes that do not allow for the Mott transition in 3D, an orbital Mott-selective behaviour that can properly mimic the fundamental characteristics of Iron-based superconductor materials.
The similarities between the energetic structure of Iron hybrid *d*-shaped orbitals and nuclear-spin states coupled by two-photon Raman interaction have been stressed out in section 6.1.1.
This section is devoted to introduce the possibilities offered by a 3D lattice system in which the onsite repulsion (quantified in equation 2.3.13 by U) can cooperate with the Raman coupling in order to create exotic phases of matter as orbital-selective Mott-insulators are.
As introduced in section 2.3.1, in the absence of Raman coupling ($\Omega = 0$), the Fermionic Hubbard Hamiltonian supports three different phases of matter that are:

- a metallic phase, in which the interactions strength U is much smaller than the tunneling energy t and the particles are delocalized over the whole lattice (see equation 2.3.16);
- a band insulator, in which each particle is delocalized over the whole lattice but the total system results an insulator because the lowest energy band is completely filled by particles;
- a Mott insulating phase, that sets in when the interaction strength U dominates the tunneling energy t. In this phase the system cannot carry currents because the interaction energy U gained by the system when two particles can interact in one lattice site is not the lowest energetic configuration possible.

In a real lattice system, in which the shape of the lattice beams creates a harmonic confinement (described by equation 2.2.5), the theory that describes the system (still in absence of the Raman coupling) is equation 2.3.13, in which V_i is the onsite potential. When real systems are considered, if the number of atoms for each spin state is sufficiently low not to occupy excited bands of the lattice, an important quantity that can be used to characterize the state of the system is the number of atoms residing on lattices sites that are already occupied by two atoms. In the ideal non-interacting case this double-occupancy number should increase with the number of atoms in the trap.

When strong repulsive interactions are taken into account, a very different behaviour can be predicted and a Mott insulator will appear in regions of the trap where the local filling is of one atom per site. For regimes in which the repulsive interaction completely dominates the tunneling and the local trapping potential, in the entire center of the trap a proper Mott insulating phase forms and the number of doubly-occupied sites is suppressed [260].

So far the effect of finite entropy has been neglected. When we consider a 3D real lattice system that is loaded by starting from a degenerate fermionic gas at a finite temperature, thermal fluctuations have a non-negligible role in the formation of insulating or ordered phases as it can be clearly observed in reference [261].

In this section we will study $\mathbb{SU}(3)$ Fermi-Hubbard models realized by loading a 3D optical lattice with approximately 70×10^3 ^{173}Yb atoms in three different nuclear spin states.

From a theoretical point of view, the number of doubly-occupied lattice sites in a balanced $\mathbb{SU}(3)$ sample can be evaluated by extending the model presented in reference [262] to the case of 3 interacting spins. The model introduced by Zhou and Ho evaluates the number of doubly-occupied (and triply-occupied in the case of $\mathbb{SU}(3)$) lattice sites in the so-called “atomic limit” (introduced in section 2.3.1), taking into account the effective entropy per particle confined in the lattice.

6.2.1 Photoassociation spectroscopy in ^{173}Yb sample

The number of doubly-occupied lattice sites, as suggested by reference [261], is a remarkable observable quantity to determine the state in which the system is for defined experimental values of trapping frequencies and initial temperature of the mixture. The derivative of this quantity, with respect to the number of particles $\partial\#_D/\partial N$, is an indirect measurement of compressibility, identifying unequivocally the state of the system.

From the experimental point of view, the number of atoms in doubly-occupied sites can be measured by following the procedure exploited in chapter 4 to remove doubly-occupied sites from the system. In the case described in section 4.2, in order to remove multiply-occupied lattice sites from the confined system, we exploited the 556 nm photoassociation transition from the ground state to the bound-state generated by a ground-state atom and a ^{3}P$_1$ atom.

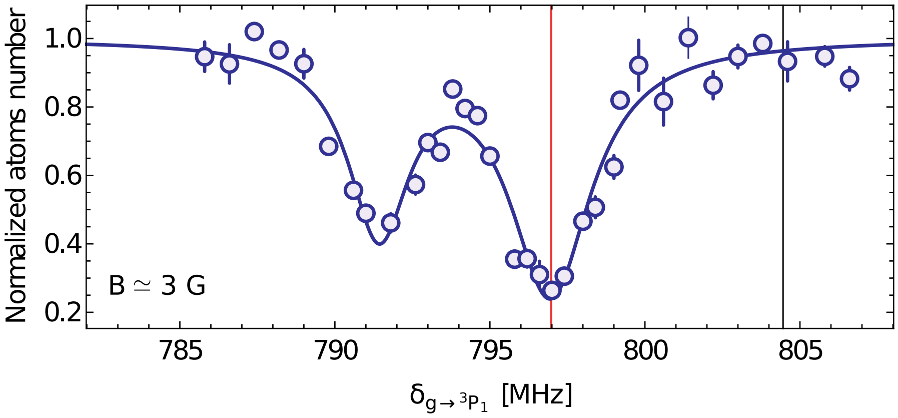

Figure 6.2.1. Typical photoassociation spectrum obtained by scanning the frequency of 556 nm light, red-shifted by about 790 MHz with respect to the atomic transition $|g\rangle \rightarrow |^3\mathrm{P}_1\rangle$. The spectrum has been obtained by exciting a $\mathbb{SU}(3)$ $(\pm 5/2 \cap +1/2)$ atomic sample with 0.5 W of radiation on a waist of about 100 μm for 5 ms. An external magnetic field, of about 3 G, is applied to define a quantization axis of the system. The red line represents the frequency employed to excite the photoassociation resonance while the black line, that is red-shifted with respect to the red line by about 7.2 MHz, is employed as "out of resonance" frequency.

In this case, we employ the 556 nm transition from the $|2g\rangle$ to the bound state $|g;\ ^3P_1\rangle$ that is 796.2 MHz red-detuned with respect to the single-particle excitation $|g\rangle \rightarrow |^3\mathrm{P}_1\rangle$ in ^{173}Yb (as reported in reference [263]).
The specified photoassociation transition is based on the $^3\mathrm{P}_1$ magnetic-sensitive triplet state (the first-order Zeeman splitting corresponds to about $\simeq 600$ kHz/G), thus the transition frequency depends on the external magnetic field applied to the trapped sample.
As studied in reference [263] and in the next sections, the specified photoassociation-transition dependence with respect to the magnetic field can be exploited to selectively address different photoassociation processes that, fixed the light polarization, can occur only when atoms in certain spin states are trapped in the same lattice site.

In order to determine the number of lattice sites occupied by two particles we need to evaluate the difference between the number of atoms in the sample when the photoassociation transition is excited by shining resonant light (the resonant frequency is represented by a red line in figure 6.2.1) and when the light is out of resonance (the chosen frequency is represented as a black line in figure 6.2.1). The main source of uncertainty associated to this kind of measurement can be attributed to the instability of the total number of atoms loaded in the lattice.

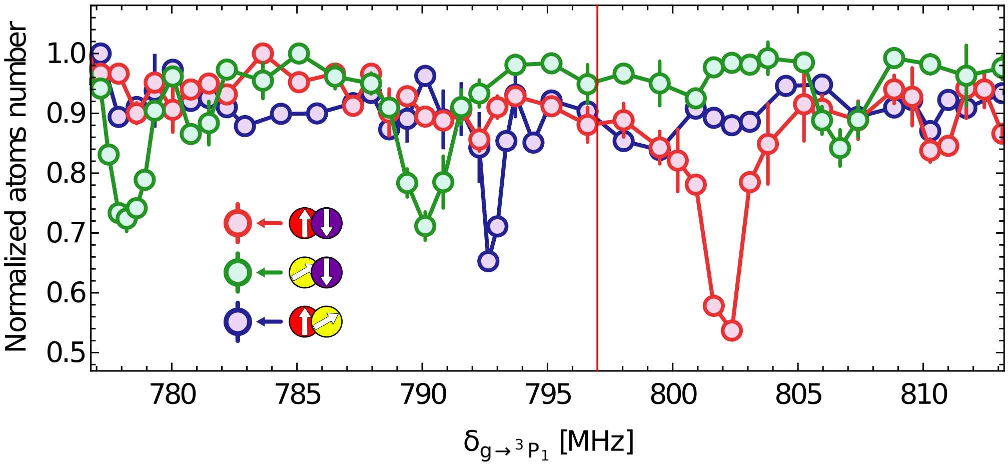

Figure 6.2.2. The result of several spectroscopies near the previously determined photoassociation resonance frequency are reported. In particular, by applying an external magnetic field of about 60 G, the photoassociation transition observed in figure 6.2.1, where position is marked by the red line, splits into several peaks. As it can be observed, transitions corresponding to different spin mixtures can be selectively addressed, allowing us to detect the number of doubly-occupied sites for each couple. Each spectroscopy is performed by exciting a sample confined in a deep 3D lattice with 0.5 W of 556 nm radiation on a beam that has a waist of about 100 μm.

A typical resonance spectrum near the photoassociation frequency, for an applied external magnetic field of about $\simeq 3$ G, is reported in figure 6.2.1. It is necessary to apply an external magnetic field to define a system quantization axis and, therefore, to avoid the depolarization of the $\mathbb{SU}(3)$ sample.

To selectively address the photoassociation resonances related to the nuclear-spin pairs that can be found in the cited $\mathbb{SU}(3)$ sample:

- $|-5/2\rangle$, $|+5/2\rangle$;
- $|-5/2\rangle$, $|+1/2\rangle$;
- $|+5/2\rangle$, $|+1/2\rangle$;

we performed three different high-magnetic-field spectroscopy runs starting from $\mathbb{SU}(2)$ atomic clouds constituted by each of the mentioned spin mixtures. The results of this measurement are reported in figure 6.2.2, where the photoassociation peak of figure 6.2.1 (centered at the position determined by the red line) generates singular addressable resonances when a magnetic field of about $\simeq 60$ G is applied to the confined atomic sample.

6.2.2 Doubly-occupied lattice sites in a balanced $\mathbb{SU}(3)$ sample

In the absence of Raman coupling, the trapped atomic system can be described by the Fermi-Hubbard model with a site dependent potential, as described by equation 2.3.13. As a first "test bench", we determined the number of the doubly-occupied sites as a function of the total number of atoms in the sample at different 3D lattice depths.
In order to compare the results of these measurements with the case studied in the following sections, where the $\mathbb{SU}(3)$ symmetry is controllably broken by the Raman coupling, we choose to work with a balanced $\mathbb{SU}(3)$ nuclear spin mixture that is realized by performing the optical pumping scheme described in section 3.4.4.
After the evaporation stage the resulting sample is constituted by about 70×10^3 ^{173}Yb atoms with a temperature of about $0.25\times T_{\mathsf{F}}$. The number of atoms in the obtained $\mathbb{SU}(3)$ gas can be finely set by slightly modifying the final light power of the 1064 nm laser beams constituting the crossed trap.
However, changing the total number of atoms trapped in the system by only varying the power of the laser beams employed to realize the crossed trap, also affects the harmonic trap frequencies of the confined system, as it can be noted by the FOR Trap characterization reported in appendix B. Therefore, measurements realized at different number of atoms cannot be directly compared. In order to characterize the same system by only modifying the number of particles after the evaporation stage that fixes the number of atoms constituting the sample, the power of the beams that form the crossed trap is enhanced by performing a linear ramp of 300 ms in order to reach trap frequencies $\omega_{\{x,y,z\}} = 2\pi\times\,(56, 96, 73)$ Hz; the sample preparation procedure is sketched in figure 6.2.3.

Once the number of atoms in the trap characterized by the aforementioned harmonic frequencies has been set, by following the lattice loading procedure employed also in reference [264], in order to avoid the increasing of the harmonic confinement caused by the lattice beams intensity ramp, the light power of the crossed trap beams is lowered accordingly, as shown in the inset of figure 6.2.3. In the first step, the 3D lattice depth is increased up to s = 4 in 2 s by performing a spline ramp in order to avoid band excitations and transfer atoms in the lowest lattice band [265]. Finally, the second spline ramp shown in the inset of figure 6.2.3 is performed in 1 s and increases the 3D lattice depth from s = 4 to the final s at which the sample has to be probed in order to measure the number of doubly-occupied sites.
Figure 6.2.3 reports the result of a typical measurement of doubly-occupied sites

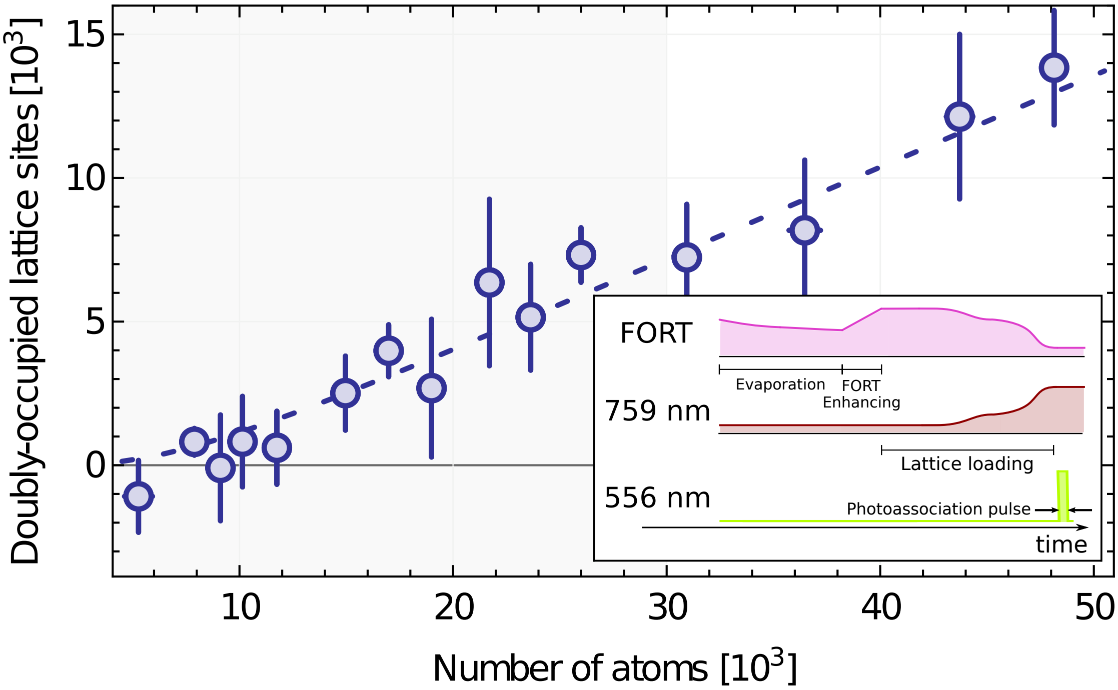

Figure 6.2.3. The plot reports the number of doubly-occupied sites in the 3D lattice (characterized by a depth s = 8) as a function of the total number of atoms in the $\mathbb{SU}(3)$ $(\pm 5/2,\ +1/2)$ sample. When the number of atoms is below $5{\times}10^3$ experimental instabilities do not allow reliable measurements. Moreover, when the number exceeds about $30{\times}10^3$, the atoms start to occupy higher lattice bands and, therefore, the system can not be described by equation 2.3.13. The dashed line is the generalization of the model proposed in reference [203] for 3 spins ($T/T_\mathsf{F} = 0.27$). The inset shows the procedure used to load atoms in the lattice and observe the number of doubly-occupied sites.

as a function of the total number of atoms in the 3D lattice system. The experimental points are obtained as the difference between the total number of atoms and the population remained after a photoassociation pulse performed at $\simeq 3$ G of external applied magnetic field. The errorbars are determined as the result of a bootstrapping procedure over the experimental data. The number of doubly-occupied sites for final lattice depth s = 8 shows a nearly linear behaviour with respect to the number of atoms N, with no evident incompressible regions at small N, because for the specified lattice depth the ratio between the interaction energy and the tunneling is still lower than the critical value[1] evaluated for $\langle\hat{n}\rangle \approx 1$: $(\mathsf{U}/\mathsf{t}) \ll (\mathsf{U}/\mathsf{t})_\mathsf{c}$. Technical issues on the experimental procedure do not allow experimentally stable atom numbers lower than $\sim 5{\times}10^3$, for that reason it has not

---

[1] The critical ratio between U and t has been introduced in section 2.3.1 for $\langle\hat{n}\rangle \approx 1$ and, for a cubic geometry, it corresponds to $\zeta{\times}5.8 \sim 34.8$. In ^{173}Yb the transition should occur at $\mathsf{s} \approx 11$.

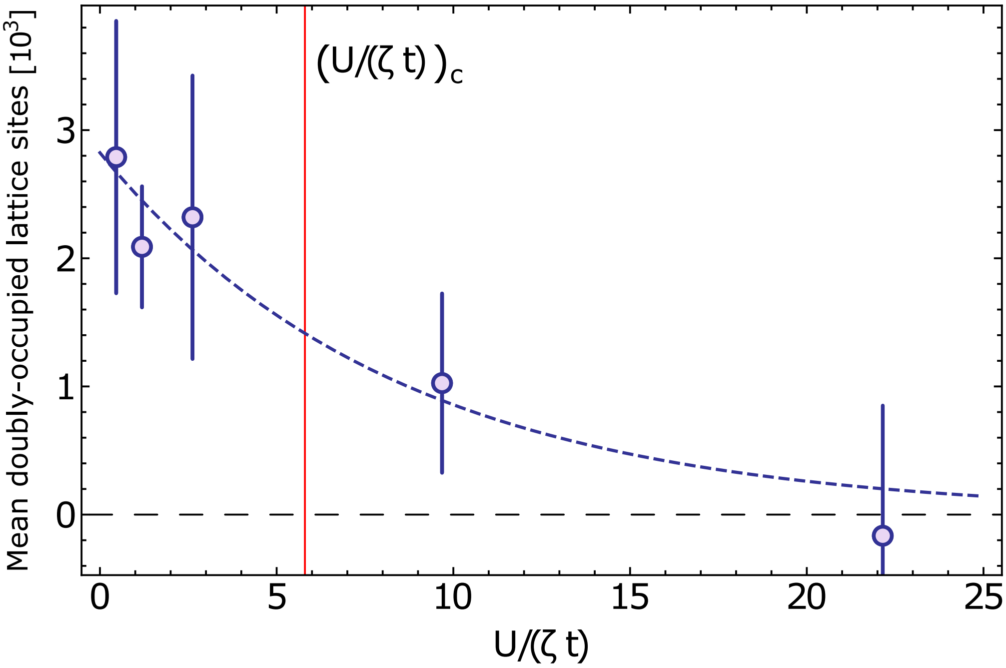

Figure 6.2.4. Experimental points are the result of the doubly-occupied sites measurements for different 3D lattice depths s. The red line represents the theoretical critical value $(U/(\zeta t))_c$. When the ratio U/t exceeds the critical value the mean number of doubly-occupied sites in the system is strongly suppressed suggesting the formation of a Mott insulating core in the center of the trap. The dashed line is a guide to the eye to emphasize the decreasing behaviour of the mean number of doubly-occupied sites.

been possible to collect data in that interval. When the total number of particles exceeds $\sim 30\times10^3$, the atoms start to populate higher lattice bands; in this condition the lattice dynamics can not be determined by the simple FHM described by equation 2.3.13 and therefore the number of doubly-occupied sites in the sample can not be associated to the single-band description.

In order to characterize the transition from a metallic phase, in which the parameter $U/(\zeta t) \ll 5.8$, to a state in which the sample, or part of it, is in a localized Mott phase, and therefore $U/(\zeta t) \gg 5.8$, we performed several measurements of the doublon number as a function of the total number of atoms N for different values of final lattice depths s. The results of these measurements are shown in figure 6.2.4. The experimental points reported represent the mean number of doubly-occupied sites in the interval from $N = 5\times10^3$ to 30×10^3, that is, for the reason described above, the interval that ensures that the system can be described by equation 2.3.13. The change in the mean number of doubly-occupied sites, from a nonzero value at small $U/(\zeta t)$ to a vanishing value above the critical value $U/(\zeta t)_c$ reflects the transition from a delocalized metallic state to a localized Mott state where strong interactions suppress the multiple occupation of the lattice sites.

6.2.3 Raman ground-state loading procedure

In this section we will discuss the experimental procedures developed to prepare the atomic sample in the ground state of the lattice system described in section 6.1.1 in which the $\mathbb{SU}(3)$ symmetry can be controllably broken by exploiting Raman coupling between nuclear-spin states of ^{173}Yb atoms.
In order to realize the ground state of the Fermi-Hubbard Hamiltonian that includes also the Raman coupling described in section 6.1.1, we start from an unbalanced $\mathbb{SU}(2)$ sample constituted by $|\pm 5/2\rangle$ nuclear-spin states; the population of each spin state has been optimized by changing the frequencies of optical pumpings to obtain a sample composed by about 2/3 of the whole atomic population in the $|+5/2\rangle$ state. Although the reason for this choice will be made clear later in this section, we can anticipate that this condition will allow us to obtain a balanced sample composed by an equal, steady population of $(+5/2,\ +1/2,\ -5/2)$ bare spin states, coherently coupled as in the scheme shown in figure 6.1.2. The $\mathbb{SU}(2)$ unbalanced sample is therefore loaded in a deep 3D lattice by performing two-step intensity lattices spline ramps, by following the experimental procedure described in section 6.2.2.
Before explaining the details of the Raman loading protocol, let us discuss some technical aspects of the Raman scheme that we have implemented. As discussed in the previous sections and shown in figure 6.1.2, we want to create a coupling between $|+5/2\rangle$ and $|+1/2\rangle$ nuclear-spin states, leaving the $|-5/2\rangle$ state uncoupled. The coupling between the first two states is realized by using 556 nm Raman beams, detuned by 1756 MHz with respect to single-photon $g \rightarrow {}^3\mathrm{P}_1$ transition. The polarization is in the horizontal plane orthogonal to the quantization axis, enabling the excitation of σ^+/σ^- transitions with $\Delta m = 2$ (see section 3.3). As specified in section 3.3, the energy separation between two nuclear-spin components is generated by applying an external magnetic field. The resulting splitting is linear, that also implies that the shift between $+5/2$ and $+1/2$ spin states is the same generated between $+1/2$ and $-3/2$ and between $-1/2$ and $-5/2$ nuclear components. Therefore, in order not to populate the "unwanted" $-1/2$ and $-3/2$ states, we need to resolve the different Raman processes by using spin-dependent light shifts[2], as described in reference [112]. In order to ensure the effective two-level coupling $+5/2 \leftrightarrow +1/2$ induced by the σ^+-σ^- Raman transition, for each

---

[2] As specified in chapter 5 of this work, that implies that each light beam has σ^+ and σ^- polarizations.

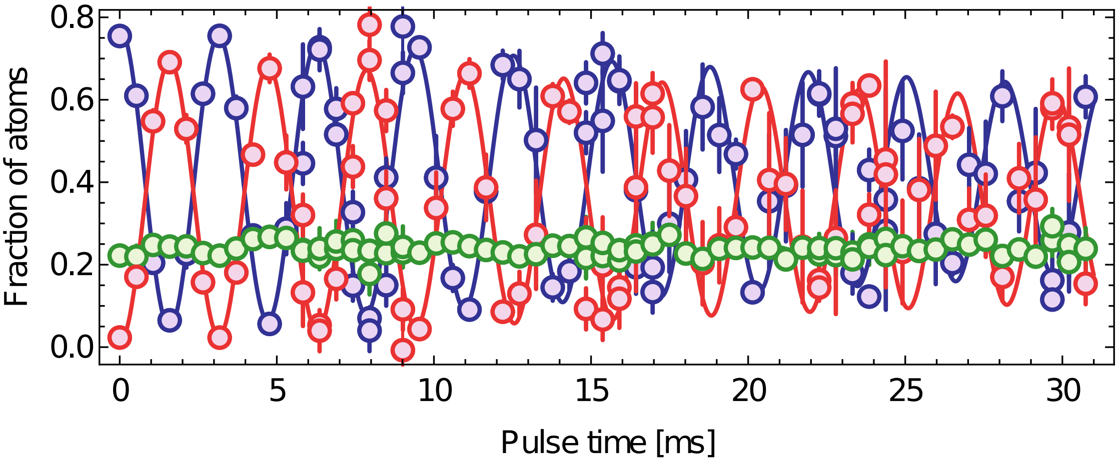

Figure 6.2.5. Starting from an unbalanced mixture of $\pm 5/2$ spin states, we show the Raman dynamics induced by a magnetic field of 150 G and a Raman coupling realized by shining 700 μW of horizontally polarized 556 nm radiation (on a waist of $\simeq 350$ μm). When the two-photon Raman coupling is resonant with the $+5/2$ - $+1/2$ transition, the dynamics is limited to two spin components (blue and red experimental points). The third state, in this case the $-5/2$ spin state, is not affected by the Raman transition, as shown explicitly by green points.

value of the external magnetic field and light power of the Raman beams, we had to experimentally find the resonance condition, i.e. the two-photon detuning that matches the energy shift caused by the differential light shift and the magnetic field.
As also shown in figure 5.4.1, the possibility to selectively address the two-photon transition for the specified nuclear spin components can be achieved. As additional evidence, in figure 6.2.5, we demonstrate the possibility to coherently address the transition between $|+5/2\rangle$ and $|+1/2\rangle$ nuclear spin components without coupling the $|-5/2\rangle$ spin state.

Finally, we discuss the procedure that we have followed to load the lowest-energy Raman band of the Fermionic coupled system described in section 6.1.1. To achieve this scope, after the lattice loading of the unbalanced $\mathbb{SU}(2)$ sample, we turn on the Raman beams with an initial two-photon Raman frequency difference δ_{in} that is out of resonance with respect to the resonance condition δ_{fin} for the $+5/2 \rightarrow +1/2$ transition selected transition Raman detuning, and perform an exponential frequency sweep of the form:

$$\delta_{\mathsf{out}}(t) = \delta_{\mathsf{in}} + (\delta_{\mathsf{fin}} - \delta_{\mathsf{in}}) \left(\frac{1 - e^{-t/\tau}}{1 - e^{-T/\tau}} \right) \tag{6.2.1}$$

This frequency sweep results in an adiabatic passage that brings atoms in the $+5/2$ state into a superposition of equally populated $+5/2$ and $+1/2$ states, as in the lowest-energy state shown in figure 6.1.2. Parameters such as the total time of the ramp T and the exponential constant τ are determined by verifying experimentally the possibility to revert the procedure in order to recover the initial spin composition of the initial sample [112].

At the end of this procedure, we have a balanced mixture of $\mathsf{N} + \mathsf{N}$ atoms in the coherently coupled $+5/2$ and $+1/2$ states $+$ N in the uncoupled state $-5/2$. The numerical solution of the few-site version of the full Hamiltonian, including tunneling and interactions, (based on exact diagonalization and time evolution) show that this procedure ensures the loading of the many-body ground state with the constraints of equal populations described above.

6.2.4 Enhancement of localization and state-selectivity induced by the Raman coupling

In section 6.2.2 the number of atoms in doubly-occupied sites, measured with a photoassociation detection technique, was used as an indicator of the transition from a metallic phase to a localized Mott phase in a $\mathbb{SU}(3)$ sample in the absence of Raman coupling. In this section we will compare those results with those obtained in the $\mathbb{SU}(3)$-broken case in the presence of the Raman coupling, after the loading procedure presented in the previous section. In order to perform a photoassociation measurement of the total number of doubly-occupied sites, the magnetic field has to be decreased from the value used in the loading procedure (150 G) to a smaller value (3 G), as discussed in section 6.1.

The whole experimental procedure employed to evaluate the number of doubly-occupied lattice sites is graphically sketched in the inset of figure 6.2.6.

The number of doubly-occupied sites, as reported in section 6.2.2, is measured by evaluating the difference between the total number of atoms in the sample when the 556 nm pulse is on resonance with respect to the photoassociation transition and the total number of atoms in the sample when the photoassociation pulse is out of resonance. The results of these measurements, performed at fixed trap frequencies $\omega_{\{x,y,z\}} = 2\pi\times\,(56, 96, 73)$ Hz and for lattice depth $\mathsf{s} = 8$ are reported, as a function of the coupling strength $\Omega/\left(\zeta\mathsf{t}\right)$, in figure 6.2.6. As it can be noted, in absence of Raman coupling, the interaction strength U for $\mathsf{s} = 8$ does not allow to have a localized phase, as also shown in figure 6.2.4. Increasing the Raman coupling strength, we observe a clear suppression of double occupancies, which we associate to an enhancement of localization induced by the $\mathbb{SU}(3)$ symmetry breaking by the Raman coupling. The measurements reported in figure 6.2.6 have

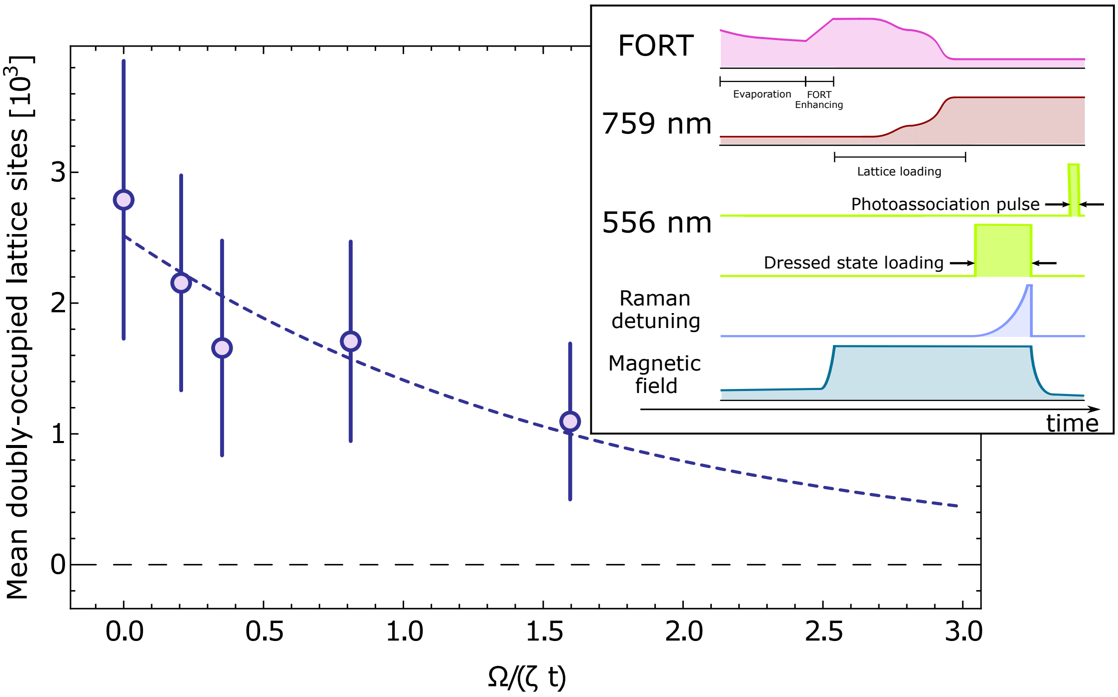

Figure 6.2.6. The **experimental points** are measurements of the number of doubly-occupied sites performed at the same lattice depth $s = 8$ as a function of the Raman coupling strength Ω. At $s = 8$ the repulsive interaction alone is not sufficient to cause an effective localization, as also shown in figure 6.2.4. By increasing the energy difference between $|+\rangle$ and $|-\rangle$ states, that results proportional to Ω, the system is driven into a more localized phase. The **dashed line** represents a guide to the eye.

been performed for different values of lattice depth s keeping unvaried the trap frequencies. The results of these measurements as a function of the lattice depth (reported as a function of $U/\zeta t$) and of the Raman coupling are shown in figure 6.2.7.

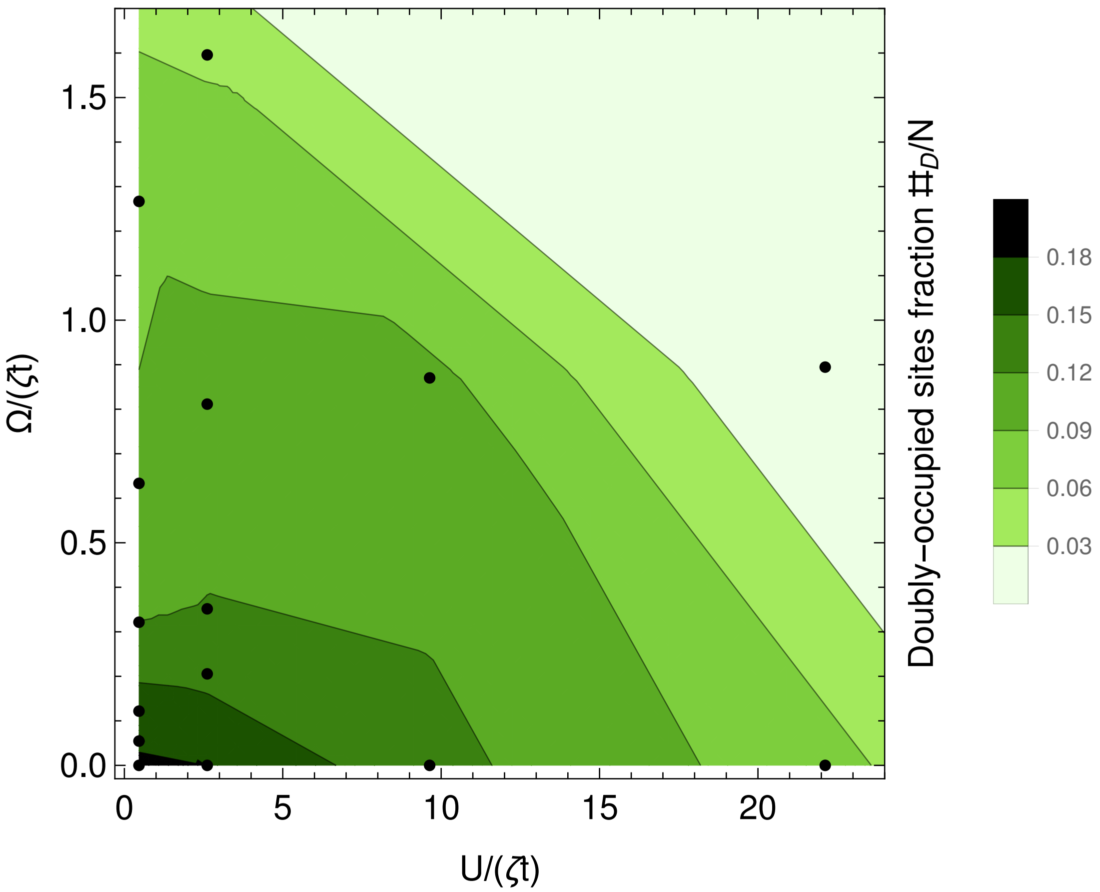

Figure 6.2.7. Two-dimensional plot obtained as first order interpolation of experimental measurements (black points). Darker colours imply a higher mean number of doubly-occupied sites (reported as $\#_D/\mathsf{N}$) while light green represents nearly absent doubly-occupied sites in the interval between 5×10^3 and 30×10^3 atoms. It is evident that both the interaction strength U and the Raman coupling Ω co-operate to localize the atoms in the lattice sites, as also observed from the measurements reported in figure 6.2.6.

Figure 6.2.7 shows clearly that, increasing the Raman coupling, i.e. extending the energy difference between $|+\rangle$ and $|-\rangle$ dressed states (as it is graphically sketched in figure 6.1.2), the mean number of doubly occupied sites decrease, as a result of increased atom localization in the lattice sites. This behaviour can be observed for each interaction strength measured, below and above the critical $\mathsf{U}/(\zeta\ \mathsf{t})$ ratio, confirming the decreasing behaviour shown for $\mathsf{s}=8$ in figure 6.2.6.

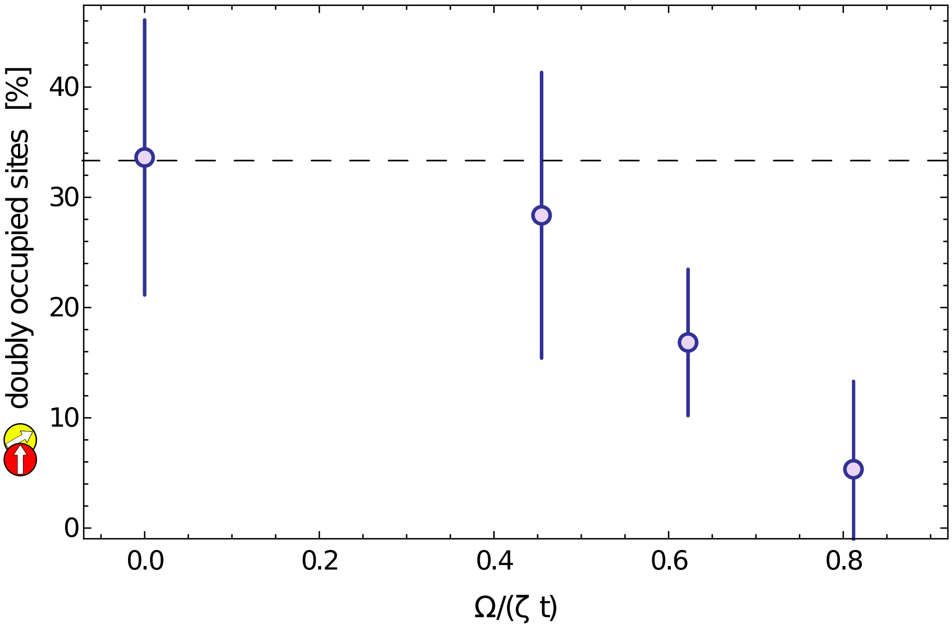

Figure 6.2.8. Fraction of observed doubly occupied sites for the mixture composed by $|+5/2\rangle$ and $|+1/2\rangle$ bare states (see text for definition) as a function of the Raman coupling strength.

As last experimental result, we performed a state-selective measurement of the mean number of doubly-occupied sites by repeating the measurement described above at an external magnetic field of $\simeq 60$ G. As shown in figure 6.2.2 and in reference [263], by applying an external magnetic field the photoassociation peak splits into several transitions that have been exploited to selectively evaluate the number of doubly-occupied sites corresponding to two nuclear-spin combinations.

The fraction of $|+5/2\rangle$ and $|+1/2\rangle$ spin states in doubly-occupied sites ($\%_{(+5/2;+1/2)}$) has been experimentally measured by evaluating the ratio

$$\%_{(+5/2,+1/2)} = \frac{\#_{(+5/2;+1/2)}}{\#_{(+5/2;+1/2)} + 2\times\#_{(+5/2;-5/2)}} \times 10^2 \qquad (6.2.2)$$

where $\#_{(+5/2;+1/2)}$, $\#_{(+5/2;-5/2)}$ are the numbers of doubly-occupied sites of $|+5/2\rangle$, $|+1/2\rangle$ and $|+5/2\rangle$, $|-5/2\rangle$ spin states, respectively. We assumed that the uncoupled spins mixtures have the same behaviour in such a way that $\#_{(+5/2;-5/2)} = \#_{(+1/2;-5/2)}$ and therefore the total number of doubly-occupied sites can be written as

$$\#_D = \#_{(+5/2;+1/2)} + 2\times\#_{(+5/2;-5/2)}.$$

The fraction of doubly-occupied sites for the spin-mixture composed by $|+5/2\rangle$ and $|+1/2\rangle$ states as a function of Raman coupling strength for a fixed lattice depth ($\mathsf{s} = 8$) has been reported in figure 6.2.8.

As it can be noted, this quantity decreases when the Raman coupling strength is increased, from $1/3$ at $\Omega = 0$ (as expected by the $\mathbb{SU}(3)$ symmetry of the Hamiltonian) down to 0 at large Ω.
This behaviour is consistent with the theoretical prediction reported in reference [109]. We can provide an intuitive explanation to describe the observed behaviour. When the Raman coupling is absent ($\Omega = 0$) all the nuclear-spin combinations have the same energy and, therefore, they behave in the same way, as a consequence of the $\mathbb{SU}(3)$ symmetry.
When the coupling is enabled ($\Omega \neq 0$), the degeneracy between levels is lifted (see figure 6.1.2). In the rotated basis, where the Raman coupling is diagonal, (constituted by $|+\rangle$, $|-\rangle$, $|-5/2\rangle$ states, as shown in section 6.1.1) the configuration corresponding to $|+5/2\rangle$, $|+1/2\rangle$ atoms occupying the same lattice site requires the population of both $|+\rangle$ and $|-\rangle$ states, that is energetically more onerous than the configuration corresponding to either $|+5/2\rangle$, $|-5/2\rangle$ or $|+1/2\rangle$, $|-5/2\rangle$, that can be realized with the less energetically-costly population of $|+\rangle$ and $|-5/2\rangle$.

This observation represents a first experimental evidence of a state-selective localization in an atomic lattice system in which the $\mathbb{SU}(3)$ symmetry has been controllably broken via two-photon Raman coupling.
While it is not the observation of an orbital-selective Mott behaviour yet [109], this state-selective behaviour is the first demonstration of the microscopic mechanism underlying a whole class of phenomena under intense study in the physics of strongly-correlated multi-orbital materials.

7 Conclusions and future perspectives

In this thesis we have reported on a set of experiments aimed out the characterization of strongly interacting states of ultracold bosonic and fermionic Ytterbium (^{174}Yb and ^{173}Yb, respectively) trapped in an optical lattice. The results of these experiments provided a further proof of the extreme versatility that these ultracold atomic systems have demonstrated in recent past. In particular, the possibilities offered by two-electron atoms confined in optical lattices are multiple: lattices allow for the fine control of interaction and hopping energies while the external electronic structure of the atoms offer possibilities of coherent control over two different internal degrees of freedom: the orbital d.o.f., corresponding to the possibility to excite ultranarrow transitions between the ground state $^1\mathsf{S}_0$ and the metastable states $^3\mathsf{P}_0$, and the nuclear-spin d.o.f., that instead is related to the possibility to couple coherently atoms in different nuclear-spin projections. Moreover, due to the high symmetry of states characterized by null electronic total momentum, fermionic isotopes allow the realization of systems with tunable $\mathbb{SU}(\mathsf{N})$ symmetry, a valuable resource for the quantum simulation of various systems from few-body to solid-state materials, to high-energy physics.

The first set of measurements reported in this thesis exploited the orbital degree of freedom in ^{174}Yb. The possibility to excite the ultranarrow transition $^1\mathsf{S}_0 \rightarrow {}^3\mathsf{P}_0$ in a deep 3D lattice allowed the experimental determination of scattering parameters (in s-wave approximation) regarding the ground-to-metastable interactions, before unknown. The obtained values are reported in table 4.2.1 and are consistent with similar measurement performed in the same period [44, 45].

In a second set of measurements [159], the orbital degree of freedom of ^{173}Yb was exploited in order to produce homo-nuclear molecules supported by the recently discovered Orbital Feshbach Resonance, that occurs when a nuclear spin mixture of ground and excited atoms is considered. Photoassociation processes in a 3D optical lattice have been characterized as a function of lattice confinement and magnetic field, observing the effect of the OrbFR on the binding energy of the molecular state and allowing an accurate measurement of the scattering length a_{eg}^{+}. We also developed a detection technique based on Raman bound-to-bound transitions, employed to determine the lifetime of molecules in isolated lattice sites and in a many-body environment realized by creating a stack of vertical pancakes. In the latter case we observed a lifetime of about 80 ms, currently limited by interactions between molecules and unpaired atoms still populating the sample.

The third set of experiments reported in this work was focused on the quantum simulation of analogues of the orbital-selective Mott insulating behaviour recently studied in the context of high-temperature iron-based supercondutor materials. In order to mimic orbital mixing in iron-based superconductors we considered a $\mathbb{SU}(3)$ system of ^{173}Yb atoms in a 3D optical lattice in the presence of a Raman coupling between two nuclear-spin states, that lifted the spin degeneracy, providing a controllable explicit breaking the $\mathbb{SU}(3)$ symmetry. We experimentally demonstrate that, by increasing the strength of the Raman coupling, the mean number of doubly occupied sites decreases, implying an enhancement of localization in the atomic sample. Finally, we performed a spin-selective measurement of the number of doubly-occupied sites, providing a direct demonstration of the onset of state-selective localization behaviour, that is the fundamental mechanism in the microscopic description of iron-based superconductors materials. A further characterization of the state-dependent behaviour of the system will benefit from the implementation of single-site imaging in the current experimental setup [111–113]. To this aim, first technical improvements have been implemented for increasing the stabilization of the setup, as reported in chapter 3.

The experiments described in this thesis provide a further demonstration of the versatility of ultracold systems of Yb for a variety of applications, ranging from quantum simulation to metrology. Many theoretical proposals regarding the possibilities offered by the degrees of freedom of fermionic and bosonic isotopes of Ytterbium (Yb) have been made or can be easily adapted in order to be realized in our experimental setup.

The study of the interaction properties of bosonic ^{174}Yb in 3D optical lattices, presented in chapter 4, is relevant for applications in the field of high-precision spectroscopy and metrology. Optical lattice clocks realized by probing confined bosonic atoms reached the performances achieved by fermionic optical lattice clocks. Bosonic clocks (that overcome the current definition of the SI second by about two orders of magnitude), with respect to the fermionic clocks, rely on the simpler internal structure, the higher natural abundancy, and the possibility to control the transition by applying an external field [34, 266–268]. ^{174}Yb, with respect to other elements such as ^{88}Sr, having a bigger mass and similar induced clock linewidths, is a good candidate for metrological applications.

Recent theoretical proposals have relied on the interaction strength and inelastic loss rate of ground-to-excited on-site ^{174}Yb collisions characterized in this work

in order to study the feasibility of an optical molecular clock based on ultranarrow clock transitions in $^{174}\mathsf{Yb}$ molecules prepared in high vibrational states [202]. These molecules could promise unparalleled sensitivity to the temporal variation of the electron-to-proton mass ratio and insight into possible new physics beyond the standard model [202, 269].
Moreover, the possibility to generate a coherent clock coupling between the ground state and the $^3\mathsf{P}_0$ metastable state by applying an external magnetic field suggests the use of this isotope to build a reliable quantum-information platform based on a nearly ideal two-level system [31]. In this perspective, the first characterization of state-dependent $^{174}\mathsf{Yb}$ interactions reported in this work could serve for the design and characterization of collisional quantum gates.

The results reported in chapters 5 and 6 of this thesis are a further demonstration of the richness of the $^{173}\mathsf{Yb}$ system for diverse applications in the field of quantum simulation. Many different proposal, exploiting the coherent control of both electronic and nuclear-spin degrees of freedom in $^{173}\mathsf{Yb}$, have been recently advanced. Regarding the nuclear spin d.o.f., the first observation of chiral currents in a Hall-like system by exploiting the picture of "synthetic dimension" [12, 38, 112, 145] provided a significant boost to the investigation of strongly-correlated topological states of matter. Many theoretical works highlighted intriguing possibilities resulting from the interplay between the synthetic-dimension approach and strong interactions in the system, leading e.g. to the emergence of properties that are intimately connected with the fractional quantum Hall effect [270, 271] or the identification of universal regimes in the Hall response [272]. In this respect, the experimental work reported in chapter 6 of this thesis provides an important demonstration of the possibility to study interacting $^{173}\mathsf{Yb}$ systems in the presence of a coherent coupling between internal components, i.e. of the compatibility of the synthetic-dimension approach with the strongly interacting regime. Extensions of these results to the case of spin-orbit coupling could enable the realization of those proposal and stimulate novel approaches for the study of topological effects in interacting states of matter. Regarding the coherent control of the orbital degree of freedom, i.e. the possibility to excite the doubly-forbidden transition $^1\mathsf{S}_0 \rightarrow {}^3\mathsf{P}_0$, many proposals focused on the possibilty to obtain degenerate orbital Feshbach molecules samples have been realized. In particular, due to the peculiar character of the observed Feshbach resonance, that is based on the strong orbital spin-exchange interaction in $^{173}\mathsf{Yb}$, now exciting possibility for the study of the crossover from BEC to BCS in unexplored regimes are opened [41–43]. The results presented in chapter 5, with the demonstration of novel manipulation capabilities and the characterization of the experimental lifetimes, represent a first, important step in this direction.

Appendices

A About the nature of the effective range

Let us consider the one-dimensional Schrödinger equation:

$$y'' + (\epsilon - U(x))\, y = 0. \tag{A.1}$$

By definition, the Wronskian of two function y_1, y_2 is,

$$W(y_1, y_2) \equiv y_1 y_2' - y_1' y_2. \tag{A.2}$$

From the definition we derive that, if $W(y_1, y_2)$ vanishes in each point of the entire interval $(-\infty, \infty)$, the two functions differ by a multiplicative constant.
If y_1 and y_2 are solutions of equation A.1 corresponding to the values ϵ_1, ϵ_2, for any pair of values a, b of the variable x, located in the interval where these solutions are defined:

$$W(y_1, y_2)|_a^b = (\epsilon_1 - \epsilon_2) \int_a^b y_1 y_2 \, \mathrm{d}x \tag{A.3}$$

Proof. To verify this statement is sufficient to multiply by y_1 equation A.1 evalued for y_2 and multiply equation A.1 evaluated for y_1 by y_2, then substract term by term the two resulting equations. ☐

This general result, here briefly reported, is obtained by only supposing to know two solutions of the initial differential equations and, as we will see in the following part, can be used to obtain the well-known Bethe formula. In fact, in the framework introduced in chapter 2, in which the problem of a particle that scatters in a central potential is considered, by directly using the equation introduced above, it is possible to extract the exact relation of the phase shift δ_l for the case $l = 0$.
Let us now consider two functions u_1, u_2, corresponding to the regular solutions of equation 2.1.13 and consider also the irregular solutions $\hat{u}_1$, $\hat{u}_2$ corresponding to the same energy values ϵ_1, ϵ_2 respectively. According to equation A.3

$$W(\hat{u}_1, \hat{u}_2) - W(u_1, u_2)|_a^b = (\epsilon_1 - \epsilon_2) \int_a^b (\hat{u}_1 \hat{u}_2 - u_1 u_2) \, \mathrm{d}r. \tag{A.4}$$

As $b \to \infty$, since u and $\hat{u}$ have the same asymptotic behaviour, the integral converges and the difference among the two Wronskians, evaluated at b tends to zero. Moreover, $\lim_{a\to 0} W(u_1, u_2) = 0$, so, by choosing properly the normalization for u and considering only the s wave scattering limit ($l = 0$) it is possible, by selecting also $\hat{V} = 0$ (where $\hat{V}$ is the potential corresponding to the Schrödinger equation for $\hat{u}$), to obtain

$$W(\hat{u}_1, \hat{u}_2)|_{a\to 0} \equiv k_1 \cot\delta_1 - k_2 \cot\delta_2 = (\epsilon_1 - \epsilon_2) \int (\hat{u}_1 \hat{u}_2 - u_1 u_2)\, \mathrm{d}r \tag{A.5}$$

Now, by setting $\epsilon_1 \equiv \varepsilon$, $\epsilon_2 = 0$ and by remembering that

$$\hat{u}_0 = 1 - \frac{a}{r} \qquad\qquad \lim_{\varepsilon\to 0} k\cot\delta = -\frac{1}{a} \tag{A.6}$$

it is possible to obtain the well known Bethe formula [273]:

$$k\cot\delta = -\frac{1}{a} + \varepsilon \int (\hat{u}\hat{u}_0 - u u_0)\, \mathrm{d}r \tag{A.7}$$

where solutions designated by the index 0 correspond to the zero-energy case and a is the scattering length. This relation is exact and has been used in reference [274] to express the phase shift as a series of powers of the energy.
The right-hand side of equation A.7 is usually approximated by considering $V(r)$ as a short-range potential, as it happens usually in nuclear and in atomic physics. In this case, it is possible to divide the space in two zones, one where the potential $|V| \gg \varepsilon$ and it gives a non-negligible contribution to the right-side integral, and the other one where the potential can be neglected with respect to the energy scale of the system. In this case the contribution to the integral can be neglected without committing large numerical errors. Equation A.7 can be therefore written as

$$k\cot\delta \simeq -\frac{1}{a} + \varepsilon \int_0^\infty \left(\hat{u}_0^2 - u_0^2\right)\, \mathrm{d}r \equiv -\frac{1}{a} + \varepsilon\frac{\rho_{eff}^2}{2} = -\frac{1}{a} + k^2 \frac{r_{\mathsf{eff}}}{2} \tag{A.8}$$

where r_{eff} is the so-called effective range and it is a characteristic parameter of the scattering potential $V(r)$.

B

Far-off resonance trap and lattices confinement characterization

In order to characterize experimentally the 1064 nm trap frequencies along the three orthogonal directions we performed measurements by switching on an attractive red-detuned far-off resonance laser beam (probe beam), slightly misplaced with respect to the trap equilibrium position. The total light potential felt by atoms when the probe light is shone has an absolute minimum displaced with respect to the initial equilibrium position. In order to minimize the system energy, atoms start to move to the absolute minimum as shown in figure B.1.
After a fixed pulse time (of the order of the trapping frequency), the probe beam is abruptly turned off, the light potential felt by atoms returns to be the initial one and the atoms start to oscillate in the initial harmonic trap, allowing us to

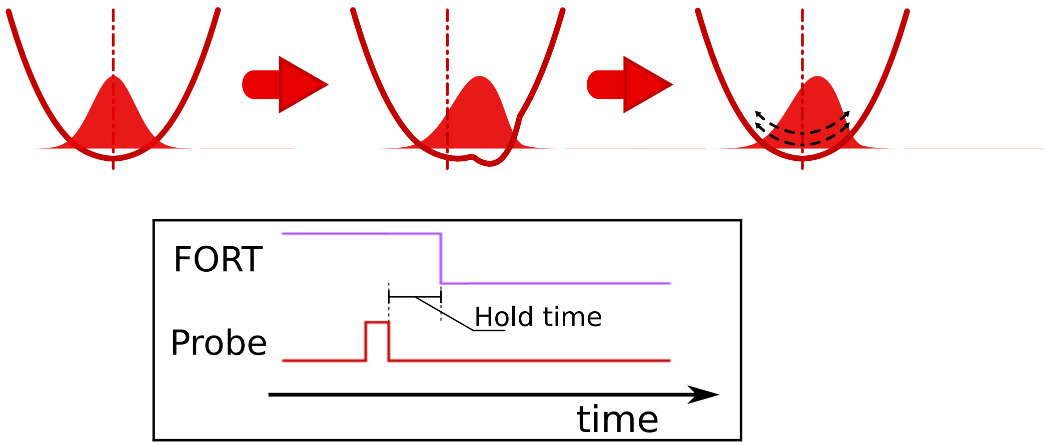

Figure B.1. Sketch of experimental sequence performed in order to measure the trapping frequencies of the harmonic confinement of the FOR Trap described in section 3.4.2. The displacement of the waist of the proble laser (wavelength 759 nm) with respect to the center of the trap is driven by changing the voltage on a piezo actuator on a mirror mounting.

measure directly the harmonic confinement frequencies, as sketched in figure B.1.

To characterize the crossed trap we recorded the mean atomic cloud position of a $^{174}\mathsf{Yb}$ BEC as a function of the hold time after the probe pulse for several values of light intensity of transport and crossed beams[1].
The obtained frequencies have been employed to determine experimentally the waist of the trap beams and the shift δz between the waist positions.
The total beam intensity in a certain spatial point $\vec{\mathsf{r}}$ can be written as

$$I\left(\vec{\mathsf{r}}\right) = \frac{2}{\pi}\frac{P_c}{w_c^2}e^{-2\frac{y^2+z^2}{w_c^2}} + \frac{2}{\pi}\frac{P_t}{w_t^2}e^{-2\frac{x^2+(z+\delta z)^2}{w_t^2}} \tag{B.1}$$

where $\{P_t,\ w_t\}$ and $\{P_c,\ w_c\}$, are the light power and the waist of the transport and of the crossed beam, respectively, and δz takes into account a possible vertical displacement of the crossed trap beams in order to obtain the maximum vertical frequency available in the combined system[2].
The complete potential can be obtained by substituting in equation 3.4.2 relation B.1 evaluated for the ground state $^1\mathsf{S}_0$ of Yb and 1064nm radiation and taking into account, on the vertical direction, the effect of gravity.
The resulting potential has been used to perform a fit in which the only free parameters are the beam waists and the dispacement δz. Best fitted parameters are: $w_c = 32.0\ \mu\mathsf{m}$, $w_t = 61.0\ \mu\mathsf{m}$, $\delta z = 11.0\ \mu\mathsf{m}$. The frequencies that it is possible to obtain from the resulting trap model have an average mean error of about 5.8 Hz with respect to the measured values (typical values at the end of the evaporative cooling are $(92.8, 72.6, 86.3)$ Hz).

In order to increase our knowledge on the trapping frequencies caused by the shape of the Gaussian beams employed to experimentally realize a 3D cubic lattice we performed a second series of experiments focused on the determination of the harmonic confinement of each lattice beam.
As a first step, to measure the harmonic frequencies corresponding to the vertical lattice we loaded the atomic sample in vertical pancakes and thus, as in the case of FOR Trap, we shone a red-detuned probe beam in order to induce an oscillation of the center of the atomic cloud in the pancakes. In order to describe the light potential of the lattice on the directions perpendicular to the strong confinement

---

[1] We choose to measure the trap frequencies by employing a $^{174}\mathsf{Yb}$ BEC in order to maximize the resolution but, since the potential felt by the $^{173}\mathsf{Yb}$ is the same, the results can be extended to this isotope (if we rescale the frequencies following the relation $f_{173}/f_{174} = \sqrt{m_{174}/m_{173}}$).

[2] The waists of the beams w_c, w_t are different, for that reason the maximum number of trapped atoms, that is the condition in which we perform all the experimental measurements, can not correspond to the condition in which the position of the transport beam on the z axis corresponds exactly to the position of the crossed beam.

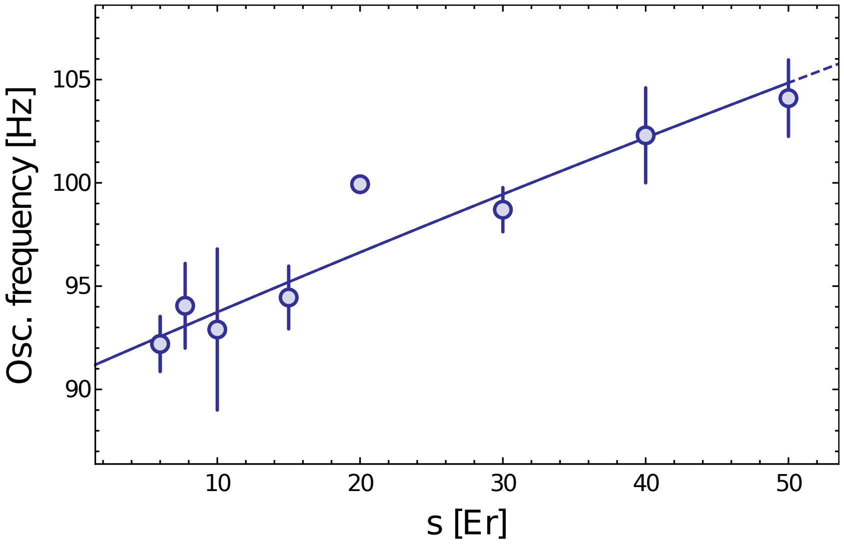

Figure B.2. A BEC is loaded in a vertical lattice and, in order to induce trap oscillations a displaced FOR probe beam is pulsed for 5 ms. Blue points are the oscillation frequency measurement results. Each point is the mean value over five experimental realizations and the error is calculated as standard deviation. The solid blue line is the best fitted function that is obtained for $A = (7.42 \pm 0.41)$ Hz.

direction, it is possible, by following equation 2.2.5, to write:

$$\mathsf{V}_{\mathsf{vlat}} = -\mathsf{s}_{\mathsf{vlat}} E_{\mathsf{r}}\ e^{-2\frac{m\pi^2}{E_{\mathsf{r}}} A^2_{\mathsf{vlat}}\left(x^2+y^2\right)} \tag{B.2}$$

where $\mathsf{s}E_{\mathsf{r}}$ represents the light intensity of the lattice beam introduced in section 2.2 and A is a parameter introduced to describe the harmonic trap confinement. We performed oscillation measurements for several values of the vertical lattice depth from $\mathsf{s}_{\mathsf{vlat}} = 6$ to $\mathsf{s}_{\mathsf{vlat}} = 50$. In each case the probe beam employed to create a perturbation on the atomic cloud is the FOR T crossed beam, that has a piezo actuator mounted on the last mirror and thus can be used to dislocate the beam waist from the initial atomic position.

The results of these measurements are reported in figure B.2; the observed frequencies have been employed to perform a fit choosing $\omega/2\pi = \sqrt{A^2\mathsf{s}_{\mathsf{vlat}}}$ as a fitting function, in which the only free parameter is the quantity A introduced in relation B.2. The best fitted model, that is represented as solid blue line in figure B.2, is obtained for $\omega_{\mathsf{vlat}}/2\pi = (7.42 \pm 0.41)\sqrt{\mathsf{s}_{\mathsf{vlat}}}$. It is also possible to directly estimate the waist of the lattice by reverting the relation [275]

$$w_{\mathsf{vlat}} = \frac{1}{\omega_{\mathsf{vlat}}}\sqrt{\frac{4\mathsf{V}_{\mathsf{vlat}}}{m}}. \tag{B.3}$$

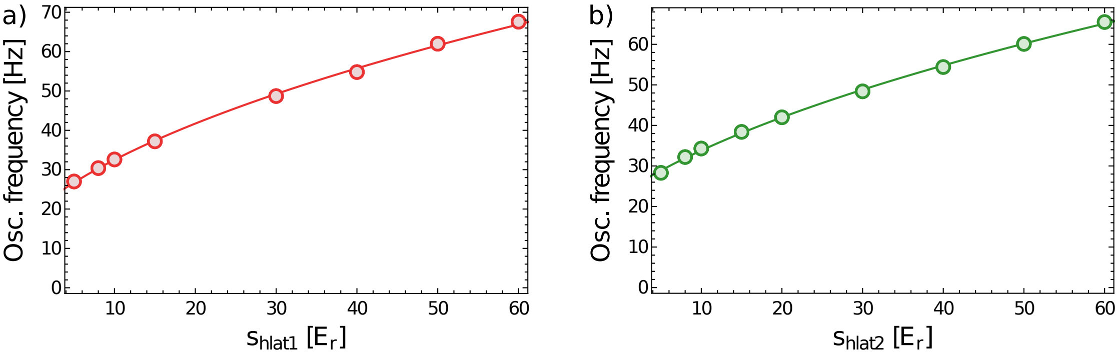

Figure B.3. A BEC is loaded in a two-dimensional lattice generated the vertical lattice beam and a horizontal lattice. Oscillations are induced by illuminating the atomic sample with a displaced FOR light. In panel a) we report frequency measurements regarding the two-dimensional lattice obtained by shining the vertical lattice and the horizontal lattice 1 described by relation B.4. Panel b) instead shows the measurements realized by shining the vertical lattice and the horizontal lattice 2 described by relation B.5. Red and green solid lines are the results of two fits (see the main text).

It allows us to determine experimentally the waist of the lattice beam considered, that corresponds to $w_{\mathrm{vlat}} \simeq 92.2\ \mu\mathrm{m}$.

In order to measure the harmonic trapping frequencies induced by the horizontal lattices it is not possible to use the same technique employed for the vertical lattice, because the horizontal lattices are not able to trap atoms by compensating the gravitational potential. In order to measure the oscillation frequency due to the harmonic confinement of the horizontal lattices, we decided to load the atoms in a two-dimensional lattice, generated by shining both the vertical lattice and a horizontal lattice onto the atoms.

Also in this case, the oscillation in the two-dimensional optical lattice was induced by a FOR probe beam, slightly displaced with respect to the waist of the lattice beam. The oscillation frequency in the transverse direction with respect to the propagation directions of the two lattice beams used to trap the atoms was measured for several horizontal lattice depths, while the vertical lattice have a depth $s_{\mathrm{vlat}} = 15$ for each horizontal lattice considered. The results of these measurement are reported in figure B.3, where the experimental data have been fitted taking into account the optical potentials

$$\mathrm{V}_{\mathrm{tot1}} = \underbrace{-s_{\mathrm{hlat1}} E_{\mathrm{r}}\, e^{-2\frac{m\pi^2}{E_{\mathrm{r}}} A^2_{\mathrm{hlat1}}\left(z^2+(\cos(\theta)x-\sin(\theta)y)^2\right)}}_{\mathrm{V}_{\mathrm{hlat1}}} + \mathrm{V}_{\mathrm{vlat}}, \qquad \text{(B.4)}$$

where θ is the angle between the crossed beam and the horizontal lattice 1 (approx.

Lattice propagation direction	Frequency $\omega/\left(2\pi\sqrt{\mathsf{s}}\right)$ [Hz]	Waist w [μm]
Horizontal 1	8.27 ± 0.06	82.8
Horizontal 2	7.87 ± 0.05	86.7
Vertical	7.42 ± 0.41	92.3
Transport		31.0
Crossed		62.0

Table B.1. In the higher part of the table we report the lattice beam waists and trap frequencies obtained by a fit following the procedure described in the main text. In the lower part we report the beam waists that allow us, knowing the reciprocal waists shift $\delta z = 11.0\ \mu$m and relation B.2, to evaluate the 3D trap frequencies.

35 degree), and

$$\mathsf{V}_{\mathsf{tot2}} = \underbrace{-\mathsf{s}_{\mathsf{hlat2}} E_{\mathsf{r}}\ e^{-2\frac{m\pi^2}{E_{\mathsf{r}}} A^2_{\mathsf{hlat2}}\left(z^2+(\cos(\theta)y+\sin(\theta)x)^2\right)}}_{\mathsf{V}_{\mathsf{hlat2}}} + \mathsf{V}_{\mathsf{vlat}}, \tag{B.5}$$

that is the corresponding relation for the horizontal lattice 2. Due to the two-dimensional lattice confinement the fitting function induced by the complete potentials B.4, B.5 is $\omega/2\pi = \sqrt{\mathsf{const.} + A^2 s}$ where const. is the constant contribution due to the vertical confinement at fixed lattice depth $\mathsf{s}_{\mathsf{vlat}} = 15$. The obtained values of waist (from equation B.3) and A for horizontal lattice 1 and lattice 2 are reported in table B.1.

Bibliography

[1] M. Inguscio and L. Fallani. *Atomic Physics*. Oxford University Press, 2018.

[2] M. H. Anderson, J. R. Ensher, M. R. Matthews, C. E. Wieman, and E. A. Cornell. Observation of Bose-Einstein Condensation in a Dilute Atomic Vapor. *Science*, 269(5221):198–201, 1995.

[3] K. B. Davis, M. O. Mewes, M. R. Andrews, N. J. van Druten, D. S. Durfee, D. M. Kurn, and W. Ketterle. Bose-Einstein Condensation in a Gas of Sodium Atoms. *Phys. Rev. Lett.*, 75:3969–3973, Nov 1995.

[4] J. R. Anglin and W. Ketterle. Bose–Einstein condensation of atomic gases. *Nature*, 416(6877):211–218, March 2002.

[5] B. DeMarco and D. S. Jin. Onset of Fermi Degeneracy in a Trapped Atomic Gas. *Science*, 285(5434):1703–1706, 1999.

[6] Richard P. Feynman. Quantum mechanical computers. *Foundations of Physics*, 16(6):507–531, June 1986.

[7] D.-W. Zhang, Y.-Q. Zhu, Y. X. Zhao, H. Yan, and S.-L. Zhu. Topological quantum matter with cold atoms. *Advances in Physics*, 67(4):253–402, 2018.

[8] G. Jotzu, M. Messer, R. Desbuquois, M. Lebrat, T. Uehlinger, D. Greif, and T. Esslinger. Experimental realization of the topological Haldane model with ultracold fermions. *Nature*, 515(7526):237–240, November 2014.

[9] H.-S. Kim and H.-Y. Kee. Realizing Haldane model in Fe-based honeycomb ferromagnetic insulators. *npj Quantum Materials*, 2(1):20, December 2017.

[10] F. D. M. Haldane. Model for a Quantum Hall Effect without Landau Levels: Condensed-Matter Realization of the "Parity Anomaly". *Phys. Rev. Lett.*, 61:2015–2018, Oct 1988.

[11] B. K. Stuhl, H.-I. Lu, L. M. Aycock, D. Genkina, and I. B. Spielman. Visualizing edge states with an atomic Bose gas in the quantum Hall regime. *Science*, 349(6255):1514–1518, 2015.

[12] M. Mancini, G. Pagano, G. Cappellini, L. Livi, M. Rider, J. Catani, C. Sias, P. Zoller, M. Inguscio, M. Dalmonte, and L. Fallani. Observation of chiral edge states with neutral fermions in synthetic Hall ribbons. *Science*, 349(6255):1510–1513, 2015.

[13] M. Aidelsburger, M. Atala, M. Lohse, J. T. Barreiro, B. Paredes, and I. Bloch. Realization of the Hofstadter Hamiltonian with Ultracold Atoms in Optical Lattices. *Phys. Rev. Lett.*, 111:185301, Oct 2013.

[14] N. F. Mott. Metal-Insulator Transition. *Rev. Mod. Phys.*, 40:677–683, Oct 1968.

[15] M. Imada, A. Fujimori, and Y. Tokura. Metal-insulator transitions. *Rev. Mod. Phys.*, 70:1039–1263, Oct 1998.

[16] L. Tarruell and L. Sanchez-Palencia. Quantum simulation of the Hubbard model with ultracold fermions in optical lattices. *Comptes Rendus Physique*, 19(6):365 – 393, 2018. Quantum simulation / Simulation quantique.

[17] H. Feshbach. Unified theory of nuclear reactions. *Annals of Physics*, 5(4):357 – 390, 1958.

[18] U. Fano. Sullo spettro di assorbimento dei gas nobili presso il limite dello spettro d'arco. *Il Nuovo Cimento (1924-1942)*, 12(3):154–161, Mar 1935.

[19] U. Fano. Effects of Configuration Interaction on Intensities and Phase Shifts. *Phys. Rev.*, 124:1866–1878, Dec 1961.

[20] T. Köhler, K. Góral, and P. S. Julienne. Production of cold molecules via magnetically tunable Feshbach resonances. *Rev. Mod. Phys.*, 78:1311–1361, Dec 2006.

[21] K. M. Jones, E. Tiesinga, P. D. Lett, and P. S. Julienne. Ultracold photoassociation spectroscopy: Long-range molecules and atomic scattering. *Rev. Mod. Phys.*, 78:483–535, May 2006.

[22] D. S. Jin and J. Ye. Introduction to Ultracold Molecules: New Frontiers in Quantum and Chemical Physics. *Chemical Reviews*, 112(9):4801–4802, September 2012.

[23] C. Chin, R. Grimm, P. Julienne, and E. Tiesinga. Feshbach resonances in ultracold gases. *Rev. Mod. Phys.*, 82:1225–1286, Apr 2010.

[24] B. J. Bloom, T. L. Nicholson, J. R. Williams, S. L. Campbell, M. Bishof, X. Zhang, W. Zhang, S. L. Bromley, and J. Ye. An optical lattice clock with accuracy and stability at the 10-18 level. *Nature*, 506(7486):71–75, January 2014.

[25] T. Bothwell, D. Kedar, E. Oelker, J. M. Robinson, S. L. Bromley, W. L. Tew, J. Ye, and C. J. Kennedy. JILA SrI Optical Lattice Clock with Uncertainty of 2.0×10^{-18}. *arXiv (preprint)*, 2019.

[26] R. Tyumenev, M. Favier, S. Bilicki, E. Bookjans, R. Le Targat, J. Lodewyck, D. Nicolodi, Y. Le Coq, M. Abgrall, J. Guéna, L. De Sarlo, and S. Bize. Comparing a mercury optical lattice clock with microwave and optical frequency standards. *New Journal of Physics*, 18(11):113002, nov 2016.

[27] M. A. Cazalilla and A. M. Rey. Ultracold Fermi gases with emergent SU(N) symmetry. *Reports on Progress in Physics*, 77(12):124401, nov 2014.

[28] C. V. Raman and K. S. Krishnan. A New Type of Secondary Radiation. *Nature*, 121(3048):501–502, March 1928.

[29] W. Kaiser and C. G. B. Garrett. Two-Photon Excitation in CaF_2: Eu^{2+}. *Phys. Rev. Lett.*, 7:229–231, Sep 1961.

[30] E. Noether. Invariant variation problems. *Transport Theory and Statistical Physics*, 1(3):186–207, 1971.

[31] G. Pagano, F. Scazza, and M. Foss-Feig. Fast and Scalable Quantum Information Processing with Two-Electron Atoms in Optical Tweezer Arrays. *Advanced Quantum Technologies*, 2(3-4):1800067, January 2019.

[32] M. Takamoto, F.-L. Hong, R. Higashi, and H. Katori. An optical lattice clock. *Nature*, 435(7040):321–324, May 2005.

[33] A. D. Ludlow, M. M. Boyd, J. Ye, E. Peik, and P. O. Schmidt. Optical atomic clocks. *Rev. Mod. Phys.*, 87:637–701, Jun 2015.

[34] S. Origlia, M. S. Pramod, S. Schiller, Y. Singh, K. Bongs, R. Schwarz, A. Al-Masoudi, S. Dörscher, S. Herbers, S. Häfner, U. Sterr, and Ch. Lisdat. Towards an optical clock for space: Compact, high-performance optical lattice clock based on bosonic atoms. *Phys. Rev. A*, 98:053443, Nov 2018.

[35] P. S. Jessen, I. H. Deutsch, and R. Stock. Quantum Information Processing with Trapped Neutral Atoms. *Quantum Information Processing*, 3(1):91–103, Oct 2004.

[36] M. L. Wall, A. P. Koller, S. Li, X. Zhang, N. R. Cooper, J. Ye, and A. M. Rey. Synthetic Spin-Orbit Coupling in an Optical Lattice Clock. *Phys. Rev. Lett.*, 116:035301, Jan 2016.

[37] S. Kolkowitz, S. L. Bromley, T. Bothwell, M. L. Wall, G. E. Marti, A. P. Koller, X. Zhang, A. M. Rey, and J. Ye. Spin–orbit-coupled fermions in an optical lattice clock. *Nature*, 542(7639):66–70, December 2016.

[38] L. F. Livi, G. Cappellini, M. Diem, L. Franchi, C. Clivati, M. Frittelli, F. Levi, D. Calonico, J. Catani, M. Inguscio, and L. Fallani. Synthetic Dimensions and Spin-Orbit Coupling with an Optical Clock Transition. *Phys. Rev. Lett.*, 117:220401, Nov 2016.

[39] G. Cappellini, M. Mancini, G. Pagano, P. Lombardi, L. Livi, M. Siciliani de Cumis, P. Cancio, M. Pizzocaro, D. Calonico, F. Levi, C. Sias, J. Catani, M. Inguscio, and L. Fallani. Direct Observation of Coherent Interorbital Spin-Exchange Dynamics. *Phys. Rev. Lett.*, 113:120402, Sep 2014.

[40] F. Scazza, C. Hofrichter, M. Höfer, P. C. De Groot, I. Bloch, and S. Fölling. Observation of two-orbital spin-exchange interactions with ultracold SU(N)-symmetric fermions. *Nature Physics*, 10(10):779–784, August 2014.

[41] L. He, J. Wang, S.-G. Peng, X.-J. Liu, and H. Hu. Strongly correlated Fermi superfluid near an orbital Feshbach resonance: Stability, equation of state, and Leggett mode. *Phys. Rev. A*, 94:043624, Oct 2016.

[42] J. Xu, R. Zhang, Y. Cheng, P. Zhang, R. Qi, and H. Zhai. Reaching a Fermi-superfluid state near an orbital Feshbach resonance. *Phys. Rev. A*, 94:033609, Sep 2016.

[43] Y.-C. Zhang, S. Ding, and S. Zhang. Collective modes in a two-band superfluid of ultracold alkaline-earth-metal atoms close to an orbital Feshbach resonance. *Phys. Rev. A*, 95:041603, Apr 2017.

[44] L. Franchi, L. F. Livi, G. Cappellini, G. Binella, M. Inguscio, J. Catani, and L. Fallani. State-dependent interactions in ultracold 174Yb probed by optical clock spectroscopy. *New Journal of Physics*, 19(10):103037, nov 2017.

[45] R. Bouganne, M. Bosch Aguilera, A. Dareau, E. Soave, J. Beugnon, and F. Gerbier. Clock spectroscopy of interacting bosons in deep optical lattices. *New Journal of Physics*, 19(11):113006, nov 2017.

[46] F. Low and G. F. Chew. *Lecture Note on Scattering Theory Seminar at University of Illinois.* 1953.

[47] T. Sasakawa. The wave packet interpretation of the scattering. *Supplement of the Progress of Theoretical Physics*, 11, 1959.

[48] A. Messiah. *Quantum Mechanics.* Dover Publications, 1999.

[49] J. T. M. Walraven. *Quantum Gases.* 2018.

[50] L. De Broglie. Recherches sur la théorie des Quanta. *Ann. Phys.*, 10(3):22–128, 1925.

[51] Z. Yan. General thermal wavelength and its applications. *European Journal of Physics*, 21:625, 11 2000.

[52] R. Shankar. *Principles of Quantum Mechanics.* Springer US, 1994.

[53] A. M. Legendre. Recherches sur l'attraction des sphéroïdes homogènes. *Mémoires de Mathématiques et de Physique*, X:411–435, 1785.

[54] M. Abramowitz and I. A. Stegun. *Handbook of Mathematical Functions with Formulas, Graphs, and Mathematical Tables.* Dover Publications, 1964.

[55] J. D. Jackson. *Classical electrodynamics.* Wiley, 1999.

[56] S. Yi and L. You. Trapped atomic condensates with anisotropic interactions. *Phys. Rev. A*, 61:041604, Mar 2000.

[57] S. Yi and L. You. Trapped condensates of atoms with dipole interactions. *Phys. Rev. A*, 63:053607, Apr 2001.

[58] A. Dalgarno and D. W. Davison. *Advances in Atomic and Molecular Physics.* Academic, 1966.

[59] S. G. Porsev, M. S. Safronova, A. Derevianko, and C. W. Clark. Long-range interaction coefficients for ytterbium dimers. *Phys. Rev. A*, 89:012711, Jan 2014.

[60] R. J. Swenson. Relation between bound-state energies and the nature of force laws. *American Journal of Physics*, 49(7):694–694, 1981.

[61] J. F. Liebman and E. D. Yorke. Are there negative bound states for the 1/r n potential? *American Journal of Physics*, 51(3):274–274, 1983.

[62] K. M. Case. Singular Potentials. *Phys. Rev.*, 80:797–806, Dec 1950.

[63] A. F. Nicholson. Simple S and D Deuteron Ground State Wavefunctions Assuming Central and r2 Tensor Potentials. *Aust. J. Phys.*, 15:169–173, 1962.

[64] Chris H. Greene, A. R. P. Rau, and U. Fano. General form of the quantum-defect theory. II. *Phys. Rev. A*, 26:2441–2459, Nov 1982.

[65] B. Gao. Solutions of the Schrödinger equation for an attractive $1/r^6$ potential. *Phys. Rev. A*, 58:1728–1734, Sep 1998.

[66] B. Gao. Repulsive $1/r^3$ interaction. *Phys. Rev. A*, 59:2778–2786, Apr 1999.

[67] B. Gao. Zero-energy bound or quasibound states and their implications for diatomic systems with an asymptotic van der Waals interaction. *Phys. Rev. A*, 62:050702, Oct 2000.

[68] B. Gao. Binding energy and scattering length for diatomic systems. *Journal of Physics B: Atomic, Molecular and Optical Physics*, 37(21):4273–4279, oct 2004.

[69] B. Gao. General form of the quantum-defect theory for $-1/r^\alpha$ type of potentials with $\alpha > 2$. *Phys. Rev. A*, 78:012702, Jul 2008.

[70] B. Gao. Quantum-defect theory of atomic collisions and molecular vibration spectra. *Phys. Rev. A*, 58:4222–4225, Nov 1998.

[71] H. Duan, L. You, and B. Gao. Ultracold collisions in the presence of synthetic spin-orbit coupling. *Phys. Rev. A*, 87:052708, May 2013.

[72] B. Gao. Quantum-defect theory for $-1/r^4$-type interactions. *Phys. Rev. A*, 88:022701, Aug 2013.

[73] R. B. Dingle. *Asymptotic Expasions: Their Derivation and Interpretation.* Academic Press, 1973.

[74] G. F. Gribakin and V. V. Flambaum. Calculation of the scattering length in atomic collisions using the semiclassical approximation. *Phys. Rev. A*, 48:546–553, Jul 1993.

[75] V. V. Flambaum, G. F. Gribakin, and C. Harabati. Analytical calculation of cold-atom scattering. *Phys. Rev. A*, 59:1998–2005, Mar 1999.

[76] C. Cohen-Tannoudji and D. Guéry-Odelin. *Advances in Atomic Physics: An Overview.* World Scientific Publishing Co. Pte. Ltd., 2011.

[77] R. Grimm, M. Weidemüller, and Y. B. Ovchinnikov. Optical Dipole Traps for Neutral Atoms. volume 42 of *Advances In Atomic, Molecular, and Optical Physics*, pages 95 – 170. Academic Press, 2000.

[78] G. Giusfredi. *Manuale di Ottica.* Springer-Verlag Mailand, 2015.

[79] M. Born and E. Wolf. *Principles of Optics: Electromagnetic Theory of Propagation, Interference and Diffraction of Light (VII Edition).* Cambridge University Press, 7th edition, 1999.

[80] É. Mathieu. Mémoire sur le mouvement vibratoire d'une membrane de forme elliptique. *Journal de Mathématiques Pures et Appliquées*, 13:137–203, 1868.

[81] N. W. Ashcroft and N. D. Mermin. *Solid State Physics.* Harcourt College Publishers, 1976.

[82] N. Marzari, A. A. Mostofi, J. R. Yates, I. Souza, and D. Vanderbilt. Maximally localized Wannier functions: Theory and applications. *Rev. Mod. Phys.*, 84:1419–1475, Oct 2012.

[83] M. Pini. *Signatures of magnetic crystals in a three-leg ladder system with synthetic gauge fields.* Master thesis, Università degli Studi di Firenze, 2016.

[84] E. Fermi. Sul moto dei neutroni nelle sostanze idrogenate. *Nuovo Cim.*, 13:434, 1936.

[85] K. Huang and C. N. Yang. Quantum-Mechanical Many-Body Problem with Hard-Sphere Interaction. *Phys. Rev.*, 105:767–775, Feb 1957.

[86] K. Huang. *Statistical Mechanics.* John Wiley & Sons, 2 edition, 1987.

[87] T. Busch, B.-G. Englert, K. Rzazewski, and M. Wilkens. Two Cold Atoms in a Harmonic Trap. *Foundations of Physics*, 28, 04 1998.

[88] D. S. Petrov, G. V. Shlyapnikov, and J. T. M. Walraven. Regimes of Quantum Degeneracy in Trapped 1D Gases. *Phys. Rev. Lett.*, 85:3745–3749, Oct 2000.

[89] G. Zürn, F. Serwane, T. Lompe, A. N. Wenz, M. G. Ries, J. E. Bohn, and S. Jochim. Fermionization of Two Distinguishable Fermions. *Phys. Rev. Lett.*, 108:075303, Feb 2012.

[90] F. Deuretzbacher, K. Plassmeier, D. Pfannkuche, F. Werner, C. Ospelkaus, S. Ospelkaus, K. Sengstock, and K. Bongs. Heteronuclear molecules in an optical lattice: Theory and experiment. *Phys. Rev. A*, 77:032726, Mar 2008.

[91] G. Cappellini, M. Mancini, G. Pagano, P. Lombardi, L. Livi, M. Siciliani de Cumis, P. Cancio, M. Pizzocaro, D. Calonico, F. Levi, C. Sias, J. Catani, M. Inguscio, and L. Fallani. Direct Observation of Coherent Interorbital Spin-Exchange Dynamics. *Phys. Rev. Lett.*, 113:120402, Sep 2014.

[92] I. Bloch, J. Dalibard, and W. Zwerger. Many-body physics with ultracold gases. *Rev. Mod. Phys.*, 80:885–964, Jul 2008.

[93] W. Pauli. Exclusion Principle and Quantum Mechanics. *Nobel Lectures, Physics 1942-1962*, 1964.

[94] D. Jaksch and P. Zoller. The cold atom Hubbard toolbox. *Annals of Physics*, 315(1):52 – 79, 2005. Special Issue.

[95] D. Jaksch, C. Bruder, J. I. Cirac, C. W. Gardiner, and P. Zoller. Cold Bosonic Atoms in Optical Lattices. *Phys. Rev. Lett.*, 81:3108–3111, Oct 1998.

[96] M. P. A. Fisher, P. B. Weichman, G. Grinstein, and D. S. Fisher. Boson localization and the superfluid-insulator transition. *Phys. Rev. B*, 40:546–570, Jul 1989.

[97] N. F. Mott. *Metal-insulator transitions.* Taylor & Francis Ltd., London, 1974.

[98] D. van Oosten, P. van der Straten, and H. T. C. Stoof. Quantum phases in an optical lattice. *Phys. Rev. A*, 63:053601, Apr 2001.

[99] Elliott H. Lieb and F. Y. Wu. Absence of Mott Transition in an Exact Solution of the Short-Range, One-Band Model in One Dimension. *Phys. Rev. Lett.*, 20:1445–1448, Jun 1968.

[100] F. H. L. Essler, V. E. Korepin, and K. Schoutens. Complete solution of the one-dimensional Hubbard model. *Phys. Rev. Lett.*, 67:3848–3851, Dec 1991.

[101] H. Yokoyama and H. Shiba. Variational Monte-Carlo Studies of Hubbard Model. I. *Journal of the Physical Society of Japan*, 56(4):1490–1506, 1987.

[102] M. Salmhofer. Continuous Renormalization for Fermions and Fermi Liquid Theory. *Communications in Mathematical Physics*, 194(2):249–295, Jun 1998.

[103] C. J. Halboth and W. Metzner. Renormalization-group analysis of the two-dimensional Hubbard model. *Phys. Rev. B*, 61:7364–7377, Mar 2000.

[104] A. Georges, G. Kotliar, W. Krauth, and M. J. Rozenberg. Dynamical mean-field theory of strongly correlated fermion systems and the limit of infinite dimensions. *Rev. Mod. Phys.*, 68:13–125, Jan 1996.

[105] Masatoshi Imada, Atsushi Fujimori, and Yoshinori Tokura. Metal-insulator transitions. *Rev. Mod. Phys.*, 70:1039–1263, Oct 1998.

[106] Thomas Obermeier, Thomas Pruschke, and Joachim Keller. Ferromagnetism in the large-U Hubbard model. *Phys. Rev. B*, 56:R8479–R8482, Oct 1997.

[107] P. T. Brown, D. Mitra, E. Guardado-Sanchez, R. Nourafkan, A. Reymbaut, C.-D. Hébert, S. Bergeron, A.-M. S. Tremblay, J. Kokalj, D. A. Huse, P. Schauß, and W. S. Bakr. Bad metallic transport in a cold atom Fermi-Hubbard system. *Science*, 363(6425):379–382, 2019.

[108] D. J. Scalapino. *Numerical Studies of the 2D Hubbard Model.* Handbook of High-Temperature Superconductivity, 01 2007.

[109] L. Del Re and M. Capone. Selective insulators and anomalous responses in three-component fermionic gases with broken SU(3) symmetry. *Phys. Rev. A*, 98:063628, Dec 2018.

[110] W. Hofstetter, J. I. Cirac, P. Zoller, E. Demler, and M. D. Lukin. High-Temperature Superfluidity of Fermionic Atoms in Optical Lattices. *Phys. Rev. Lett.*, 89:220407, Nov 2002.

[111] G. Pagano. *Many-body physics with Ytterbium Fermi gases in optical lattices: from one-dimensional systems to orbital magnetism.* Phd thesis, Scuola Normale Superiore di Pisa, 2014.

[112] M. Mancini. *Quantum Simulation with Ytterbium Atoms in Synthetic Dimensions.* Phd thesis, Università degli Studi di Firenze, 2015.

[113] G. Cappellini. *Two-orbital quantum physics in Yb Fermi gases exploiting the $^1S_0 \to {}^3P_0$ clock transition.* Phd thesis, Università degli Studi di Firenze, 2016.

[114] B.H. Bransden, C.J. Joachain, and T.J. Plivier. *Physics of Atoms and Molecules.* Pearson Education. Prentice Hall, 2003.

[115] G. Breit and Lawrence A. Wills. Hyperfine Structure in Intermediate Coupling. *Phys. Rev.*, 44:470–490, Sep 1933.

[116] A. Lurio, M. Mandel, and R. Novick. Second-Order Hyperfine and Zeeman Corrections for an (sl) Configuration. *Phys. Rev.*, 126:1758–1767, Jun 1962.

[117] M. M. Boyd, T. Zelevinsky, A. D. Ludlow, S. Blatt, T. Zanon-Willette, S. M. Foreman, and J. Ye. Nuclear spin effects in optical lattice clocks. *Phys. Rev. A*, 76:022510, Aug 2007.

[118] M. Baumann and G. Wandel. Lifetimes of the excited states (6s6p)1 P1 and (6s6p)3 P1 of ytterbium. *Physics Letters*, 22(3):283 – 285, 1966.

[119] C. Bowers, D. Budker, E. D. Commins, D. DeMille, S. J. Freedman, T. Nguyen, S.-Q. Shang, and M. Zolotorev. Experimental investigation of excited-state lifetimes in atomic ytterbium. *Physical review. A*, 53:3103–3109, 06 1996.

[120] M. Kleinert, M. E. Gold Dahl, and S. Bergeson. Measurement of the Yb I $^1S_0$–$^1P_1$ transition frequency at 399 nm using an optical frequency comb. *Phys. Rev. A*, 94:052511, Nov 2016.

[121] K. B. Blagoev and V. A. Komarovskii. Lifetimes of Levels of Neutral and Singly Ionized Lanthanide Atoms. *Atomic Data and Nuclear Data Tables*, 56(1):1 – 40, 1994.

[122] D. Das, S. Barthwal, A. Banerjee, and V. Natarajan. Absolute frequency measurements in Yb with 0.08 ppb uncertainty: Isotope shifts and hyperfine structure in the 399−nm $^1S_0 \to^1 P_1$ line. *Phys. Rev. A*, 72:032506, Sep 2005.

[123] K. Pandey, A. K. Singh, P. V. K. Kumar, M. V. Suryanarayana, and V. Natarajan. Isotope shifts and hyperfine structure in the 555.8-nm $^1S_0 \to {}^3P_1$ line of Yb. *Phys. Rev. A*, 80:022518, Aug 2009.

[124] D. L. Clark, M. E. Cage, D. A. Lewis, and G. W. Greenlees. Optical isotopic shifts and hyperfine splittings for Yb. *Phys. Rev. A*, 20:239–253, Jul 1979.

[125] J. Meija, T. B. Coplen, M. Berglund, W. A. Brand, P. De Bièvre, M. Gröning, N. E. Holden, J. Irrgeher, R. D. Loss, T. Walczyk, and T. Prohaska. Isotopic compositions of the elements 2013 (IUPAC Technical Report). *Pure and Applied Chemistry*, 88:293–306, 2016.

[126] A. Banerjee, U. D. Rapol, D. Das, A. Krishna, and V. Natarajan. Precise measurements of UV atomic lines: Hyperfine structure and isotope shifts in the 398.8 nm line of Yb. *Europhysics Letters (EPL)*, 63(3):340–346, aug 2003.

[127] W. F. Meggers, C. H. Corliss, and B. F. Scribner. Tables of spectral-line intensities. Technical report, 1975.

[128] J. J. Sakurai. *Modern quantum mechanics; rev. ed.* Addison-Wesley, Reading, MA, 1994.

[129] W. R. Johnson, K. T. Cheng, and D. R. Plante. Hyperfine structure of 2^3P levels of heliumlike ions. *Phys. Rev. A*, 55:2728–2742, Apr 1997.

[130] S. G. Porsev and A. Derevianko. Hyperfine quenching of the metastable $^3P_{0,2}$ states in divalent atoms. *Phys. Rev. A*, 69:042506, Apr 2004.

[131] Th. Becker, J. v. Zanthier, A. Yu. Nevsky, Ch. Schwedes, M. N. Skvortsov, H. Walther, and E. Peik. High-resolution spectroscopy of a single In^+ ion: Progress towards an optical frequency standard. *Phys. Rev. A*, 63:051802, Apr 2001.

[132] E. Peik, G. Hollemann, and H. Walther. Laser cooling and quantum jumps of a single indium ion. *Phys. Rev. A*, 49:402–408, Jan 1994.

[133] S. G. Porsev, A. Derevianko, and E. N. Fortson. Possibility of an optical clock using the $6^1S_0 \to 6^3P_0^o$ transition in ^{171,173}Yb atoms held in an optical lattice. *Phys. Rev. A*, 69:021403, Feb 2004.

[134] L. F. Livi. *Generation of coherent atomic states through forbidden transitions in ultracold Fermi gases.* Master thesis, Università degli Studi di Firenze, 2015.

[135] C. Clivati, G. Cappellini, L. F. Livi, F. Poggiali, M. Siciliani de Cumis, M. Mancini, G. Pagano, M. Frittelli, A. Mura, G. A. Costanzo, F. Levi, D. Calonico, L. Fallani, J. Catani, and M. Inguscio. Measuring absolute frequencies beyond the GPS limit via long-haul optical frequency dissemination. *Opt. Express*, 24(11):11865–11875, May 2016.

[136] C. W. Hoyt, Z. W. Barber, C. W. Oates, T. M. Fortier, S. A. Diddams, and L. Hollberg. Observation and Absolute Frequency Measurements of the $^1S_0$–$^3P_0$ Optical Clock Transition in Neutral Ytterbium. *Phys. Rev. Lett.*, 95:083003, Aug 2005.

[137] E. Arimondo, M. Inguscio, and P. Violino. Experimental determinations of the hyperfine structure in the alkali atoms. *Rev. Mod. Phys.*, 49:31–75, Jan 1977.

[138] R. Santra, K. V. Christ, and C. H. Greene. Properties of metastable alkaline-earth-metal atoms calculated using an accurate effective core potential. *Phys. Rev. A*, 69:042510, Apr 2004.

[139] A. V. Taichenachev, V. I. Yudin, C. W. Oates, C. W. Hoyt, Z. W. Barber, and L. Hollberg. Magnetic Field-Induced Spectroscopy of Forbidden Optical Transitions with Application to Lattice-Based Optical Atomic Clocks. *Phys. Rev. Lett.*, 96:083001, Mar 2006.

[140] Z. W. Barber, C. W. Hoyt, C. W. Oates, L. Hollberg, A. V. Taichenachev, and V. I. Yudin. Direct Excitation of the Forbidden Clock Transition in Neutral ^{174}Yb Atoms Confined to an Optical Lattice. *Phys. Rev. Lett.*, 96:083002, Mar 2006.

[141] V. D. Ovsyannikov and E. V. Chaplygin. Radiative properties of Zeeman components of atomic multiplets: Magnetically induced decay of metastable 3P2 and 3P0 states of inert gases. *Optics and Spectroscopy*, 90(2):149–156, Feb 2001.

[142] B. Odom, D. Hanneke, B. D'Urso, and G. Gabrielse. New Measurement of the Electron Magnetic Moment Using a One-Electron Quantum Cyclotron. *Phys. Rev. Lett.*, 97:030801, Jul 2006.

[143] D. A. Steck. *Quantum and Atom Optics (revision 0.12.6, 23 April 2019)*. 2007.

[144] W. F. Meggers and J. L. Tech. The first spectrum of Ytterbium (Yb I). *Journal of Research of the National Bureau of Standards*, 83:13, 1978.

[145] L. F. Livi. *New quantum simulations with ultracold Ytterbium gases*. Phd thesis, Università degli Studi di Firenze, 2018.

[146] N. Poli, Z. W. Barber, N. D. Lemke, C. W. Oates, L. S. Ma, J. E. Stalnaker, T. M. Fortier, S. A. Diddams, L. Hollberg, J. C. Bergquist, A. Brusch, S. Jefferts, T. Heavner, and T. Parker. Frequency evaluation of the doubly forbidden $^1S_0 \rightarrow ^3 P_0$ transition in bosonic ^{174}Yb. *Phys. Rev. A*, 77:050501, May 2008.

[147] P. Zeeman. Doublets and triplets in the spectrum produced by external magnetic forces. *The London, Edinburgh, and Dublin Philosophical Magazine and Journal of Science*, 44(266):55–60, 1897.

[148] A. Landé. Über den anomalen zeemaneffekt. *Zeitschrift fur Physik*, 5:231–241, jul 1921.

[149] J. Bateman, A. Xuereb, and T. Freegarde. Stimulated Raman transitions via multiple atomic levels. *Phys. Rev. A*, 81:043808, Apr 2010.

[150] Standard Atomic Weight of Ytterbium Revised. *Chemistry International*, 37(5-6), January 2015.

[151] C. R. Hammond. *The Elements, in Handbook of Chemistry and Physics (81st ed.)*. CRC press., 2000.

[152] R. Mayurama. *Optical trapping of ytterbium atoms.* Phd thesis, University of Washington, 2003.

[153] M. Wieser. Atomic weights of the elements 2005 (IUPAC Technical Report). *Pure and Applied Chemistry*, 78, 01 2006.

[154] G. Audi, O. Bersillon, J. Blachot, and A.H. Wapstra. The Nubase evaluation of nuclear and decay properties. *Nuclear Physics A*, 729(1):3–128, December 2003.

[155] T. Fukuhara, S. Sugawa, Y. Takasu, and Y. Takahashi. All-optical formation of quantum degenerate mixtures. *Phys. Rev. A*, 79:021601, Feb 2009.

[156] S. Taie, Y. Takasu, S. Sugawa, R. Yamazaki, T. Tsujimoto, R. Murakami, and Y. Takahashi. Realization of a SU(2) $\times$ SU(6) System of Fermions in a Cold Atomic Gas. *Phys. Rev. Lett.*, 105:190401, Nov 2010.

[157] S. Sugawa, K. Inaba, S. Taie, R. Yamazaki, M. Yamashita, and Y. Takahashi. Interaction and filling-induced quantum phases of dual Mott insulators of bosons and fermions. *Nature Physics*, 7(8):642–648, June 2011.

[158] M. Borkowski, R. Ciuryło, P. S. Julienne, R. Yamazaki, H. Hara, K. Enomoto, S. Taie, S. Sugawa, Y. Takasu, and Y. Takahashi. Photoassociative production of ultracold heteronuclear ytterbium molecules. *Phys. Rev. A*, 84:030702, Sep 2011.

[159] G. Cappellini, L. F. Livi, L. Franchi, D. Tusi, D. Benedicto Orenes, M. Inguscio, J. Catani, and L. Fallani. Coherent Manipulation of Orbital Feshbach Molecules of Two-Electron Atoms. *Phys. Rev. X*, 9:011028, Feb 2019.

[160] Y. Takasu, K. Komori, K. Honda, M. Kumakura, T. Yabuzaki, and Y. Takahashi. Photoassociation Spectroscopy of Laser-Cooled Ytterbium Atoms. *Phys. Rev. Lett.*, 93:123202, Sep 2004.

[161] S. G. Porsev, Yu. G. Rakhlina, and M. G. Kozlov. Electric-dipole amplitudes, lifetimes, and polarizabilities of the low-lying levels of atomic ytterbium. *Phys. Rev. A*, 60:2781–2785, Oct 1999.

[162] J. W. Cho, H.-g. Lee, S. Lee, J. Ahn, W.-K. Lee, D.-H. Yu, S. K. Lee, and C. Y. Park. Optical repumping of triplet-P states enhances magneto-optical trapping of ytterbium atoms. *Phys. Rev. A*, 85:035401, Mar 2012.

[163] P. Papagiannis, P. Karaiskos, E. Georgiou, D. Baltas, G. Lymperopoulou, E. Pantelis, and L. Sakelliou. On the use of high dose rate Ir192 and Yb169

sources with the MammoSite®radiation therapy system. *Medical Physics*, 34(9):3614–3619, August 2007.

[164] W. Grotrian. *Graphische Darstellung der Spektren von Atomen und Ionen mit ein, zwei und drei Valenzelektronen.* Springer Berlin Heidelberg, 1928.

[165] G. Cappellini, P. Lombardi, M. Mancini, G. Pagano, M. Pizzocaro, L. Fallani, and J. Catani. A compact ultranarrow high-power laser system for experiments with 578 nm ytterbium clock transition. *Review of Scientific Instruments*, 86(7):073111, 2015.

[166] T.W. Hansch and B. Couillaud. Laser frequency stabilization by polarization spectroscopy of a reflecting reference cavity. *Optics Communications*, 35(3):441 – 444, 1980.

[167] W. Nagourney. *Quantum Electronics for Atomic Physics.* Oxford Graduate Texts. OUP Oxford, 2010.

[168] I. Goti. *Optical spectroscopy of molecular iodine for a new frequency reference at 556nm.* Bachelor thesis, Università degli Studi di Firenze, 2016.

[169] R. W. P. Drever, J. L. Hall, F. V. Kowalski, J. Hough, G. M. Ford, A. J. Munley, and H. Ward. Laser phase and frequency stabilization using an optical resonator. *Applied Physics B*, 31(2):97–105, Jun 1983.

[170] F. Poggiali. *Ultranarrow laser stabilization with long-distance optical-fiber link for experiments with Ytterbium ultracold gases.* Master thesis, Università degli Studi di Firenze, 2015.

[171] L. Franchi. *Control of ultracold fermions with an optical clock transition: spin-orbit coupling and synthetic dimensions.* Master thesis, Università degli Studi di Firenze, 2016.

[172] W. Gerlach and O. Stern. Das magnetische Moment des Silberatoms. *Zeitschrift für Physik*, 9(1):353–355, Dec 1922.

[173] T. Sleator, T. Pfau, V. Balykin, O. Carnal, and J. Mlynek. Experimental demonstration of the optical Stern-Gerlach effect. *Phys. Rev. Lett.*, 68:1996–1999, Mar 1992.

[174] V. A. Dzuba and A. Derevianko. Dynamic polarizabilities and related properties of clock states of the ytterbium atom. *Journal of Physics B: Atomic, Molecular and Optical Physics*, 43(7):074011, mar 2010.

[175] B. Zimmermann, T. Müller, J. Meineke, T. Esslinger, and H. Moritz. High-resolution imaging of ultracold fermions in microscopically tailored optical potentials. *New Journal of Physics*, 13(4):043007, apr 2011.

[176] T. L. Gustavson, A. P. Chikkatur, A. E. Leanhardt, A. Görlitz, S. Gupta, D. E. Pritchard, and W. Ketterle. Transport of Bose-Einstein Condensates with Optical Tweezers. *Phys. Rev. Lett.*, 88:020401, Dec 2001.

[177] T. Kuwamoto, K. Honda, Y. Takahashi, and T. Yabuzaki. Magneto-optical trapping of Yb atoms using an intercombination transition. *Phys. Rev. A*, 60:R745–R748, Aug 1999.

[178] J. Weiner, V. S. Bagnato, S. Zilio, and P. S. Julienne. Experiments and theory in cold and ultracold collisions. *Rev. Mod. Phys.*, 71:1–85, Jan 1999.

[179] L. F. Livi. *Trasporto ottico di atomi ultrafreddi a lunga distanza.* Bachelor thesis, Università degli Studi di Firenze, 2012.

[180] *ISO 14644-1:2015 Cleanrooms and associated controlled environments – Part 1: Classification of air cleanliness by particle concentration.* 2 edition, Dec 2015.

[181] T. Tomita, S. Nakajima, Y. Takasu, and Y. Takahashi. Dissipative Bose-Hubbard system with intrinsic two-body loss. *Phys. Rev. A*, 99:031601, Mar 2019.

[182] A. J. Daley, M. M. Boyd, J. Ye, and P. Zoller. Quantum Computing with Alkaline-Earth-Metal Atoms. *Phys. Rev. Lett.*, 101:170504, Oct 2008.

[183] A. Negretti, P. Treutlein, and T. Calarco. Quantum computing implementations with neutral particles. *Quantum Information Processing*, 10(6):721, Sep 2011.

[184] R. Santra, E. Arimondo, T. Ido, C. H. Greene, and J. Ye. High-Accuracy Optical Clock via Three-Level Coherence in Neutral Bosonic ^{88}Sr. *Phys. Rev. Lett.*, 94:173002, May 2005.

[185] T. Hong, C. Cramer, W. Nagourney, and E. N. Fortson. Optical Clocks Based on Ultranarrow Three-Photon Resonances in Alkaline Earth Atoms. *Phys. Rev. Lett.*, 94:050801, Feb 2005.

[186] N. Poli, C. W. Oates, P. Gill, and G. M. Tino. Optical atomic clocks. *La Rivista del Nuovo Cimento*, 36(12):555–624, December 2013.

[187] R. H. Dicke. The Effect of Collisions upon the Doppler Width of Spectral Lines. *Phys. Rev.*, 89:472–473, Jan 1953.

[188] A. D. Ludlow. *The Strontium Optical Lattice Clock: Optical Spectroscopy with Sub-Hertz Accuracy.* Phd thesis, University of Colorado, 2008.

[189] D. Leibfried, R. Blatt, C. Monroe, and D. Wineland. Quantum dynamics of single trapped ions. *Rev. Mod. Phys.*, 75:281–324, Mar 2003.

[190] Boyd M. M. *High Precision Spectroscopy of Strontium in an Optical Lattice: Towards a New Standard for Frequency and Time.* Phd thesis, University of Washington,, 2002.

[191] T. Zelevinsky, M. M. Boyd, A. D. Ludlow, T. Ido, J. Ye, R. Ciuryło, P. Naidon, and P. S. Julienne. Narrow Line Photoassociation in an Optical Lattice. *Phys. Rev. Lett.*, 96:203201, May 2006.

[192] S. Tojo, M. Kitagawa, K. Enomoto, Y. Kato, Y. Takasu, M. Kumakura, and Y. Takahashi. High-Resolution Photoassociation Spectroscopy of Ultracold Ytterbium Atoms by Using the Intercombination Transition. *Phys. Rev. Lett.*, 96:153201, Apr 2006.

[193] M.-S. Kim, J. Lee, J. H. Lee, Y. Shin, and J. Mun. Measurements of optical Feshbach resonances of ^{174}Yb atoms. *Phys. Rev. A*, 94:042703, Oct 2016.

[194] M. Kitagawa, K. Enomoto, K. Kasa, Y. Takahashi, R. Ciuryło, P. Naidon, and P. S. Julienne. Two-color photoassociation spectroscopy of ytterbium atoms and the precise determinations of s-wave scattering lengths. *Phys. Rev. A*, 77:012719, Jan 2008.

[195] P. R. Johnson, E. Tiesinga, J. V. Porto, and C. J. Williams. Effective three-body interactions of neutral bosons in optical lattices. *New Journal of Physics*, 11(9):093022, sep 2009.

[196] R. H. Dicke. Coherence in Spontaneous Radiation Processes. *Phys. Rev.*, 93:99–110, Jan 1954.

[197] A. Yamaguchi, S. Uetake, D. Hashimoto, J. M. Doyle, and Y. Takahashi. Inelastic Collisions in Optically Trapped Ultracold Metastable Ytterbium. *Phys. Rev. Lett.*, 101:233002, Dec 2008.

[198] A. D. Ludlow, N. D. Lemke, J. A. Sherman, C. W. Oates, G. Quéméner, J. von Stecher, and A. M. Rey. Cold-collision-shift cancellation and inelastic scattering in a Yb optical lattice clock. *Phys. Rev. A*, 84:052724, Nov 2011.

[199] A. Traverso, R. Chakraborty, Y. N. Martinez de Escobar, P. G. Mickelson, S. B. Nagel, M. Yan, and T. C. Killian. Inelastic and elastic collision rates for triplet states of ultracold strontium. *Phys. Rev. A*, 79:060702, Jun 2009.

[200] F. Dalfovo, S. Giorgini, L. P. Pitaevskii, and S. Stringari. Theory of Bose-Einstein condensation in trapped gases. *Rev. Mod. Phys.*, 71:463–512, Apr 1999.

[201] Y. Nakamura, Y. Takasu, J. Kobayashi, H. Asaka, Y. Fukushima, K. Inaba, M. Yamashita, and Y. Takahashi. Experimental determination of Bose-Hubbard energies. *Phys. Rev. A*, 99:033609, Mar 2019.

[202] M. Borkowski. Optical Lattice Clocks with Weakly Bound Molecules. *Phys. Rev. Lett.*, 120:083202, Feb 2018.

[203] T.-L. Ho. Spinor Bose Condensates in Optical Traps. *Phys. Rev. Lett.*, 81:742–745, Jul 1998.

[204] D. M. Stamper-Kurn and M. Ueda. Spinor Bose gases: Symmetries, magnetism, and quantum dynamics. *Rev. Mod. Phys.*, 85:1191–1244, Jul 2013.

[205] A. V. Gorshkov, M. Hermele, V. Gurarie, C. Xu, P. S. Julienne, J. Ye, P. Zoller, E. Demler, M. D. Lukin, and A. M. Rey. Two-orbital SU(N) magnetism with ultracold alkaline-earth atoms. *Nature Physics*, 6(4):289–295, February 2010.

[206] E. Merzbacher. *Quantum Mechanics.* Wiley, 1998.

[207] Á. Rapp, G. Zaránd, C. Honerkamp, and W. Hofstetter. Color Superfluidity and "Baryon" Formation in Ultracold Fermions. *Phys. Rev. Lett.*, 98:160405, Apr 2007.

[208] D. Banerjee, M. Bögli, M. Dalmonte, E. Rico, P. Stebler, U.-J. Wiese, and P. Zoller. Atomic Quantum Simulation of $\mathbf{U}(N)$ and SU(N) Non-Abelian Lattice Gauge Theories. *Phys. Rev. Lett.*, 110:125303, Mar 2013.

[209] T. Ozawa and G. Baym. Population imbalance and pairing in the BCS-BEC crossover of three-component ultracold fermions. *Phys. Rev. A*, 82:063615, Dec 2010.

[210] M. Höfer, L. Riegger, F. Scazza, C. Hofrichter, D. R. Fernandes, M. M. Parish, J. Levinsen, I. Bloch, and S. Fölling. Observation of an Orbital Interaction-Induced Feshbach Resonance in ^{173}Yb. *Phys. Rev. Lett.*, 115:265302, Dec 2015.

[211] X. Zhang, M. Bishof, S. L. Bromley, C. V. Kraus, M. S. Safronova, P. Zoller, A. M. Rey, and J. Ye. Spectroscopic observation of SU(N)-symmetric interactions in Sr orbital magnetism. *Science*, 345(6203):1467–1473, 2014.

[212] K. Ono, J. Kobayashi, Y. Amano, K. Sato, and Y. Takahashi. Antiferromagnetic interorbital spin-exchange interaction of ^{171}Yb. *Phys. Rev. A*, 99:032707, Mar 2019.

[213] R. Zhang, Y. Cheng, H. Zhai, and P. Zhang. Orbital Feshbach Resonance in Alkali-Earth Atoms. *Phys. Rev. Lett.*, 115:135301, Sep 2015.

[214] C.J. Joachain. *Quantum collision theory.* North-Holland, 1983.

[215] A. J. Moerdijk, B. J. Verhaar, and A. Axelsson. Resonances in ultracold collisions of ^{6}Li, ^{7}Li, and ^{23}Na. *Phys. Rev. A*, 51:4852–4861, Jun 1995.

[216] G. Pagano, M. Mancini, G. Cappellini, L. Livi, C. Sias, J. Catani, M. Inguscio, and L. Fallani. Strongly Interacting Gas of Two-Electron Fermions at an Orbital Feshbach Resonance. *Phys. Rev. Lett.*, 115:265301, Dec 2015.

[217] M. S. Safronova, S. G. Porsev, and Charles W. Clark. Ytterbium in Quantum Gases and Atomic Clocks: van der Waals Interactions and Blackbody Shifts. *Phys. Rev. Lett.*, 109:230802, Dec 2012.

[218] A. Micheli, G. K. Brennen, and P. Zoller. A toolbox for lattice-spin models with polar molecules. *Nature Physics*, 2(5):341–347, April 2006.

[219] I. Bloch, J. Dalibard, and S. Nascimbène. Quantum simulations with ultracold quantum gases. *Nature Physics*, 8(4):267–276, April 2012.

[220] R. Barnett, D. Petrov, M. Lukin, and E. Demler. Quantum Magnetism with Multicomponent Dipolar Molecules in an Optical Lattice. *Physical Review Letters*, 96(19), May 2006.

[221] M. S. Safronova, D. Budker, D. DeMille, Derek F. Jackson Kimball, A. Derevianko, and Charles W. Clark. Search for new physics with atoms and molecules. *Rev. Mod. Phys.*, 90:025008, Jun 2018.

[222] J. L. Bohn, A. M. Rey, and J. Ye. Cold molecules: Progress in quantum engineering of chemistry and quantum matter. *Science*, 357(6355):1002–1010, 2017.

[223] L. D. Carr, D. DeMille, R. V. Krems, and J. Ye. Cold and ultracold molecules: science, technology and applications. *New Journal of Physics*, 11(5):055049, may 2009.

[224] L. De Marco, G. Valtolina, K. Matsuda, W. G. Tobias, J. P. Covey, and J. Ye. A degenerate Fermi gas of polar molecules. *Science*, 363(6429):853–856, 2019.

[225] S. A. Moses, J. P. Covey, M. T. Miecnikowski, D. S. Jin, and J. Ye. New frontiers for quantum gases of polar molecules. *Nature Physics*, 13:13–20, January 2017.

[226] A. V. Gorshkov, S. R. Manmana, G. Chen, J. Ye, E. Demler, M. D. Lukin, and A. M. Rey. Tunable Superfluidity and Quantum Magnetism with Ultracold Polar Molecules. *Phys. Rev. Lett.*, 107:115301, Sep 2011.

[227] B. Capogrosso-Sansone, C. Trefzger, M. Lewenstein, P. Zoller, and G. Pupillo. Quantum Phases of Cold Polar Molecules in 2D Optical Lattices. *Phys. Rev. Lett.*, 104:125301, Mar 2010.

[228] S. Ospelkaus, K.-K. Ni, D. Wang, M. H. G. de Miranda, B. Neyenhuis, G. Quéméner, P. S. Julienne, J. L. Bohn, D. S. Jin, and J. Ye. Quantum-State Controlled Chemical Reactions of Ultracold Potassium-Rubidium Molecules. *Science*, 327(5967):853–857, 2010.

[229] H. R. Thorsheim, J. Weiner, and P. S. Julienne. Laser-induced photoassociation of ultracold sodium atoms. *Phys. Rev. Lett.*, 58:2420–2423, Jun 1987.

[230] A. Fioretti, D. Comparat, A. Crubellier, O. Dulieu, F. Masnou-Seeuws, and P. Pillet. Formation of Cold Cs_2 Molecules through Photoassociation. *Phys. Rev. Lett.*, 80:4402–4405, May 1998.

[231] S. Inouye, M. R. Andrews, J. Stenger, H.-J. Miesner, D. M. Stamper-Kurn, and W. Ketterle. Observation of Feshbach resonances in a Bose–Einstein condensate. *Nature*, 392(6672):151–154, March 1998.

[232] Xia-Ji Liu and Hui Hu. Topological superfluid in one-dimensional spin-orbit-coupled atomic Fermi gases. *Phys. Rev. A*, 85:033622, Mar 2012.

[233] H. Zhai. Degenerate quantum gases with spin–orbit coupling: a review. *Reports on Progress in Physics*, 78(2):026001, feb 2015.

[234] Y. Cheng, R. Zhang, and P. Zhang. Quantum defect theory for the orbital Feshbach resonance. *Phys. Rev. A*, 95:013624, Jan 2017.

[235] S. L. Campbell, R. B. Hutson, G. E. Marti, A. Goban, N. Darkwah Oppong, R. L. McNally, L. Sonderhouse, J. M. Robinson, W. Zhang, B. J. Bloom, and

J. Ye. A Fermi-degenerate three-dimensional optical lattice clock. *Science*, 358(6359):90–94, 2017.

[236] Z. Fu, L. Huang, Z. Meng, P. Wang, L. Zhang, S. Zhang, H. Zhai, P. Zhang, and J. Zhang. Production of Feshbach molecules induced by spin–orbit coupling in Fermi gases. *Nature Physics*, 10(2):110–115, December 2013.

[237] B. H. McGuyer, M. McDonald, G. Z. Iwata, M. G. Tarallo, A. T. Grier, F. Apfelbeck, and T. Zelevinsky. High-precision spectroscopy of ultracold molecules in an optical lattice. *New Journal of Physics*, 17(5):055004, may 2015.

[238] S. Taie, S. Watanabe, T. Ichinose, and Y. Takahashi. Feshbach-Resonance-Enhanced Coherent Atom-Molecule Conversion with Ultranarrow Photoassociation Resonance. *Phys. Rev. Lett.*, 116:043202, Jan 2016.

[239] O. Dulieu and C. Gabbanini. The formation and interactions of cold and ultracold molecules: new challenges for interdisciplinary physics. *Reports on Progress in Physics*, 72(8):086401, jul 2009.

[240] J. G. Danzl, E. Haller, M. Gustavsson, M. J. Mark, R. Hart, N. Bouloufa, O. Dulieu, H. Ritsch, and H.-C. Nägerl. Quantum Gas of Deeply Bound Ground State Molecules. *Science*, 321(5892):1062–1066, 2008.

[241] A. N. Nikolov, E. E. Eyler, X. T. Wang, J. Li, H. Wang, W. C. Stwalley, and P. L. Gould. Observation of Ultracold Ground-State Potassium Molecules. *Phys. Rev. Lett.*, 82:703–706, Jan 1999.

[242] J. M. Sage, S. Sainis, T. Bergeman, and D. DeMille. Optical Production of Ultracold Polar Molecules. *Phys. Rev. Lett.*, 94:203001, May 2005.

[243] Y. Takasu, Y. Fukushima, Y. Nakamura, and Y. Takahashi. Magnetoassociation of a Feshbach molecule and spin-orbit interaction between the ground and electronically excited states. *Phys. Rev. A*, 96:023602, Aug 2017.

[244] S. A. Moses, J. P. Covey, M. T. Miecnikowski, B. Yan, B. Gadway, J. Ye, and D. S. Jin. Creation of a low-entropy quantum gas of polar molecules in an optical lattice. *Science*, 350(6261):659–662, 2015.

[245] J. Herbig, T. Kraemer, M. Mark, T. Weber, C. Chin, H.-C. Nägerl, and R. Grimm. Preparation of a Pure Molecular Quantum Gas. *Science*, 301(5639):1510–1513, 2003.

[246] S. Dürr, T. Volz, A. Marte, and G. Rempe. Observation of Molecules Produced from a Bose-Einstein Condensate. *Phys. Rev. Lett.*, 92:020406, Jan 2004.

[247] K. Xu, T. Mukaiyama, J. R. Abo-Shaeer, J. K. Chin, D. E. Miller, and W. Ketterle. Formation of Quantum-Degenerate Sodium Molecules. *Phys. Rev. Lett.*, 91:210402, Nov 2003.

[248] G. Thalhammer, K. Winkler, F. Lang, S. Schmid, R. Grimm, and J. Hecker Denschlag. Long-Lived Feshbach Molecules in a Three-Dimensional Optical Lattice. *Phys. Rev. Lett.*, 96:050402, Feb 2006.

[249] M. Mark, F. Ferlaino, S. Knoop, J. G. Danzl, T. Kraemer, C. Chin, H.-C. Nägerl, and R. Grimm. Spectroscopy of ultracold trapped cesium Feshbach molecules. *Phys. Rev. A*, 76:042514, Oct 2007.

[250] T. Stöferle, H. Moritz, K. Günter, M. Köhl, and T. Esslinger. Molecules of Fermionic Atoms in an Optical Lattice. *Phys. Rev. Lett.*, 96:030401, Jan 2006.

[251] C. A. Regal, M. Greiner, and D. S. Jin. Lifetime of Molecule-Atom Mixtures near a Feshbach Resonance in ^{40}K. *Phys. Rev. Lett.*, 92:083201, Feb 2004.

[252] A. Chotia, B. Neyenhuis, S. A. Moses, B. Yan, J. P. Covey, M. Foss-Feig, A. M. Rey, D. S. Jin, and J. Ye. Long-Lived Dipolar Molecules and Feshbach Molecules in a 3D Optical Lattice. *Phys. Rev. Lett.*, 108:080405, Feb 2012.

[253] C.-H. Wu, J. W. Park, P. Ahmadi, S. Will, and M. W. Zwierlein. Ultracold Fermionic Feshbach Molecules of $^{23}\mathrm{Na}^{40}\mathbf{K}$. *Phys. Rev. Lett.*, 109:085301, Aug 2012.

[254] Y. Kamihara, T. Watanabe, M. Hirano, and H. Hosono. Iron-Based Layered Superconductor La[O1-xFx]FeAs (x= 0.05-0.12) withTc= 26 K. *Journal of the American Chemical Society*, 130(11):3296–3297, March 2008.

[255] S. Lafuerza, H. Gretarsson, F. Hardy, T. Wolf, C. Meingast, G. Giovannetti, M. Capone, A. S. Sefat, Y.-J. Kim, P. Glatzel, and L. de' Medici. Evidence of Mott physics in iron pnictides from x-ray spectroscopy. *Phys. Rev. B*, 96:045133, Jul 2017.

[256] F. Hardy, A. E. Böhmer, L. de' Medici, M. Capone, G. Giovannetti, R. Eder, L. Wang, M. He, T. Wolf, P. Schweiss, R. Heid, A. Herbig, P. Adelmann, R. A. Fisher, and C. Meingast. Strong correlations, strong coupling, and *s*-wave superconductivity in hole-doped $\mathrm{BaFe_2As_2}$ single crystals. *Phys. Rev. B*, 94:205113, Nov 2016.

[257] L. de' Medici, G. Giovannetti, and M. Capone. Selective Mott Physics as a Key to Iron Superconductors. *Phys. Rev. Lett.*, 112:177001, Apr 2014.

[258] M. Yi, D. H. Lu, R. Yu, S. C. Riggs, J.-H. Chu, B. Lv, Z. K. Liu, M. Lu, Y.-T. Cui, M. Hashimoto, S.-K. Mo, Z. Hussain, C. W. Chu, I. R. Fisher, Q. Si, and Z.-X. Shen. Observation of Temperature-Induced Crossover to an Orbital-Selective Mott Phase in $\mathrm{A}_x\mathrm{Fe}_{2-y}\mathrm{Se}_2$ (A=K, Rb) Superconductors. *Phys. Rev. Lett.*, 110:067003, Feb 2013.

[259] R. Yu and Q. Si. Orbital-Selective Mott Phase in Multiorbital Models for Alkaline Iron Selenides $\mathbf{K}_{1-x}\mathrm{Fe}_{2-y}\mathrm{Se}_2$. *Phys. Rev. Lett.*, 110:146402, Apr 2013.

[260] R. Jördens, N. Strohmaier, K. Günter, H. Moritz, and T. Esslinger. A Mott insulator of fermionic atoms in an optical lattice. *Nature*, 455(7210):204–207, September 2008.

[261] R. Jördens, L. Tarruell, D. Greif, T. Uehlinger, N. Strohmaier, H. Moritz, T. Esslinger, L. De Leo, C. Kollath, A. Georges, V. Scarola, L. Pollet, E. Burovski, E. Kozik, and M. Troyer. Quantitative Determination of Temperature in the Approach to Magnetic Order of Ultracold Fermions in an Optical Lattice. *Phys. Rev. Lett.*, 104:180401, May 2010.

[262] T.-L. Ho and Q. Zhou. Squeezing out the entropy of fermions in optical lattices. *Proceedings of the National Academy of Sciences*, 106(17):6916–6920, April 2009.

[263] J. H. Han, J. H. Kang, M. Lee, and Y. Shin. Photoassociation spectroscopy of ultracold ^{173}Yb atoms near the intercombination line. *Phys. Rev. A*, 97:013401, Jan 2018.

[264] Hofrichter C. *Probing the SU(N) Fermi-Hubbard model with ytterbium atoms in an optical lattice.* Phd thesis, Ludwig-Maximilians-Universität München, 2016.

[265] M. Miranda, R. Inoue, N. Tambo, and M. Kozuma. Site-resolved imaging of a bosonic Mott insulator using ytterbium atoms. *Phys. Rev. A*, 96:043626, Oct 2017.

[266] T. Akatsuka, M. Takamoto, and H. Katori. Three-dimensional optical lattice clock with bosonic ^{88}Sr atoms. *Phys. Rev. A*, 81:023402, Feb 2010.

[267] P. Morzyński, M. Bober, D. Bartoszek-Bober, J. Nawrocki, P. Krehlik, Ł. Śliwczyński, M. Lipiński, P. Masłowski, A. Cygan, P. Dunst, M. Garus,

D. Lisak, J. Zachorowski, W. Gawlik, C. Radzewicz, R. Ciuryło, and M. Zawada. Absolute measurement of the 1S0 - 3P0 clock transition in neutral 88Sr over the 330 km-long stabilized fibre optic link. *Scientific Reports*, 5(1), December 2015.

[268] Z. Barber, C. Hoyt, J. Stalnaker, N. Lemke, C. Oates, T. Fortier, S. Diddams, and L. Hollberg. Lattice-based optical clock using an even isotope of Yb. *Proceedings of SPIE - The International Society for Optical Engineering*, 6673, 10 2007.

[269] P. Tecmer, K. Boguslawski, M. Borkowski, P. S. Żuchowski, and D. Kędziera. Modeling the electronic structures of the ground and excited states of the ytterbium atom and the ytterbium dimer: A modern quantum chemistry perspective. *International Journal of Quantum Chemistry*, 119(18), 2019.

[270] S. Barbarino, L. Taddia, D. Rossini, L. Mazza, and R. Fazio. Magnetic crystals and helical liquids in alkaline-earth fermionic gases. *Nature Communications*, 6(1), September 2015.

[271] S. Barbarino, L. Taddia, D. Rossini, L. Mazza, and R. Fazio. Synthetic gauge fields in synthetic dimensions: interactions and chiral edge modes. *New Journal of Physics*, 18(3):035010, mar 2016.

[272] M. Filippone, C.-E. Bardyn, S. Greschner, and T. Giamarchi. Vanishing Hall Response of Charged Fermions in a Transverse Magnetic Field. *Phys. Rev. Lett.*, 123:086803, Aug 2019.

[273] H. A. Bethe. Theory of the Effective Range in Nuclear Scattering. *Phys. Rev.*, 76:38–50, Jul 1949.

[274] G. F. Chew and M. L. Goldberger. On the Analysis of Nucleon-Nucleon Scattering Experiments. *Phys. Rev.*, 75:1637–1644, Jun 1949.

[275] M. N. Bishof. *Understanding atomic interactions in an optical lattice clock and using them to study many-body physics.* Phd thesis, University of Colorado, 2014.